



**Development of a Rapid Compression Machine for Screening
Alternative Fuel for Gas Turbines.**

Oku Ekpenyong Nyong

Supervisors

Dr Robert Woolley

Professor Yang Zhang

A Thesis submitted to the Department of Mechanical Engineering

In partial fulfilment of the requirement for the degree of

“Doctor of Philosophy”

Department of Mechanical Engineering

Sheffield, United Kingdom

The University of Sheffield

January 2017

UNIVERSITY OF SHEFFIELD

RESEARCH AND INNOVATION SERVICES

The signatories certify that they have read, and recommend to Research and Innovation Services for acceptance, a thesis entitled "Development of a Rapid Compression Machine for Screening Alternative Fuels for Gas Turbine Plant" submitted by Oku Ekpenyong Nyong in partial fulfilment of the requirements of the degree of "Doctorate of Philosophy".

Supervisors, Dr. Robert Wooley, Mechanical Engineering

Supervisors, Prof. Yang Zhang, Mechanical Engineering

Date

Abstract

The reduction of NO_x, soot and other emissions in aero or industrial gas turbines are engaged by the concept of new combustion system such as the lean premixed pre-vaporized system. Which brings with it several engineering solutions such as combustion instabilities, flashback and autoignition. An experimental test rig named Sheffield Rapid Compression Machine (Shef-RCM) is designed to investigate the autoignition chemistry of alternative fuels relevant to gas turbine plant and to handle high boiling point long chain hydrocarbon fuels.

The Shef-RCM incorporates a hydraulic stopping mechanism, piston release mechanism, an optimal crevice piston design and a reactor chamber is designed which utilises the direct test chamber method for easy admittance of fuels. The machine is pneumatically driven and hydraulically stopped. The novelty in the design of the Shef-RCM is the introduction of a piston release mechanism (brake) pneumatically operated use to hold the reactor piston in position at its bottom dead centre.

A computational fluid dynamics study on crevice piston was undertaken to produce the best-optimized crevice piston head design that will suppress the roll-up vortex to enhance the homogeneity of the temperature field of the reactor chamber. The simulation used a 2-Dimensional computational moving mesh axisymmetric in the commercial code of Ansys fluent. The model adopted for this calculation was the laminar flow. Appropriate choice of the model parameter was taken into consideration during the simulation to reduce errors caused by a poor mesh quality. These parametric studies examine the time step size and the mesh density, which was deemed necessary for running the simulation to handle errors of negative cell volume. The parameters maintained for the model are a constant stroke length of 142 mm with a volume clearance height of 17 mm. Further optimisation of a 282 mm³ crevice volume on the width resulted to five different crevice widths of 3 mm, 5 mm, 7mm, 9 mm and 12 mm respectively. The widths of the piston head crevice of 5mm gave a better result regarding the peak pressure profile and maintained a homogeneous temperature field at the end of the TDC at post compression time of about 40ms.

Performance characterization of the Shef-RCM, using inert gases, N-Heptane and Jet A-1 showed that the experimental data obtained was highly reproducible and repeatable. The machine is vibration free, allows for fast compression, less than 35 ms, an obtainable compressed gas pressure of 22 bar. The estimation of the compressed gas temperature at the top dead centre using numerical modelling was 698 K; the heat loss implemented in the model used an effective volume approach, which showed a perfect match for the model with experiment.

Ignition delay time measurement for Jet A-1 are reported for low to intermediate temperatures regime ($734 \leq T_c \leq 815$)K, compressed gas pressure, $P_c = 6$ and 10 bar and equivalent ratios, $\phi = 0.5, 0.75$ and 1.0 in air. Jet A-1 exhibited Arrhenius behaviour at 6 bar and 10 bar except for some suspected traces of NTC at $\phi = 0.5$, which needed to be fully

established. No evident of Negative Temperature Coefficients (NTC) behaviour at a higher pressure of 10 bar. The kinetic modelling conducted for Jet A-1 used Ranzi et al.[1] model with Dooley et al. [2] and Aachen[3] surrogate mixture. At a compressed pressure of 6 bar, $\phi=0.75$, the model predicted a shorter ignition delay time and displayed a two stage ignition delay time for Jet A-1 fuel, and the model was in agreement with the experiment. The Shef-RCM facility has also been used to measure the combustion behaviour of Banner-Solvent at low to intermediate temperature regime ($718 \leq T_C \leq 916$) K at compressed pressure, $P_C =$ of 6 and 10 bar, and equivalence ratios, $\phi=0.5, 0.75$ and 1.0 in air. Various diluent mixtures were carried out to alter the end gas temperature, it was found that ignition delay within the temperature range of 718 – 916 K exhibited NTC behaviour at lean condition and stoichiometric. Banner-Solvent reacts faster compare to Jet A-1, and this showed some trend of Negative Temperature Coefficient behaviour at a compressed gas pressure of 6 bar. Experimental measurement of the ignition delay response of UCO-HEFA at low to intermediate temperature regime ($680 \leq T_C \leq 777$) K at compressed gas pressure, $P_C =$ 6 and 10 bar, and equivalence ratios, $\phi=0.5, 0.75$ and 1.0 in air was studied. The effects of temperature, pressure, and equivalence ratio and oxygen concentration on the ignition delay time was investigated. The overall reactivity of the three fuels showed that Banner-Solvent had showed a higher reactivity than Jet A-1 and UCO-HEFA at 10 bar compressed gas pressure. At 6 bar compressed gas pressure, UCO-HEFA showed some signs of NTC behaviour. The uncertainty for the three fuels was considered and this was seen to be within the limits compared in literature. The global correlation for Jet A-1 and UCO-HEFA were derived for both fuels.

Acknowledgements

My profound gratitude to God Almighty for his immeasurable favour, deity and sufficiency, which has kept me throughout my research work. My thanks go to my supervisors: my principal supervisor, Dr Robert Woolley, and Professor Yang Zhang, Dr.Simon Blakey and late professor Chris Wilson for their support, time and guidance throughout my research work. I want to commend my colleague Ryan Marshall who started the design of the rig but eventually transited out of the program. Thanks, goes to Malcolm Nettleship, the laboratory technician now retired, for his involvement in the Design of the Shef-RCM rig, he has been a great asset in the workshop, I indeed learnt from his wealth of experience. Oliver Cooper has been supportive and always there in the lab to render his assistance. Not forgetting Andrian Lumby from Chemical Engineering Department, he has been very helpful supplying me with inert gases when needed. Also from the Low Carbon Combustion Centre, I acknowledge Dr. Bhupendra Khandelwal for his assistance in providing Banner-Solvent for running the rig, Dr. Ehsan Albozi so his support and advice. Dell, David and others do not mention here for all their supports throughout my coursework in Sheffield.

I acknowledge Tertiary Education Trust Fund (TETFUND), Nigeria, for the privilege accorded me to study in the UK, but unfortunately did not provide for my needs for the rest part of my PhD program. I was not discouraged despite the setbacks and the terrible situation I strived harder and was the focus until the end of my PhD work.

Immeasurable thanks go to my lovely wife and my three kids(Deborah, Mirabel and Daniel) for their love, understanding and patience, and particularly, during the periods I have been away from them for more than two years. My parents have been inspirational; I acknowledge them for their parental love, support and tolerance.

I also recognise and appreciate the effort of my friends and colleagues Emamode Ubogu, Martin Balogun, Benjamin Oluwadare, Olatunde Ojo, David Akindede and a few not mention because of limited space, which has impacted positively to the progress of my study in Sheffield. I wish everyone the best in their human endeavour.

Table of Contents

Chapter 1. Introduction	1
1.0 Background Information	1
1.1 Processing pathway.....	2
1.1.1 Hydroprocess Fatty Acids.....	2
1.1.2 Fischer-Tropsch Process.....	3
1.2 Potential Alternative Fuels.....	4
1.2.1 Cryogenic Fuels.....	5
1.2.2 Bio-Derived Fuels	6
1.2.3 Alcohol to Jet (ATJ).....	7
1.3 Approval Process	8
1.4 Motives for Diversification into Use of Alternative Fuels.	10
1.4.1 Political Crisis and Depletion of Natural Resources	11
1.4.2 Air quality issues	12
1.4.3 Exorbitant Price Issues.....	12
1.4.4 Technical Requirements.....	14
1.5 Research Objectives	18
1.6 Layout of the Thesis.....	19
Chapter 2. Literature Review.....	21
2.1 Introduction.....	21
2.2 Historical Development of Rapid Compression Machine (RCM).....	21
2.3 Progress in Rapid Compression Machine Technology	27
2.3.1 Single Piston RCM.....	27
2.3.2 Twin piston RCM.....	29
2.3.3 The Camshaft connection RCM.....	29
2.3.4 The hydraulic braking mechanism.....	30
2.3.5 Design of combustion chamber and charge preparation Approach	30
2.4 Other Instrument for measuring Autoignition Delay.....	31
2.4.1 Shock Tube	31
2.4.2 Flow Reactor	33
2.4.3 Well-Stirred Reactors.....	34
2.4.4 Static Reactor	35
2.5 Current Fuels Studied	36
2.5.1 Current Fuel Formulation	36
2.5.2 Jet A-1.....	38

2.5.3	Banner Solvent.....	40
2.5.4	Used cooking oil (UCO-HEFA).....	41
2.6	Basic Concept of Autoignition	41
2.6.1	Ignition Limits	42
2.7	Basic Concept of Chemical Kinetics.....	44
2.7.1	Hydrocarbon Oxidation and Mechanisms.....	45
2.7.2	Surrogate Fuel as a Representative of Alternative Aviation Fuel.	48
2.7.3	The concept of Surrogate Fuels.	48
2.7.4	Surrogate Formulations.	49
Chapter 3.	Experimental Facility and Technique.....	51
3.1	Developmental Overview of Sheffield Rapid Compression Machine (Shef-RCM) 51	
3.2	Driving Section of the Shef-RCM.....	52
3.3	Combustion Chamber Design	53
3.3.1	Combustion Chamber Volume Estimation.....	55
3.4	Hydraulic Damping Mechanism.....	57
3.5	Piston release mechanism.....	62
3.6	Piston Design	63
3.6.1	Piston Stroke and Velocity Profile.	64
3.7	Compression Time Measurement	67
3.8	Direct Premixed Charge Preparation.....	68
3.8.1	Fuel Evaporation and Mixing Time.....	69
3.8.2	Mixture Preparation.....	70
3.9	Triggering System and Data Acquisition	70
3.9.1	LVDT Measurement and Calibration.....	71
3.10	Static Pressure Transducer and Calibration.....	71
3.11	Uncertainty in the Parameters in RCM Experiment.....	72
3.11.1	Uncertainty in the Stroke Measurement.....	72
3.11.2	Uncertainty in the Initial Pressure	72
3.11.3	Uncertainty in the Initial Temperature.....	72
3.11.4	Uncertainty in the Compressed Pressure.....	73
3.11.5	Uncertainty of Liquid Fuel Mass.....	73
3.11.6	Uncertainty in the compressed gas temperature.....	74
3.12	Experimental Procedure and Operations.	75
3.13	Conclusion.....	76
Chapter 4.	Computational Aerodynamics study of a Rapid Compression Machine... 78	

4.1	Introduction.....	78
4.2	Computational Specification.....	79
4.2.1	CFD Model Development	80
4.2.2	Mesh Generation.....	80
4.2.3	Thermodynamic Properties and Heat Transfer.....	81
4.3	Parametric Studies.....	81
4.3.1	Time Step Size.....	81
4.3.2	Mesh independence	82
4.4	Effect of Using Piston Head Configuration in a Rapid Compression Machine. ...	82
4.4.1	Flat Piston Head Simulation.....	83
4.5	Optimisation of Piston Head Crevice Design.....	84
4.5.1	Crevice with flat Channel Design.	84
4.5.2	Piston Crevice with an Angle Channel Design.....	85
4.6	Influence of Piston Crevice Height on Pressure Profile.	87
4.7	Computational Result and Discussions.	87
4.7.1	Flat Piston Modelling.....	87
4.7.2	Piston crevice without a chamfered.....	89
4.7.3	Piston crevice with Angle Head.....	91
4.7.4	Influence of Piston Crevice Height.....	93
4.7.5	Conclusions.....	97
Chapter 5. Performance Characterization and Ignition Chemistry in a Rapid		
	Compression Machine.	99
5.1	Introduction.....	99
5.1.1	Definition of Ignition Delay.....	99
5.2	Numerical Modelling.	100
5.2.1	Homogeneity and Estimation of Temperature Field of the Reaction Chamber	104
5.2.2	Heat Loss Model.....	105
5.3	Results and Discussion	108
5.3.1	Experimental Characterization: Non-Reactive Experiment	108
5.3.2	Experimental Characterization: Reactive Experiment.	109
5.3.3	Ignition Delay Correlation.....	115
5.3.4	Comparison of Experiment with Literature.....	116
5.3.5	Numerical Modelling: Model Comparison with Experiment.....	117
5.4	Conclusion.....	124

Chapter 6. Autoignition Study of Banner-Solvent in RCM.....	125
6.1 Introduction.....	125
6.2 Experimental Procedures.....	125
6.3 Experimental Repeatability of Banner Solvent	126
6.4 Experimental Results	127
6.4.1 Influence of temperature on Banner-Solvent ignition delay time.....	128
6.4.2 Influence of Equivalence ratio on Banner-Solvent ignition delay time.....	130
6.4.3 Influence of Pressure on combustion of Banner-Solvent.....	133
6.4.4 Comparison of Combustion of Jet A-1 with Banner-Solvent.....	134
6.5 Conclusion and Discussions	136
Chapter 7. Autoignition Study of Used Cooking Oil (UCO-HEFA).....	137
7.1 Experimental Conditions	137
7.2 Experimental Repeatability.....	137
7.3 Experimental Procedure.....	138
7.3.1 Influence of compressed gas temperature on ignition delay times	138
7.3.2 Influence of Pressure on combustion of UCO-HEFA.....	140
7.3.3 Influence of Equivalence Ratio on the combustion of UCO-HEFA	140
7.3.4 Influence of Oxygen Mole Fraction on combustion of UCO-HEFA.....	141
7.3.5 Comparison of UCO-HEFA with Banner solvent and Jet A-1.	142
7.3.6 Ignition Delay Correlation.....	146
7.4 Conclusion and Discussion.....	146
7.5 ACKNOWLEDGMENTS.....	147
Chapter 8. Conclusion and Proposed Future Work	148
8.1 Contribution to Knowledge	150
8.2 Future Work.....	150
Appendix 1 Cantera Code for determining the Piston Velocity for Cantera Simulation. 168	
Appendix 2 Cantera Code for Determining the Ignition Delay Simulation.	170
Appendix 3: Formula for Determining the Volume of Fuel.	174
Appendix 4: Python/Cantera Code for Calculating T_c	176
Appendix 5: Hydraulic Piston Ring Design	179
Appendix 6: Hydraulic Piston Groove	180
Appendix 7: Guard Assembly for Shaft Section.....	181
Appendix 8: Exploded View of Combustion chamber	182
Appendix 9: LabVIEW Code.....	183

List of Figure.

Figure 1-1: Hydroprocessing of vegetable oil[22]	3
Figure 1-2; Show Transesterification Process[25]	7
Figure 1-3: Gas turbine fuel approval protocol[6]	9
Figure 1-4: Schematic picture of a conventional combustor[74].	15
Figure 1-5: Schematic diagram of an LPP combustor[72]	16
Figure 2-1: A picture of the RCM designed by Falk[83].	21
Figure 2-2: shows a horizontal Rapid Compression Machine from University of Connecticut[106, 114]	27
Figure 2-3: Sectional view of a vertical RCM from MIT[113]	28
Figure 2-4: Twin piston RCM[115]	29
Figure 2-5: Shows top view plan of RCM with Camshaft orientation[104]	30
Figure 2-6: A Pictorial diagram of the High-Pressure Shock Tube[121].	32
Figure 2-7: Shows the ignition delay measurement from Shock Tubes	33
Figure 2-8: shows a diagram of variable pressure flow reactor in Princeton University[125].	34
Figure 2-9: Showing the GC x GC analysis of a conventional Jet A-1 fuel (FST-265638) composition.	40
Figure 2-10: Showing the GC x GC analysis of a typical Banner Solvent.	40
Figure 2-11: Showing the GC x GC analysis of a typical UCO-HEFA fuel composition.....	41
Figure 2-12: illustrates the basic definition of ignition delay of a single stage ignition. $P(t)$ is the pressure as a function of time, and $P'(t)$ is the time derivative of the pressure as a function of time.	42
Figure 2-13: shows the Ignition limit (P-T explosion diagram) for hydrocarbon fuels [163].	43
Figure 2-14: shows the schematic diagram of a chemical reaction [191].	45
Figure 2-15: showing the three temperature regimes (low, intermediate and high) for an Alkane Oxidation [115].	46
Figure 2-16: shows the chemical kinetics pathway for low-temperature oxidation of alkane [131].	47

Figure 3-1: Schematic diagram of the University of Sheffield RCM (Shef-RCM).....	51
Figure 3-2: A photograph of the University of Sheffield RCM (Shef-RCM) test facility.....	52
Figure 3-3: shows the diameter of the cylindrical tube in mm.	53
Figure 3-4: showing the three ports (a) front view and (b) isometric view of the end combustion chamber.....	54
Figure 3-5: showing the Isometric and Sectional view design of the Combustion Chamber Unit.....	55
Figure 3-6: Pressure-Time for reactor chamber volume calculation.	57
Figure 3-7: Schematic Drawing of the Hydraulic Damping Mechanism.....	57
Figure 3-8: (a).shows the exploded isometric view of the Hydraulic Ring and Groove. (b) Shows the sectional view of the Hydraulic Ring and Groove.....	58
Figure 3-9: shows the pressure trace for the hydraulic damping using three-step sizing for four driving pressure. (a) One step, (b) two steps, and (c) three Steps.....	60
Figure 3-10: shows the pressure trace for the hydraulic damping using three-step sizing for five driving pressure. (a) One step, (b) two steps, and (c) three Steps.....	62
Figure 3-11: Piston release mechanism.	63
Figure 3-12: Shows the sectional view of the Flat and Crevice Piston Design.	64
Figure 3-13: Pictorial view of Viton seals.....	64
Figure 3-14: showing the Piston Displacement/Stroke for three different driving pressure, 4, 5 and 6 bars.....	65
Figure 3-15: showing the velocity profile 4 bar driving pressure.....	66
Figure 3-16: Shows the timing for the Optical sensor and the LVDT.....	67
Figure 3-17: 4 bar driving pressure showing a compression time of 32 ms.....	68
Figure 3-18: 5 bar driving pressure showing 28 ms compression time.....	68
Figure 3-19: Repeatability pressure test for different Timing. (a) 1-hour timing, (b)1.5-hour timing, (c) 2 hours timing.....	69
Figure 3-20: Calibration of Static pressure transducer	71
Figure 3-21: End section of the rig.....	76
Figure 4-1: The sensitivity of mesh on the core pressure of the reaction chamber.....	82

Figure 4-2: shows (a). The diagram of the crevice region of the piston with a flat face (b). Isometric view of the crevice head design with flat channel piston showing the crevice volume.....	84
Figure 4-3: shows (a). The diagram of the crevice region of the piston (b). an isometric view of the angle channel design showing the crevice volume.	86
Figure 4-4: calculated temperature field at 0ms compression time and 20ms post compression time, using different sizes of crevice volume. (a) 2% (b) 4% (c) 6 % (d) 8% (e) 10% of the entire chamber volume at TDC.....	91
Figure 4-5: Shows the contour of temperature profile of piston crevice head with angled channel. (a) volume 282 mm ³ (b) volume 564 mm ³ (c) volume 846 mm ³ (d) volume 1128 mm ³ (e) volume 1410 mm ³	93
Figure 4-6: Shows the contour of the temperature profile for piston crevice head with varying height. (a)3 mm (b) 5 mm (c) 7 mm (d) 9 mm (e) 12 mm.	95
Figure 4-7: shows (a) temperature profile (b) pressure profile at $T_i=298$ K, $P_i= 1016.6$ mb, with improved crevice height.....	96
Figure 4-8: Comparison of Experimental pressure trace with the CFD Model	97
Figure 4-9: End of compressed gas temperature corresponding to $P_c =15$ bar, $T_c = 615$	97
Figure 5-1: Illustrate the definition of ignition delay used in this study. $P(t)$ is the pressure as a function of time, and $P'(t)$ is the time derivative of the pressure as a function of time.	100
Figure 5-2: Obtainable pressure trace for Shef-RCM (Flat and Crevice Piston).....	108
Figure 5-3: illustrates a repeatability of four experimental pressure trace of nitrogen and argon. Colour line – Nitrogen pressure trace and Black lines-Argon pressure trace at an initial pressure of 0.7 bar.	109
Figure 5-4: Demonstration of experimental repeatability of n-heptane data. Molar composition: $nC_7H_{16}/O_2/N_2 =1/11/41.36$. Conditions: $P_c=15.6$ bar; $T_i= 310$ K;.....	110
Figure 5-5: Demonstration of experimental repeatability for Jet A-1 and air at equivalent ratio of 1.0. Conditions: $P_c = 10.7$ bar; $T_i = 408$ K.	110
Figure 5-6: Experimental pressure trace at various EOC temperature for Jet A-1/air mixture at an equivalent ratio of 1.0 at $P_c = 6$ bar. Conditions: oxidizer to mass ratio of 14.6.(a) at $\phi = 1.0$ (b) at $\phi = 0.75$	111
Figure 5-7: Measured ignition delay as a function of compressed gas temperature, at 6 bar for Jet A-1/air mixture corresponding to (a). $\phi = 1.0$, oxidizer to mass ratio of 14.6.....	112

Figure 5-8: Influence of pressure on ignition delay post compression pressure of 6 bar and 10 bar for Jet A-1/air mixture corresponding to $\phi = 0.75$, molar ratio: $O_2 : N_2 = 1 : 3.76$	113
Figure 5-9: Measured ignition delay as a function of compressed gas temperature, at post compression pressure at (a) 10 bar and (b) 6 bar for Jet A-1/air mixture corresponding to $\phi = 0.75 - 1.0$, oxidizer to mass ratio of 14.6.	114
Figure 5-10: Global Correlation for Jet A-1 (FST-265638) Aviation Fuel.	115
Figure 5-11: Experimental comparison current rig data with literature for Jet Fuel.	117
Figure 5-12: shows the (a). Effective Volume profile as a function of time and (b). the volume expansion trace for Argon non-reactive modelling. Red broken lines – indicate the high degree polynomial fit to the data. The blue line – effective volume profile.	119
Figure 5-13: shows the (a). Effective Volume profile as a function of time and (b). the volume expansion trace for Nitrogen non-reactive modelling. Red broken lines – indicate the high degree polynomial fit to the data. The blue line – effective volume profile.	120
Figure 5-14: Non-reactive model comparison with experimental pressure traces. Initial conditions: argon –: $P_i = 1$ bar, $T_i = 300$ K. Coloured line – experimental pressure. Black line – model prediction.	120
Figure 5-15: (a) non reactive test with Cantera model (b) Comparison of model with experimental pressure profile for a reactive n-Heptane mixture at stoichiometric. Molar composition: n-C ₆ H ₁₄ /O ₂ /N ₂ = 1/11/41.36. Initial conditions: $P_i = 1.0$ bar, $T_i = 315$ K. Solid and broken black line – experiment.	121
Figure 5-16: Comparison of Model with Experiment at 6 bar at EOC pressure at 6 bar, $\phi = 0.75$. Molar ratio: $O_2:N_2 = 1 : 3.76$. Green colour fill-Experiment, red colour and rectangle unfilled -Dooley mixture indicating 1 st stage and total IDT. Aachen mixture-triangle is indicating 1 st stage and total IDT.	123
Figure 5-17: Comparison of Model with Experiment at 6 bar at EOC pressure at 6 bar, $\phi = 1.0$. Molar ratio: $O_2:N_2 = 1 : 3.76$. Green colour fill-Experiment, red colour and rectangle unfilled -Dooley mixture indicating 1 st stage and total IDT. Aachen mixture-triangle is indicating 1 st stage and total IDT.	123
Figure 6-1: Experimental repeatability for Banner Solvent at a compressed gas pressure of 6 bar.	127
Figure 6-2: Influence of temperature on ignition delay time at 10 bar, $\phi = 0.5$, Molar ratio: $O_2:N_2 = 1 : 3.76$ (a) experimental pressure trace (b) ignition delay time as a function of temperature.	129

Figure 6-3: Influence of temperature on ignition delay time at 6 bar, $\phi = 0.5$, Molar ratio: $O_2:N_2 = 1: 3.76$ (a) experimental pressure trace (b) ignition delay time as a function of temperature.	130
Figure 6-4: Experimentally measured ignition delay of Banner-Solvent at 6 bar with (a).Molar ratio: $O_2 : N_2= 1 : 3.76$, (b). Diluent molar ratio: $O_2 : N_2: Ar = 1: 2.82 : 0.94$, (C). Diluent molar ratio: $O_2 : N_2: Ar = 1: 2.82:0.94$,(d) varying diluent molar ratio(e). at 10 bar Molar ratio: $O_2 : N_2= 1 : 3.76$	133
Figure 6-5: Influence of pressure on ignition delay time post compression pressure of 6 bar and 10 bar, $\phi = 0.5$, for Banner-Solvent/air mixture corresponding to $\phi = 0.5$, Molar ratio: $O_2 : N_2= 1 : 1.376$	134
Figure 6-6: Comparison of Jet A-1 with Banner-Solvent at(a),(b) 10 bar, $\phi = 0.5$. Molar ratio: $O_2 : N_2= 1: 3.76$	135
Figure 7-1: Experimental Repeatability of UCO-HEFA at 6 bar compressed pressure	138
Figure 7-2: Influence of compressed gas temperature on ignition delay time of UCO at 10 bar, $\phi = 0.5$, Molar concentration: Fuel = 0.6%, $O_2 = 20.89\%$, $N_2 = 78.52\%$ (a) experimental pressure trace (b) ignition delay time as a function of compressed gas temperature.	139
Figure 7-3: Influence of pressure on combustion of UCO-HEFA at 6 bar and 10 bar, $\phi = 1.0$, for UCO/air mixture corresponding. Molar concentration: Fuel = 1.19%, $O_2 = 20.75\%$, $N_2 = 78.06\%$	140
Figure 7-4: Effect of equivalence ratio on measured ignition delay time of UCO at 10 bar.	141
Figure 7-5: influence of Oxygen mole fraction on combustion of UCO-HEFA.	142
Figure 7-6: Comparison of UCO ignition delay with Jet A-1 and Banner-solvent at compressed gas pressure of $P_C = 10$ bar, $\phi = 0.5$ and molar concentration =0.79.	144
Figure 7-7: Comparison of UCO ignition delay with Jet A-1 and Banner-solvent at $P_C = 6$ bar (a) $\phi = 0.75$, (b) $\phi = 1.0$ and molar concentration =0.79.	145
Figure 7-8: Global correlation for UCO-HEFA.	146

List of Tables

Table 2-1: Table showing design feature and experimental conditions	26
Table 2-2: Jet fuel Formulation data.....	36
Table 2-3: shows hydrocarbon identification base on their chemical structures[144].....	37
Table 2-4: Characteristic Properties of Kerosene Jet Fuel[60].....	39
Table 3-1: Shows the settings of Charge Amplifier (Kistler type 5007)	70
Table 3-2: Shows the operating characteristic of the present Shef-RCM.....	76
Table 4-1: Shows the crevice dimension in mm.....	85
Table 4-2: shows the angled channel crevice volume in mm.....	86
Table 4-3: The dimensions of the angled channel crevice volume in mm.....	87
Table 6-1: Mixture composition for Banner solvent experiment.....	126
Table 7-1: Mixture composition for UCO-HEFA ignition delay experiment	137

List of Symbol

τ_1	First stage ignition
τ_2	Second stage ignition
τ	Total(overall) ignition delay
ϕ	Equivalence ratio
C_p	Constant-pressure heat capacity
C_v	Constant-volume heat capacity
h_c	Heat transfer coefficient
M	Molecular weight
O/F	Oxidizer-to-fuel ratio
t	time
P	pressure
P_i	Initial pressure
T_i	Initial temperature
P_c	Compressed pressure
T_c	Compressed temperature
V_c	Combustion cylinder volume
V_{eff}	Effective volume
V_{exp}	Volume expansion profile
V_p	Volume expansion polynomial
O_2	Oxygen molecule
N_2	Nitrogen molecule
T_b	Mixture boiling temperature
A, B	Fitting parameter for molecular weight correlation
T_m	Molal average boiling point

σ_{θ}	Hoop stress
r	internal radius
P	internal pressure
F	thrust
D	Cylinder bore diameter
R_u	Universal gas constant
V	volume of chamber
V_i	Initial volume
t_{comp}	Total compression time
t_{accel}	Acceleration time
t_{const}	Constant time
t_{decel}	Deceleration time
S_s	Systematic uncertainty
U_s	Uncertainty of stroke length
$U_{Pi, Pc}$	Uncertainty in the initial pressure and final pressure
U_{Ti}	Uncertainty in the initial temperature
σ_{Ti}, σ_{Pc}	Standard deviation of manufacturer specification
σ_m	Standard deviation in the mass of fuel
a, b	fitting parameters
W	Lambert's W function
ρ	density
u	velocity vector field
K_H	Heat conduction coefficient
h_{min}	Critical minimum value for height
h_{ideal}	Ideal cell height
a_1, a_2, a_3, a_4, a_5	NASA polynomials
M	mass

m_k	Mass of kth species
W_k	Molecular weight of kth species
w_k	Molar production rate
e	internal energy
\bar{W}	Mean molecular weight
h_k, h	Enthalpy of kth species, Total enthalpy
T_{ac}, P_{ac}	Adiabatic temperature and pressure at end of compression
λ	Thermal conductivity
δ_h	Thermal boundary layer
Nu	Nusselt dimensionless number
Re	Reynolds number
Pr	Prandtl's number
μ	Viscosity
Q_c	Apparent heat release
T_w	Wall temperature
N	Total number of moles
J	Species index for 1D computational grid
V_g	Geometrical volume
V_{add}	Additional dead volume
sp	Total number of species in 1D computational cells

List of Abbreviations

AHRR	Apparent heat release rate
AJT	Alcohol to jet
AMW	Average molecular weight
ASTM	America society for testing and materials
ATDC	After top dead centre
BDC	Bottom dead centre
BTDC	After bottom dead centre
BTL	Biomass to liquid
CFD	Computational fluid dynamics
CHEKIN	Chemical kinetic
CN	Cetane Number
CONV	constant volume
CR	Compression Ratio
DCN	Derived Cetane Number
EOC	End of compression
FAAE	Fatty acid methyl ester
FT	Fischer-Tropsch
FR	Flow reactor
GC/MS	Gas chromatography/mass spectrometry
HEFA	Hydroprocessed esters and fatty acids
HRM	Homogenous reactor model
IDT	Ignition delay time
ITAKA	Initiatives Towards sustainable Kerosene for Aviation
LP/TVC	lean premixed trapped vortex combustor
MZM	Multi-zone model

NTC	Negative temperature coefficient
ODM	Zero dimensional modelling
PLIF	Planar laser-induced fluorescence
PM	Particulate matter
PPRM	Pneumatic piston release mechanism
PSR	Perfectly stirred reactor
RCM	Rapid compression machine
SENKIN	Sensitivity kinetics
Shef-RCM	Sheffield rapid compression machine
SPK	Synthetic paraffin kerosene
ST	Shock tube
TDC	Top dead centre
UHC	Unburn hydrocarbon
VTIM	Volume as a function of time
2D	Two-dimensional

List of Journal In Preparation

- Performance Characterization and ignition chemistry in a Rapid Compression.
- Experimental study and oxidation of Banner-Solvent in a Rapid compression Machine.
- Combustion study of Used Cooking Oil (UCO-HEFA) in a Rapid Compression Machine.

Conferences In Preparation

- CFD Study of the Effect of Piston Head Crevice Design in a Rapid compression Machine.
- Computational Aerodynamics study in a Rapid Compression Machine.
- Effect of inert gas on ignition delay time of Used Cooking Oil in a rapid compression.

Chapter 1. Introduction

1.0 Background Information

The development of alternative fuels and diversification from conventional fossil fuels depends on the sustainability of the new fuels. Economic factors to consider are fuel cost, adapting to new technological advancements, and the related infrastructural changes. Environmental factors consist of greenhouse gas emissions, land use, and air and water quality. An alternative jet fuel must be readily available yet not result in the shortage of natural resources. Shortly, liquid hydrocarbon fuels will still dominate the transportation and aviation sector[4]. Alternative jet fuels such as synthetic fuels, biofuels, alcohol fuels, liquid hydrogen, etc. may combat greenhouse emissions[5], reduce fuel import dependency and ensure the security of supply and decrease costs for energy value. They are most important sustainable fuel, look promising and useful for limiting greenhouse gas emissions[6]. They are considered as ‘drop-in’ jet fuels and are potential alternative fuels in the near future. These ‘drop-in’ are substituted for the conventional fossil fuels that could adequately replace them and require no modification of the existing infrastructures. However, in this work, the ‘drop-in’ jet fuels are restricted to hydrocarbon-carbon based ‘drop-in’ jet fuels that have energy content compared with the conventional jet fuels.

Synthetic jet fuels derived from the Fischer-Tropsch (FT) process and non-synthetic and bio-jet fuels (HRJ) derived from biomass have good carbon emission gains compared to conventional jet fuels. However, if demand for biomass fuels increases there are worries that they will compete for farmland with food[7]. Governments and the international aviation community have instituted programs that can produce sustainable drop-in synthetic jet fuels. An example is ‘Initiatives Towards Sustainable Kerosene for Aviation’ (ITAKA), which has produced a Synthetic Paraffin Kerosene (SPK) known as HEFA. This fuel has economic benefits as well as limiting or reducing the greenhouse gases (GHG)[8] emissions. The organisation also ensures that the drop-in fuels produced should be sustainable and can be made available for testing in the current aviation systems and during normal flight operations in Europe[8]. ITAKA has explored the possible production

route then based fuels on vegetable oils and fats from feedstock such as oil seeds, algae or used cooking oil [9, 10].

1.1 Processing pathway

Researchers have investigated the thermochemical (liquefaction, hydrotreating, pyrolysis), and enzymatic conversion technologies of alternative jet fuels. The thermochemical pathway is based on high-temperature oxygen gasification, developed by German scientist Fischer-Tropsch in the early 1900's[11]. Synthetic jet fuels are derived from feedstock that comes from non-renewable fossil sources such as natural gas and coal (Synthetic fuels). The feedstock is processed through gasification to produce hydrogen and carbon monoxide referred as the synthetic gas. These gases are then converted into liquid hydrocarbon through Fisher-Tropsch (FT) process. The FT process of fuel derived from natural gas is referred to as Gas-to-liquid (GTL), and that derived from coal is coal-to-liquid (CTL).

Non-synthetic jet fuels are derived from renewable biological sources, such as crops, vegetable oil, animal fat (biofuels)[12]. The most common synthetic jet fuel process is based on the Fisher-Tropsch (F-T)[13] and bio-derived hydro-processed renewable Jet (HRJ)[14]. The main routes are (1) hydrotreating processing of lipid (bio-jet fuel) and (2) synthetic process of natural gas or coal (synthetic jet fuels)[8]. Within the limit of this work, the only hydrocarbon-based jet fuels produced via hydroprocessing and Fischer-Tropsch permitted by ASTM[15] would be given further consideration.

1.1.1 Hydroprocess Fatty Acids.

The oil from animals and plants are known as biomass oil and can be used as a hydrocarbon feedstock for the production of alternative jet fuels. Bio-jet fuels are produced through hydroprocessing of the biomass oil and are referred to as Hydroprocessed Renewable Jet (HRJ)[16]. The process eliminates the chemically bound oxygen and by the addition of hydrogen which gives a suitable molecular weight constituent for jet fuels. Biomass oil is made up of triglycerides. The fats are processed to fully saturated hydrocarbons by the addition of oxygen and double-carbon bonded with hydrogen. These hydrocarbons are then cracked and isomerised to produce normal, and isoparaffinic

hydrocarbons, which are the primary constituents of diesel and jet fuel. This method is combined with existing fossil fuel refining facilities and has similar costs to petroleum refining. The first work on hydroprocessing of biomass oil was done in 1986, which describes the reaction of soy oil with hydrogen using silica and alumina catalysis[17]. The fatty acid was then hydrocracked, to yield a straight chain hydrocarbon comparable to the conventional hydrocarbon fuels [18]. The processing of other feedstocks has also been reported for example rapeseed [19], cottonseed[20]. The HEFA SPK fuels produced from this process are similar to FT SPK, and it does not contain aromatics. Approval was given in 2011[15] for the use of HEFA SPK and blends of 50/50 petroleum-derived jet fuels [21]. HRJ composition depends on the feedstock, but they are mainly made up of iso-paraffins with a small percentage of normal paraffin, the carbon numbers range from C9-C16. Figure 1-1 shows the hydroprocessing of vegetable oil. The composition of hydroprocessed or Synthetic Paraffin Kerosene (SPK) and that of the conventionally refined fuels are different. They have a combination of two (normal and iso-) or three (normal, iso- and cyclo-) that constitute the primary structure of fuel.

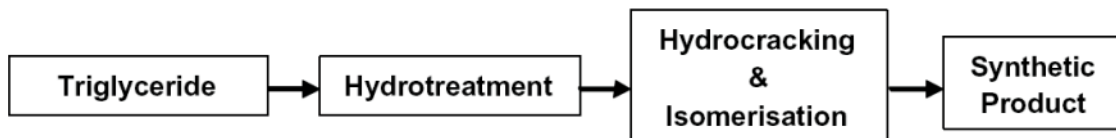


Figure 1-1: Hydroprocessing of vegetable oil[22]

1.1.2 Fischer-Tropsch Process

During the World War II, Franz Fischer and Han Tropsch developed the Fischer-Tropsch process. The process was designed to convert coal to liquid fuel to capitalise on Germany's large coal resources[23]. The FT technology was able to provide Germany's with 9% of its military aircraft with fuels, and 25% of its automotive fuel came from coal feedstock[24]. Jet fuels produced from this process depends on the feedstock used. The method uses chain building and needs synthesis gas as its feedstock. If coal is used as the feedstock, then the

process is referred to coal-to-liquid (CTL). Similarly, for Biomass, biomass-to-liquid (BTL) and natural gas, gas-to-liquid (GTL).

The process mainly makes straight chain hydrocarbons; the end product depends on the hydrogen to carbon monoxide ratio, the catalyst and the process conditions. F-T treated fuels are chemically similar to conventional kerosene jet fuels and can be used as a substitute. They have low viscosity at ambient temperature, thermally stable and have high energy density. In comparison with conventional jet fuel, they have demonstrated to have higher efficiencies[25]. The first approval of synthetic fuel was that of CTL from Sasol [26] in South Africa. It was in September 2009 that a 50% blends of generic FT fuels with Jet A-1 was approved by the American Society for Testing and Materials (ASTM) in its new D7566 standards[27].

Sulphur and nitrogen containing compounds and aromatics are not present in FT fuels but found in conventional jet fuels. Aromatic-free fuels have numerous advantages that they emit of fewer particulates and burn cleaner in aircraft engines than the conventional fuels[28, 29]. However synthetic fuels suffer from the high cost of production and CO₂ emission from the manufacturing process. They can also provide inadequate lubrication, lower volumetric heat content(fuel density specification) and result in elastomer leakage due to lack of aromatics, which reduces seal swell[25]. Blending with Jet A-1 avoids seal issues although the advantage of lower emission is minimised. If the CO₂ production were captured and stored from the manufacturing process, then the fuel might help GHG emission reduction.

1.2 Potential Alternative Fuels

During the energy crisis in 1973, when fuel prices increased drastically the need to reduce dependence on fossil fuels has been the primary driver for the introduction of alternative fuel. his section will briefly discuss the potential of other alternative fuel sources for road and air transport.

1.2.1 Cryogenic Fuels

These fuels refer to gases at normal ambient conditions that are cooled to their condensation point and kept as low-temperature liquids. Typical examples are liquid hydrogen and liquid methane. These fuels have high gravimetric energy content, but the low density that leads to low volumetric energy content.

1.2.1.1 Hydrogen

A number of feedstocks can be used in the production of hydrogen. Examples are fossil fuel sources from natural gas and coal, and renewable sources from biomass processed using renewable energy such as sunlight, hydropower and wind energy. Hydrogen can be produced by chemical, biological, electrolytic, photolytic and thermochemical means. Each technology is in a different stage of development, and each offers unique opportunities, benefits, and challenges. The benefits are its combustion is free from emission like CO₂, SO_x, CO, HC, but thermal NO_x is formed when burnt at a higher temperature, this can be overcome using a lean technology. It produces a clean when burned with oxygen for generating thrust. The combustion temperature is approximately 2300 K, which has a higher burning velocity than conventional jet fuels[30, 31].

In aircraft engines, it could be used as a potential jet fuel[32] but has technical challenges. It requires a more intricate fuel control system for operations like storage of high pressured liquid hydrogen, cooling of the fuel and its warming for use. Modifications would be imperative in aircraft structures to accommodate these fuels. It should be kept at 24 K in aircraft to maintain its liquid form, and this process absorbs energy. Likewise maintaining the hydrogen's liquid could require the usage of more heavy and complex fuel tanks. Liquid hydrogen has a high energy density per unit mass (weight), but its volumetric energy density is one-quarter that of jet fuel. The storage tanks for hydrogen as a cryogenic liquid would increase the weight of large commercial aircraft by over 10%. The liquid hydrogen fuel is in pressurised form; it cannot be stored in the wings because complications may arise in heat exchangers and fuel pump when using liquid hydrogen fuels[33]. A fuel distribution network would be necessary to accommodate liquid hydrogen.

1.2.2 Bio-Derived Fuels

Bio-derived fuels are an alternative raw material for gas turbine engines. Typical examples are the bio-ethanol and biodiesel, which have been used as blended components for gasoline and diesel fuels respectively[34]. Because of the desire to diversify energy sources, their usage is likely to expand in the near future.

1.2.2.1 Bio-ethanol

The fermentation of corn, sugar or sucrose, which contain about 60-70% starch produces ethanol. The process of fermentation in sugar is an anaerobic biological process where it's been converted to alcohol by the action of microorganisms, normally yeast. Ethanol is the result of alcohol. Ethanol boils at 78°C and contains about 35% oxygen by weight. It has a lower gravimetric energy content and more volatile than kerosene, which boils over the range of 150° to 300°C[35]. Its clean burning characteristics extend turbine life, possibly by double[36]. Its intermolecular hydrogen bonding means that ethanol has a higher heat of vaporisation than hydrocarbons, which impacts on fuel vaporisation and atomization. It has a low vapour pressure and miscible with water and also have a rapid evaporation; these factors can create handling issues[36]. Furthermore, there are safety issues as it burns with an invisible flame outside the turbine, which might be harmful[37]. Blends of ethanol with diesel have been shown to have a significant reduction in the emission of particulate matter(PM)[38]. Fang et al.[39] concluded that ethanol blends with diesel reduce NOx emissions. They also found that emission of UHC and CO was higher as the high latent heat of vaporisation lead to complete combustion in a diesel engine[39].

1.2.2.2 Biodiesel

Biodiesel can be produced from animal fat and vegetable oils using the process shown in Figure 1-2. The final product is FAME (fatty acid methyl esters).

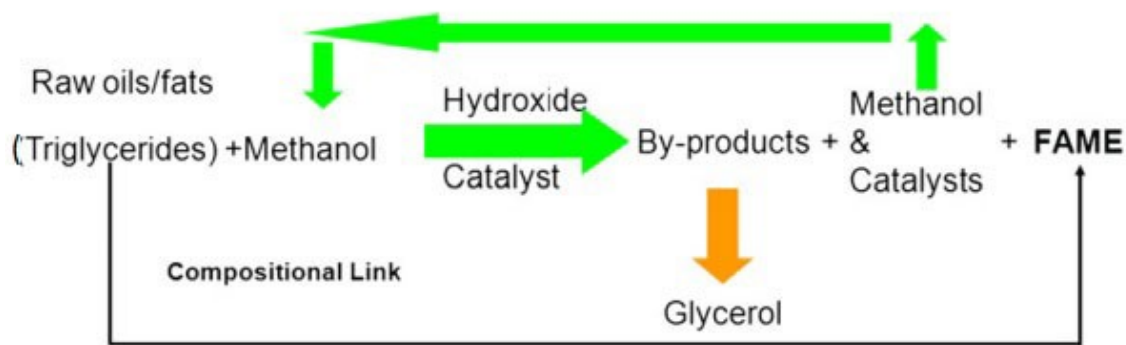


Figure 1-2; Show Transesterification Process[25]

The setback of using FAME as a commercial fuel is its propensity to freeze at normal operating cruise temperatures and its high viscosity, which could impact on atomization. The thermal stability of FAME and its blends are still under investigation. Furthermore, it has been shown that running a pure diesel on engines produces high levels of NO_x, soot, UHC and CO emission compare to a blended ethanol biodiesel fuel [40].

1.2.3 Alcohol to Jet (ATJ).

Alcohol can be produced which serves as a starting material for conversion into jet fuel. There are two methods:

1. Using microorganism to the convert carbon monoxide into alcohol.
2. Biomass product containing sugar can be fermented.

ATJ is made through alcohol oligomerization; this includes connecting short-chain alcohol molecules together to produce a range of jet-fuel hydrocarbons. The volume of ATJ produced from this processes is low and, this is not encouraging for large-scale production

1.3 Approval Process

Aviation jet fuels must be compatible with existing aircraft engines, fuel handling, and storage infrastructure before been considered as “drop-in” fuels. Since the aircraft engines and infrastructure must not change, fuel properties must be specified to ensure safety and reliable fleet operation. Alternative jet fuels should be compared with the current jet fuels before integrating them into the existing infrastructure. For this to happen, they have to be certified fit for use as a single fuel or blended with conventional jet fuels as detailed in the DEFSTAN 91-91[41].

The specification controls the product quality through a series of laboratory test to ascertain if fuels met a minimum standard[42]. The tests are not restricted to gas turbine performance alone but also make available an assurance built on extensive operational experience. Considering drop-in product refined from non-conventional sources like biomass and coal, these products may meet the specification pass off test, but the performance in a gas turbine is not known. The facts remain that the specification provides only information on quality control of the crude product and not the suitability of an alternative jet fuel in gas turbine operation. A typical example is residual heavy metals which are not considered within the specification but cause damage in the hot section of a gas turbine and the absence of certain hydrocarbon groups which can hinder the fuel system performance[43].

The suitability of a drop-in product is assessed through Fit For Purpose analysis and specification property pass off test. Fit for purpose test describes the performances of fuels in airframe and engine fuel systems. It considers assessing the additive compatibility, materials, seal swell and lubricity[43]. When the detailed information is established, approval is given, if only the fuel has no negative influence on the Fit For Purpose properties, specification testing and engine component fuel system. Full-scale endurance testing may be recommended before engine manufacturer’s approval is finally granted [6]. Once this is done the product enters into the fuel specification. Figure 1-3, shows the gas turbine fuel approval protocol.

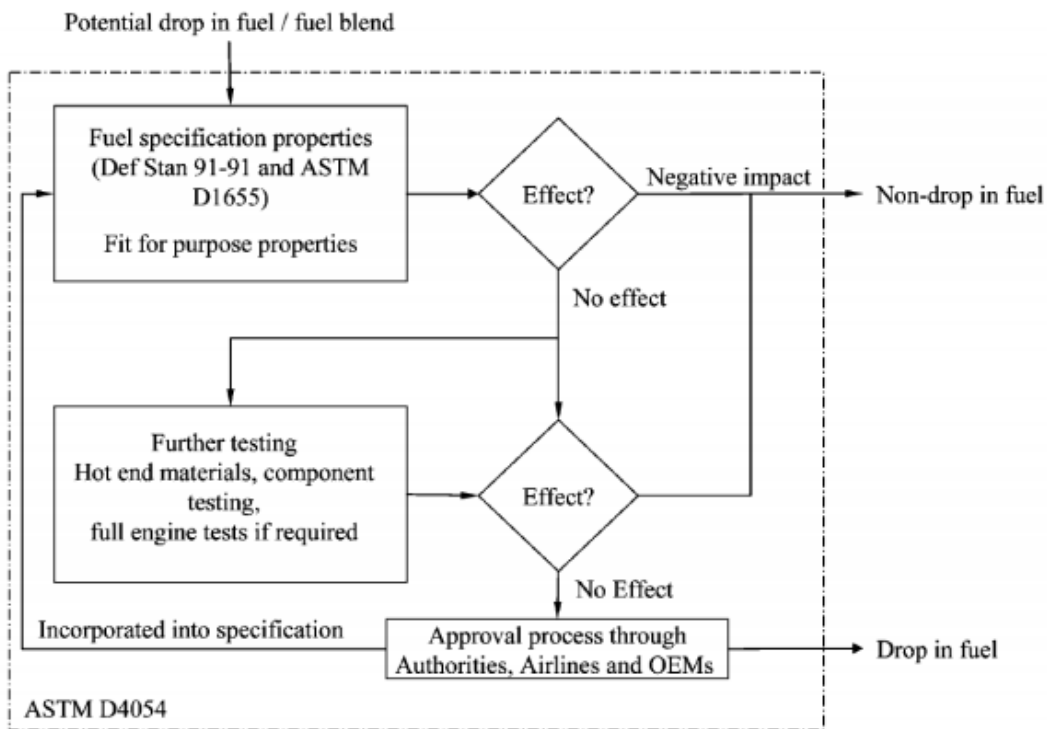


Figure 1-3: Gas turbine fuel approval protocol[6]

Two international recognised bodies monitor and approve aviation Jet fuels and blends. The British Ministry of Defence (MOD), whose duty is to set the condition in the defence standard 91-91(DS91-91)[44] and the American Specification for Testing and Materials (ASTM), responsible for the establishing the requirements for aviation turbine fuels[45]. Both agencies are actively involved in endorsing new turbine engine fuels blend components, and this has produced results such as the approval of Sasol Synthetic fuel produced from Fisher-Tropsch(FT) to be used as 50% blends with the conventional jet A-1 fuels at Johannesburg International Airport[43].

Currently, certified alternative jet fuels consist mostly of n-paraffinic and isoparaffinic compounds with negligible aromatic and sulphur contents. The blends were necessary because synthetic fuels have low aromatic content, this issue has raised concern about the seals in the aircraft engine, which shrinks because of a relatively low aromatic content in the fuel. For this reason, the aromatic content of synthetic fuel blends is presently peaked

at 8%, but this value has not been scientifically proven. The maximum blend limit of SPK with conventionally refined jet fuel set by the certifying bodies early discussed at 50% because there was no experience at that time with blends of greater than 50% SPK with refined jet fuel[46]. The refinement process determines the exact difference between normal, iso and cyclic found in fuel and it varied depending on the raw sources used in the process[25]. The high hydrogen to carbon ratio for n- and isoparaffin gives a high heat to weight ratio, and a clean burn compares to the conventional jet fuels, a crucial criterion for appraising the viability of these fuels. The effect of cycloparaffin in jet fuel is that it reduces the hydrogen to carbon ratio which reduces the heat release per unit weight as this helps in reducing the fuel freeze point which is an important parameter for high altitude flight[25].

1.4 Motives for Diversification into Use of Alternative Fuels.

The use of petroleum-based fuels has been the preferred means of fuelling gas turbine since the early days of their designs[47]. It is readily available, easy to handle, offers good performance. Industrialisation in the world today's is increasing, which has led to a progressive increase in the demand for conventional fossil fuel[48]. Presently, the estimation of oil consumed by aviation sector is about 5 million barrels per day, which represents 5.8% of the world total oil consumption[49]. The sources of this fossil fuel are becoming exhausted, and a major contributor to greenhouse gases (GHG) emission, which has a negative effect on the climate[50]. The industry over-reliance on conventional fossil fuels has raised concerns over the future supply, security and operational cost[51, 52]. This move is equally concerned about the cost and insecurity of the conventional fossil fuel in comparison to the growing population and demand for these fuels in the nearest future[51, 52].

1.4.1 Political Crisis and Depletion of Natural Resources

The projection of world population as estimated by the United Nations is to increase from 6.5 billion to about 9 billion, and it has been estimated to reach 11 billion by 2050[53]. The fear of depletion of natural resources is alarming because of the rapid growth in population size and the high demand for energy has drastically increased, mounting more pressure on the exploitation of the conventional fuels. Global conventional oil supply is currently at political risk and shortages are inevitable unless a drastic change occurs in the supply of conventional hydrocarbon fuels. In the nearest future, the sources for traditional fuels including petroleum will soon decline[53]. The decline of conventional crude is practical examined by using Hubbert peak oil theory[54]. Hubbert suggested that the production rate in a new oil field would continue to increase with infrastructure setup until a maximum output is reached. Then at a stage, the pressure of the oilwell would be reduced, this effect lowers the extraction rate[54]. The maximum production point reached is referred to as peak oil. However, such time at which this occurs is difficult to evaluate.

In contrast, oil company's claims that sufficient reserves that are not yet tapped exist to meet global demand for decades, sampled opinions have it that production has or is about to peak. Kjartad et al.[55] findings reveal from their estimates that the resources appear to be sufficient to meet demand up to 2030. Because these fuels are typically not renewable, society is concerned that at a certain time the demand of these fuels would be more than the supply, triggering a considerable world crisis. Industrialist also agreed that the majority of oil fields situated in the Middle East of the world are confronted with problems with a political crisis. Africa oil producing countries are not left out in the political crisis scenario, for instance, Nigeria which is the largest producer of oil in Africa are presently faced with a political and religious crisis, which has reduced the production rate from 2.7 million barrel to about 1.2 million barrel a day. This shortfall cannot be replaced with other conventional sources. However, countries need to take a drastic step in securing and creating new alternatives fuels to avoid unrest, fear and differences resulting from the world dependence on fuel supply from the Middle East and politically troubled regions in the world. The depletion of petroleum resources is one of the contributing factors that have led to a renewed interest in alternative energy sources and innovating environmentally viable[6].

1.4.2 Air quality issues

Currently, the leading sector with significant growth in demand for oil is the air transport; also, there are high demands for global jet fuels by emerging economical countries, such as China, USA and India. This demand in response to atmospheric pollution, which affects public health because of the harmful increase in air and land traffic emissions. Air and ground transportation produces the same type of emissions; this includes carbon monoxide (CO), sulphur oxides (SO_x), nitrogen oxides (NO_x), carbon dioxide (CO₂), unburned hydrocarbons (UHC), and particulate matters (PM). These emissions from air and land transport are classified as greenhouse gases (GHG), this causes global climate change. Although aviation sector contributes, a small amount of pollutant compared to other sectors but estimated to account for 2-3% of CO₂ emissions[49]. Because of the rapid growth in the aviation sector in the nearest future, its emission will reflect a greater portion than other does[56]. According to Penner et al.[57], the airliners fly within the stratosphere where emissions in this zone are more devastating and have a considerable impact on the climate change. The effect of Green House Gas emissions from fossil fuels combustion on climate change is a critical issue and the long-term effect on human existence. The effects on human beings are airborne, which causes respiratory illnesses, complex cardiovascular diseases and devastating effect of sulphur, which causes acid rain that could damage infrastructures. A Recent study also shows that the impact associated with aviation emission degrade surface air quality and the Particulate Matter (PM) precursor gases (SO_x and NO_x) plays a significant role related to the direct emission of primary PM. The challenges to handle different environmental and energy needs is decarbonizing the energy chain and finding clean, viable source of fuel. This requires consented effort by airlines, government and aircraft manufacturer collectively setting up an initiative for the promotion and development of alternative fuels.

1.4.3 Exorbitant Price Issues

The price differences compared with conventional jet fuel in the short term is a setback that paves ways for the deployment of alternative fuels in aviation. This setback could be managed by setting up a mechanism to reward industries buying these fuels as environmental benefits to bridge the price gap for airlines wanting to buy fuels[58]. Also,

the renewable energy policies in most countries are very tight. Stipulation of technical requirements for fuels is stringent. Thus, it is imperative that policies also consider the use of supporting measures for sustainable alternative fuels in aviation. In 2001, European Commission launched an initiative to facilitate the commercialization of bio-derived fuel in Europe. This initiative was a road map to achieve by 2020 an annual production of two million tonnes of biofuel for aviation[59]. This task looks challenging due to strict fuel specification like the fuel freezing point, flash point, energy density and flammability limit[60, 61]. In 2006, the USA Commercial Aviation Alternative Fuel Initiative(CAAFI) was launched, which incorporated government, industry, academia and non-profit organisation working collectively for the purpose of securing a stable fuel supply, involving in research and analysis of the fuel and air manufactures improving on aircraft operations. This initiative made tremendous progress, information on the results was shared through a conference to stakeholders and various aviation supply chains. This process focussed on commercialisation, environment impact and fuel certification. In 2009, a program was initiated by the European Commission called ‘Sustainable Way for Alternative Fuels and Energy in Aviation’ (SWAFEA) was designed to explore the usefulness and the effect of using alternative fuels with an aim to support EU air transport policy. In that year a breakthrough of ‘drop-in’ fuels as sustainable alternative fuels in aviation was then approved. In 2013, a Corporate Biofuel Program was launched by KLM; this provided KLM customers with the chance to enumerate their air travel footprint by contributing to the acquisition of sustainable fuel, instead of purchasing carbon credits to offset staff travel. In July 2011, introducing synthetic fuels up to 50% synthesised hydrocarbon into the fuel specification was approved[62]. In March 2013, ITAKA initiated the first series of intercontinental flight using a blend of 20% of HEFA made from used cooking oil. All these efforts were gear towards providing sustainability in the production of alternative aviation fuels.

The conversion of coal, gas or biomass has been made possible through the advancement of process technologies. Refinement of biomass product as an alternative feedstock is necessary, because of its potential to reduce emission, and improve savings, unlike fossil feedstocks, which are not a renewable resource, thus subjected to peak supply issues. These fuels need approval, which is achieved by extensive testing. These provide liquid

hydrocarbons as potential drop-in alternative products, which have similar properties to Jet A-1, fully compatible with existing systems and use with no limitations in aircraft operations.

1.4.4 Technical Requirements

The introduction of lean-premixed or lean premixed pre-vaporise combustors which replace diffusion flame combustors is the latest development in the gas turbine industry[63, 64]. These new combustors are proposed for both land and air based gas turbine engines as a means of reducing NO_x and improving efficiency. This results in significant challenges for the fuels, particularly, on the technical requirements like the flash point, freezing point, energy density and autoignition[45]. The combustion properties of fuel have high responsiveness to a fuel composition, temperature, equivalence ratio and pressure. In turn, this affects engine performance through ignition, relight and blow out limits. This is driving research into autoignition chemistry, extinction limits and flame propagation. Regulatory requirements for low emissions from gas turbine power plant have increased during the past ten years. The expectation of a new aircraft engines is to perform with maximum combustion efficiency as well as providing stability and low emissions. This has increased the need for low NO_x turbine engines. The dry low emission (DLE) system has achieved success when used with natural gas to meet emission requirement[65]. However, the complexities the fuelling system low emission engine have made the burning of liquid fuels a challenge.

LPP combustors provide low pollutant emissions while burning liquid fuels[66]. Jet fuel has a short ignition delay time when heated, and pre-ignition can occur in the chamber making it difficult to use in an LPP combustor[67]. Several approaches have been investigated in the literature[68-71] to remedy this. These methods attempt to achieve low NO_x emissions by designing premixer and combustors that permit rapid mixing and combustion before the onset of spontaneous ignition of the fuel can occur[66]. An alternative approach is directly spray fuel into the premixer so that the liquid fuel droplets vaporise and mix with air at lean conditions[72, 73].

1.4.4.1 Combustion in Gas Turbines

A gas turbine engine emits pollutants such as carbon monoxide (CO), nitrogen oxides (NO_x), particulate matter, sulphur and unburned hydrocarbons (UHC). NO_x formation in gas turbine plant is the result of high temperatures heating, in the combustor. Other pollutants like CO, UHC and particulate matter are the result of insufficient oxygen to complete the combustion process. The operating point of the combustor defined regarding temperature, pressure, time and concentration can influence the extent of pollutant emissions in gas turbines. Figure 1-4, shows the main component of a conventional gas turbine combustor. Fuel and air are introduced separately into the combustion chamber and burn with a diffusion flame.

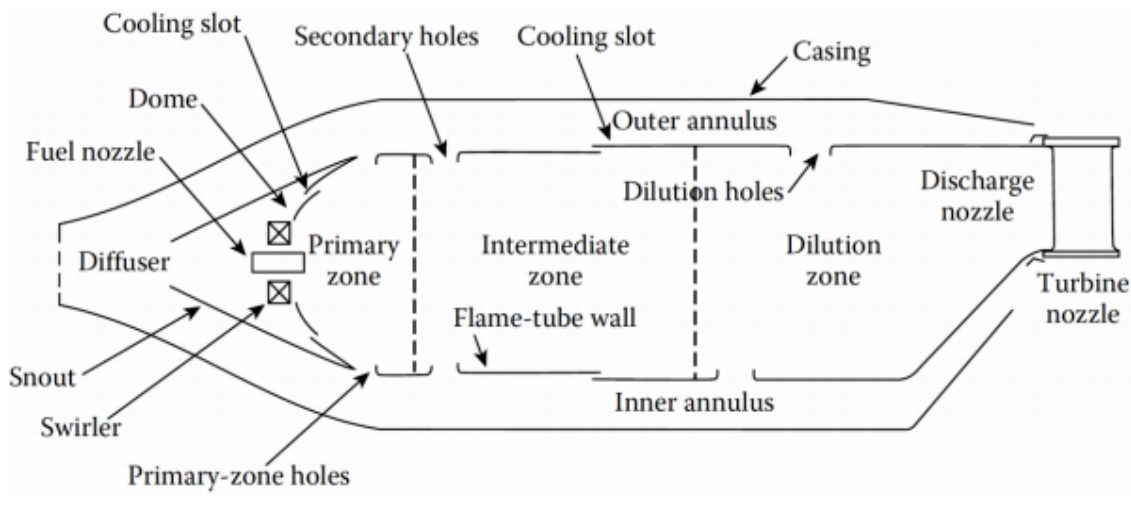


Figure 1-4: Schematic picture of a conventional combustor[74].

Gas turbine combustors are categorised into tubular, annular and can-annular. Each type has its advantages regarding size and structural strength. The combustion chamber is where the combustion and release of heat take place. The essential part of a combustor are the air swirler, casing, diffuser, flame tubes, fuel nozzles and ignitor. Air swirlers achieve better fuel-air mixing and flame stabilisation. The diffuser mounted at the

entrance of the combustor reduces the velocity of air entering the combustor and recover the dynamic pressure. The general function of the combustor is to minimise the pressure drop across the combustor. The combustor is primarily made up of three zones; primary, intermediate and dilution zones. The primary zone accommodate one-fourth of the airflow into the combustor is used to support the combustion processes. The intermediate or secondary zone dilutes the hot gases reducing their temperature regulating the flame pattern and cooling the liner walls of the combustor.

1.4.4.2 Lean premixed combustion

Lean premixed combustion is designed to maintain low and uniform temperature flame. This results in a reduction of NO_x and soot emission, improved durability and performance, and fuel flexibility[75, 76]. However, improved efficiency is achieved with higher temperatures, but this enhances formation of the NO_x formation. Reducing the oxygen concentration reduces the NO_x , resulting in carbon monoxide (CO) and unburnt hydrocarbon (UHC) emissions due to incomplete combustion. To attain an ultra-low NO_x emission a more controlled technology is required. One of the problems of LPP combustors is the issue of longer residence times[77, 78] and combustion instability[79].

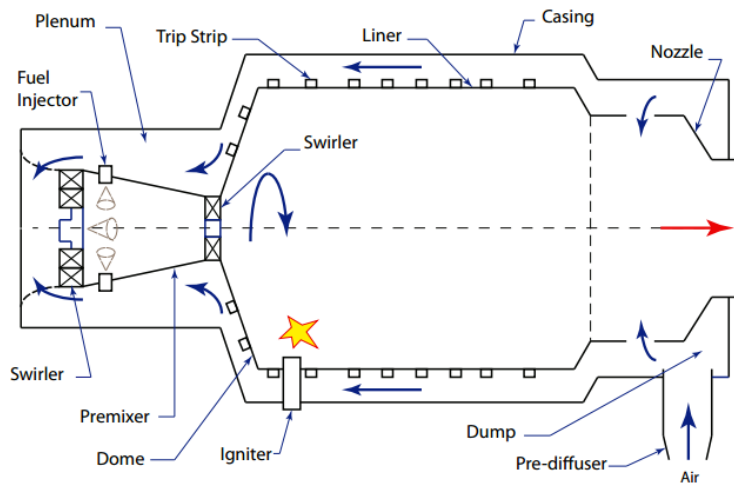


Figure 1-5: Schematic diagram of an LPP combustor[72]

Figure 1-5, shows a schematic diagram of an LPP combustor. The combustor operates near the lean blowout limit, reducing the flame temperature. To achieve this the fuel and air are premixed before the onset of combustion[76]. Air from the compressor flows through the pre-diffuser before being discharged into the annular section of the combustor. The holes in walls of the combustor admit air into the annulus to dilute the hot combustion gases. Enhanced cooling is achieved via the strip trip at the outer liner of the walls. The cooled air from the annulus then passes into a plenum from which it enters the premixer. Within the premixer, air passes through axial swirlers and mixes with vaporised fuel; the exiting fuel-air charge is deposited into the primary zone by other axial swirlers, where it is ignited and burned. Due to the high pressures and temperatures, the fuel/air mixture may spontaneously ignite generating unsteadiness in the combustor[80]. This can cause catastrophic failure of the combustor components. Understanding the spontaneous autoignition is paramount in the design of a viable combustor. These combustors are also susceptible to the thermo-acoustic instabilities, LPP combustors operate fuel lean conditions, where the rate of combustion is actively driven by fuel-air ratio. If there is a drop in the fuel-air ratio significantly, local extinctions can occur. This instability initiates combustor unsteadiness.

1.4.4.3 Lean Direct Injection.

In an attempt way to control, the short ignition delay associated with LPP, the use of lean direct injection (LDI) has potential. The difference between the LLP and LDI is not having a premix duct attached upstream of the combustion chamber. LDI may cause non-uniform combustion and create local hot spots increasing NO_x.

1.4.4.4 Lean Premixed Trapped Vortex Combustor (LPTVC)

Another proposed method of premixed combustion in gas turbines is the trapped vortex combustor (TVC) first proposed by Hsu et al.[81] in 1993. The stabilisation of flame is achieved with recirculation zones to provide a continuous ignition source, which enhances the mixing of hot combustion products with the incoming fuel and air mixture. This process results in a significant pressure drop since most of the combustion occurs in the recirculation zone while a flameless regime is achieved[82].

Tapped vortex combustors have the following advantages,

- It improves flame stability and flammability limits.
- It allows operation at the high excess air premixed regime and supports high-speed injections that help to avoid flashback in combustors.
- It is compatible with the combustion of a variety of fuels with medium and low calorific value.
- Very low NO_x emissions are achieved without dilution and post-combustion treatments.

1.5 Research Objectives

The objective of this work is to measure the autoignition properties of liquid fuels relevant to the practical gas turbine conditions. This requires an experimental test rig that can replicate the physical and chemical environment of the combustor. In this work, a rapid compression machine was designed and manufactured. It compresses fuel-air mixture under adiabatic conditions, replicating a single stroke event in Spark Ignition (SI) engines. These can provide data for the study of the chemical kinetics at gas turbine like conditions. The following are specific objectives of the research work:

- To develop a Rapid Compression Machine that will provide ignition delay times of aviation fuels relevant to gas turbine conditions (elevated pressure and low to intermediate temperature).
- Validation of the experimental data with the existing models found in the literature.
- Test synthetic-derived aviation fuels and compare with the conventional jet fuel.

1.6 Layout of the Thesis

The whole thesis divided into the following chapters:

- Chapter 1: This introduces a practical problem faced by the aviation industry, which also highlights the importance of this study. The processing pathway for alternative fuels was discussed, and potential alternative fuels were considered. An approval process of synthetic fuel was looked was discussed. The modification to diversification into the use of alternative fuels was mentioned. Detailed research objectives and procedures used, in addition to the framework of the thesis are presented.
- Chapter 2: This chapter presents a comprehensive literature review on the historical design of rapid compression machine; the progress in rapid compression technology; single piston RCM, twin piston RCM, the camshaft connection RCM, the hydraulic braking mechanism and the design of combustion chamber and charge preparation approach. Another instrument for studying RCM was considered like the shock tubes, flow reactors, well-stirred reactor and the static reactor. Furthermore, this chapter also contains the study of the current fuels, the core concepts of auto ignition, the basic concept of chemical kinetics and surrogate fuels as a representative of alternative aviation fuel.
- Chapter 3: Presented in chapter 3, are the details on the experimental facility and techniques. This includes the design and development of the current rapid compression machine; the optimised reactor piston design, hydraulic damping mechanism, the pneumatic driving cylinder, the reactor combustion, piston trajectory of the RCM, direct premixed charge preparation chamber, mixture preparation, the triggering system and data acquisition and the uncertainty associated with the rig. The novelty of the piston-released mechanism is discussed, the experimental procedures of the machine and finally, conclusion.
- Chapter 4: This chapter presents computational aerodynamics studies of Rapid Compression Machine: Here the model discussed in details, e.g., the solver used, and mesh generation. The parametric study carried out on the time step size and mesh independence conducted. The effect of using differing Piston head configuration in an RCM is considered looking at the flat piston and the optimised

crevice head configuration. The effect of further design optimisation of the piston crevice and conclusion.

- Chapter 5: This chapter presents, the characterization and auto ignition performance of fuels using the RCM; the chapter started with the introduction, then looked at the experimental characterization, considers the reactive and non-reactive test, the definition of ignition delay. Numerical modelling: examined the homogeneity and peak temperature field of the reactor chamber, the heat loss model was applied using the effective volume approach. Results: considered the characterization of the reactive and non-reactive experiment, model comparison with experiment, global ignition delay correlation was determined, numerical model and then conclusion.
- Chapter 6: Autoignition study of Banner-Solvent in RCM; the chapter examines the procedures for conducting the test, experimental repeatability of Banner Solvent, the influence of temperature, pressure and equivalence ratio on the ignition delay of Banner-Solvent; comparison of Jet A-1 with literature, comparison of Jet A-1 with Banner-Solvent and finally conclusion and conclusion.
- Chapter 7: Present the measurement of ignition delay of UCO-HEFA; the experimental conditions and the experimental repeatability was presented. References to the experimental procedures were given. Discussion on the experimental result focusses on experimental repeatability, the influences of compressed gas temperature, compressed gas pressure, equivalence ratio and varying oxygen concentration on ignition delay. Comparison of UCO-HEFA with Jet A-1 and Banner-Solvent was discussed. The ignition correlation for Banner Solvent was determined and conclusion of the chapter drawn.
- Chapter 8: Conclusions drawn based on the results and discussions in previous chapters. A brief summary of recommendations for future improvement of the present design. This chapter also provides keys findings with recommendations for future work.

Chapter 2. Literature Review

2.1 Introduction.

This section presents a review of the literature regarding the development of a rapid compression machines from the 1914's.

2.2 Historical Development of Rapid Compression Machine (RCM).

The historical evolution of the rapid compression machine started in the early 1900's when the first RCM was designed by Falk[83]. He used the adiabatic compression apparatus to investigate the ignition temperature of homogeneous hydrogen-oxygen mixtures. The machine was driven by the momentum transfer of the falling weight and flywheel driven crank[84]. The device lacked a stopping mechanism to bring the piston to a halt, so the reactor piston did not maintain a steady volume at the end of compression stroke. Hemp seals were use lubricated with lanoline. Falk was able to characterise the autoignition of the temperature of H_2/O_2 [83]. Figure 2-1 shows a picture of RCM designed by Falk.

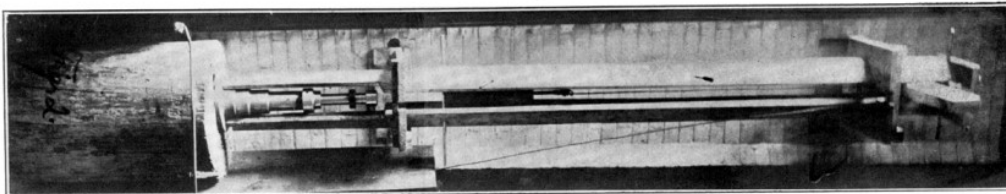


Figure 2-1: A picture of the RCM designed by Falk[83].

A few years later the first optically accessible RCM was built by Dixon et al.[85]. The RCM was driven by falling pendulum, which drove a piston horizontally into a glass tube filled with premixed gases. The stroke was adjusted by varying the stopping height of the pendulum. They noted that some time elapsed between the end of the motion of the piston

and the start of the flame. They referred to this as the pre-flame period now known as ignition delay time[86].

In 1914, Dixon and Crofts[86] built a modified version of the Falk's machine where a falling weight drove a piston vertically into a cylinder producing results on H_2/O_2 [86]. They changed the cylinder width to stop significant cooling from the walls, and the piston movement was gas-tight without lubricant meeting the gas mixtures. Despite these changes made, two issues remained; firstly, there was no apparatus installed to haul the piston at the end of the stroke and, secondly, there were difficulties in measuring the in the cylinder[86].

In 1917, Cassel[87] designed a rapid compression machine to compress gas mixtures without piston rebound. He observed that rebound of the piston at the end of compression resulted in a cooling of the gas, which would eventually quench ignition. The rebound was avoided by a set of brake shoes install to secure the falling weight, which was falling into the piston. Also, the generated energy was dissipated by a set of lead washers[87].

In 1922 and 1926 Tizard and Pye [88] built an RCM whose piston was driven by a flywheel with a crank and connecting rod similar to that of the I.C engine. The machine used a unique setup for moving and locking the piston at its maximum compression. The connecting rod and the crank arm operated by a clutch. The piston was secured at the top dead centre by the rigid connection of the connecting rod. They were able to measure in-cylinder pressure through the use pressure sensor. They investigated the autoignition of premixed gases and observed that the heat loss from their pressure trace had an effect on the thermodynamic state before the onset of ignition. They concluded that RCM experiments were not truly adiabatic and they attributed it to heat loss to the cylinder wall and fluid motion. They were able to build a model to account for heat loss in the cylinder[88].

In 1929, Pignot built a machine based on Dixon's design. In his design, the stroke length was adjustable. The reaction chamber was fitted with a heating tape, and a thermocouple was positioned in the chamber to measure its initial temperature. Their piston was halted

at the end of compression using spring-loaded clamps that snapped into a groove; however, this was an inefficient way of preventing the piston from rebounding.

In 1930, Fenning and Cotton[89] carried out a series of experiments to determine ignition temperatures using Tizard and Pye's RCM[90]. They found that their results were not reproducible which they attributed to friction in the moving parts of the piston and fine particles suspended in the reaction chamber. This issue was overcome by replacing the upper cylinder with a mild steel plate to which a rubber bulb was clamped. However, their results were still not reproducible, and they later found that the issue was with the rubber bulb, which absorbed the test gas.

During the late 30's and the early 40's, Jost and Roegen[91] and Scheuermayer and Steigerwald[92] described an experiment using compressed air to push the piston along the cylinder. They were able to achieve a velocity up to 60 m/s but stopping the piston without rebound, or mechanical fracture was not resolved.

Leary et al.[93] and Taylor[94] designed the M.I.T rapid compression machine, which overcame the issue of rebound or mechanical fracture by using a gas-cushioning device to brake and arrest the piston. An achievable compression time of 10 ms was achieved without piston damage. Nitrogen was used to drive and brake the driving piston.

In the early 1960's another rapid compression machine was designed in M.I.T by Rogowski[95]. This comprises of three pistons in three cylinders arranged along a common shaft. One piston is driven pneumatically; the second one moves through the hydraulic fluid, and the third one compresses the mixture under study. With this arrangement, the piston was brought to rest maintaining a constant volume.

From the 1960's numerous designs of RCM appeared all adopting, one or two features from the previous designs and modifying them to suit their condition of operations.

In 1969, Affleck and Thomas[84] developed an opposed-piston rapid compression machine, which they used to study the pre-flame reactions. This was adopted from Rogowski's [95] ideas; the piston was pneumatically driven and stopped by hydraulic means using an in-line design. A compression time of 10 ms was achieved with a piston diameter of 1.5 inches.

In 1974, Rife and Heywood [96] studied diesel combustion, and Matekunas [97] studied the SI engine combustion in 1979. Both adopted the same principle design of Rogowski [95]. Zigan[98] investigated diesel combustion in an RCM. He used compressed air to drive a piston mounted on a common shaft with the compression piston. A compression time of 130 ms was recorded with a stroke length of 750 mm; a mechanical device was used to halt the piston at the end of compression.

In 1980, Beeley, Griffiths and Gray[99] investigated the spontaneous ignition of isopropyl nitrate on a rapid compression machine, that was initially built by Shell and based on Affleck and Thomas design. This was first known rapid compression machine to incorporate a creviced piston head design was made in the early 1990's by Park[100] which was used to suppress the roll up vortex from the wall of the chamber.

In 2004, University of Michigan built a free-piston rapid compression machine. It consisted of a driver section of length 5.54 m. The test manifold was made of four components, extension section; which provided the contact surface used to halt the motion of the sabot, the converging section, thermocouple manifold and instrumented section. The designed sabot was in two parts, an acetal resin body and an ultra-high molecular weight polyethylene replaceable nose cone. Spring-loaded U-rings sealed the sabot to the test section. The machine is charged with inert gas for running the driver section. A globe valve connecting the driver section was used to release high-pressure gas, which actuated the sabot onward down the driven section, compressing the test gas ahead of it. Compression ratios between 16 and 37 were achieved in approximately 100 ms compression time. A compressed gas pressure of 20 bars and temperature of 1000 K for nitrogen, 2000 K for argon could be achieved.

Also in 2004, an RCM was built in Japan in Keio University by Lim et al.[101], this used air as the driving force and hydraulic oil to decelerate the piston and bring it to a halt and maintained a constant volume at the end of compression.

At the University of Pierre et, Marie Curie an RCM was built in 2007 by Guibert et al.[102]. The chamber diameter was 40 mm while the length of the chamber ranged between 30-50 mm. Their RCM had a high compression ratio, 16, with a short compression time 29 ms.

Fast compression was achieved by a hydraulic system and controlled by a multistage servo valve permitting accurate piston motion control. The design had optical access, and the combustion chamber included the turbulence control using a grid fastened between the pre-compression and combustion chambers.

In 2012, Casey[103] designed an RCM, which used the direct test chamber(DTC) approach, enabling efficient gas-phase testing of non-volatile fuels that may not otherwise be tested with the traditional large batch mixture analysis approach. The large batch approach has a mixing tank separate from the reaction chamber. The fuel is manually injection into this mixing tank maintained at a temperature close to reaction chamber temperature. Batch chambers also have stirrers that provide mixing before metering of the mixture into the reaction chamber. The DTC method means the mixture is injected directly into the combustion chamber not being held at high temperature where cracking might occur and it eliminates the potentialof fuel condensing in the process of transferring to the chamber.

In 2015, John[104] developed a rapid compression controlled expansion machine. The machine was pneumatically, driven with a custom-designed cam, which governed the volumetric compression and expansion of the combustion chamber. To control the rate of heat loss in his rig through volumetric expansion, the machine was fitted with cam assembly are modulated to incorporate different cams with unique compression and expansion profiles. A table showing various designs of RCM is shown in Table 2-1.

Table 2-1: Table showing design feature and experimental conditions

Facility/ Affiliation	P_c (bar)	CR	Compression time (ms)	Piston control	Chamber charge preparatio n approach	Key Features
University of Sheffield (Shef-RCM).	22 bar	8.9 – 13.6	25 - 32 ms	Pneumatically driven, hydraulically stopped, Pneumatic pin release mechanism	DTC, Manual injection.	Crevice piston, Adjustable stroke, and clearance. Detachable combustion
Michigan State University[105]	20 bar	Flat piston 4-17 and crevice piston 4.8 - 21	< 30 ms	Pneumatically driven, hydraulically stopped.	DTC, spray ignition and Aerosol Wet- compression	Crevice piston, Adjustable stroke, and clearance, Optically accessed
Marquette University[104]	40 bar	4 - 17	30 – 50ms	Pneumatically driven, hydraulically stopped, cam driven	DTC, spray ignition.	Crevice piston, Adjustable stroke, and clearance, Optically accessed
Case Western Reserve University[106]	>50bar	Flat piston-21 crevice piston- 15.1	25-40 ms	Pneumatically driven, hydraulically stopped	Mixing tank	Crevice piston, Adjustable stroke, and clearance, Optically accessed
University of Leeds[99]	20 bar	<14.6	22 ms	Pneumatically driven, hydraulically stopped	Mixing tank	Crevice piston, Adjustable stroke, and clearance, Optically accessed.
University of Ireland, Galaway[84]	40 bar	13.4	22 ms	Dual-opposed piston configuration. Pneumatically driven hydraulically	Mixing tank	Crevice piston, Adjustable Stroke.
University of Michigan[107]	20 bar	16 – 37	100 ms	Sabot deformation	Mixing tank	Optically accessed, Gas sampling.
University of Connecticut[10 5]	70 bar	7 - 15	30 - 45	Pneumatically driven, hydraulically stopped	Mixing tank	Crevice piston, Adjustable stroke and clearance, Optically accessed Gas
University of Lille-Science and Technology[108]	40 bar	9.8	20 - 70	Pneumatically driven, stopped by cam.	Mixing tank	Crevice piston, Adjustable stroke and clearance, Optically accessed. Gas
MIT[100]	40 bar	12.5 – 16.5	15 ms	Pneumatically driven, hydraulically stopped	Mixing tank	Crevice piston, Adjustable stroke. Detachable combustion chamber

2.3 Progress in Rapid Compression Machine Technology

Rapid compression machine design started with a vertical single piston apparatus with no braking mechanism. Today technologies are used which differs in chamber design, stopping mechanism and the number of pistons. Modern designs of RCM's have incorporated multiple features, for example; an optically assessed windows for the measurement of species concentration [84, 109], optimised piston crevice[110, 111], adjustable stroke[109], hydraulic damper[111], cam operated piston[104, 109], and the DTC preparatory techniques[104, 105]. The five main categories of RCM will be discussed here: single piston RCM, twin piston RCM, the camshaft connection RCM, the hydraulic braking mechanism and design of combustion chamber [112].

2.3.1 Single Piston RCM

The single piston RCM could be a horizontal [104, 106] or vertical[113] single apparatus run by the expansion compressed gas or piston driven by compressed gas/air. Figure 2.2 and 2.3 shows the horizontal and vertical RCM. Most designs are fired by the expansion of compressed gas [83, 85].

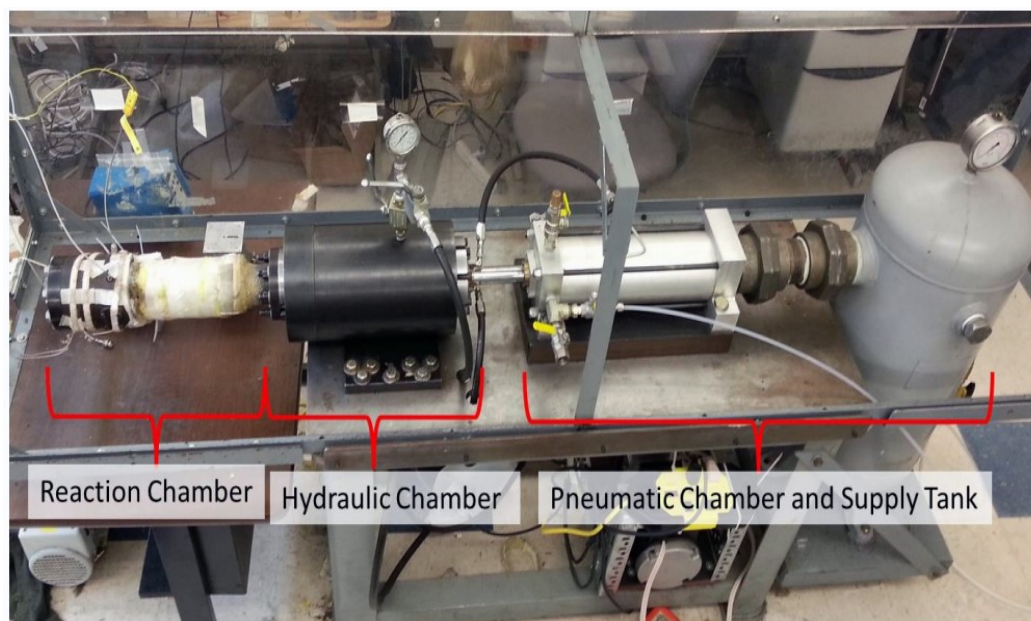


Figure 2-2: shows a horizontal Rapid Compression Machine from University of Connecticut[106, 114]

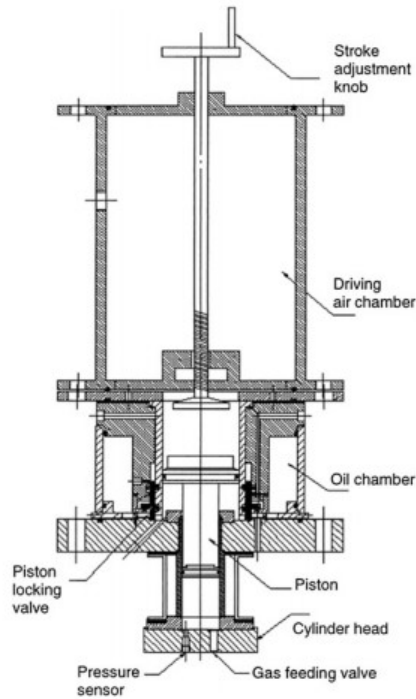


Figure 2-3: Sectional view of a vertical RCM from MIT[113]

In any RCM design, fast compression is essential to prevent heat loss during compression and in the post-compression phases. So they are pneumatically driven, and hydraulically stopped. RCMs are limited by compression ratio and speed. The maximum compression time taken in RCM is less than 100ms[107]. The control of the piston velocity is necessary as this is achieved by venting oil through a small orifice in the hydraulic chamber. The piston is held in position at its bottom dead centre (BDC) in two ways; by using a pressurised oil hydraulic unit that keeps the piston seated and using an air pressurised pneumatic pin. The piston design plays a significant role in maintaining the homogeneity of the chamber.

Lee and Hochgreb[113] performed a computational study on the aerodynamics in the combustion chamber. They found out that the piston rolls up a cold layer of mixture on the wall during compression to form a vortex. This can be avoided by designing a special crevice behind the piston head. Wurmel and Simmie[115] performed further studies and that 10% of the combustion chamber volume was found to be the optimal crevice volume for trapping the cold boundary layer.

2.3.2 Twin piston RCM

Figure 2-4 shows the twin piston RCM. It consists of two similar mechanisms connected opposing each other. The machine was first designed by Shell-Thornton in 1968 and then later modified in the early 1990's[115].



Figure 2-4: Twin piston RCM[115]

The twin piston design reduces of compression time to below 17 ms. This type of RCM is more complicated as it required that the two pistons be synchronised. Unequal balancing or alignment of the shaft could increase the vibration of the system influencing the results.

2.3.3 The Camshaft connection RCM

The camshaft connection RCMs has the actuator and combustion chamber aligned at right angles. The motion is transmitted through a linear cam mechanism, which governs the trajectory of the reactor piston and brings it to a stop at the end of compression.

The advantage of this type of RCM is that the cam permits control over the conditions during compression and post-compression stage[109, 116]. This orientation allows the stroke, and combustion chamber volume trajectory to be changed by using different cams with unique profiles[104]. Figures 2-5, shows the top view of RCM with camshaft connections.

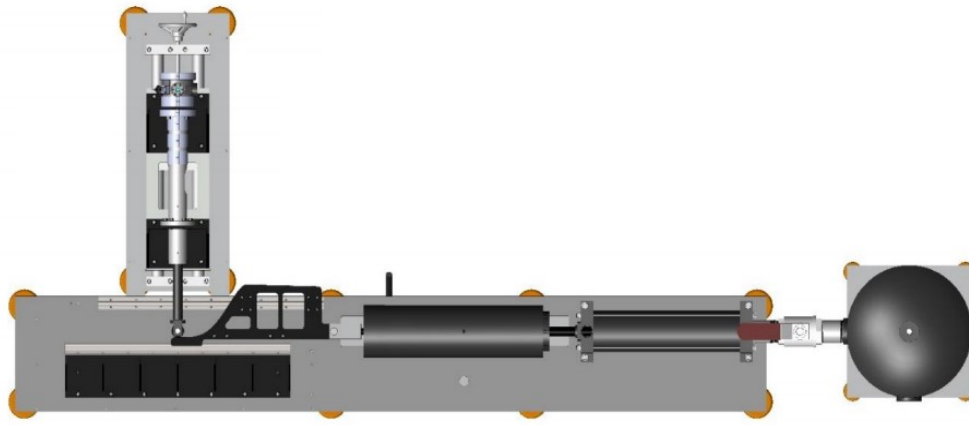


Figure 2-5: Shows top view plan of RCM with Camshaft orientation[104]

2.3.4 The hydraulic braking mechanism

Piston speed and control is essential in RCM design as this is governed by the fluid dynamics and mechanics. The expansion of air or gas in the driving section builds up a force behind the reactor piston accelerating it. The piston is controlled by hydraulic fluid (oil). These hydraulic mechanisms can both hold the piston in its initial position and halt it so that no rebound occurs. This is achieved using a hydraulic damping unit. The unit consists of a piston ring and groove arrangement where a hydraulic piston ring is machined at the surface in steps giving way to small clearance on the peripheral face of the hydraulic piston ring[99, 105, 106, 111]. This allows the high pressure of oil in the trap groove to vent through the small clearances on the ring surface decelerating the reactor piston until it is maintained at a constant volume at TDC.

2.3.5 Design of combustion chamber and charge preparation Approach

The design of combustion chambers varies between RCMs. The combustion chamber is one of the largest components, and houses measuring sensors. Some chambers are fixed[105, 106] while others have an adjustable chamber[104]. Typical sensors and ports are a dynamic pressure transducer, static pressure transducer, thermocouples, an inlet port for admitting fuel-air mixtures and a window for visualisation of species in the chamber. There are two kinds of combustion chamber design used in RCM; the direct test chamber(DTC)[104, 105] and the non-direct test chamber type(NDTC)[84, 95, 100, 106, 117]. Most commonly found is the non-direct test chamber type. This design has its charge mixture prepared in a mixing tank maintained at the temperature of the combustion chamber. The advantage of this is that the charge mixture composition does not vary during the test condition since large volumes of charge mixtures are prepared in the mixing tank. In the mixing tank, the preheat temperature is kept at the saturation temperature of the fuel to ensure complete vaporisation. However, condensation of the charged mixture may occur along the piping leading to the inlet port of the combustion chamber changing the fuel air ratio. This can happen if the piping network is not properly insulated and the temperature of the pipe is not maintained with that of the mixing tank. In DTC, the charge mixture is directly

admitted into the combustion chamber. The heating of the reactor chamber is also essential to maintaining temperature uniformity of the combustion chamber walls. The heating equipment varies depending on the shape of the combustion chamber. Typically, heat tape and 6-band heaters are wrapped around the combustion chamber and insulated to control the initial temperature of the mixtures.

2.4 Other Instrument for measuring Autoignition Delay.

Besides the rapid compression machines, other devices are used. The next section would briefly discuss the experimental tools.

2.4.1 Shock Tube

In shock tubes, the generation of the shock wave is used to compress (almost instantly) a test gas mixture. Higher pressures and temperature are achieved than that found in flow reactors and well-stirred reactors. Temperatures in the range of 500 to 3000 K can be achieved for pressures ranging from 1 - 50 bar, rapidly occurring chemical reactions that occur between 0.03 to 5.0 ms can be measured.

The device has two compartments, driver and the driven compartment. It is made up of a long metal cylinder and contains two gas volumes separated by a thin diaphragm.

The driven compartment contains the charged mixture, while the driver compartment maintains the gas at high pressure, where the gas is compressing the driven section. This gas is of low molecular weight to give a high speed of sound. The diaphragm bursts at a particular pressure admitting the driver gas to rapidly compress the driven gas with a shockwave. The burst can be achieved by either high pressurising the driver section or igniting it. Typical diaphragm materials are a metal foil or glass paper[118].

After the diaphragm is burst, the driver gas expands, and a travelling shock wave is generated. The charged mixture is initial shock heated as the wave travels through and further heated by the reflected shock from the back wall of the reaction. The charge is rapidly heated, and its temperature and pressure maintained for up to 5 ms. Most shock tubes also have optical access to the collection of laser-based intermediate species data[119]. Species concentrations may be captured using a GC/MS systems [120]. A pictorial diagram of a high-pressure shock tube from combustion and Energy System Laboratory at Rensselaer Polytechnic Institute[121] is shown in figure 2-6.

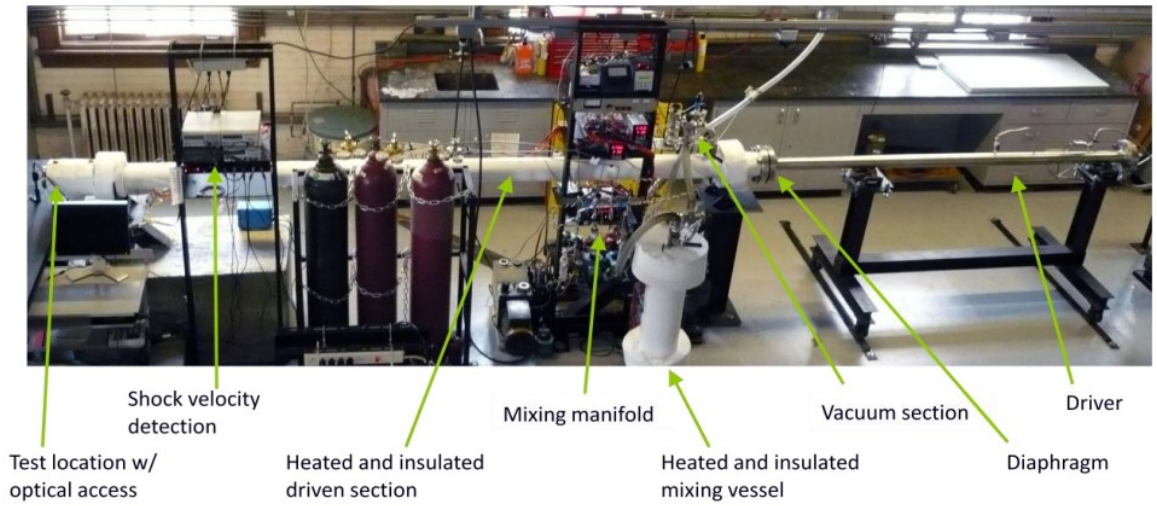


Figure 2-6: A Pictorial diagram of the High-Pressure Shock Tube[121].

The temperature and pressure a shock tube can attain vary from rig to rig. Sivaramakrishnan et al. could achieve a pressure and temperature up to 550 bar and 2800 K, while rig reported by De Toni et al.[122]] attains a reflected-shock pressure up to 500 bar. Lately, development in shock tubes design has been made which introduces an aerosol shock that can handle non-volatile fuels[123]. In this design, a fuel aerosol in an oxidizer including diluent bath gas is used. The fuel aerosol is rapidly heated by the initial shock, vaporised, and diffusively mixed before the advent of the reflected shock. A gas-phase test then proceeds after the reflected shock.

In shock tubes, the ignition delay time is defined as the elapsed time between the arrival of the shock wave at the driven section end wall and the onset of ignition at that same location. The start of ignition is identified by the rapid growth in electronically excited OH (OH*) emission that occurs at ignition. Conventionally, the ignition point is defined by extrapolating the peak in the slope of the measured OH* emission signal to the baseline pre-shock value. The observation of the OH* emission around at 306 nm with appropriate sensors and optical filters[124].Figure 2-7 shows the ignition delay measurement from shock tube.

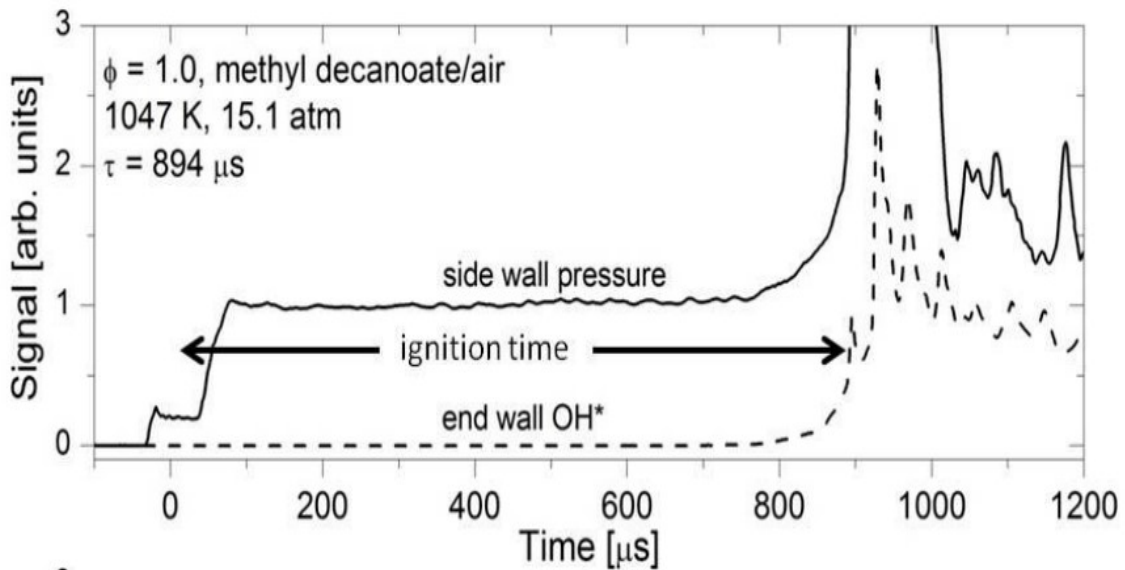


Figure 2-7: Shows the ignition delay measurement from Shock Tubes

One of the limits of shock tube is that due to interference from boundary layer effects and reflected waves, observation times are limited to less than 5 ms. Therefore, the experimental conditions are constrained to pressure and temperature regimes where chemical induction times are very short.

2.4.2 Flow Reactor

A flow reactor brings reactive mixture to required temperature and pressure and then allows it to travel down a tube as the reaction takes place. It is used to investigate reactions at low to high temperatures in the range of 500 – 1500 K at pressures up to 15 bar. Flow reactor experiments are conducted by first mixing fuel, oxidizer and diluent gases upstream of the reaction chamber vessel, or within the reactor. The mixture residence times in the heated reaction chamber span from 0.1 to 10 seconds, limiting the apparatus for investigating combustion phenomena such as an ignition process. The mixture is diluted with inert gas, which minimises gas thermal and compositional stratification within the reaction chamber. The core gas is a sample as chemical explosion progress and analysed by GC/MS systems to get species concentration data of stable intermediates. Figure 2-8 shows a schematic of the variable pressure flow reactor.

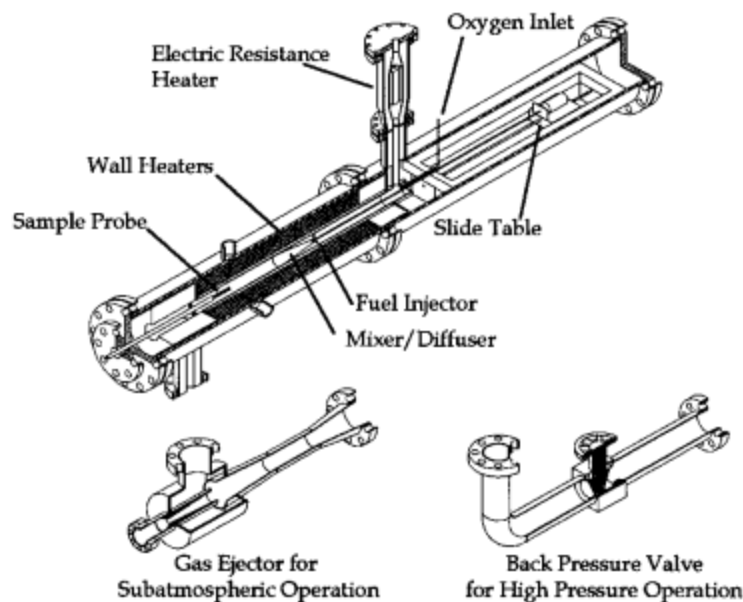


Figure 2-8: shows a diagram of variable pressure flow reactor in Princeton University[125].

2.4.3 Well-Stirred Reactors.

Well-stirred reactors (WSR) are instruments used to achieve a perfect mixing inside a reactor, see Figure 2-9. They have a fixed volume with an inlet and outlet port. They are operated at steady state and constant pressure. WSRs typically employ high-velocity inlet-jet approaches giving high-intensity turbulent mixing. Species concentrations and temperature are assumed to be uniformly distributed. The rapid mixing results in sample conditions that are purely kinetically controlled. The composition of exiting mixture is a function of residence time. There are three characteristic times in WSR.

A significant issue with stirred reactors is the achievement of sufficiently rapid mixing. At high temperatures, most combustion reactions are very fast and chemical time constants may be comparable to mixing time. Under these conditions, experimental results are mixing influenced. One of the advantages of WSR is that it can operate with low dilution and short residence times, and this permits the study of reactions at higher temperatures than flow reactors. A high degree of dilution is still used to reduce temperature gradients and heat release. A typical example is the study of Dagaut et al.[126] where they investigated n-heptane oxidation in a jet-stirred reactor in the temperature range of 550 K to 1150 K and a pressure of up to 40 bar. The mixture was highly dilute (0.1% fuel) this was necessary to reduce the temperature gradients, control heat release inside the reactor and maintain a steady state. Since these reactors operate under steady state condition, information regarding time evolution of chemical reactions is not readily available. Several studies on the oxidation of various hydrocarbons and oxygenated compound[127] have been conducted both experimental[128-132] and numerically[133-135] using WSR.

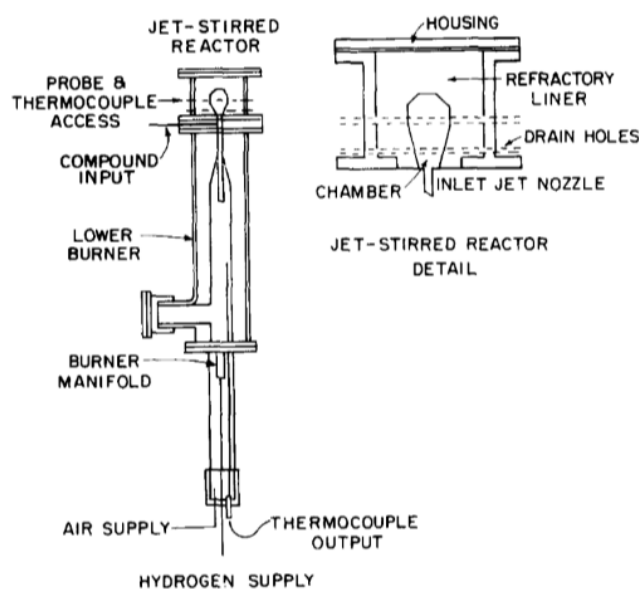


Figure 2-9: Pictorial view of Well-stirred reactor[133]

2.4.4 Static Reactor

Static reactors are a simplified constant volume apparatus used to study slow reactions characterised by low and intermediate temperature oxidation chemistry. The device consists of a spherical vessel filled with the reactive mixture and located inside a temperature-controlled compartment. This compartment could be an oven or a thermostatic bath that maintains the gas phase reactants at the desired temperature. The evolution of reaction is checked by measuring the change in pressure or by detecting concentrations as a function of time for one or several species from withdrawn, quenched gas samples. In most cases, another vessel is used to premix the gaseous fuel-oxidizer reactant and admitted to the evacuated preheated reaction vessel by way of a valve[136]. The hypothesis associated with static reactors is that the reacting mixture is homogeneous. To adhere to this, the characteristic reaction times in static reactor experiments should be longer than characteristic diffusion times. This constraint places significant limitations on the operating range of static reactors (typically lower than 750 K), which results in comparatively long experimental timescales. Therefore, static reactors are frequently useful for comparatively slow reactions. Experimental studies have been performed on the oxidation of alkene using static reactor over the temperature range of 670-770 K[137-139] and on the oxidation of propane at low and intermediate temperature [140-142]. Due to its high sensitivity to surface effects under conditions of long reaction times, static reactor experiments are not useful for quantitative analysis compares with alternative techniques.

2.5 Current Fuels Studied

In the course of the research work three fuels would be considered in this study, conventional Jet A-1, which serves as a baseline fuel; used cooking oil(UCO-HEFA) processed through an F-T process (HEFA), and a Banner solvent comprises a blend of five hydrocarbon species (decane, dodecane, undecane, tridecane, and tetradecane).

2.5.1 Current Fuel Formulation

In this study, the hydrogen-carbon content by (% mass) was used to determine the average molecular weight as described in page 102 of Lucas [143] work. Table 2.2 shows the fuel formulation data derived from the GC analysis of the fuels. The formulation data in figure 2-2 were obtained using the GC*GC data in Figures 2-9, 2-10 and 2-11. This was necessary to determine the correct equivalent ratio accurately. The hydrocarbons identified within the fuel samples were classified based on their chemical structures as per Table 2-3.

Table 2-2: Jet fuel Formulation data

Formulation Data	Jet Fuel (FST-265638)	Used cooking oil (FST-265640)	Banner Solvent
Molecular formula	$C_{11.89}H_{22.89}$	$C_{11.31}H_{24.23}$	$C_{11.75}H_{25.49}$
M.W(g/mol)	166.0	160.3	167
Total C(g)	142.93	135.86	141.09
Total H(g)	23.07	24.42	25.70
Cx(mol)	11.89	11.31	11.745
Hy(mol)	22.89	24.23	25.49
%C	86.1	84.76	84.49
%H	13.9	15.23	18.21
HC Ratio	1.92	2.14	2.17
Specific Gravity	0.8067	0.7596	0.755
DCN	43.74	56.38	75

Table 2-3: shows hydrocarbon identification base on their chemical structures[144].

Symbol	Description	Structure (simple)
n-P	Normal alkane (linear, normal paraffin) Formula: C_nH_{2n+2}	
i-P	Iso alkane (branched, iso paraffin) Formula: C_nH_{2n+2}	
N	Cyclo alkane (naphthene) Formula: C_nH_{2n}	
diN	di-cyclo alkane (di-naphthene) Formula: C_nH_{2n-2}	
mAr	mono-aromatic (+alkyl substitution) Formula: C_nH_{2n-6}	
NmAr	Naphthenic mono-aromatic (+cyclo alkane ring) Formula: C_nH_{2n-8} (for $C_n \geq 9$)	
diAr	di-aromatic Formula: C_nH_{2n-12} (for $10 \leq C_n \leq 12$) ^f	
	Formula: C_nH_{2n-14} (for $C_n > 12$)	
NdiAr	Naphthenic di-aromatics Formula: $C_{12}H_{10}$ (for $C_n = 12$) ^f	
	Formula: C_nH_{2n-16} (for $C_n > 12$)	

2.5.1.1 Estimation of Average Molecular Formulae

The fuel average molecular formulae must be determined so that the required equivalence ratios can be prepared. This is estimated through an approach which uses input from the distillation and specific gravity data to calculate the average molecular weight of single and blended fuels[145]. In this method coupling of the fuel specification data describing the hydrogen content was used to determine the average molecular formula of fuels. Rao[145] proposed this where he correlated the average molecular weight (M) as a function of the boiling point (T_b) as shown below.

$$M = \left(\frac{T_b}{A} \right)^B \quad 2-1$$

From Equation 2-1, the parameter A and B are calculated based on the molal average boiling point, T_M .

2.5.2 Jet A-1

Jet A-1 consists of various classes of hydrocarbon [146]. It is mainly derived from crude oil and composed of hundreds of aliphatic and aromatic hydrocarbon compounds with carbon chain length of C8-C16. Principal components are normal alkanes, branched alkanes, cycloalkanes, aromatics, and alkenes. A survey has shown that the average composition of Jet fuel worldwide contains 58% alkanes, 21% cycloalkanes, 13% aromatics[147].

Jet fuels contain a significant amount of naphthenes, which enhances storage and thermal stability[60]. Additional chemical additives improves the thermal stability and storage of fuel; a typical example is the JP-8 +100[148]. Because the naphthenes undergo endothermic fuel decomposition at low temperatures, it can act as a heat sink for the cooling with the jet engines[149]. The presence of aromatics the fuel influences autoignition at low temperature. Because jet fuel is associated with the production of soot, they are limited to 20-25% and naphthalene content to 3% in volume. For economic reasons, the aromatic contents have increased since the 1960s[150]. Each hydrocarbon group within the fuel has a different common oxidation characteristic. Roubaud et al.[151] carried out work in a rapid compression machine, and that toluene, m-xylene and p-xylene could not auto-ignite below 16 bars, while o-xylene and n-butyl benzene were able to auto-ignite at 10 bars in 50ms. Alkanes are relatively reactive while cycloalkane and aromatics are less so. The compounds of the highest concentration are n-alkanes. The characteristics of an aviation jet fuel are determined by operational needs, and they are typically developed to have good combustion characteristics combined with desired physical properties. There are three types of conventional jet fuels[152]: (i) a kerosene type (ii) a high flash point kerosene, and (iii) a broad cut. International civilian aviation companies mostly use the kerosene type Jet A-1.

Table 2-5, shows the main characteristics of JP-8 and Jet A-1 reported by various authors in the literature[149, 152-155]. This includes the average composition of chemical families and the average chemical formula for kerosene (Jet A, Jet A-1, TR0, JP8), which differs from one source to another.

Table 2-4: Characteristic Properties of Kerosene Jet Fuel[60].

Property	JP-8 [149]	JP-8 [154]	JP-8/Jet A-1 [153]	Jet A [154]	JP-8[155]	Kerosene[152]
Molecular weight		152		162		
Approximate formula		$C_{10.9}H_{20.9}$	$C_{11}H_{21}$	$C_{11.6}H_{22}$		
Number of C atoms in the fuel		10.9	11	11.6		9-13
H/C ratio		1.92	1.91	1.9		1.9-2.1
Boiling range	140–300	Average 204	165–265	Average 216		140–280
Specific gravity at 15C	0.81		0.81			0.77–0.83
Av. Composition in vol%						
Aromatics	20		18		18(monoaro.)C2 (diaro.)	10–20
Cycloalkanes	20		20		20	20–30
Paraffin	58		60		28(n-par.)C29(i-par.)	50–65
Olefins	2		2			0

It is often necessary to use a surrogate model fuel for simulating a fuels oxidation. Therefore, n-decane is primarily used as a surrogate to study practical jet fuels such as kerosene[156] and diesel[157]. A study[158] on n-decane oxidation at atmospheric pressure showed that the primary product measured were also found in kerosene oxidation [159]. In other studies using a high-pressure jet-stirred reactor [156], both n decane and kerosene showed very similar oxidation rates [156, 160] Similarly for premixed flames [161].

Military fuels are blends of JP-8 and JP-5[162]. JP-8 is a conventional petroleum-derived jet fuel widely used by the U.S. military. The JP-5, which is naphtha-typed fuel made by blending straight-run kerosene stream with lower boiling distillates to fit the ASTM specifications. The primary difference in the two blends is that JP-8 has a lower freezing point ($-47^{\circ}C$), an additive package that includes corrosion inhibitors, icing inhibitors, and lubricants and ability to handle high heat.

Figure 2-9: shows the GC x GC analysis of the present jet A-1 fuel used in this work. The primary constituents are Cyclo-paraffin 40.79% by weight, n-paraffin 19.35% by weight, iso-paraffin 20.57% by weight and aromatic 19.25% by weight.

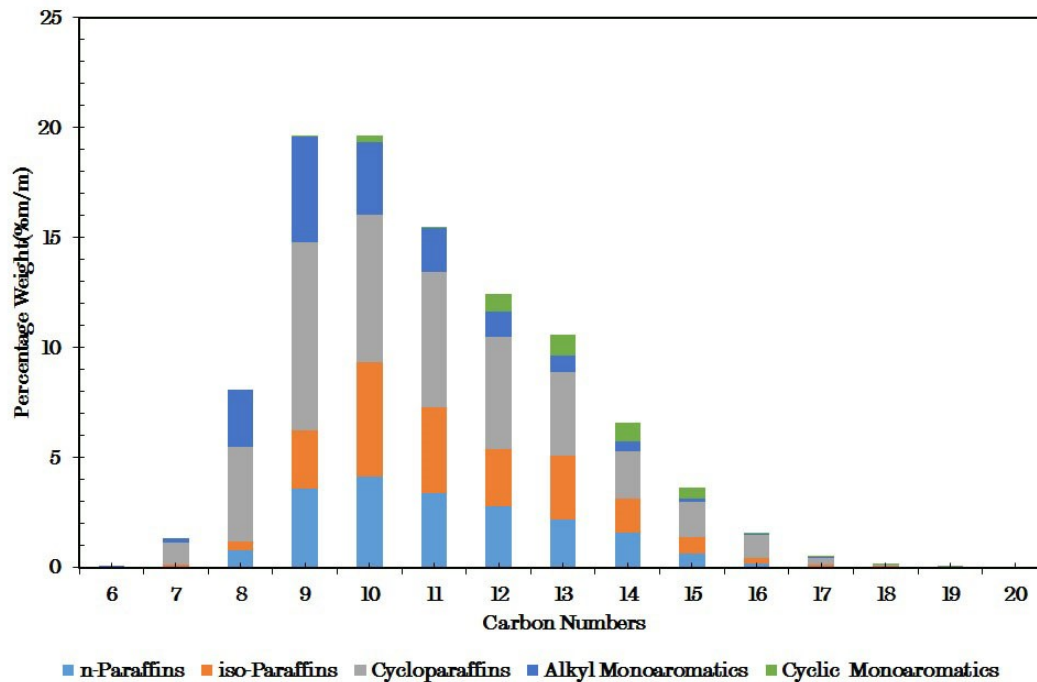


Figure 2-9: Showing the GC x GC analysis of a conventional Jet A-1 fuel (FST-265638) composition.

2.5.3 Banner Solvent

Banner solvent are purely n-paraffinic fuels with a molecular formula of C_nH_{2n+2} consisting of five major component namely: n-Decane, n-Undecane, n-Dodecane, n-Tridecane and, n-Tetradecane. Figure 2-10, shows the GC x GC analysis of the solvent fuel. At present, there is dearth information on ignition time of Banner-solvent. The understanding of chemical and physical properties of the fuel is relevant for the development of kinetic model and vital to combustor designers.

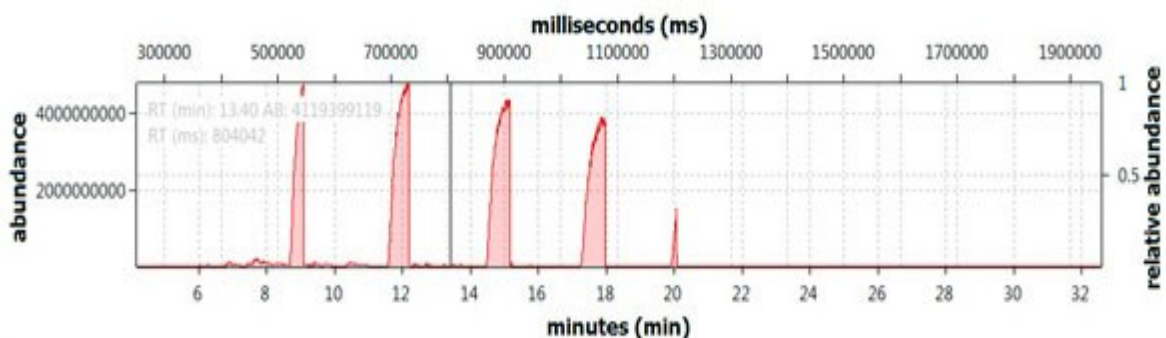


Figure 2-10: Showing the GC x GC analysis of a typical Banner Solvent.

2.5.4 Used cooking oil (UCO-HEFA)

Figure 2-11, shows the GC x GC trace of the UCO-HEFA studied in this work. It contains mostly n-paraffinic and isoparaffinic compounds with negligible aromatic. The relative proportion of each type of molecule is 19.47% n-paraffins, 71.34% iso-paraffins, 0.56% cycloparaffins, 6% naphthenes and about 1.9% aromatics by weight.

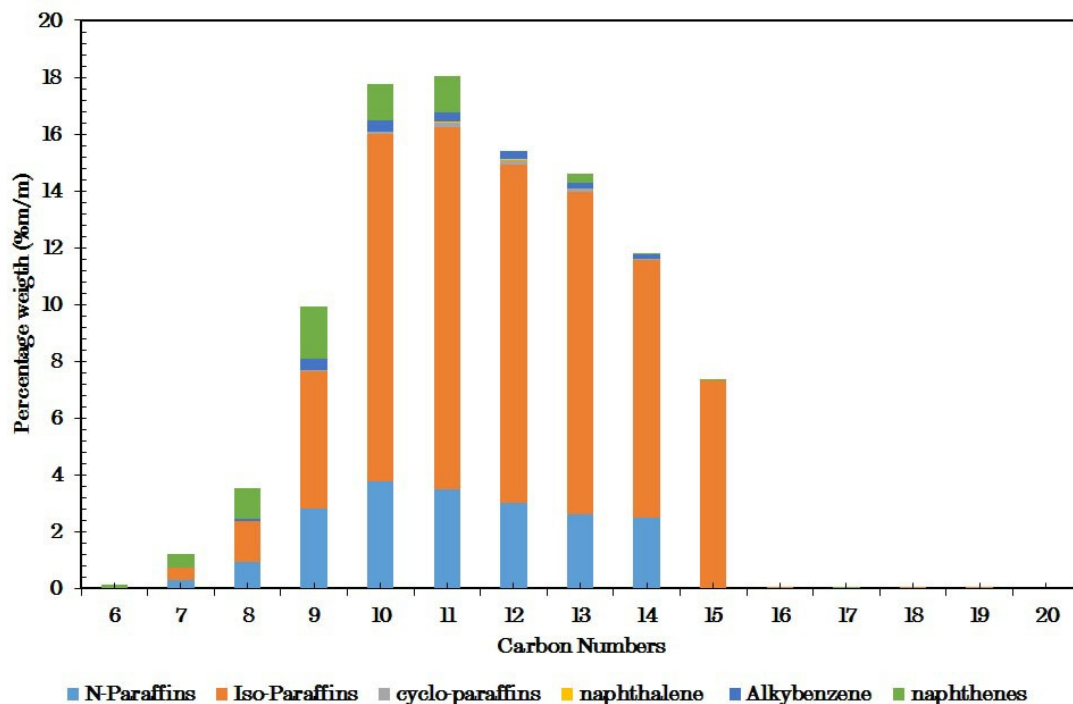


Figure 2-11: Showing the GC x GC analysis of a typical UCO-HEFA fuel composition

2.6 Basic Concept of Autoignition

Auto-ignition is one of the fundamental properties of combustion, which has a significant impact on engine emission and performance[163]. The onset of autoignition is driven by the temperature, pressure and chemical kinetics of the system[164]. It initiates when the slow thermal reactions have sufficient chain-branching components to support and accelerate oxidation. The initiation starts with a group of reactions abstracting H atom or decomposing hydrocarbon molecules into a highly reactive intermediate species (radicals). It then proceeds by propagation reactions, where the built-up radicals react to form products and more radicals. The increase in reaction rate and the increasing radicals' concentration build on themselves and in due course lead to a rapid, explosive rise in radical concentration and oxidation rate. Chain branching reactions occur where more radicals are produced in a reaction than are absorbed accelerating the reaction rate significantly. Eventually, the radical concentration is suppressed by termination reactions, which transform the active radical to stable product[165, 166]. This process releases heat

thereby increasing the temperature of the system. The reaction rates are dependent on the pressure and temperature.

When autoignition occurs, the rate at which energy is liberated by the chemical oxidation reaction exceeds the rate energy at which it is dissipated by heat loss. This increases the temperature of the mixture, and in turn the oxidation chemistry rate.

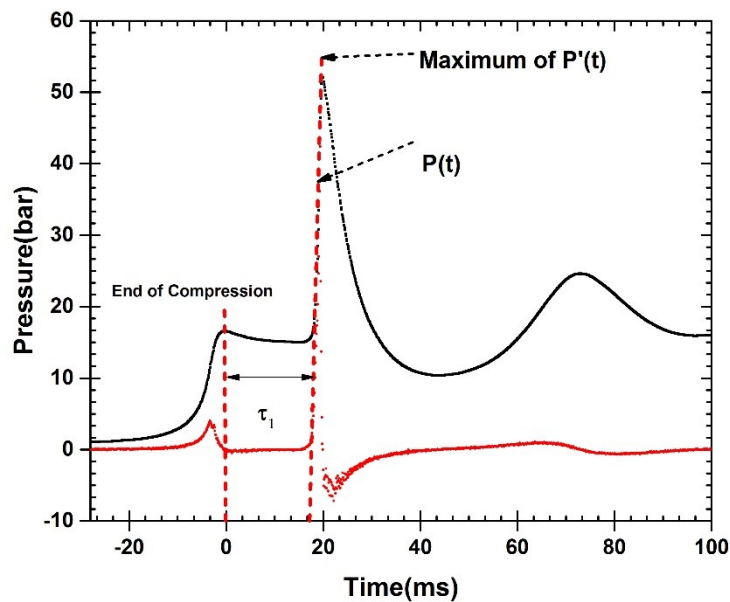


Figure 2-12: illustrates the basic definition of ignition delay of a single stage ignition. $P(t)$ is the pressure as a function of time, and $P'(t)$ is the time derivative of the pressure as a function of time.

Figure 2-12 illustrates the basic definition of autoignition delay, which is the time from the end of a rapid increase in pressure, and temperature to the spontaneous ignition of the fuel mixture. The accurate prediction of autoignition times with their dependence on pressure, temperature, and composition is essential for the application of advanced engine technologies. However, autoignition is sensitive to chain branching and chain terminating reactions and thus depends on the chemical structure of the fuel.

2.6.1 Ignition Limits

The lean ignition limit is the minimum concentration of fuel and air mixture in its vapour state and under specified condition below, which external ignition cannot initiate a self-propagating reaction. Ignition limits can be classified into two, the strong and the weak ignition limit[167]. The strong limit occurs over high temperatures and generates a blast wave, while the weak or mild ignition limit occurs at lower temperatures where the initiation of the reaction at many loci merge to form a smooth front.

Explosion limits for hydrocarbon fuels are illustrated in the P-T explosion diagram shown in Fig. 2-13. When pressure is low the system is characterised by a slow reaction, where ignition does not occur, the collisions and the production rate of chain carriers are

subsequently low. The reactive species formed in the gas phase by chemical reaction diffuses to the wall and form a stable species. Diffusion is inversely proportional to the density of the gas, so can occur with relative ease at low pressure. With increasing pressure, a threshold value is reached (first ignition limit), where the gas molecules are energised, and the production rate of the chain carrier reaction increases leading to a spontaneous ignition. The first explosion limit is governed by the chemical nature of the vessel and the limit of circumstantial processes of chain branching in the gas phase and that of chain termination to the surface. As it proceeds, the reaction is slow without observing any ignition.

In the second explosion limit, which is characterised by chain branching and chain termination in the gas phase. The chain branching reactions produce a radical pool, which is the basis for the explosion. The three-body reactions compete with branching reaction to produces weak reactive radical (hydroperoxyl radical). This reaction illustrates a typical chain termination and is slightly independent on temperature.

In the third explosion, the limit is controlled by the competitive nature of the heat production by the chemical reaction and the heat losses to the vessel wall. At this point, as pressure increases the heat production rate, also increases per volume and a transition to the explosion occurs. The multistage ignition is seen as the region where ignition proceeds after the emission of short light pulses, and this occurs at a low temperature[164].

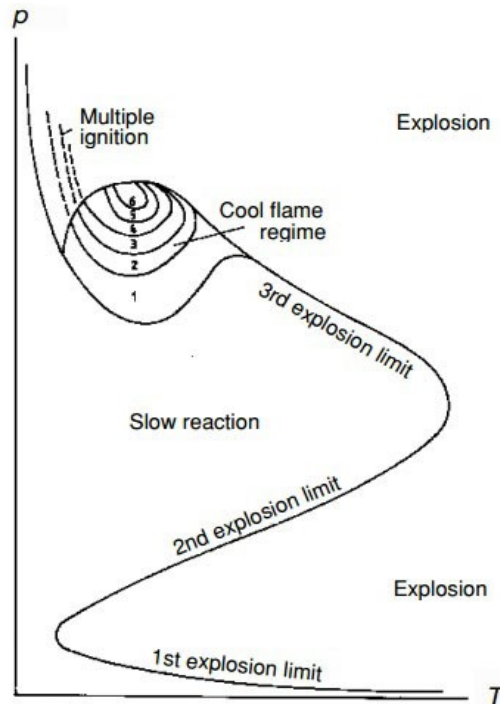


Figure 2-13: shows the Ignition limit (P-T explosion diagram) for hydrocarbon fuels [163].

2.7 Basic Concept of Chemical Kinetics

Chemical kinetics describes the sequence a chemical system follows during the transformation of reactant into a product. The time it takes for a reactant to get to the product state is of importance. The backbone of chemical kinetic is the rate of the reaction. Avery[168], defined the rate of reaction as the change of measurable quantity related to the reaction system. It can be expressed as a change in concentration of some species with time. This illustrated with the following bimolecular reactions.



Here A, B are reactants and C, D are the products. The letters a, b and c, d represent numbers that ensure the equations are balanced. The rate of reaction term of species concentration is

$$\text{Rate} = \frac{-1}{a} \frac{d[A]}{dt} = \frac{-1}{b} \frac{d[B]}{dt} = \frac{1}{c} \frac{d[C]}{dt} = \frac{1}{d} \frac{d[D]}{dt} \quad 2-3$$

The rate of reaction is proportional to the concentration of its reactants and expresses the proportionality between the rate of reaction and concentration of the reactant written in the form

$$\text{Rate} \propto [A]^x [B]^y \quad 2-4$$

$$\text{Rate} = K_f [A]^x [B]^y \quad 2-5$$

Where x and y are the exponents on the concentrations of A and B . In this rate law, K_f is the rate constant and the exponents x and y are the order of the reaction with respect to A and B . The order of reaction is the summation of the exponents x and y . The rate can be further expressed as [169].

$$\frac{-1}{a} \frac{d[A]}{dt} = K_f [A]^a [B]^b \quad 2-6$$

Arrhenius showed that the rate of a reaction is associated with the temperature

$$K_f = A * \exp \left[-\frac{E_a}{RT} \right] \quad 2-7$$

Where K is the rate coefficient, A is the pre-exponential factor or collision frequency factor, R is the universal gas constant and T , is the temperature, and E_a is the activation energy. Reactions that proceed break the reactant chemical bond with a higher kinetic energy than that needed [170]. This barrier is prescribed by the activation energy shown in figure 2-14

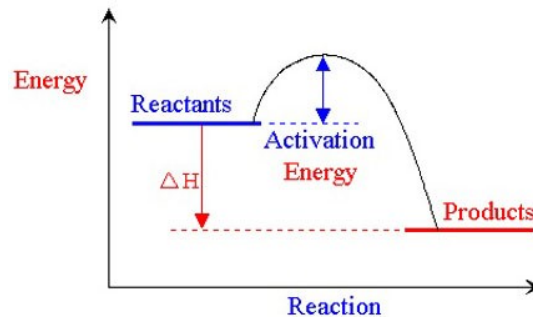


Figure 2-14: shows the schematic diagram of a chemical reaction [191].

The difference between the reactant and product is referred to ΔH . Where H , is the enthalpy. The expression $\exp \left[-\frac{E_a}{RT} \right]$ reflects on the fraction of molecules that have higher kinetic energy than the activation energy. Pressure influences the rate of reaction by subsequently increasing the molar concentration, which eventually increases the collision of the state. More recently, the Arrhenius has been modified by introducing a parameter b into equation (2-8) which expresses the dependence of collision frequency on temperature.

$$K_f = A \cdot T^b * \exp \left[-\frac{E_a}{RT} \right] \quad 2-8$$

The ignition delay depends exponentially on the reciprocal temperature that exhibits Arrhenius temperature dependence [164, 171].

2.7.1 Hydrocarbon Oxidation and Mechanisms

When hydrocarbon fuels are heating in the presence of air, they undergo a complex sequence of elementary chemical reactions. The hydrocarbon oxidation process can be separated into three distinct temperature regimes [172].

1. A low-temperature regime where the dominant branching agent is alkyl peroxy radicals.
2. The intermediate temperature regime dominated by hydroperoxyl radical
3. The high-temperature regime, the hydroxyl and atomic oxygen and hydrogen radicals are dominant.

Each regime is dominated by reactions involving different radical species and different pathways. The boundaries between each regime are influenced by the pressure, temperature and equivalent ratio. Figure 2-15, illustrates these the three distinct oxidation pathway schemes adopted as presented by Miller et al.[173] A brief description of the three distinct temperature regime given in the next section.

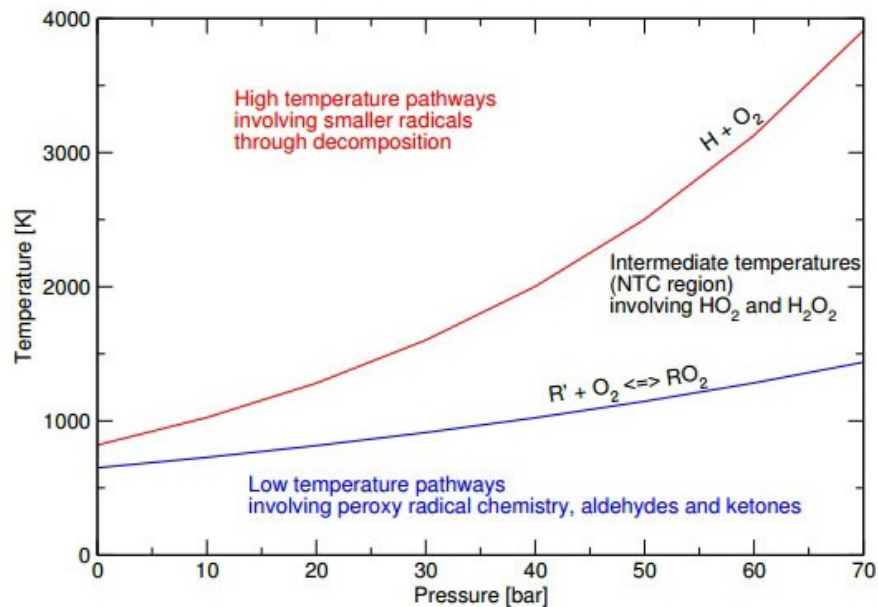


Figure 2-15: showing the three temperature regimes (low, intermediate and high) for an Alkane Oxidation [115].

In figure 2-15, illustrates the basic oxidation pathway regime for hydrocarbon fuels. At the boundary between the intermediate and high-temperature regime the reaction ($H + O_2$) is neutral. Above this line, the branching reaction ($H + O_2 \rightarrow OH + O$), dominates below at low temperature, termination reaction ($H + O_2 + M \rightarrow HO_2 + M$), and is dominated. The intermediate temperature regimes are classify as the negative temperature coefficient (NTC) state. Here, the intermediate regimes degenerate chain branching reactions starts to dominate the chain branching reactions at low temperature regime. Whereas the neutrality of the peroxy radical is link to the boundary, between the low and intermediate temperature regime.

2.7.1.1 Low-Temperature Regime

In low-temperature regime, the compressed gas temperature of the unburned gases is below 900 K. A schematic diagram is shown in figure 2-16, the branching pathway of low-temperature chemistry. The process starts with the abstraction of H atoms from the hydrocarbon RH, producing an alkyl radical R .

The alkyl radical reacts rapidly with O_2 to produce the alkylperoxy radical RO_2 . In kinetic study, the $R + O_2$ reaction displays behaviour that is much more complicated. With a slightly increased temperature, the alkylperoxy radical becomes thermally unstable and

can impact on the progress of autoignition. The alkyl and O_2 reactants can form back by the dissociation of RO_2 . Even at room temperature the conjugate alkene and HO_2 can be produced by RO_2 but is terminated as the pressure increases[174, 175]. HO_2 is a stable unreactive molecule and its only means of production is through the direct elimination of HO_2 from RO_2 , which has been demonstrated through theoretically[176, 177] and experimentally[178-180]. The removal of HO_2 produces H_2O_2 and which is stable up to 1100 K, this avenue is chain terminating at low temperature. The occurrence of this behaviour and the loss of RO_2 a chain carrier is partly responsible for the negative temperature coefficient that causes the decrease in reactivity with increasing temperature as observed in the oxidation of several hydrocarbons. The progress of alkylperoxy radical isomerization yields via a ring-like intermediate transition state containing 5, 6, 7, or 8 atoms. The rate of each H atom transfer depends on the number of atoms in this transition state ring and the sort of C-H bond that is broken during this intramolecular H atom isomerization[172, 181]. The high reactivity of alkanes at low temperature is attributed to the formation of hydroperoxides, which are degenerate branching agents that abstracts an H atom from within the RO_2 species to produce a hydroperoxyalkyl radical, $QOOH$ [182]. The $QOOH$ formed is a substituted alkyl radical, with the unpaired electron formally located at a carbon atom; it is subject to attack by a second O_2 molecule to yield O_2QOOH . These further react by a second internal isomerization (H abstraction) and dissociation to produce multiple radicals (e.g. 2 OH radicals and an oxy radical) and a chain branching pathway at low temperature and this process strongly promotes the oxidation of alkanes below 900 K.

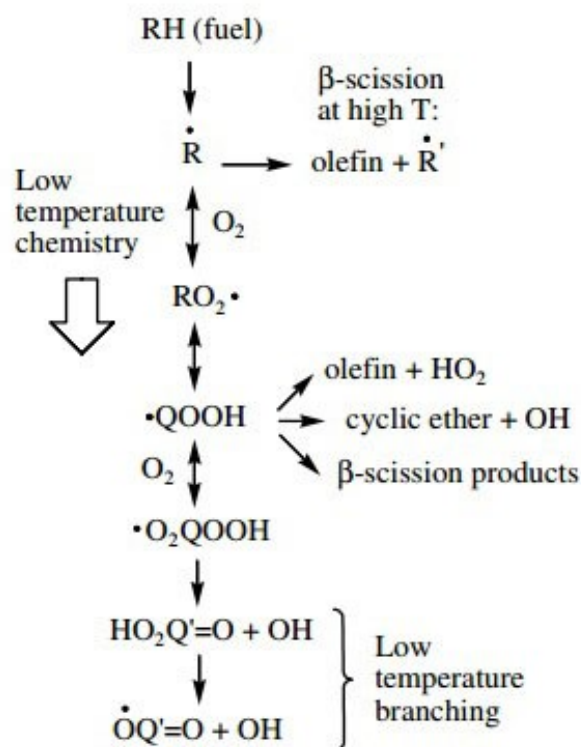


Figure 2-16: shows the chemical kinetics pathway for low-temperature oxidation of alkane [131].

2.7.1.2 Negative Temperature Coefficient (NTC)

In 1938 Pease was one of the few scientists to observe NTC during his study on the oxidation of propane using both flow and static systems[183]. This phenomenon holds significant importance in the non-isothermal oxidation of alkanes. When the temperature exceeds (< 650 K) degenerate chain branching develops and oxidation is principally by OH radicals. These are exothermically reactive, and the system itself begins to self-heat. As the temperature increases the turnover temperature is achieved, which indicates the beginning of the NTC regime[184]. The alkyl peroxy becomes unstable and reacts reversely to the oxidation of alkyl radicals. The equilibrium position of $R + O_2 \leftrightarrow RO_2$ begins to shift back to the reactant where the formation of HO_2 radicals and the conjugated alkene is more favoured compared to that of alkyl peroxy radicals. This eventually leads to slowing down of the chain branching of the reaction[185, 186]. The decomposition of QOOH radicals into cyclic ethers, aldehydes or ketone and OH radicals or by β -scission into HO_2 radicals and conjugated alkenes also decreases the reactivity in that regime.

2.7.1.3 Intermediate Temperature Regime

Within the intermediate temperature regime (800-1000 K) as the pressure increases the turnover temperature shift towards higher values where the NTC region suddenly begins to vanish. The dominated HO_2 radical's produces H_2O_2 decomposes rapidly to OH radical as they formed and is the driver for the chain branching reaction.

2.7.1.4 High-Temperature Regime

At high temperatures greater than 1000 K, the chain initiation reactions are predominantly the decomposition reactions in addition to the H-atom abstraction reactions. Hydrocarbon lumps are short lived to undergo β -scission to yield a smaller olefin and another radical. The decomposition not only involve fuel molecules but the alkyl, alkenyl, and olefins, which are the major branching mechanism. At higher temperatures, the internal H atom isomerisation dominates, while other smaller oxygenated species such as CH_2O and CO along with olefins and smaller alkanes take over as the main participants of the subsequent oxidation reactions[172].

2.7.2 Surrogate Fuel as a Representative of Alternative Aviation Fuel.

2.7.3 The concept of Surrogate Fuels.

The complexities of jet and alternative fuels mean that a direct engine simulation of the chemical kinetic behaviour is not feasible[187]. Therefore, commercial fuels are described using a limited number of representative compounds; these are called surrogate mixtures [188]. In this way, it is possible to describe the chemical oxidational process

computationally, and well-defined experiments can be performed. The physical and chemical properties of an aviation jet fuel should be reproduced by using surrogate fuels. There are two types of surrogates; physical surrogates designed to produce the physical properties of aviation fuels and the chemical surrogates intended to have a similar chemical composition of the aviation fuels. Surrogates that have both the same physical and chemical properties as the aviation fuel are referred to as comprehensive surrogates.

In a gas turbine process, the combustion processes are composed of several stages, including the premixed combustion phase, ignition delay period and the mixing-controlled combustion or diffusion burn phase[189]. The ignition of the injected liquid fuel is governed by the physical and chemical process during the ignition delay period, and it is necessary for surrogates to describe a range of real fuel properties[153, 190].

The ignitability of the fuel is referred to as the derived cetane number (DCN), which measures the ignition quality of fuels.

2.7.4 Surrogate Formulations.

Various methods have been designed to determine the critical component of surrogate of the different real fuels [191-193] and surrogate proposed for Jet A[194, 195] and FT fuels[196, 197]. Typical property targets are

- (1) The average molecular weight(MW)
- (2) The threshold sooting index(TSI)
- (3) The hydrogen to carbon ratio(H/C)
- (4) The derived cetane number (DCN).

With these four basic properties, no detailed chemical analysis of the real fuel is required, but the chemical structure must be reflected in the selection of surrogate fuel components.

Two surrogates are a first generation surrogate comprising of n-decane/iso-octane/toluene[194] and a second generation surrogate n-dodecane /iso-octane /n-propyl benzene /1,3,5 trimethylbenzene[198]. The first generation surrogate mixture could not replicate TSI and its average molecular weight commercial fuel. This led to the second-generation surrogate component, which matched Jet fuels.

A surrogate blend Optimizer (SBO) tool was used by Naik et al.,[196] to decide the best surrogate blend composition to model FT fuels. Their match combination of the properties such as H/C molar ratio, Cetane number, lower heating value, density, and actual boiling point curve. Their result showed that the surrogate fuels with the detailed kinetic model were able to precisely predict the combustion properties of the commercial FT jet fuels [196].

A comprehensive study was carried out by Edwards and Maurice[153] on various classes of a surrogate. They said that the kinetic mechanism used for the surrogate must include a proper description of chemical interactions among the components. In a situation, where

single-phase heat transfer is to be studied without chemical reaction a single component with the same critical temperature was recommended for use as a surrogate. N-dodecane, for instance, has physical properties similar to JP-8/JetA-1 and JP-7[153] whereas other properties such as mixing, injection and fuel vaporisation without a chemical reaction requires a multi-component surrogate to match the distillation curve.

Chapter 3. Experimental Facility and Technique.

3.1 Developmental Overview of Sheffield Rapid Compression Machine (Shef-RCM)

The primary design consideration in the development of a rapid compression is its ability to compress fast, yet bring the piston to a halt at top dead centre (TDC). Thus minimises the heat loss from gases to the wall of the cylinder and also avoids vibrations that would distort the experimental data [100, 199]. A diagram of the present Shef-RCM shown in figure 3-1. The SRCM consists of three chambers and four pistons. Two rods run from the front of the pneumatic driving piston to the rear of the reactor piston so that they move as one unit. The machine was mounted horizontally on a steel frame.

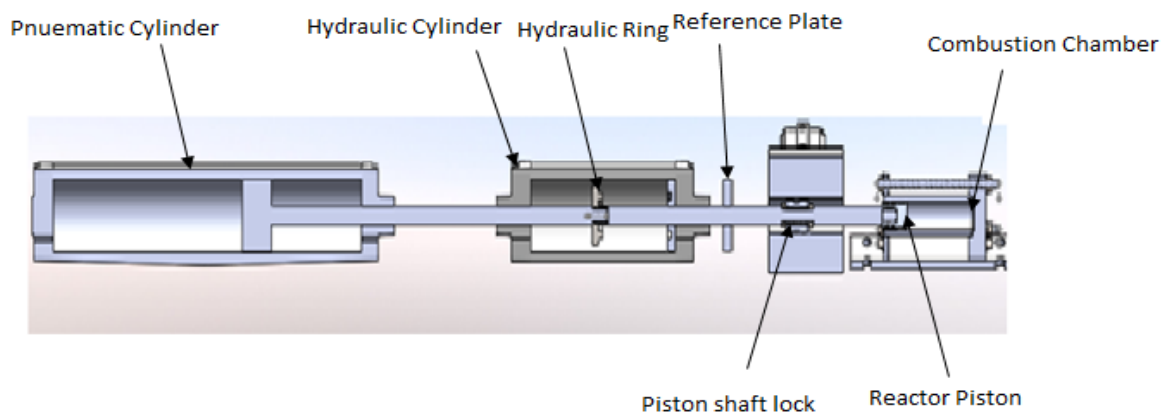


Figure 3-1: Schematic diagram of the University of Sheffield RCM (Shef-RCM).

The entire length of the rig was 2.1 m long and weighed about 40 kg; it was mounted on a heavy steel base frame of 75 kg to minimise vibrations. The rapid compression machine incorporated a hydraulic stopping mechanism, and optimised crevice design. The device was pneumatically driven. The connecting shafts had a standard outer diameter (OD) of 25 mm. The piston stroke was measured by the use of a linear variable differential transformer (LVDT) mounted on a parallel platform with the RCM. It was connected to a reference plate before the piston release mechanism. Heating tape (Omegalux) was wrapped around the reaction chamber to maintain a constant wall temperature. The chamber temperature read was from a PID controller connected to the K-type thermocouple located at the end of the reaction chamber. An optimised piston head crevice was used based on Mittal's design [115, 200].

Fuel was injected with a syringe through a septum into the reaction chamber. The pneumatic pins were charged with compressed air between 3 to 5 bar, before the runs were initiated. A solenoid valve was used to control the pneumatic pin release mechanism (brake). When the solenoid valve was triggered, the compressed air pressure in the system dropped and the pneumatic pins were released. The obtainable compressed pressure at TDC ranged between 5 – 22 bar. The RCM compression time varied between 25 - 35 ms with

a stroke length of 138 – 145 mm and compression ratios of between 6.5 – 13.8. The stroke was fine by moving the reaction chamber over 5 mm in its holding bolt slot. In addition, the thread on the shaft lock has 1.5 diameter pitch, which could be turned to slightly adjust the length of the stroke. The key features of the rig are discussed below. Figure 3-2 shows the snap shot of the present rig.



Figure 3-2: A photograph of the University of Sheffield RCM (Shef-RCM) test facility.

3.2 Driving Section of the Shef-RCM

The driving section of the rig was a single acting actuator (Norgren PRA/182/100/M/600). The pneumatic chamber was 890mm long with a bore of 100mm and a maximum stroke length of 160 mm. The charging pressure could be regulated from 1 to 11 bars. The rear of this cylinder connected to 8mm OD pipe via a ball valve an air compressor (SXC 4), which could supply up to 11 bars pressure. The rig was fitted with two pressure gauges one for the pneumatic cylinder, the other for the piston pin release mechanism (PPRM). The pressurised air supply was passed through a filter to remove moisture and contaminate and to ensure dry air was in the chamber.

The ideal of the Shef-RCM design was to use a bigger driver piston to move a smaller one in the reactor chamber. Thus high pressures are achieved in the reaction chamber with a lower pressure on the driver piston. The moving parts were kept as light as possible to reduce their inertia. The pneumatic chamber function is to store compressed air until it is required to drive the piston. The outstroke of the cylinder is determined by the product of the effective area of the piston to the working pressure. The force generated was found using

$$\text{Thrust } F = \frac{\pi D^2 P}{40}$$

3-1

Where D is the cylinder bore in millimetre, P is the Pressure in the bar and F is the thrust in Newtons. The thrust generated so far assuming a driving pressure of 5 bar driving pressure is 392.7N.

3.3 Combustion Chamber Design

The combustor chamber received the air-fuel mixture and is where the burning takes place. It designed to withstand the pressures of 100 bar. The equation for the hoop stress created by an internal pressure is

$$\sigma_{\theta} = \frac{Pr}{2t} \quad 1.1$$

Where σ_{θ} is the hoop stress, r is the internal radius of the cylindrical tube, t is the wall thickness, P is the internal pressure after combustion in the chamber. The diameter of the cylinder tube can be seen in figure 3-3.

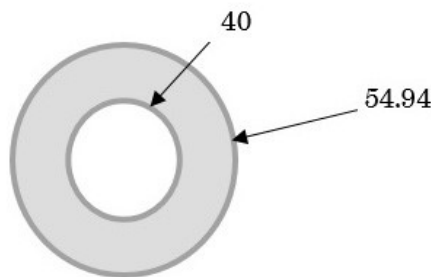
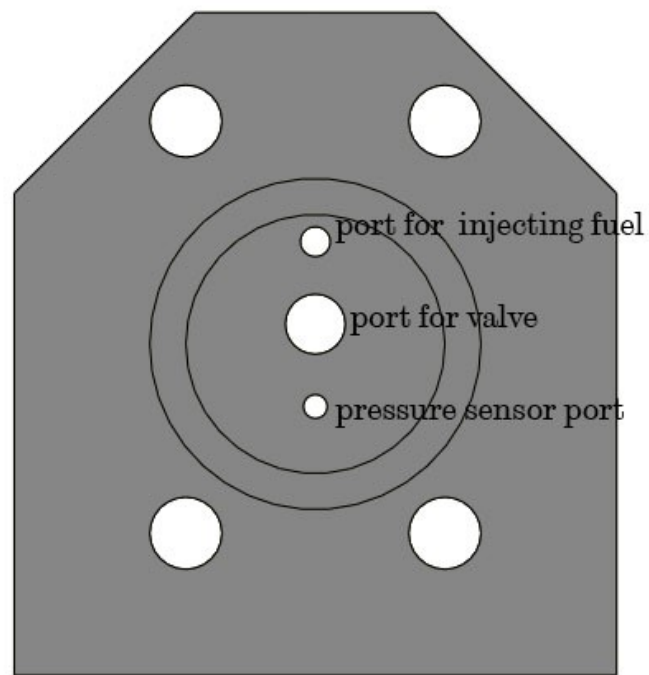


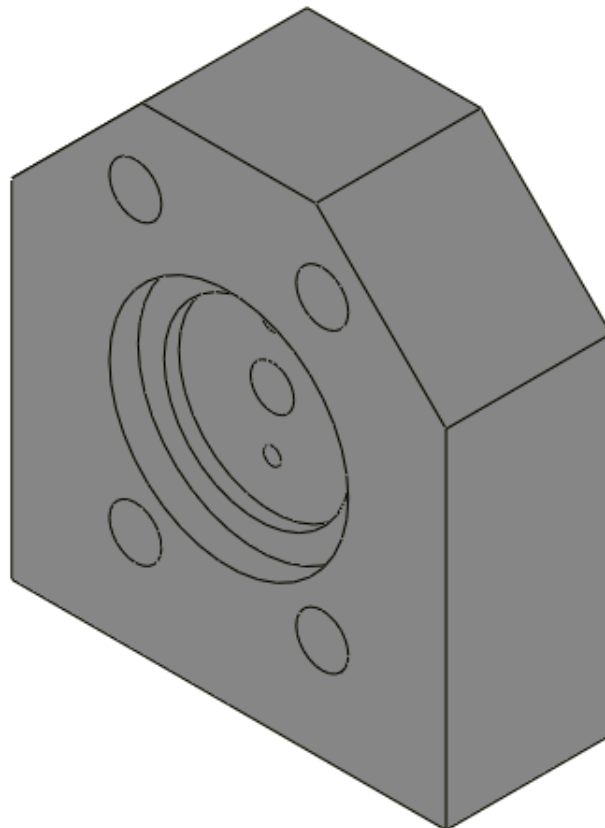
Figure 3-3: shows the diameter of the cylindrical tube in mm.

For a cylinder of internal diameter 40 mm and outer diameter 54.94 mm. The maximum stress the chamber would experience at 100 bars was 26.77MPa. This much less than the yield stress of mild steel (250MPa).

The combustion chamber made up of a cylindrical tube held in stainless steel blocks at the end of the chamber. Figure 3-4, shows the design of the combustion chamber and its unit. The blocks were machined with a bore diameter of 40mm and thickness of 6.6mm. The steel tube had an outer diameter of 40mm, a length of 190mm with a wall thickness of 7.47mm. The steel tube fitted into the blocks to form the chamber's assembly. A carbonised copper gasket was fitted in the recess of the chamber block to seal the chamber. Bolts (M10) held the rig together.



(a)



(b)

Figure 3-4: showing the three ports (a) front view and (b) isometric view of the end combustion chamber.

The end of the combustion chamber had three ports to accommodate sensing devices and fuel injection shown in figure 3-4. A thermocouple was used for measuring the initial

temperature of the chamber. The other three ports were: the pressure transducer for capturing the dynamic pressure: fuel injection port for admitting fuels with the needle valve. The needle valve had two functions: it allowed compressed air into the chamber for retracting of the piston, and it serves the purpose of shutting off the opening before the rig run. Figure 3-5 shows the assembled view of the combustion chamber and this cross sectional view.

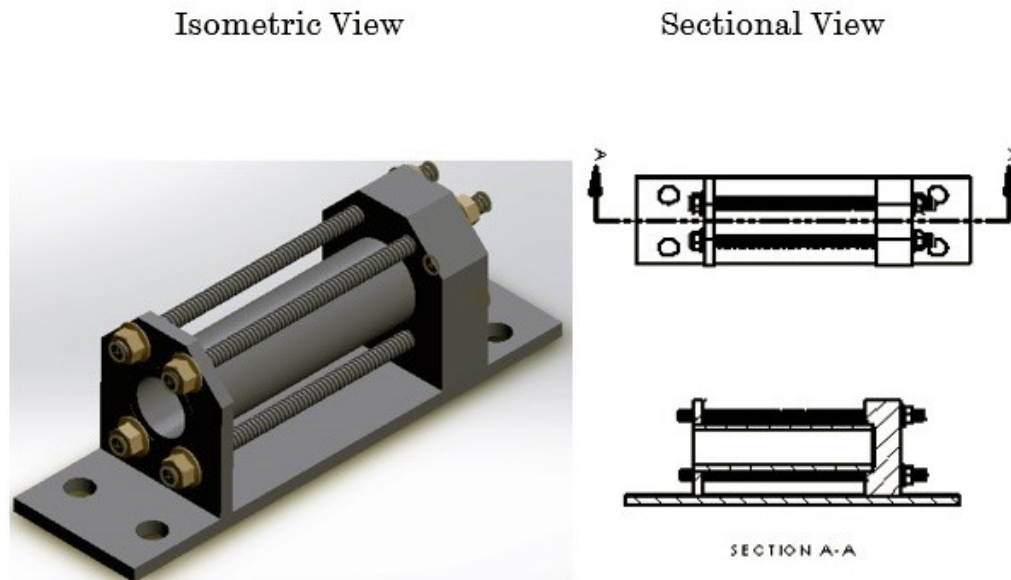


Figure 3-5: showing the Isometric and Sectional view design of the Combustion Chamber Unit.

3.3.1 Combustion Chamber Volume Estimation.

A known combustion chamber volume is required to accurately meter the right amount of fuel into the reactor chamber. The chamber volume was estimated using the ideal gas equation.

$$PV = nR_uT \quad 3-2$$

Where P is the pressure, V is the volume of the chamber, n is the number of moles, R_u is the universal gas constant.

The following assumptions made were:

1. Nitrogen behave like an ideal gas
2. The temperature of the combustion chamber remained constant.

In order to measure its volume combustion chamber was vacuumed down and injected with 50 ml nitrogen gas. Pressure readings were taken using a pressure transducer (Kistler 4045A5, 0-5bar absolute pressure) at every 600s.

Table 3-1: Combustion chamber volume calculation

Test 1					
Time(s)	Pressure(bars)		Volume (ml)		
0	0.8881	V1	129.80		
600	0.8875	V2	129.71		
612	0.6407	V3	179.80		
1212	0.6432	V4	179.10		
			Av. leak rate	0.39	ml
Test 2					
Time(s)	Pressure(bars)				
0	0.8883	V1	129.48		
600	0.8877	V2	129.39		
612	0.6404	V3	179.48		
1212	0.642	V4	179.03		
			Av. leak rate	0.27	ml
Test 3					
Time(s)	Pressure(bars)				
0	0.8859	V1	129.28		
600	0.887	V2	129.12		
612	0.6394	V3	179.12		
1212	0.6412	V4	178.62		
			Av. leak	0.33	ml
			final volume	179.47	

Three sets of measurements were obtained a volume of 179 ml determined as shown in Table 3-1. Figure 3-6 shows, the leaks rate in the combustion chamber. It was estimated to be 0.33ml amounting to about 0.18% of the entire volume and was considered negligible.

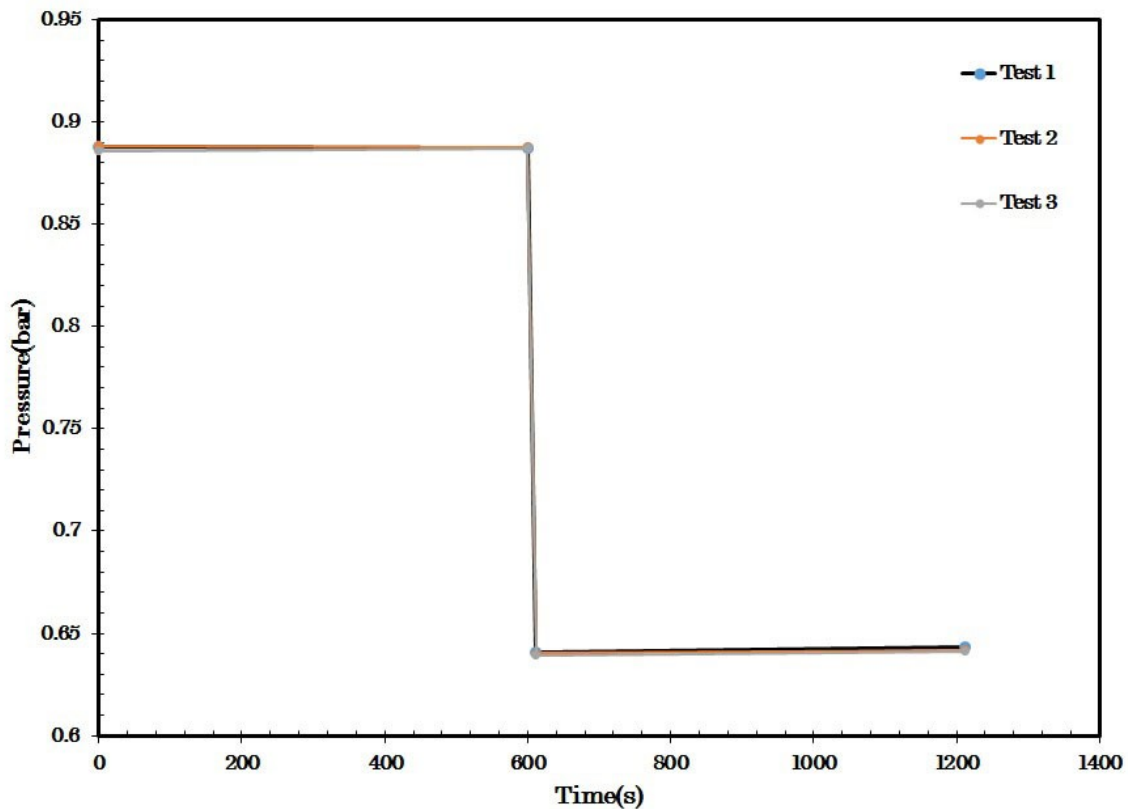


Figure 3-6: Pressure-Time for reactor chamber volume calculation.

3.4 Hydraulic Damping Mechanism

The deceleration and stopping of the piston are achieved by the hydraulic unit that was made up of a ring and groove enclosed in a cylinder filled with hydraulic oil (SAE 10). Figure 3-7 shows a schematic of the hydraulic damping device containing the casing, shaft, piston ring and groove. The hydraulic chamber had a bore diameter of 100mm and length of 400mm. The hydraulic piston ring and groove were made from stainless steel and attached to the shaft. To enhance the speed of the piston, four holes of 5mm bore were drilled on the hydraulic piston ring position.

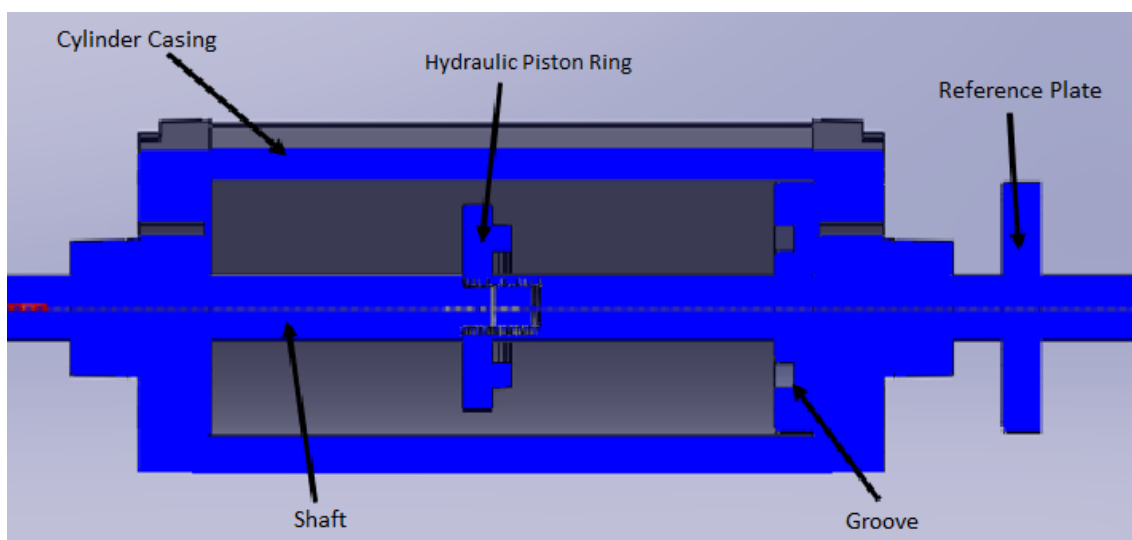
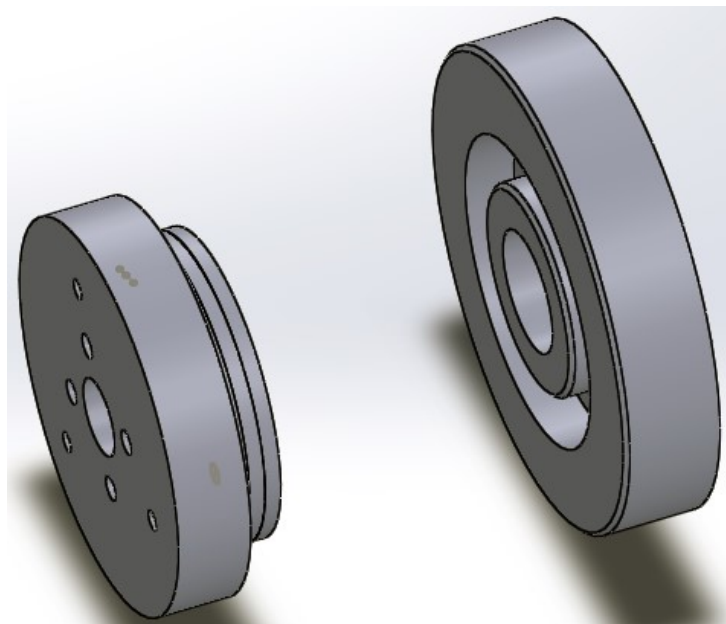


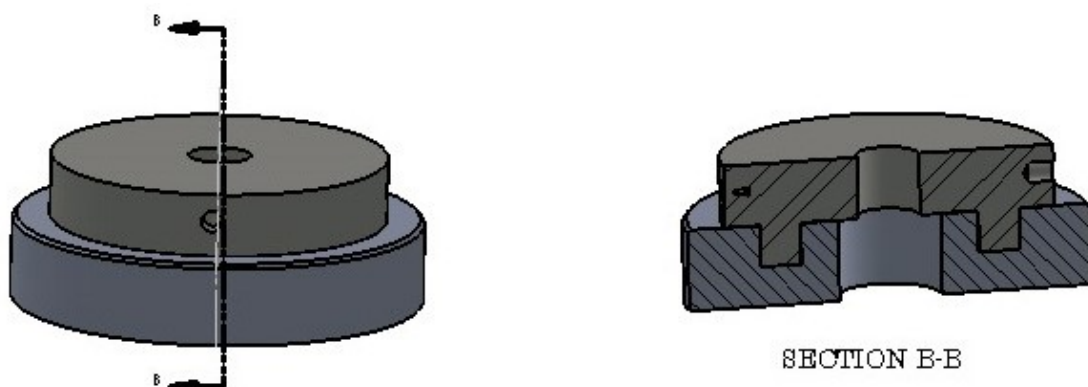
Figure 3-7: Schematic Drawing of the Hydraulic Damping Mechanism

In this present RCM design, the desire was that the piston should reach the TDC as short a time as possible to minimise heat loss from the reactants to the reactor chamber walls. That meant the driving pressure should be made as high as possible so that the maximum piston velocity was achieved. Higher piston speeds required a higher deceleration at the end of compression this was achieved by venting the hydraulic oil through the steps on the hydraulic piston ring and the surface on the front of the hydraulic groove. There are three methods of hydraulic damping: (1) Using the annular clearance method, (2) orifice method and (3) the valve deceleration method.

The first two methods use piston movement to initiate a restriction to the oil flow out of the cylinder towards the end of the stroke. While the last one dampens its piston through restricting oil flow by the use valve that is operated using a cam. The method adopted for this design was the annular clearance type. The oil in the hydraulic chamber is not pressurised [104-106, 111], but the chamber unit is filled with hydraulic oil and the load/piston itself is pressurised from the rear of the pneumatic chamber.



(a)



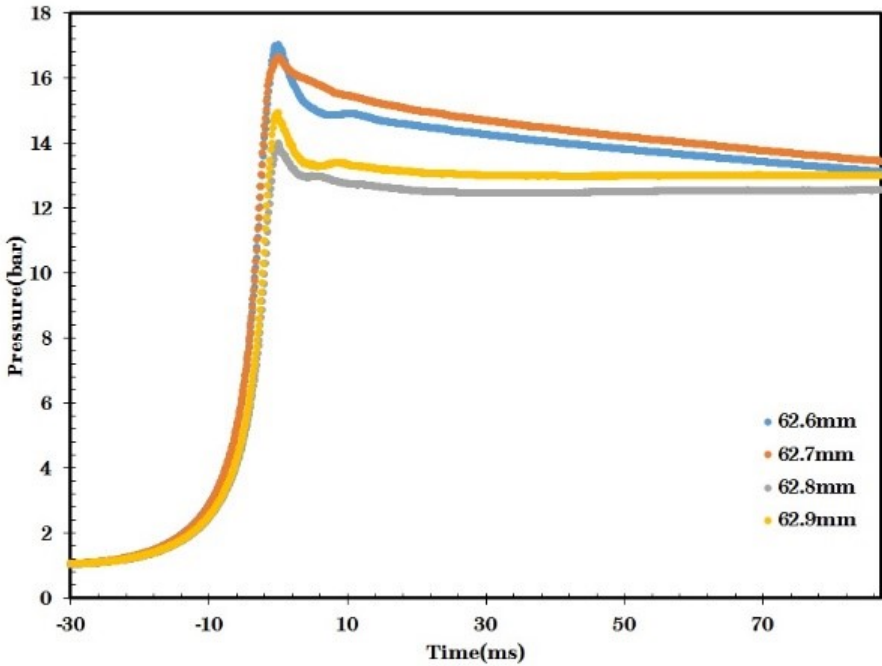
(b)

Figure 3-8: (a).shows the exploded isometric view of the Hydraulic Ring and Groove. (b) Shows the sectional view of the Hydraulic Ring and Groove.

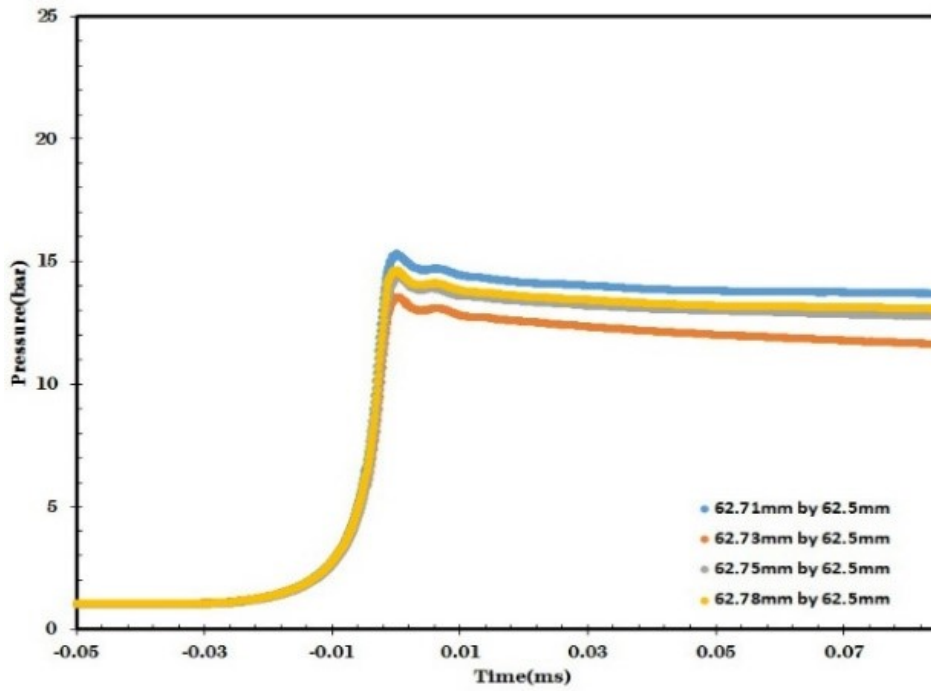
From figure 3-8, the exploded view shows hydraulic piston ring and groove, which has three steps machined on its surface with a length of 10 mm. The damping of the reactor piston is achieved by venting of the oil in the groove as the hydraulic ring moves into the cylindrical cavity of the hydraulic groove. At the full-length of the stroke, the deceleration of the reactor piston is control by by-pass of oil flow through the annular gap machined on the face of the hydraulic ring. The ring and groove clearance were made small less than 0.4mm so that the force builds up exiting in the groove is small thereby providing a braking force that eventually slows down the piston until it comes to rest as the hydraulic piston ring finally settles in the groove. Detailed drawing of the piston ring and groove are found in the appendices 5 and 6.

The design of damping mechanism [104-106, 201] required attention to obtain an acceptable result and if poorly designed may lead to piston reshoot or recoil leading to reaction chamber volume expansion at it maximum compression. This was achieved by trial and error, repeatedly machining a step ring on the periphery surface of the hydraulic piston ring until an acceptable deceleration was produced. The final result had three stepped surfaces. Experimentally this is accomplished by machining a step surface on the hydraulic pistongiving a decreasing annular gap between the hydraulic ring and the groove. The damping design could be used at two driving pressures of 4, and 5 bar. Step sizes of (62.9, 62.8, 62.7, and 62.6) mm were tried. The results of usingdifferent step surfaces and combinations for the driving pressures of 4 and 5 bar are shown in figure 3-9 and figure 3-10.

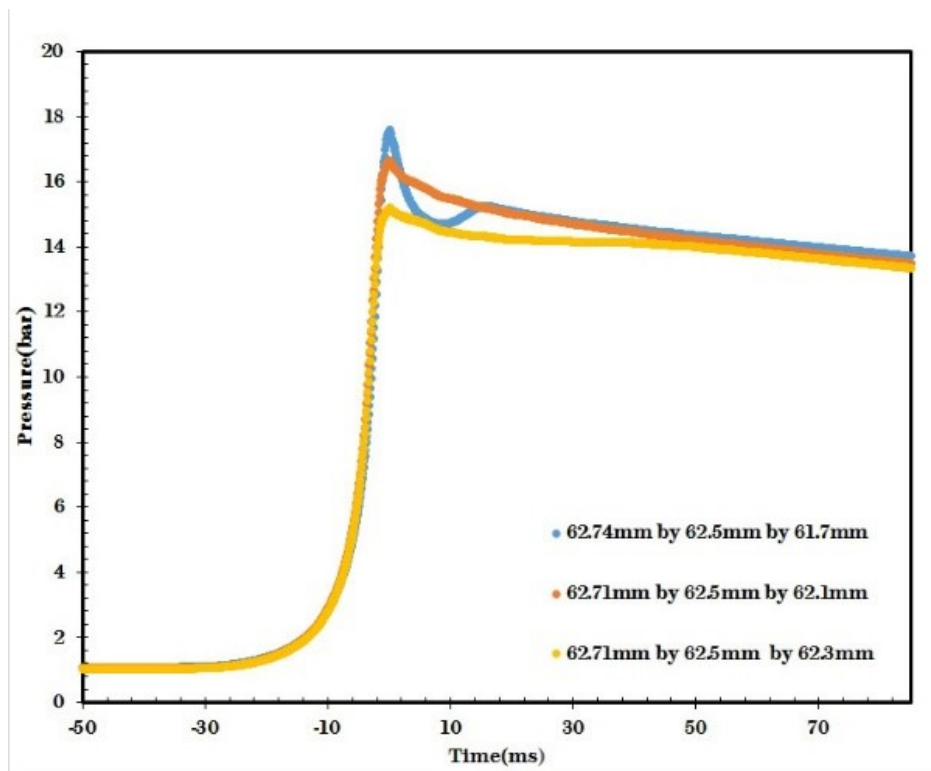
4 bar Driving Pressure



(a)



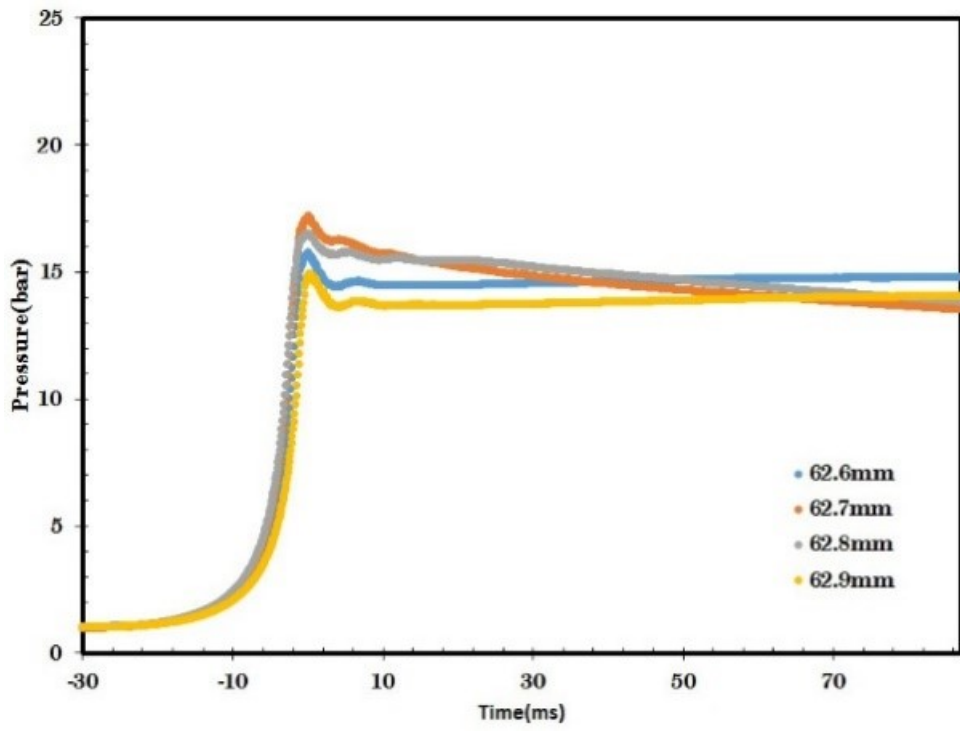
(b)



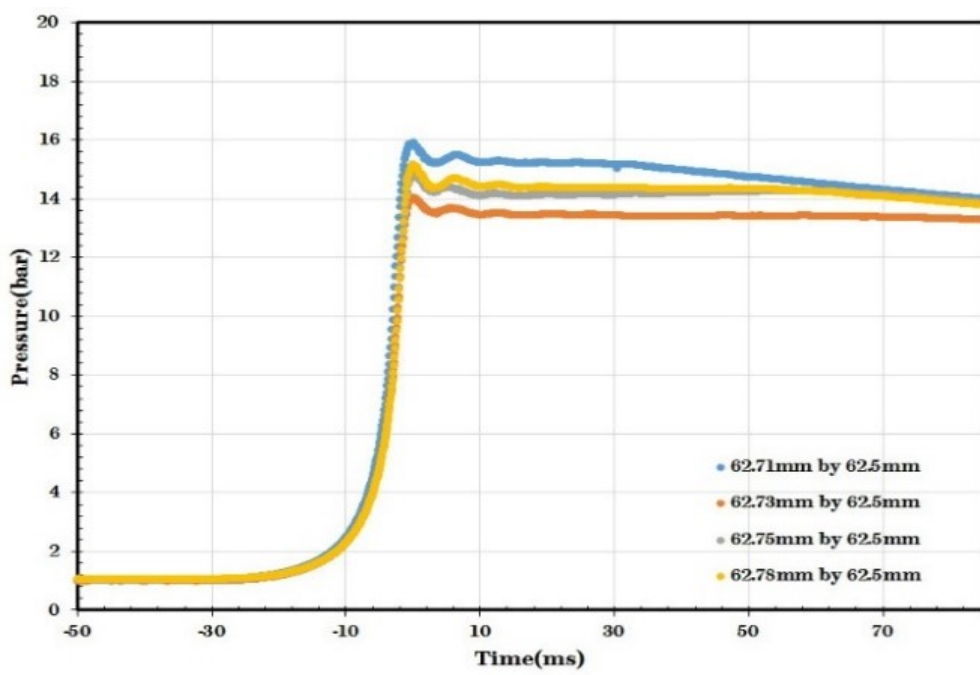
(c)

Figure 3-9: shows the pressure trace for the hydraulic damping using three-step sizing for four driving pressure. (a) One step, (b) two steps, and (c) three Steps.

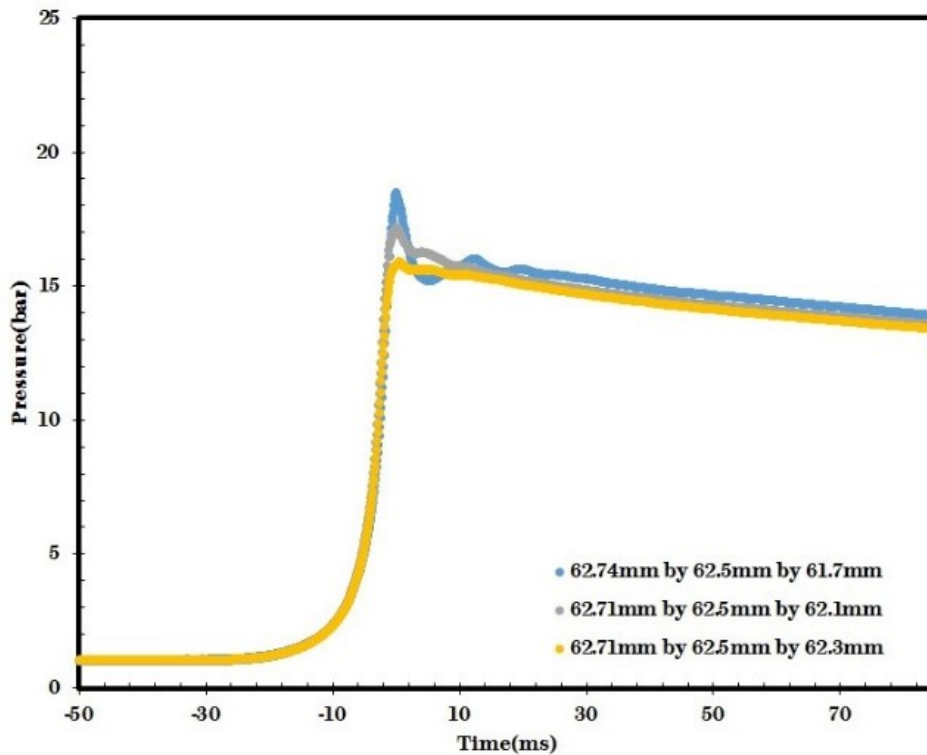
5 bar Driving Pressure



(a)



(b)



(c)

Figure 3-10: shows the pressure trace for the hydraulic damping using three-step sizing for five driving pressure. (a) One step, (b) two steps, and (c) three Steps.

3.5 Piston release mechanism

A pneumatically driven piston release mechanism (brake) was designed for the RCM. The piston release mechanism consists of a rectangular block, which holds the compact pneumatic cylinders. When retracting the reactor piston, the switch controlling the solenoid valve is depressed. Compressed air flows through the pneumatic line, which forces the reactor piston is repositioned at its bottom dead centre (BDC). When the reactor piston seats in its position, the pins are then released by depressing the switch, which releases the pins as it locks against the chamfered slot of the shaft lock. Thereby holding the reactor piston in its start position (BDC). The piston release mechanism is the main control of the rig. It acts as the break, which holds and releases the reactor piston in its initial start position. Once the control switch button is depressed, the compact cylinder is released from its pins, and the pre-charged driver cylinder drives the shaft forward. The operating pressure of the pin release mechanism is between 3-5 bars. Figure 3-11, shows the exploded view of the piston release mechanism.

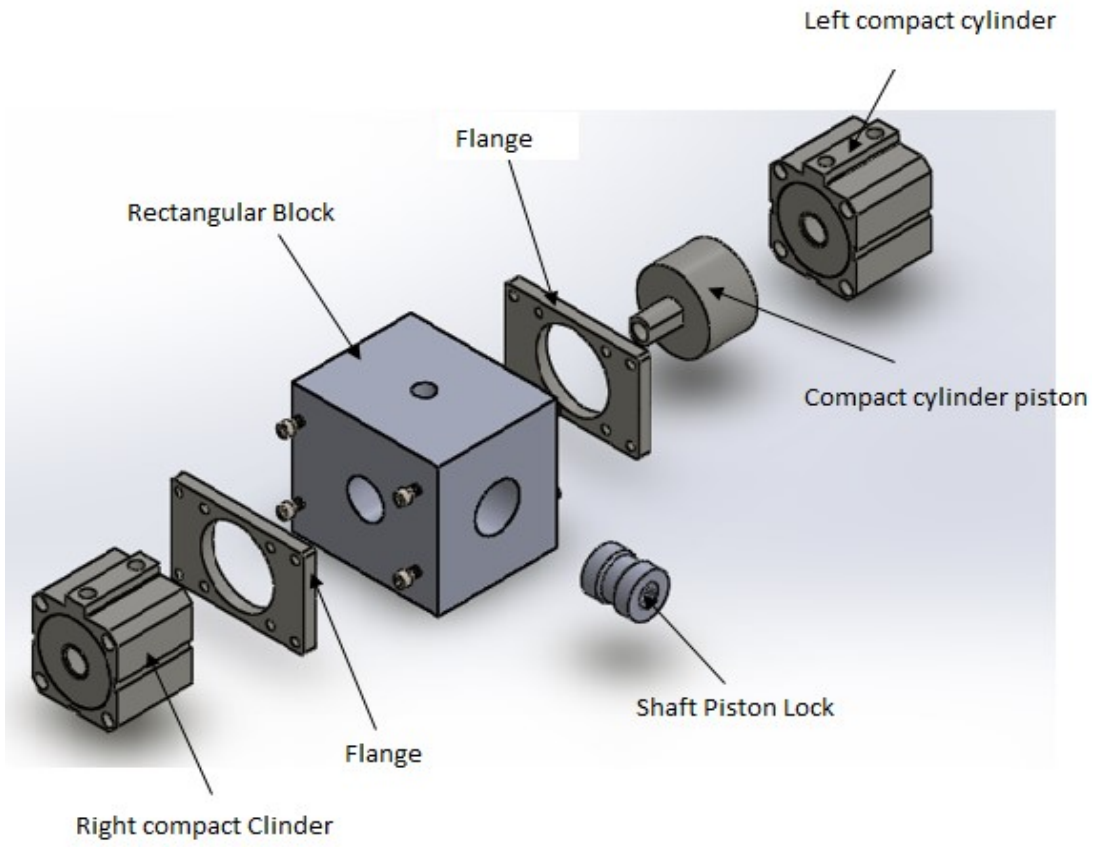


Figure 3-11: Piston release mechanism.

3.6 Piston Design

The piston inside the combustion chamber compressed a fuel/oxidizer mixture to high pressure and temperature. A reactor piston should have sufficient strength and stiffness and be thermal stability with low thermal conductivity, a low expansion coefficient and be lightweight. Aluminium alloy 6082-T6 drawn tube is used. The piston diameter was 39.6mm and 50mm long. The clearance from the wall of the cylinder to the surface of the piston was 0.2mm. Since aluminium expands when heated, sufficient clearance was required to maintain free movement. To obtain the highest compression speed possible, the piston needed to as light as possible. The piston was hollowed out to reduce its weight and to have a uniformly distributed stress throughout the entire body. The piston crown is subjected to high combustion temperatures. The piston weighed about 122 grams. Sectional views of the two piston designs are shown in figure 3-12.

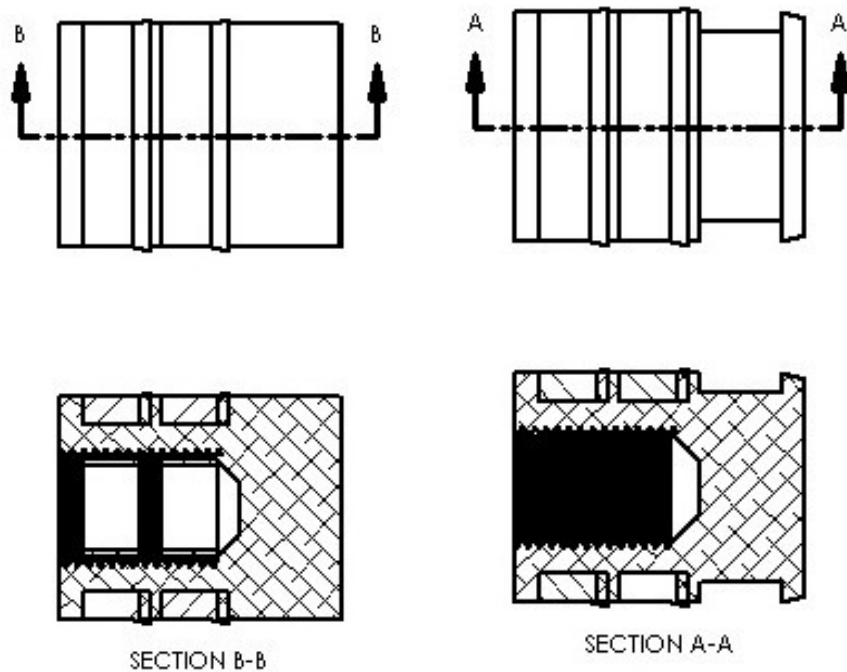


Figure 3-12: Shows the sectional view of the Flat and Crevice Piston Design.

The Viton piston seals used were produced by Martin Rubbers Company, UK. The dimensions of the Viton seals are 29, 41, 10 mm. Viton was used as it could withstand the high temperatures in the rig. Figure 3-13 shows the Viton seals used for the present rig.



Figure 3-13: Pictorial view of Viton seals.

3.6.1 Piston Stroke and Velocity Profile.

The stroke of the piston is obtained by the use of the Linear Variable Displacement Transducer (LVDT), (model DCTH 4000C). The LVDT is an electro-mechanical transducer

that converts the linear motion of the object to the corresponding electrical signal. This is mounted on a flat surface of the rig placed side by side with the hydraulic unit. When the reactor piston is released, the reference plate, which is coupled to LVDT moves and pull along the core of the LVDT. The displacement is then recorded as the piston moves from bottom dead to top dead centre. The reference plate has a reflective paper rapped on its surface, and an optical sensor was mounted close to the reference plate. The optical sensor was positioned in such a way that when the reflective plate moves the signal is seen by the optical sensor through the LabVIEW program. It was placed about 4mm from the surface of the reflective reference plate. A change in the output from the optical sensor was observed when the reference plate moved, and this was an indicative of the time of start of the reactor piston. The displacement profile of the reactor piston was logged using LabVIEW. Figure 3-14 shows the plotted measurement of piston displacement/stroke with the LVDT instrument.

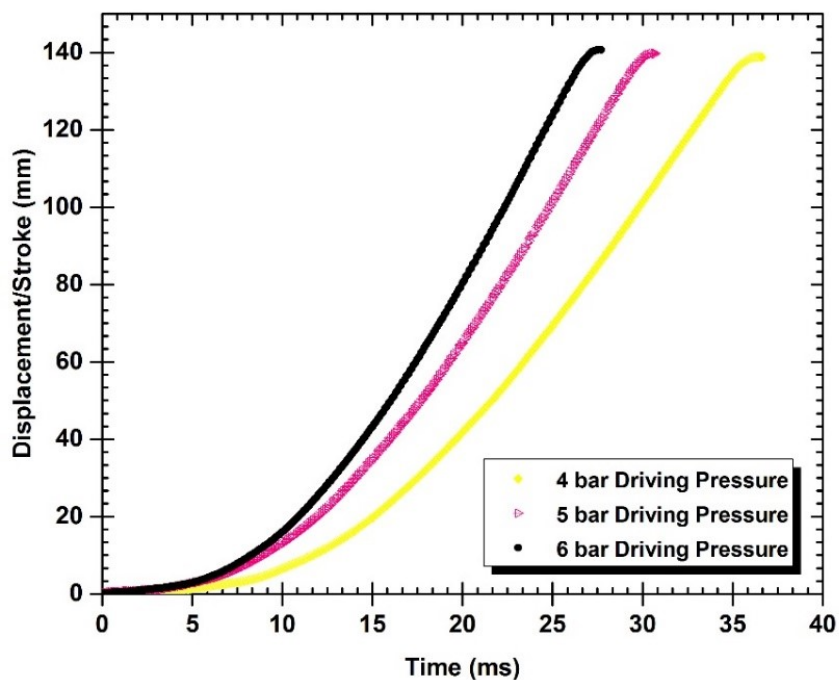


Figure 3-14: showing the Piston Displacement/Stroke for three different driving pressure, 4, 5 and 6 bars.

The velocity profile could also be derived from raw experimental pressure trace as used by Mittal [202]. The process of compression is modelled as polytropic process using the constant polytropic compression, γ is expressed by the relationship

$$\frac{P_c}{P_i} = (CR)^\gamma \quad 3-3$$

Where P_i is the initial pressure, P_c is the final compressed gas pressure and CR is the chamber compression ratio. The instantaneous volume $V(t)$ is given by the equation

$$V(t) = V_i \left[\frac{P_i}{P(t)} \right]^{1/\gamma} \quad 3-4$$

Where V_i is the initial volume prior to start of compression and $P(t)$ is the experimental pressure data from the RCM. The velocity of the piston during compression, $Velocity(t)$ can be determined by fitting a polynomial to the time history of the calculated volume of the chamber $V(t)$.

$$Velocity(t) = \frac{dV/dt}{\pi D^2/4} \quad 3-5$$

Where dV/dt is the time change of the combustion chamber volume and D is the diameter of the chamber. The equations written in a simple python code use to calculate the velocity of the piston and the generated profile is then use in the CFD simulation. The calculated velocity profile for 4 bar driving pressure is illustrated in figure 3-15.

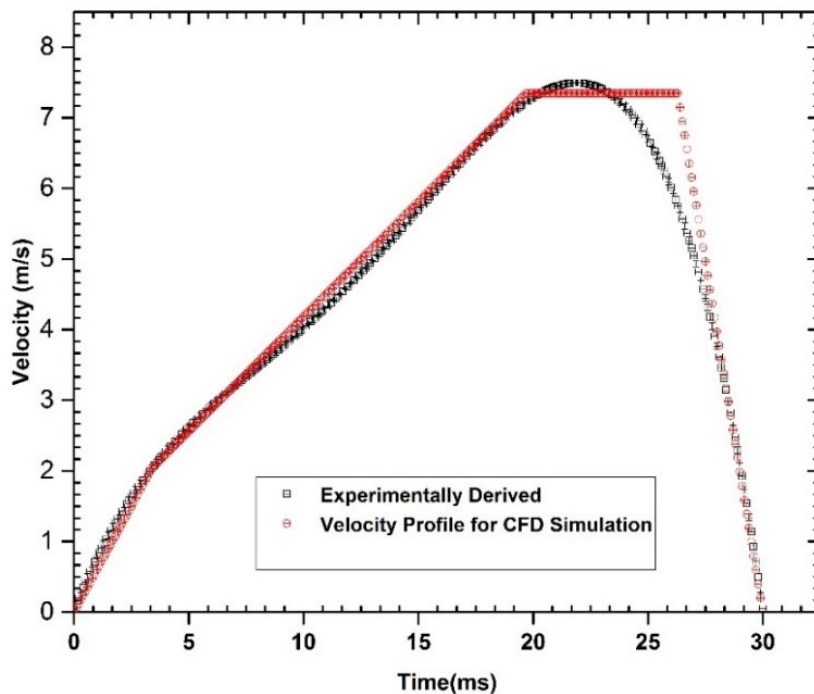


Figure 3-15: showing the velocity profile 4 bar driving pressure.

From figure 3-14, it shows that the piston initially starts from rest and travels with a constant velocity at a point, it follows a constant velocity before decelerating to rest at a constant rate. The section is divided into three-time period of the piston motion, which is

illustrated in equation 3-6. This equation is relevant for the numerical calculation where the parameters are used to model the compression stroke of the RCM.

$$t_{comp} = t_{accel} + t_{const} + t_{decel} \quad 3-6$$

Where t_{comp} overall compression time, t_{accel} acceleration time, t_{const} constant velocity time and t_{decel} deceleration time.

3.7 Compression Time Measurement

The computed compression time of the reactor piston is from the time optical sensor drops by 5 volt, which corresponds to the start time and the time when the LVDT peaks at TDC. Figure 3-16, shows how the start time of the reactor piston and the end time read from the optical sensor and the LVDT instruments. Figure 3-17 and 3-18 also shows 4 and 5 bar driving pressure with compression time of 32 and 28 ms.

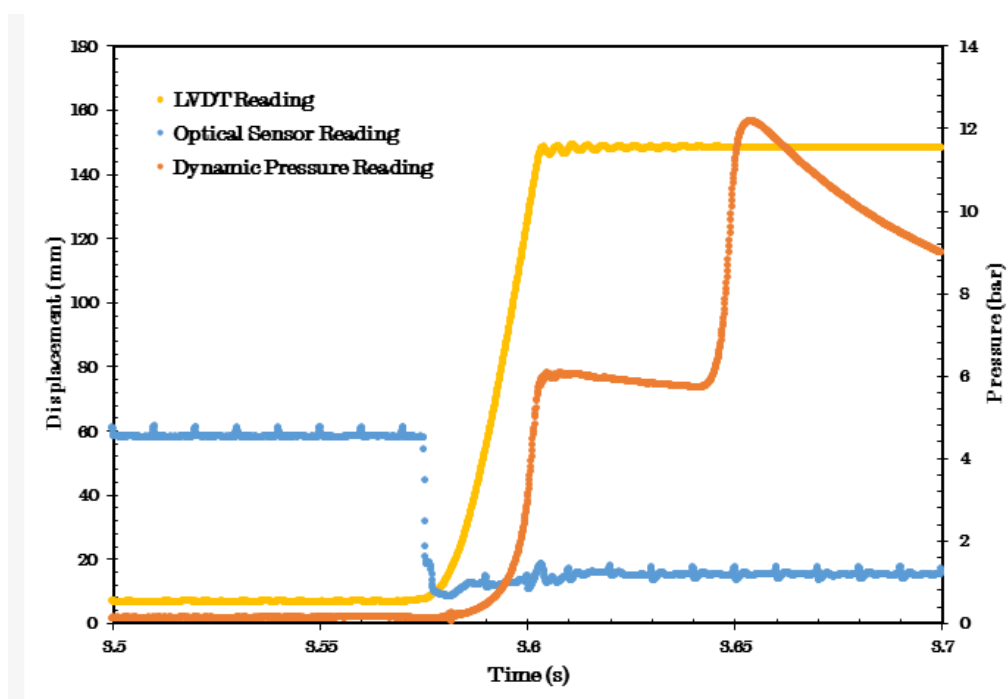


Figure 3-16: Shows the timing for the Optical sensor and the LVDT.

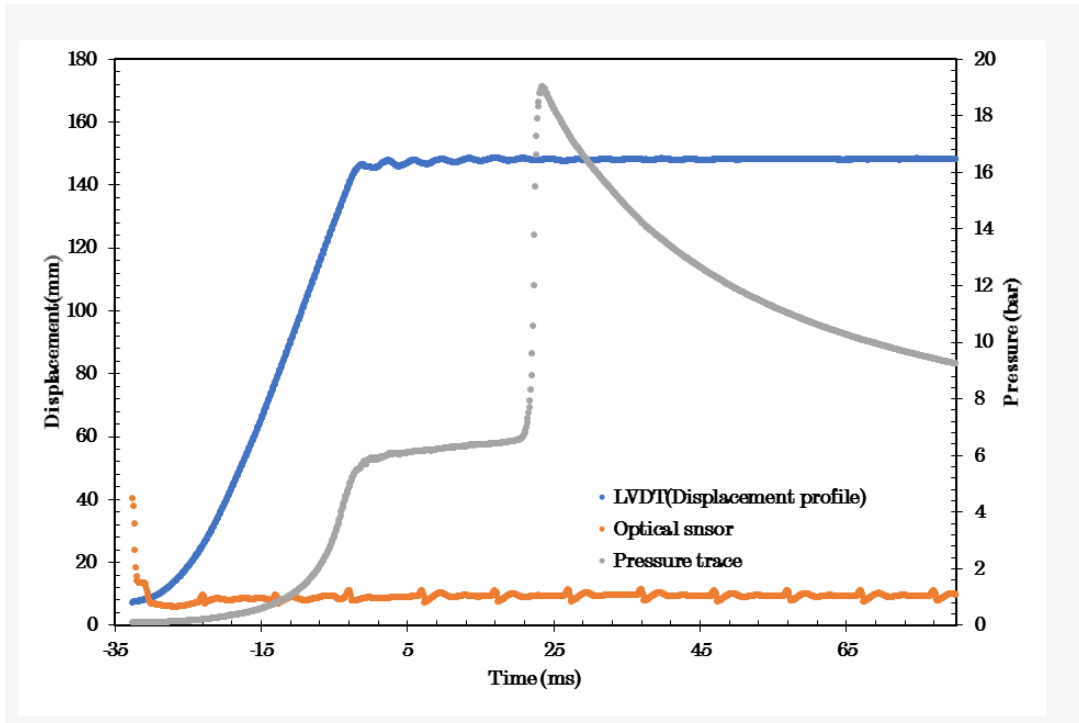


Figure 3-17: 4 bar driving pressure showing a compression time of 32 ms

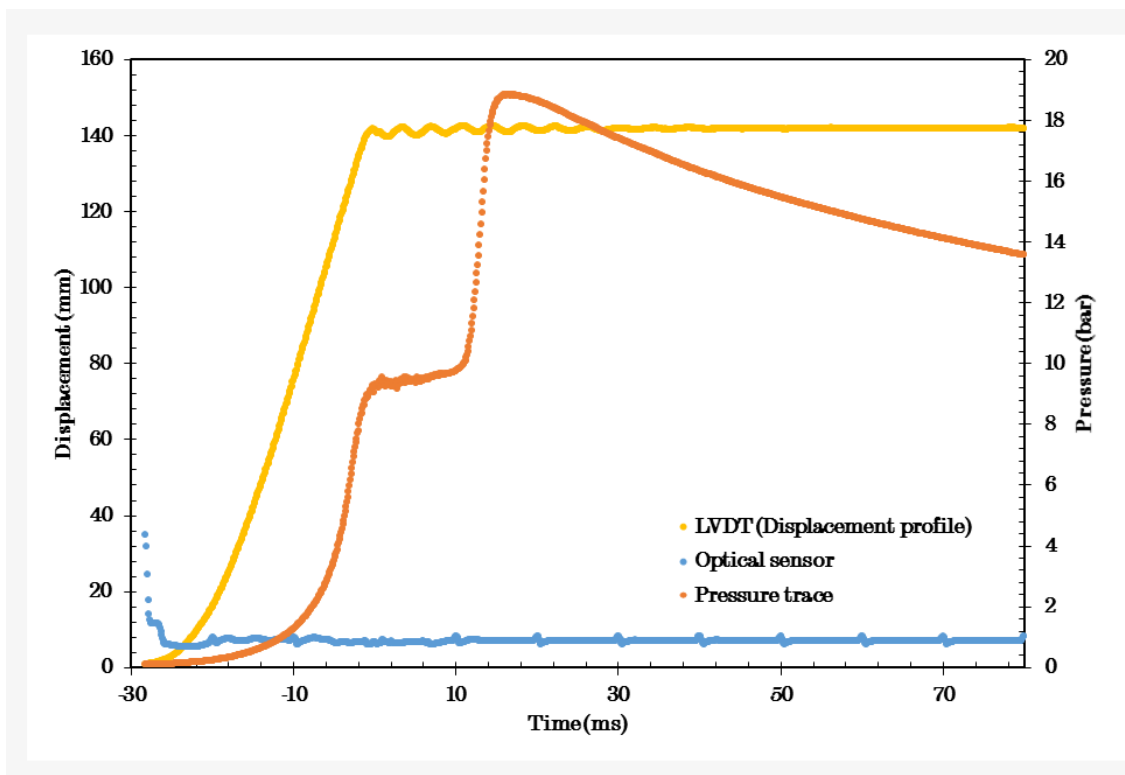


Figure 3-18: 5 bar driving pressure showing 28 ms compression time.

3.8 Direct Premixed Charge Preparation

The mixtures were prepared directly in the chamber method is used[104, 105]. Smaller residence times are experienced by the fuel compared to mixtures prepared in pre-chamber [117, 203, 204]. When a separate mixing chamber is used difficulties in controlling the temperature in the heated transfer line can cause thermal decomposition or condensation within the tubing of the transfer-heated line.

3.8.1 Fuel Evaporation and Mixing Time

Different mixing times 1, 1.5 and 2 hours were tried. Figure 3-19, shows the resulting pressure traces. A mixing and evaporating time of 1.5 hours used in this study.

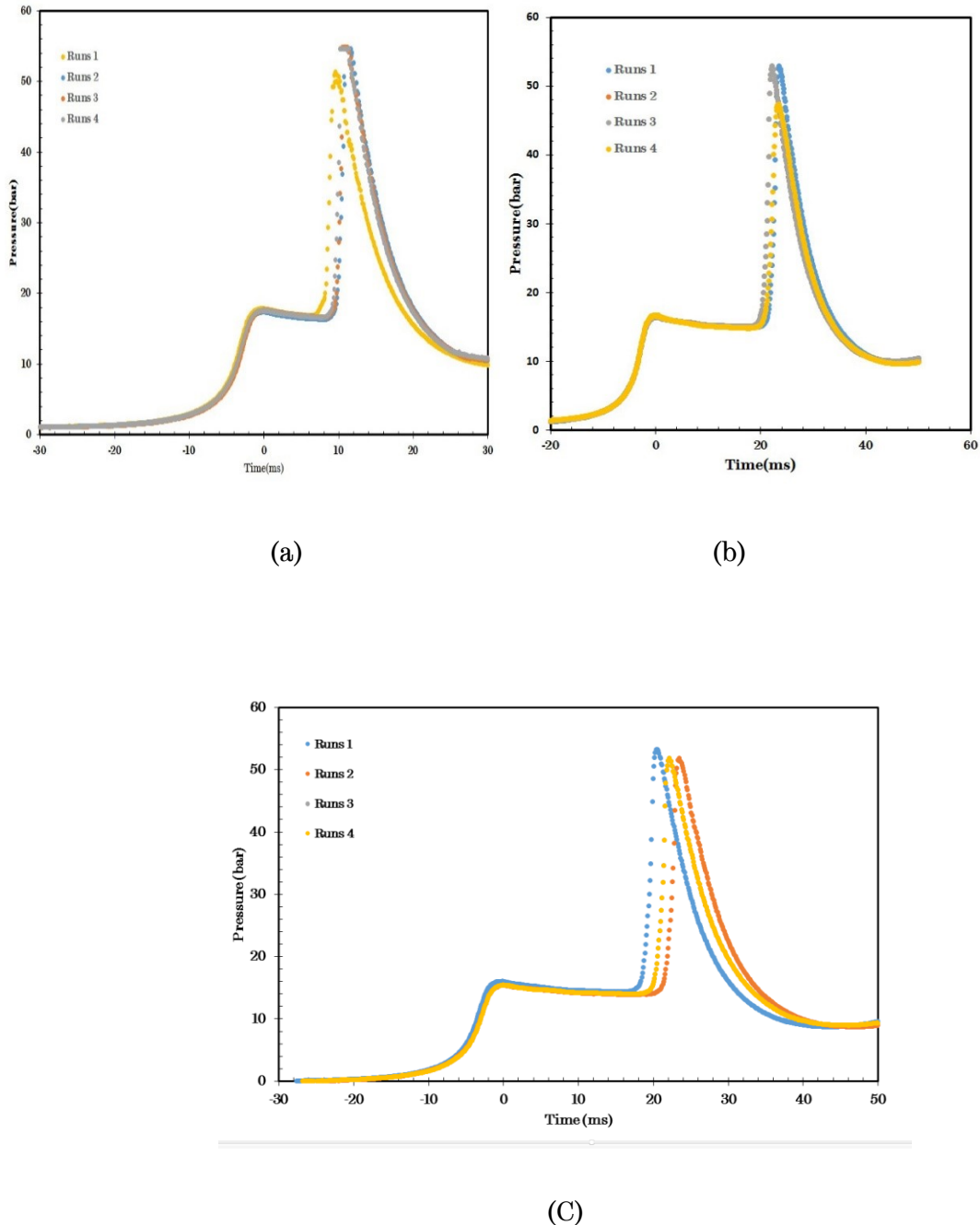


Figure 3-19: Repeatability pressure test for different Timing. (a) 1-hour timing, (b) 1.5-hour timing, (c) 2 hours timing.

The result in figure 3-8 shows the repeatability test carried out with heptane/air mixture at stoichiometric and an initial temperature of 305 K. Figure 3-18b clearly showed to have a repeatable result at about 1.5 hour of timing than other tests after making four runs at the same conditions. The discrepancy in result of figure 3-8c could be attributed to errors in measuring instruments, the way the fuel was administered into the reactor chamber maybe the fuel was not completely vaporised or a slight variation in initial pressure and temperature reading, which has led to non-repeatability of the result at 2 hours timing of

the mixtures. To avoid endlessly waiting for mixtures to homogenised and completely evaporated, the suitable time for the present rig is 1.5 hours. From literature other RCM likes Allan[105] approximately 2-4 minutes is possible in his rig for evaporation of injected fuel. This might be as a result that his rig has a fuel injector pump, which injects an atomised fuel spray at a very high pressure depending on the type of fuel injector or the model used. This high-pressure atomised spray helps to break down the fuel droplet into a tiny particle that enhances quick evaporation and promotes a high level of mixing.

3.8.2 Mixture Preparation

The fuel preparation was done manometrically by determining the mass of fuel, equivalent ratio, and the oxidizer ratio. The equivalent ratio is an informative parameter for determining mixture composition. The equivalent ratio calculation is shown in appendix 3 of this work. All gasses used were obtained from Sigma-Aldrich at a higher purity of 99.5%. During the experiment, three Teflon FEP gas sampling bags of 10 litres capacity were used each for storing nitrogen, oxygen and argon gases. The required volume of the oxidizer was collected from the gas sampling bags using a 60 ml syringe. All the fuels used in the experiment was measured using a syringe of 25 microliter capacity. In both cases, the injection was through a septum into the heated combustion chamber. Before injecting the fuel mixtures, the system is a vacuumed by with a BOC Edwards E2-M12 vacuum pump to a pressure of 0.9 bar. The chamber was flush with nitrogen to get rid of the previous combustion products from the chamber with a final vacuuming for 15 minutes. The oxidizer and fuel were injected into the preheated chamber and left to remain in the chamber for one and a half hours for vaporisation and mixing of the charge.

3.9 Triggering System and Data Acquisition

A Kistler 6009 piezoelectric sensor records the dynamic pressure trace. This is resistant to thermal shock. The charge signals were amplified and converted to a voltage by Kistler 5007 charge amplifier. The voltage output signal sent to the NI-USB 9223 DAQ card reader logging at 100 KHz frequency while the absolute pressure measured by Kistler pressure transducer typed 4045A5 with a charge amplifier type 4611 SN. All sensing devices except the thermocouple were connected to LabVIEW program. Table 3-1, shows the charge amplifiers settings.

Table 3-1: Shows the settings of Charge Amplifier (Kistler type 5007)

Settings	Values
Time Constant	Medium
Scale	5 bar/volt
Sensitivity	2.0 pC/bar

The initial temperature of the chamber is measured using the K-type thermocouple with 1.5mm thickness connected to a PIV controller.

3.9.1 LVDT Measurement and Calibration

A slip block equipment was used for the calibration of the LVDT. A slip block kit consists of standard measured stainless steel bar rectangular block in different dimensions. They are pieces of block measured in mm and more conveniently used to measure linear distance between two points. Two measurement readings were taken for both BDC and TDC and an average value determined. The initial position of BDC readings was taken from the end of the reference plate when the reactor piston sat in its right position and the pneumatic pins holding the shaft lock at the centre of the block. The timing from both initial position at (BDC) and the final position (TDC) of the reactor piston were read with their corresponding voltage output values recorded from the LVDT. The computed value was inputted into the LabVIEW.

3.10 Static Pressure Transducer and Calibration

The static pressure was recorded using Kistler pressure transducer type 4045A5, 0-5bar absolute pressure. It was calibrated with a Druck test calibrator model DPI 610. Figure 3-20, shows the result obtained from the calibration.

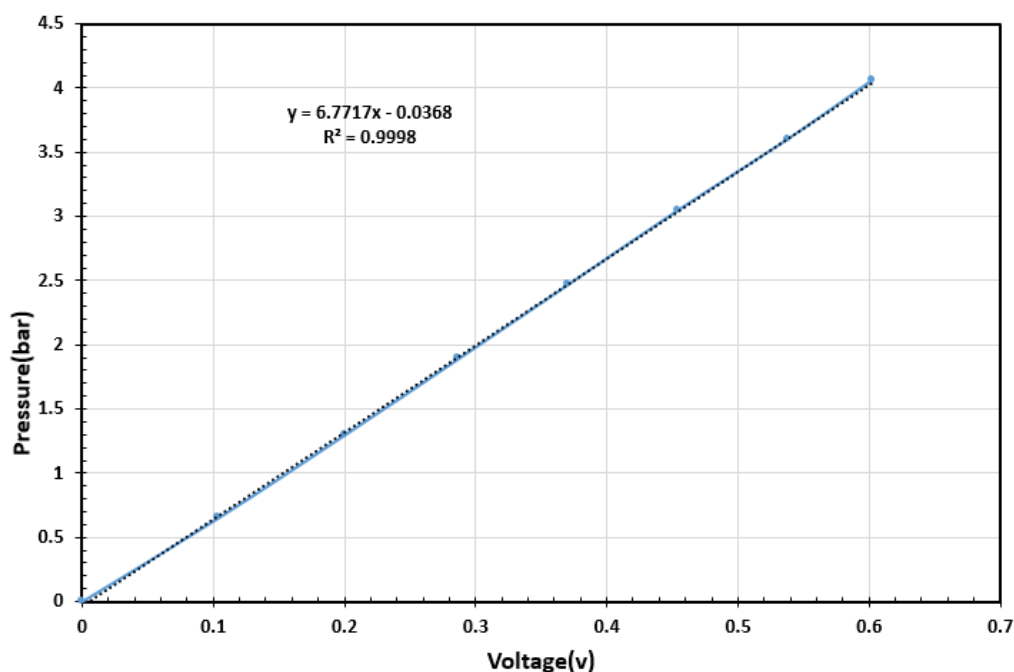


Figure 3-20: Calibration of Static pressure transducer

3.11 Uncertainty in the Parameters in RCM Experiment

The RCM is prone to some of the level of uncertainty because most of the initial physical values are directly measured, which are subject to errors of measurements.

3.11.1 Uncertainty in the Stroke Measurement

The systematic error in the stroke measurement is because of the error in the LVDT used to measure the displacement profile. The LVDT presently used was calibrated five years ago records shows that the LVDT was bought in 2011, this was necessary recalibrated to minimise the induced error. The charge signal from the LVDT reads in voltage that is acquire by an NI 9223 module mated to an NI cDAQ-9171 chassis monitored by the LabVIEW Virtual Instrument. The resolution of the DAQ is 16 bit on a ± 10 range with four analogue inputs corresponding to a resolution regarding displacement of about 21.6134mm. The full scale of the uncertainty of the LVDT type DCTH400C is 0.17%. The stroke length use in this work is limited to 142.4mm amounting to an uncertainty of ± 0.2 mm. Therefore the systematic uncertainty of the stroke length U_S is set as

$$U_S = S_S = 0.2\text{mm} \quad 3-7$$

The error found with stroke length is assumed to be normally distributed then the standard deviation of one-half of the manufacturer's specification is $\sigma S_S = 0.1$ mm

3.11.2 Uncertainty in the Initial Pressure

The static pressure in the reactor chamber was measured using the Kistler type 4045A5 with a range of 0-5 bar absolute. The charge amplifier models 4611 SN was connected with the sensor, the pressure signal from the sensor was converted to a voltage signal. The error of the pressure sensor is always specified as a percentage of the full-scale range in that regard, the full-scale uncertainty is 0.1% indicating that the systematic uncertainty, S_{P_o} of ± 0.005 bar. The random uncertainty due to the signal acquisition is negligible compared to the standard error in the pressure transducers. The systematic uncertainty in the initial pressure measurement amount given as:

$$U_{P_o} = S_{P_o} = 0.005 \text{ bar} \quad 3-8$$

The standard deviation of the initial pressure measurement is denoted by σP_o , then from the measured parameter the standard deviation is one half of the manufactures specification is $\sigma P_o = 0.0025$ bar.

3.11.3 Uncertainty in the Initial Temperature

The systematic error in the initial gas temperature results in the limits of standard error of the instrument K-type thermocouple used to measure the initial gas temperature of the

chamber. The brand of the k-type thermocouple is gotten from the Omega company with a manufacturer standard engineering specifications which tolerance is 'greater than $\pm 2.2^\circ\text{C}$ or $\pm 0.75\%$ ' as rightly stated in the ASTM standard E230[205]. The maximum initial temperature used so far in this work is 408K, leads to an uncertainty of ± 3 K. A digital CB100L controller is used to display the temperature, so there is negligibility of change in the process of A/D converter. The random uncertainty on the digital CB100L is due to the limit of display of the equipment process meter to regulate the process temperature, and this is about ± 1.224 K. The overall uncertainty (U_{T_o}) of the initial temperature is represented by the systematic uncertainty (S_{T_o}) of the thermocouple and the random uncertainty (R_{T_o}) due to the temperature measuring box which is given as

$$U_{T_o} = \sqrt{(S_{T_o})^2 + (R_{T_o})^2} \quad 3-9$$

$$= \sqrt{(3\text{k})^2 + (1.224\text{k})^2} = 3.24 \text{ K} \quad 3-10$$

The standard deviation of one-half of the manufacturer's specification, which is computed as $\sigma T_o = 1.62$ K.

3.11.4 Uncertainty in the Compressed Pressure

The pressure sensor used to measure the dynamic pressure is the kistler type 6061 with a range of 0-200bar absolute. The charge amplifier type 5007 was used in connection with the pressure sensor, converts the pressure signal into a voltage signal. The full-scale uncertainty for the sensor type 6061 is 0.3% resulting in an uncertainty of ± 0.6 bar. The uncertainties in the signal acquisition equipment are negligible compared to this uncertainty. The systematic uncertainty in the compressed pressure measurement is

$$U_{P_c} = S_{P_o} = 0.6 \text{ bar} \quad 3-11$$

The uncertainty of the compressed gas pressure is assumed normally distributed with the mean at the measured pressure. The standard deviation of the compressed pressure measurement is denoted by, σP_c , the standard deviation of the compressed pressure is one half of the manufacturer's specification is

$$\sigma P_c = 0.3 \text{ bar} \quad 3-12$$

3.11.5 Uncertainty of Liquid Fuel Mass

A microsyringe with a capacity of 50 microlitres is used to meter the liquid fuel into the chamber. It is measured on a digital Mettler PE 6000 scale before and after fuel injection to

determine the actual mass of fuel injected. Base on Bryan et al.[206] analysis the uncertainty in the measured mass has three components. First, the precision of scale. Second, the deviation from linearity. Thirdly, the repeatability of the measurement carried out on the RCM. With all these uncertainties, they are presumed to be distributed with the coverage factor of 2, which implies that the standard deviations are one-half of specified values[206]. Therefore the total standard deviation in the mass of the liquid fuel is considered by the sum in quadrature of the mentioned value of uncertainties[207]. So far, with this experiment, the weight of 50-micron syringe is 12g while with fuel plus syringe weights 12.1g at an equivalent ratio of 0.5-1.5. From the manufacturer manual documentation, the scale has a repeatability of 0.05g the precision of the scale is assume distributed with the standard deviation of 0.1g and the full-scale deviation from linearity is 0.1g. The total estimation of standard deviation in the mass of the fuel determine by summing of the quadrature of the value, which gives;

$$\begin{aligned}\sigma_m &= \sqrt{2 \cdot (0.1^2 + 0.025^2 + 0.05^2)} \\ &= 0.07 \text{ g}\end{aligned}\tag{3-13}$$

3.11.6 Uncertainty in the compressed gas temperature

The compressed gas temperature is not measured directly as discussed in section 5.2.1 of this work. This is because of the non-ideal issues like heat loss from the fluid to the wall, which could not be measured by a thermocouple because of the transient nature of the system. An adiabatic assumption is made and the end gas temperature estimated by numerical means. Based on the adiabatic core assumption the relation in equation 5-20, was used to numerically estimate the compressed gas temperature from the initial parameters like the initial pressure temperature, specific heat ratio and the compressed gas pressure at the end of compression. With the known initial parameters an approximation is made to estimate the uncertainty in the compressed gas temperature[208] which is given as

$$\frac{\Delta T}{T} = \frac{\gamma - 1}{\gamma} \times \frac{\Delta P}{P}\tag{3-14}$$

Where $\frac{\Delta T}{T}$ is the fractional uncertainty in the compressed gas temperature, $\frac{\Delta P}{P}$ fractional uncertainty in the initial pressure, γ is the specific heat ratio. Then the percentage error would be $\frac{\Delta T}{T} * 100$. The uncertainty in the compressed gas temperature depends on these parameters but mostly on the initial pressure where contribution from initial temperature and compressed gas pressure is not substantial[110]. The sensitivity of pressure sensor should be read from the manufacturer's manual since it has magnifying effect on the compressed gas pressure. Two pressure transducers are used in the present rig. one measure the static pressure Kistler type 4045A5 with a range of 0-5 bar absolute and the second kistler type 6061 with a range of 0-200 bar measures the dynamic pressure. The uncertainty in the static pressure have been stated in section 3.11.2 as 0.005 bar while systematic uncertainty in the dynamic pressure from section 3.11.4 is 0.6 bar. Therefore, the

overall uncertainty in pressure reading would be 0.605 bar.

3.12 Experimental Procedure and Operations.

It is imperative to give the procedures on how the RCM should be run to prevent machine damage or to incur fatal accident to personnel. The power supply to the device is turned on from the switch box on the wall. Figure 3-20 and 3-21, shows the front and end section of the rig carrying the valves that regulates the flow of air/fluid in the rig. The rig is charged with compressed air from the compressor. There are possibly two pressure gauges for monitoring the pressure of the rig. One for the pneumatic cylinder while the other is for pin release mechanism. The pin release mechanism is charged with air by setting the desired pressure to 3 bar. Once the pin release mechanism is charged, the line is at high pressure. For compressed air to get into the pneumatic cylinder vent 1, vent 2 and V1, must be shut and pressure gauge for the cylinder regulated to 4 bars. The next step regulates the front section of the rig, which also carries some valves that need to be isolated.

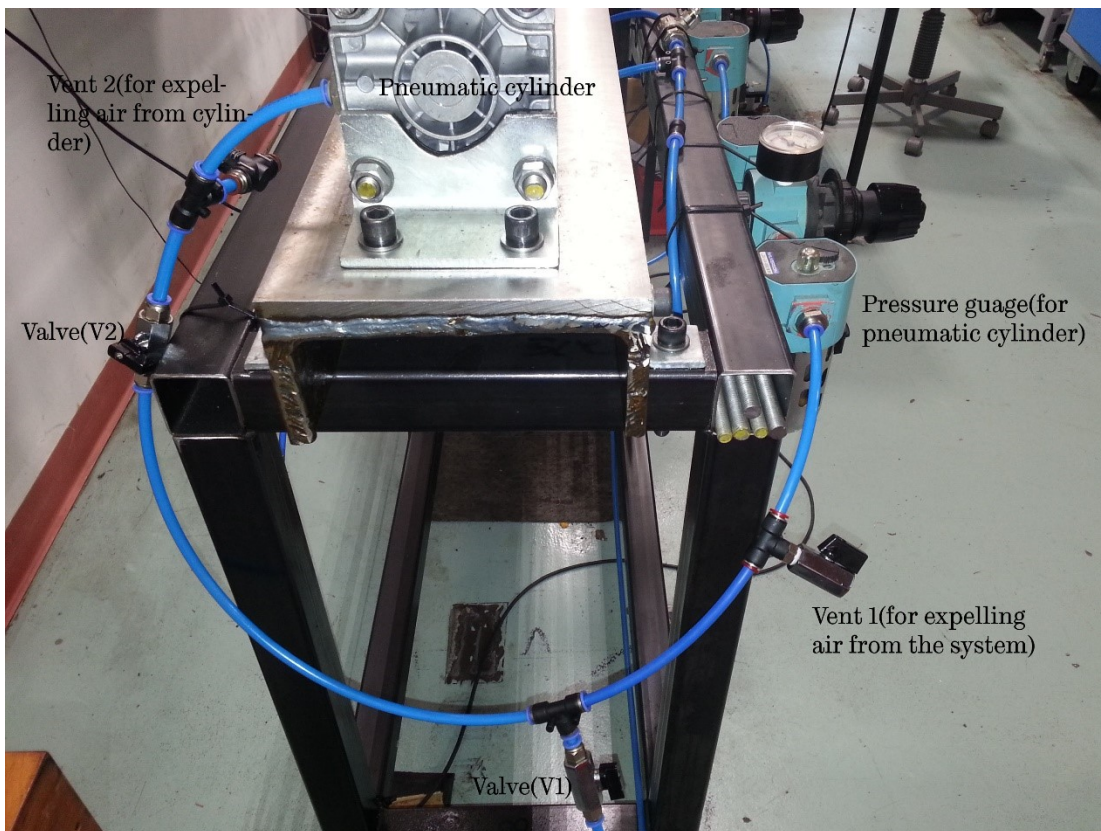


Figure 3-20: Front section of the rig

The end section of the rig is shown in figure 3-21. It starts with first, vacuuming the reactor chamber to the required pressure. At this point, two vacuum pumps are used to complement each other so that the better vacuum could be obtained. Diaphragm pump model VP 100 is connected to the line carrying the valve(V4), the other BOC Edward E2-M12 vacuum pump is connected to the line with the valve(6). During vacuuming, the VP 100 pump is first used V6 and V3 remain closed and SV, V5 is left open. When BOC Edward E2-M12 vacuum pump is then used V4, V3 remain closed while SV, V5 is open. After vacuuming is done, the next stage is to preheat the reactor chamber to an initial temperature, which

ranges from 115 -135 K. All the valves remain closed except SV. The fuel and air mixture are introduced into the chamber and left for 1.5 hours to vaporise and attain homogeneous mixture.

At this point, the rig is ready for firing and the switch pressed, which releases the pin mechanism allowing the piston to move linearly under the force of the driver cylinder. The residuals from combustion were cleared from the chambers using the VP 100 vacuum pump while opening V3 and V6 remain closed. Additionally, compressed air at 2 bar is allowed to flow through SV flushings/cleaning the chamber of the remnant residual gases. At this point V4, V6 remain closed while SV and V5 remain open.

The piston is retracted into its position by setting the pressure gauge to 2 bar, shutting off V2, V4, and V6 remain closed vent 1 & 2, SV and V5 remain opened. In retracting the piston, the pressure gauge is set to 0.7 bar of compressed air with the help of a reference arm the piston is retracted by pushing the piston back to initial position. The procedure repeated for subsequent experimental runs.

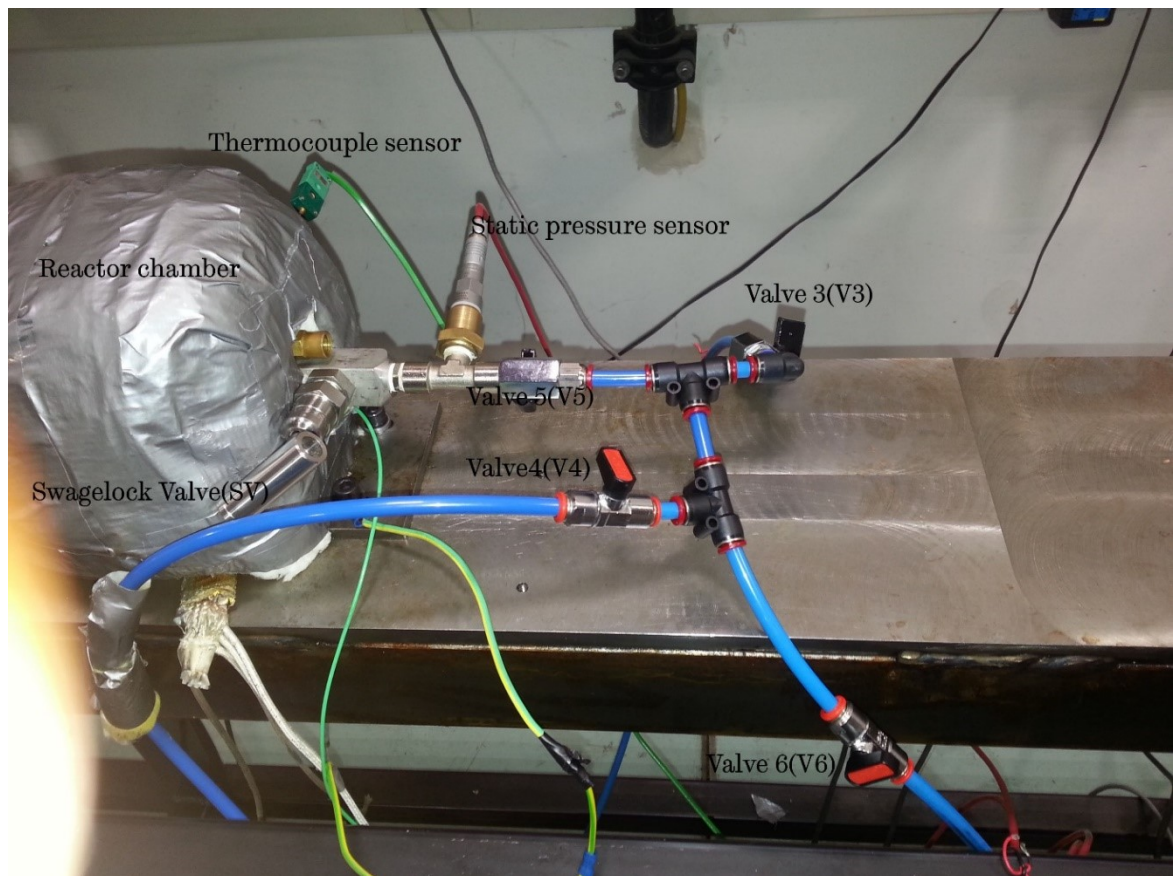


Figure 3-21: End section of the rig.

3.13 Conclusion

The Rapid Compression Machine was finally designed to operate over a wide range of experimental conditions. The final operating configuration is given in Table 3-2.

Table 3-2: Shows the operating characteristic of the present Shef-RCM

Stroke Length	138 - 145mm
Cylinder Bore Diameter	40mm
Compression Ratio	6.5 – 13.8
Compression time	25 - 35 ms
Piston Head Configuration	Optimised Crevice
Chamber Clearance Height	6.6 -15mm

Chapter 4. Computational Aerodynamics study of a Rapid Compression Machine.

4.1 Introduction

One of the challenges confronting the use of RCM's is that complex fluid dynamics features exist in the reaction chamber. These features result from the piston motion; a roll-up vortex is formed creating a non-uniform temperature profile in the chamber [209-213]. The gases in the relatively cold boundary layer mix with the hot core gas resulting in a distribution of temperatures. Figure 4-0 depicts the creation of a roll-up vortex in the chamber. A common assumption is that there is an adiabatic core in the RCM, which means the temperature can be calculated. In this context, the 'Core Area' is referred to the region where the bulk gases exist in the combustion chamber and are not influenced by heat loss. The temperature distribution with the combustion chamber is typically controlled with the use of a crevice on the edge of the piston, which suppresses vortex formation [115, 211, 213].

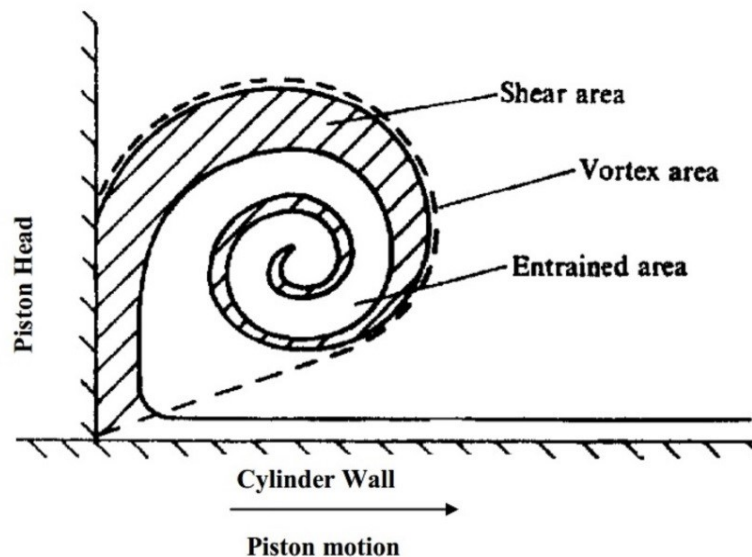


Figure 4-0: illustration of the roll-up vortex in the combustion chamber during the compression stroke[214].

The design of the crevice depends on the boundary layer thickness which itself depends on the conditions during compression[115]. During the compression stage of RCM certain level of turbulence[215], is generated in the reaction chamber this could mix of the core gases with the cooler thermal boundary layer. This has the effect of inducing a mean strain on the gases that might eventually amplify any turbulence present in the chamber before the onset of compression[215]. The effect of the initial turbulence is likely to be low at a reduced compression ratio.

Temperature uniformity can be improved if the geometric parameters of the RCM are manipulated. For example, by using a combination of shorter stroke and larger clearances[216].

Modelling studies have been performed by Wurmel et al.[115] where they compared the pressure traces obtained using laminar and turbulent flow. There was an agreement for N₂, Ar, and O₂, but He deviated because of its high thermal diffusivity [115]. They went on to conclude that using monoatomic diluent enables high temperature to be achieved compared to the diatomic diluent, because of its high specific heat. The diluent gases may also change the third body collision of the efficiency of the dilute gas. This was investigated by Di et al.[217], where they studied the effect of dilution composition on the ignition delay on the chemical dilution and thermal effect. Mittal and Sung[218] compared laminar and turbulent flow simulations with experiments. They observed that using a crevice piston, the temperature profile matched with the simulated maximum temperature from their CFD for both laminar and turbulent cases up to 100 ms. They further suggested that the fluid flow features in RCM can be modelled assuming a laminar flow[218].

In this work, extensive CFD work has been performed to optimise of piston crevice design regarding its volume, length, width and the geometry of channel connecting the crevice and the chamber[115]. The CFD work aimed to determine an optimised creviced piston head that would maintain a uniform temperature profile in the reaction chamber.

4.2 Computational Specification

The RCM has a cylindrical combustion chamber of 40 mm bore. The combustion chamber is oriented with the piston moving horizontally. A variable stroke between 138-142 mm was achievable, giving a compression ratio between 7.5 -13.5.

A transient 2-D computational mesh was used, axisymmetric symmetry was assumed, and the resolution increased near the walls. Modelling was performed using Ansys Fluent. The actual machine was not truly symmetrical, because of the inlet manifold, air inlet port, and pressure transducers have modified the geometry.

No slip is assumed at the cylindrical wall boundary, a uniform wall temperature of 298K was also assumed. The compression time was approximately 30 ms from an initial pressure of 0.7 bar. The thermal properties were generated from the NIST[219] database and specified as temperature dependent polynomials.

The governing equations for the model are the conservation of energy, momentum and mass. The laminar flow model was adopted as it has been shown that it can adequately describe the experimental pressure history and velocity field inside a rapid compression machine[218, 220, 221]. The segregated implicit solver with pressure-implicit split-operator (PISO) algorithm[222] was used for pressure-velocity coupling. The pressure staggering option (PRESTO) was chosen as it prevents errors from the interpolation and pressure gradient assumptions on boundaries are prevented [223].

This scheme works better for problems with high body forces (swirl) and the second order upwind discretization for density and momentum. The second order upwind scheme changes a differential equation into an algebraic equation by Taylor series. It is more preferred than the first order scheme because it is more accurate. However, is more computationally expensive. The Navier-Stokes equation is solved along with the energy and species transport equations for all species. This evaluates a set of equations dependent on the input in fluent are represented by the following equations based on the 2D modelling.

$$\frac{\partial \rho}{\partial t} + \nabla \cdot (\rho \mathbf{u}) = 0 \quad 4-1$$

$$\frac{\partial \mathbf{u}}{\partial t} + (\mathbf{u} \cdot \nabla) \mathbf{u} = -\frac{1}{\rho} \nabla p + \frac{\mu}{\rho} \nabla^2 \mathbf{u} + \mathbf{F} \quad 4-2$$

$$\rho \left(\frac{\partial E}{\partial t} + \mathbf{u} \cdot \nabla E \right) - \nabla \cdot (k_H \nabla T) + p \nabla \cdot \mathbf{u} = 0 \quad 4-3$$

Where \mathbf{u} is the velocity field vector, T is the temperature, p is the pressure, E is the internal energy, ρ is the density, μ is the viscosity, k_H is the heat conduction coefficient and \mathbf{F} is the force per unit mass. This equations 4-1, 4-2 and 4-3 are the continuity, momentum and, energy equation respectively. The above equation cannot be solve to give analytical result but can be solve in a discretized form. The Ansys fluent operate in a fashion by developing a result using the finite volume method and integrating the above equation to give the desired result.

4.2.1 CFD Model Development

The Ansys suite was used throughout, and the Design Modeller was used to create the geometry, meshing for, mesh generation and Fluent to solve governing equations and analyse the results. The experimental apparatus had some recesses at the top end of the combustion chamber; these were simplified the model to avoid using 3D. An estimated volume was included in the geometry.

The simplified 2-D axisymmetric is shown in figure 4-2. The actual BDC and TDC volumes of $1.93 \times 10^{-4} \text{ m}^3$ and $1.8 \times 10^{-5} \text{ m}^3$ were maintained giving a compression ratio of 10.7 and a stroke length of 142 mm. The underlying computational mesh in this research is not static but dynamic. This means that it is subject to changes in its structure, shape, refinement level, and nodal connectivity throughout the simulation.

4.2.2 Mesh Generation

The mesh was generated using Ansys fluent. It was made up of 26,042 cells, consisting of a 250 x 90 meshes with additional cells describing the clearance between the piston and the

chamber wall. Techniques such as mapped facing, sizing and bias were applied to the mesh model to achieve refinement at the walls, cylinder head, and the piston face.

The internal boundary of the chamber was mapped with a controlled rectangular structured mesh which was controlled by regulating the sizing and applying a bias factor. The aim of this was to capture the roll up vortex generated because of the movement of the piston. A bias factor of 20 was applied towards the walls and 10 on the piston face.

4.2.3 Thermodynamic Properties and Heat Transfer.

The knowledge of thermodynamic properties of the chemical species is essential for calculating the rate of temperature change of the system. The properties of chemical species are based on experimental data generally tabulated as a function of temperature. Examples of these thermodynamics data tables are found in the literature [224-226]. These properties are by default inbuilt into the Ansys database in the form of NASA polynomials. These polynomials are the linear least-squares fit to the thermodynamic data of species; this work was done by Gordon and McBride[227]. The thermodynamic properties or data typically take two seven-term polynomial coefficients. One region for low temperature, 300 to 1000 K and the second region of the coefficient for higher temperature from 1000 K to 5000 K. The NASA polynomials have the following form

$$\frac{C_p}{R} = a_1 + a_2 T + a_3 T^2 + a_4 T^3 + a_5 T^4 + a_6 T^5 \quad 4-4$$

$$\frac{H^0}{RT} = a_1 + \frac{a_2}{2} T + \frac{a_3}{3} T^2 + \frac{a_4}{4} T^3 + \frac{a_5}{5} T^4 + \frac{a_6}{T} \quad 4-5$$

$$\frac{S^0}{R} = a_1 \ln T + a_2 T + \frac{a_3}{2} T^2 + \frac{a_4}{3} T^3 + \frac{a_5}{4} T^4 + a_7 \quad 4-6$$

Where a_1, a_2, \dots, a_7 are the numerical coefficient [228].

4.3 Parametric Studies.

The parametric study is conducted in this report allows appropriate choice of model parameters to be made in the simulation. These parameters are the time step sizes and the mesh density. In a transient problem, it is important to ascertain the appropriate time step sizes for a solution. This is done by conducting a sensitivity test to see at what crank angle size is best fit for a solution to run conveniently without negative cell volume error occurring and also to save computational time.

4.3.1 Time Step Size

In a transient computation, the time between each set of calculation is called the time step, which is defined by the crank angle size. In this model, the total time step is 180 crank

angle. Since it is a single stroke event, it compresses to a constant volume. A mesh sensitivity study was carried out using four different angles for every time step. The highest step size (δt) was 0.25 and subsequent time step was generated by dividing by a factor of 2 to get the following 0.0125, 0.0625, 0.03125 and 0.015625. It is observed that time step greater than 0.03125 resulted in negative cell volume error. This error is because of the fluid domain changing without the mesh adapting to the changing geometry, thereby deleting/merging of cells adjacent to the moving piston.

To limit the computational time as well as avoiding convergence problems with the use of higher time step. A compression time of 30.8ms corresponding to the time-step size of 22.57 μ s was chosen for both compression stroke and post compression period in all the CFD simulations in this report.

4.3.2 Mesh independence

The number of cells was considered important as it can affect the accuracy of the aerodynamic flow profile in the combustion chamber. A study was conducted to reduce errors caused by a poor mesh quality and to save computational time by running unnecessarily fine mesh. Figure 4-1, shows the sensitivity of the mesh.

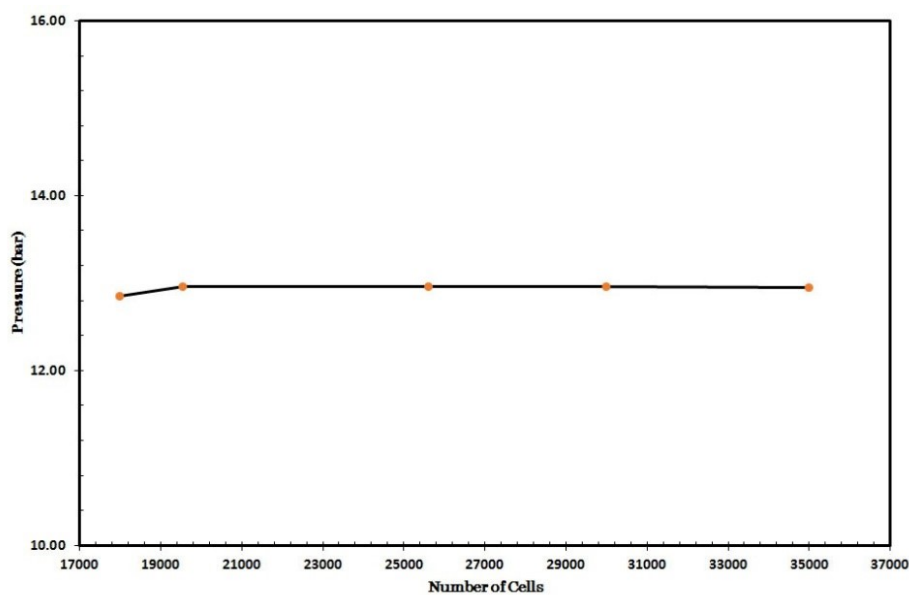


Figure 4-1: The sensitivity of mesh on the core pressure of the reaction chamber.

It shows that by varying the mesh density between 19000 and 35000 cells. The properties do not have any effect on the output results, so mesh within this range is considered proper running of the simulation.

4.4 Effect of Using Piston Head Configuration in a Rapid Compression Machine.

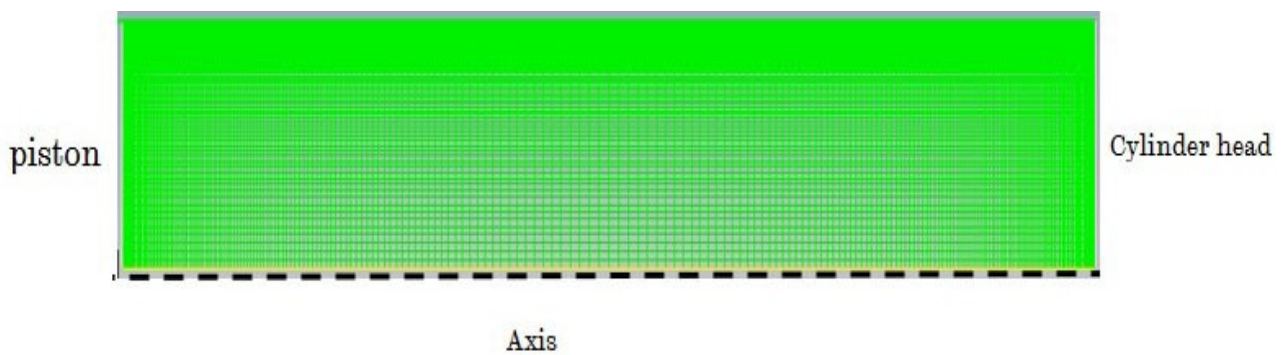
One of the issues of using a flat piston head is the generation of roll up a vortex in front of the piston face, which continue to emerge from the core region in the post-compression period[210, 212, 213, 229]. This roll up vortex increases the rate of transport of energy to/from the cold boundary layer gas out of/from the core region thereby causing an uneven

temperature profile. Variation in heat transfer and aerodynamics inside the cylinder can affect the ignition delay time making seemingly similar experimental setups produce different results.

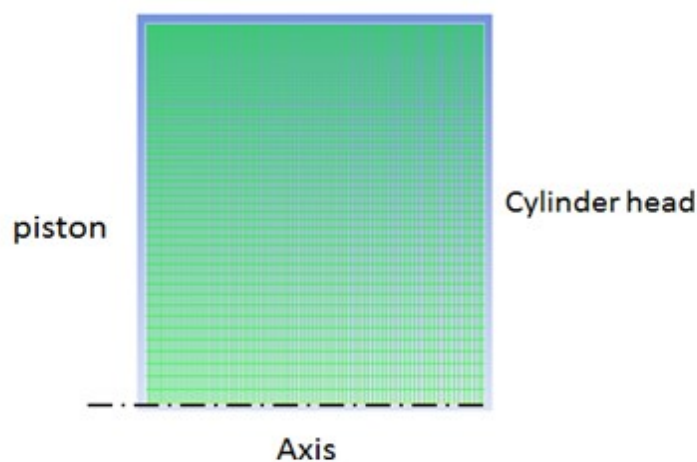
4.4.1 Flat Piston Head Simulation.

The simulation of the geometry involves a transient 2-dimension computational mesh created using the commercial Package Ansys Fluent 16.1, assuming axisymmetric nature. The initial boundary conditions of simulation from the beginning of the compression event specified with no slip condition at the cylindrical wall boundary. The gas maintained at a uniform wall temperature of 298 K with a compression time of approximately 30ms. The development of temperature field with flat piston head was simulated with unreactive gas, nitrogen. The initial temperature and pressure are $T_0 = 298 K$ and $P_0 = 1 bar$

Figure 4-2, shows a typical computational grid before and at the end of the stroke. The mesh shown to consist of 26,042 cells, fine grids were used on the walls and piston face and coarse meshes in between the piston and the top dead centre (TDC) to adequately capture the fluid flow taking place in the chambers.



(a)



(b)

Figure 4-2: shows 2D computational grid for Flat Piston (a) before compression (b) after compression for a flat piston head.

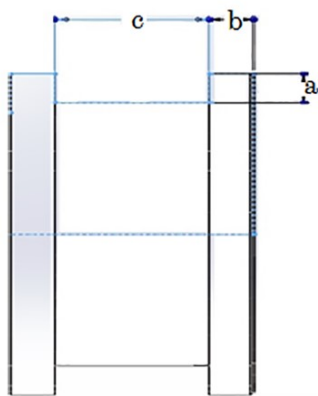
4.5 Optimisation of Piston Head Crevice Design

The object of the crevice on the periphery of the piston is to suppress the boundary layers and prevent mixing of the cool boundary layer gas with the hot adiabatic core and thereby providing a homogeneous temperature field in the reaction chamber. Four different crevice designs were considered and compared. The simulations were conducted using nitrogen as the test gas. Bath gases such helium and other monoatomic gas are commonly used for such tests, but because helium has a high specific heat capacity, it is not always recommended to be employed in the characterization of RCM[115].

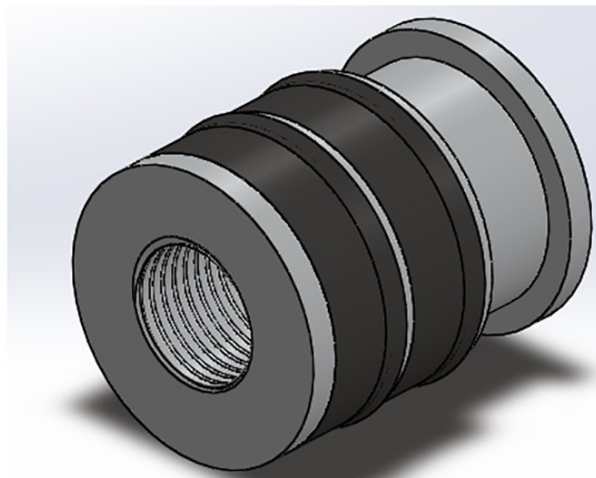
The use of creviced piston head reduces the final compressed temperature and pressure in the reactor chamber. An additional issue of mass flow of gases into the crevice could be avoided by having a chamfered piston head. This undesirable effect could adequately be handled by designing optimal crevices to overcome the shortfall in using a crevice piston. An effort to overcome such additional mass flow into the crevice was studied. This uses crevice containment by disengaging the crevice from the main reaction zone with a seal at the end of compression stroke. Thus preventing the mass flow into the crevice when ignition takes place in the chamber and also the possibility of gaining in the reduction of pressure drop in the reaction chamber[230].

4.5.1 Crevice with flat Channel Design.

Crevice volumes ranging from 282 - 1410 mm^3 (2-10% in relative to the overall reaction chamber volume) were examined. The clearance between the crevice and the cylinder wall was kept constant at 0.2 mm and the volumes varied. Figure 4-3, shows the sketch and isometric view of the piston with the flat channel.



(a)



(b)

Figure 4-3: shows (a). The diagram of the crevice region of the piston with a flat face (b). Isometric view of the crevice head design with flat channel piston showing the crevice volume.

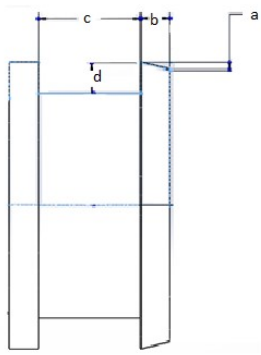
The length of the section connecting the chambers and the crevice is called the channel. From literature, it was established that longer channels increased the cooling of the boundary layer gas entering the piston head crevice and there was no noticeable gas temperature change for a channel of 4 and 5 mm[115]. Based this evidence, the design adopted a channel length of 4mm. The volume and the depth of the channel were varied which was adopted from Lee's work [113]. Table 4-1 shows the crevices used.

Table 4-1: Shows the crevice dimension in mm.

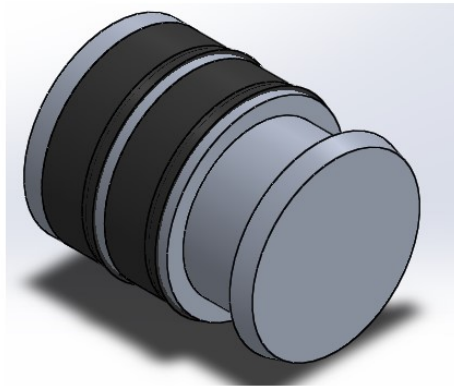
	Crevice volume (mm^3)	Crevice Number	The clearance between piston and crevice.	The height of crevice. a	Channel length. b	Crevice Channel. c
2	282	1	0.2	2.53	4	14
4	564	2	0.2	3.58	4	14
6	846	3	0.2	4.39	4	14
8	1128	4	0.2	5.06	4	14
10	1410	5	0.2	5.66	4	14

4.5.2 Piston Crevice with an Angle Channel Design.

The calculation was also performed testing an angled channel crevice design. This is designed to provide an unrestricted mass flow out of the reaction chamber into the crevice but restrict the flow from the channel back into the reaction chamber. In this case, the measured chamfered angle was 15° and the same condition applied to the flat channel was adopted for the angle head crevice. Figure 4-4, shows the design of the piston head.



(a)



(b)

Figure 4-4: shows (a). The diagram of the crevice region of the piston (b). an isometric view of the angle channel design showing the crevice volume.

Table 4-2: shows the angled channel crevice volume in mm.

Crevice number	Crevice volume (mm^3)	Percentage by volume	Clearance between piston and wall	Inclined Angle.			Height of Crevice
				a	b	c	
1	282	2	0.2	15°	2.53	4	14
2	564	4	0.2	15°	3.58	4	14
3	846	6	0.2	15°	4.39	4	14
4	1128	8	0.2	15°	5.06	4	14
5	1410	10	0.2	15°	5.66	4	14

Table 4.2 shows for the angled channel crevice head with all dimensions are in mm. All the crevice volumes with angled channels were shown to contain the cool gases at a post-

compression time of 20ms, while maintaining a homogenous temperature field. With the crevice volume of 282 mm³, the peak temperature at TDC recorded is 653 K while that of the 1410 mm³ is 621 K.

4.6 Influence of Piston Crevice Height on Pressure Profile.

The effect of crevice height is studied using the optimal crevice volume of 282 mm³. This was considered the optimal volume. Five different crevice lengths were tested. Table 4-3, shows the crevice angled channel volume dimensions tested.

Table 4-3: The dimensions of the angled channel crevice volume in mm.

Crevice	Crevice Volume (mm ³)	Clearance btw piston and cylinder wall.	a	d	Channel length. b	The height of crevice. c
A	282	0.2	15 ⁰	5.47	4	3
B	282	0.2	15 ⁰	4.23	4	5
C	282	0.2	15 ⁰	3.58	4	7
D	282	0.2	15 ⁰	3.16	4	9
E	282	0.2	15 ⁰	2.74	4	12

4.7 Computational Result and Discussions.

4.7.1 Flat Piston Modelling

Figure 4-5, show the simulated temperature and velocity field. The scraping of the cold boundary layer from the walls into the reaction chamber and the build-up of the roll up a vortex in the adiabatic core region can be clearly seen in figure 4-5a. The build-up of cold gas progresses and spans the chamber at 16.1 ms. This result is similar to that of other workers [231, 232].

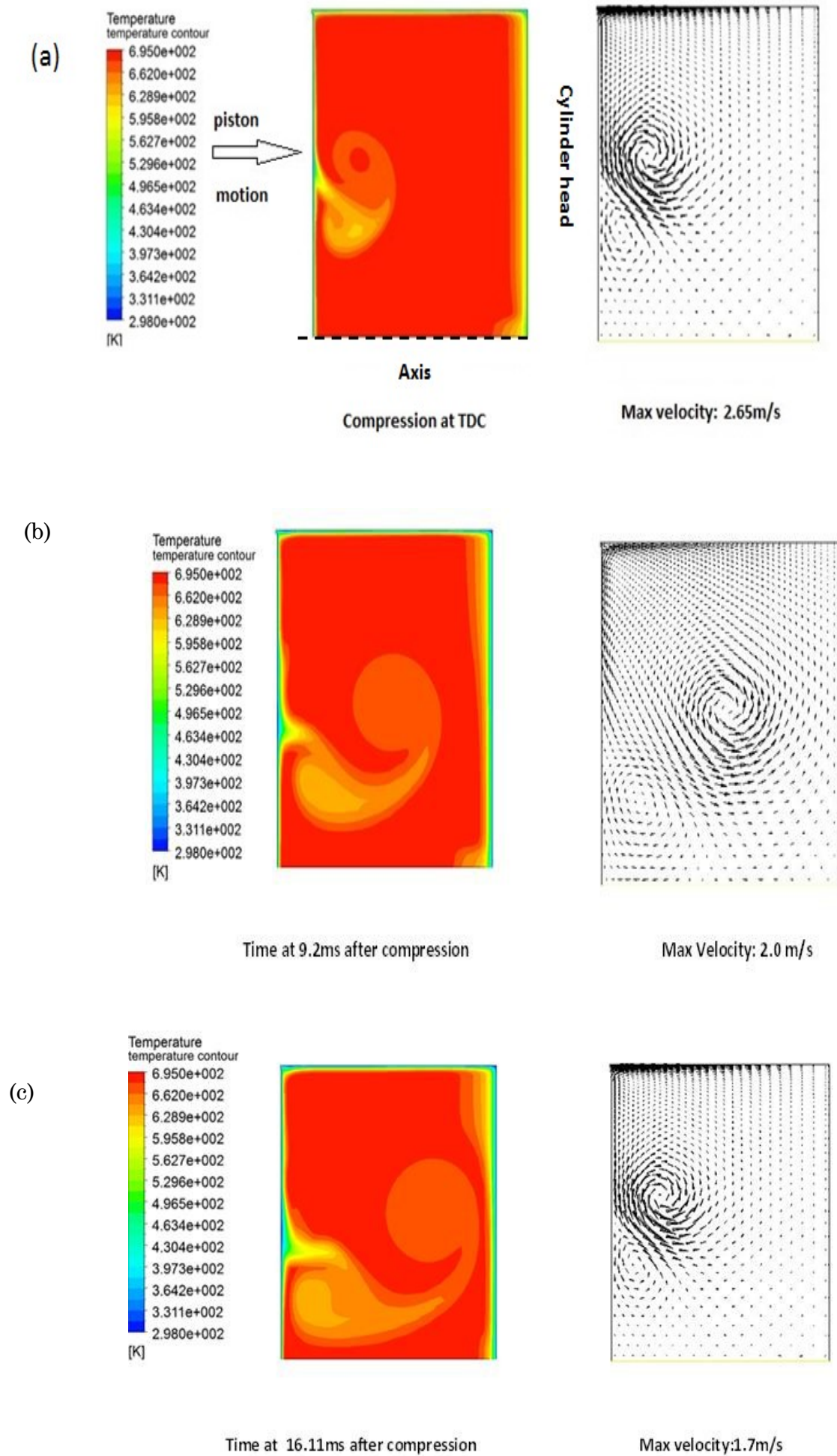
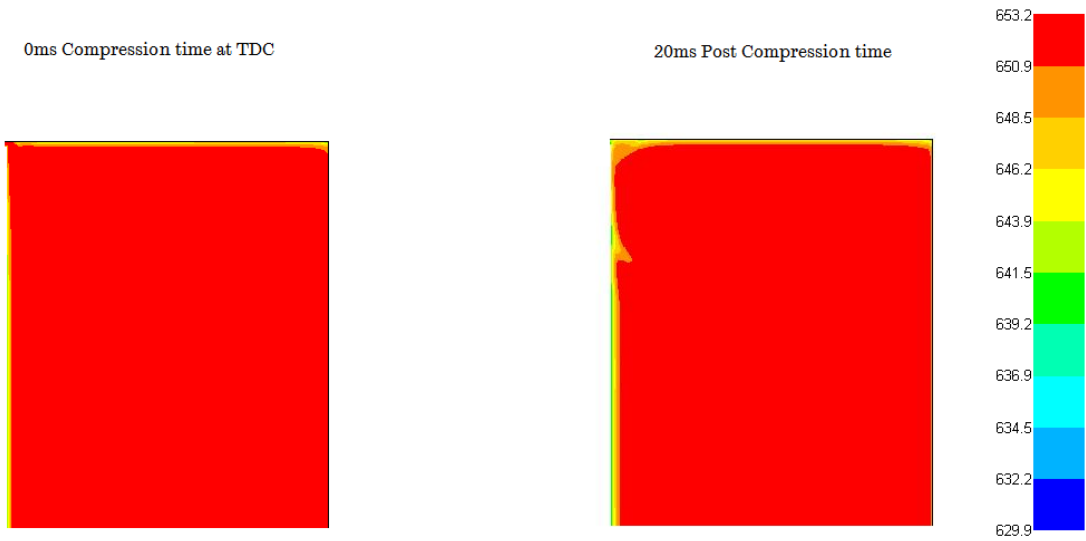


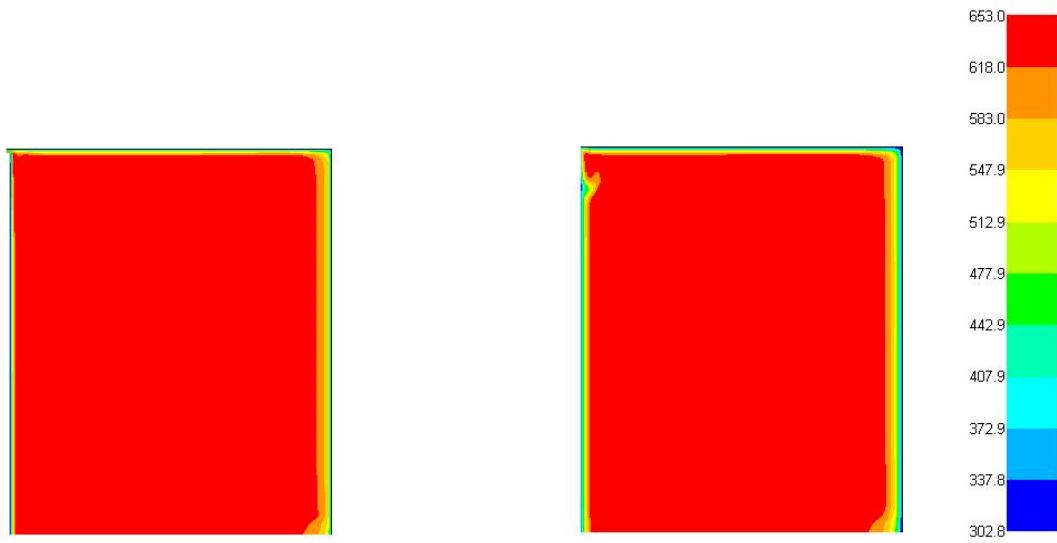
Figure 4-5: simulated velocity and temperature profile for Flat piston head at $T_i = 298$ K, $P_i = 1$ bar. (a). Compression time at TDC (b). 9.2 ms after post compression time (c). 16.11 ms after post compression time.

4.7.2 Piston crevice without a chamfered

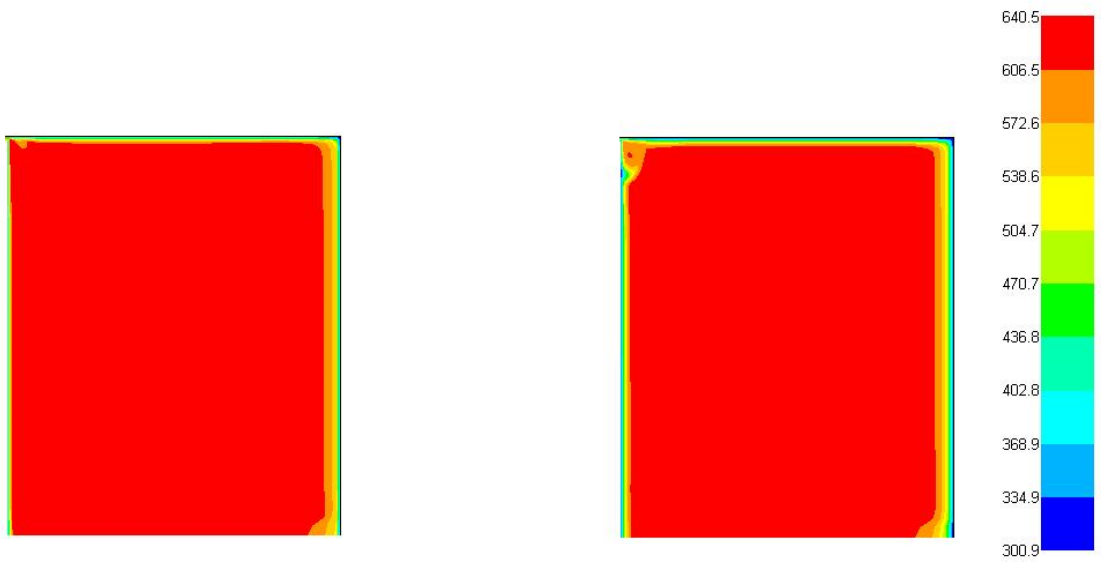
Shown in Figure 4.6, the temperature profile at 0 ms compression time and post compression time of 20 ms. The simple crevice design could not hold the cold gases scrapped from the wall into the crevice. This is because of the pressure difference between the core chamber and the crevice volume there is gas flow back into the adiabatic core region of the chamber.



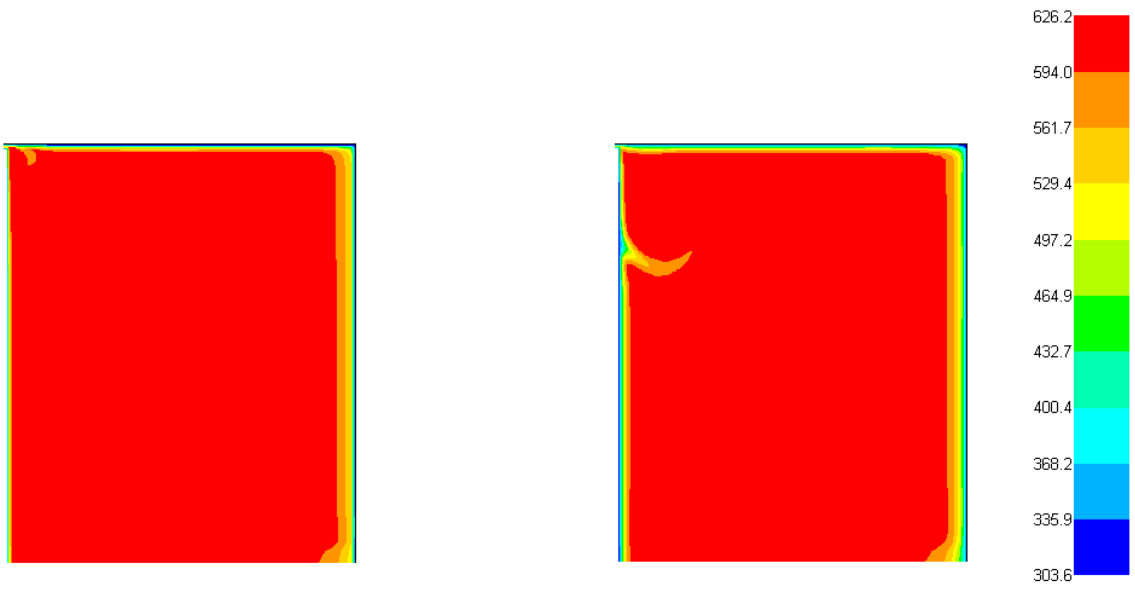
(a)



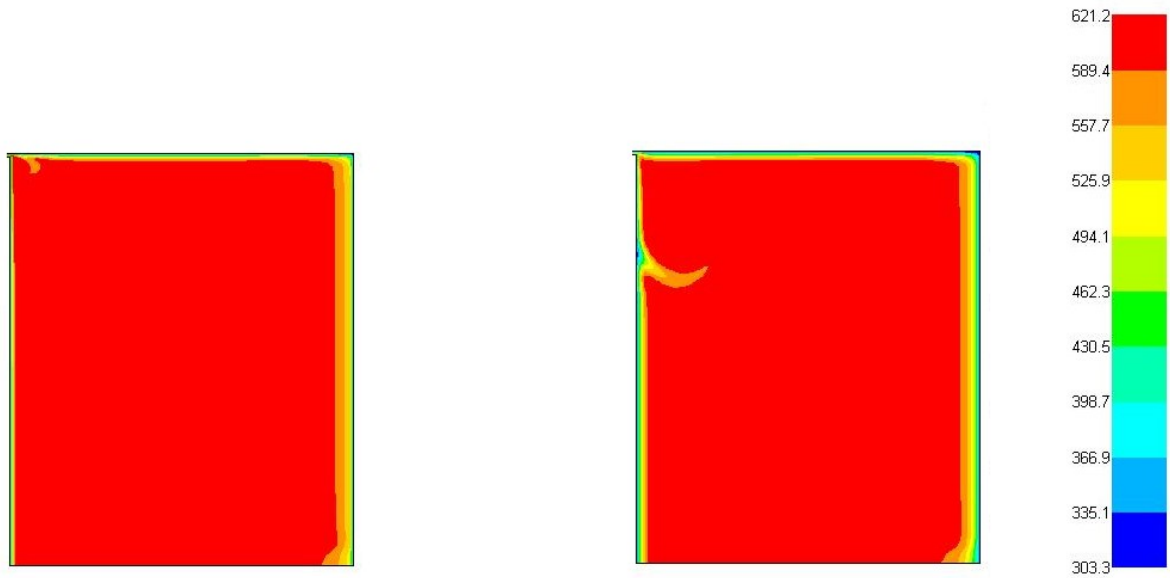
(b)



(c)



(d)

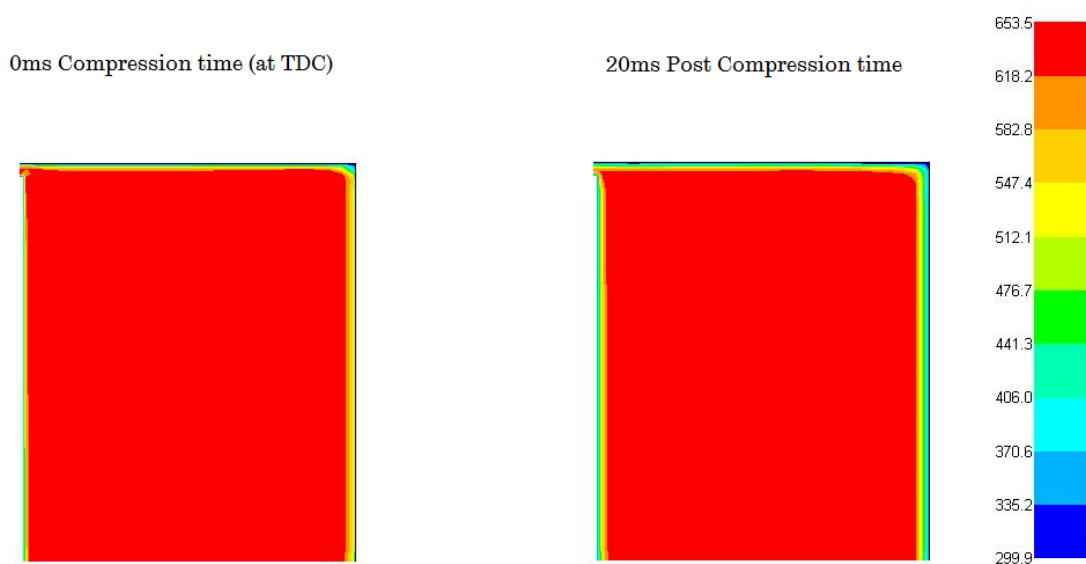


(e)

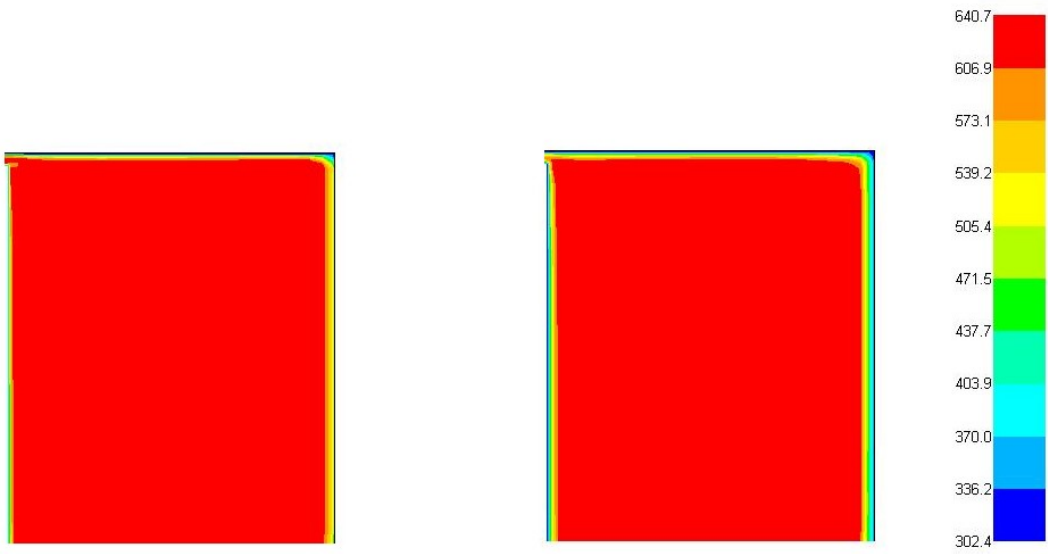
Figure 4-6: calculated temperature field at 0ms compression time and 20ms post compression time, using different sizes of crevice volume. (a) 2% (b) 4% (c) 6 % (d) 8% (e) 10% of the entire chamber volume at TDC.

4.7.3 Piston crevice with Angle Head.

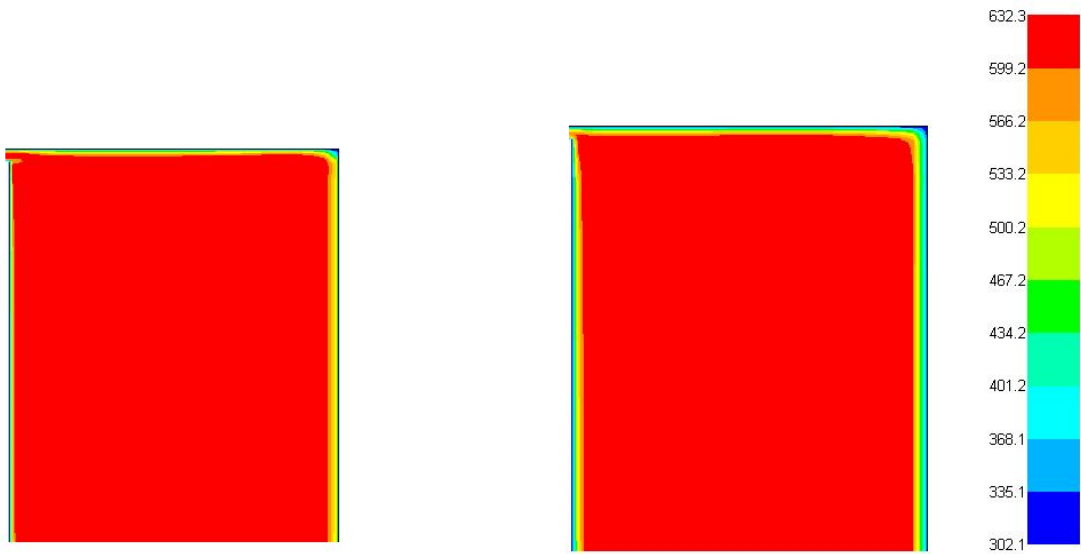
The angled crevice with 2% of the entire chamber volume, 282 mm^3 , was the best at suppressing the boundary layer and providing uniform temperature field with a minimum drop in temperature and pressure. The final compressed pressure and temperature was 16bar and 620 K while the other crevices (b-d) had lower compressed pressure and temperature than (a) as shown in figure 4-7.



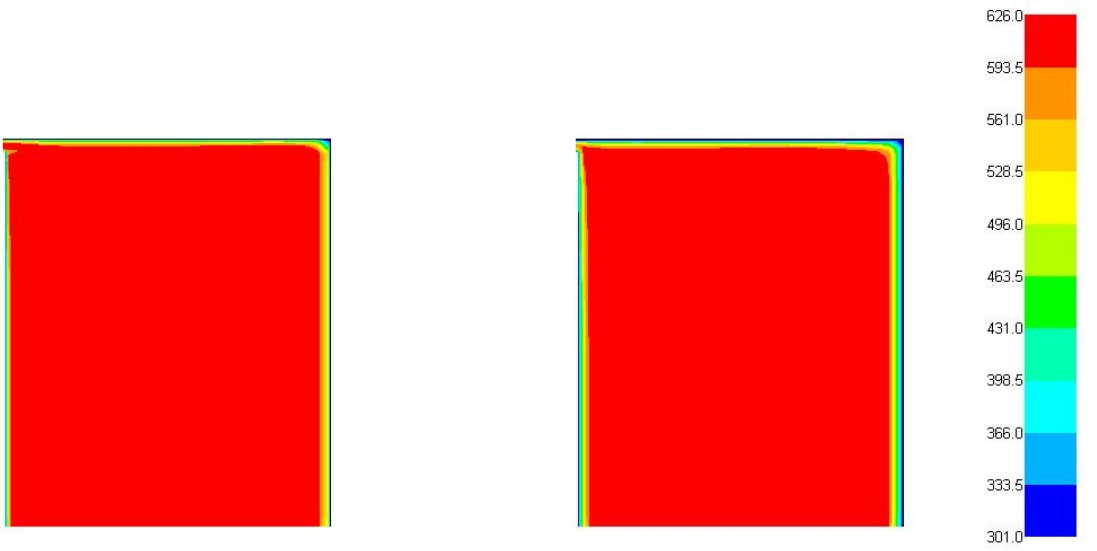
(a)



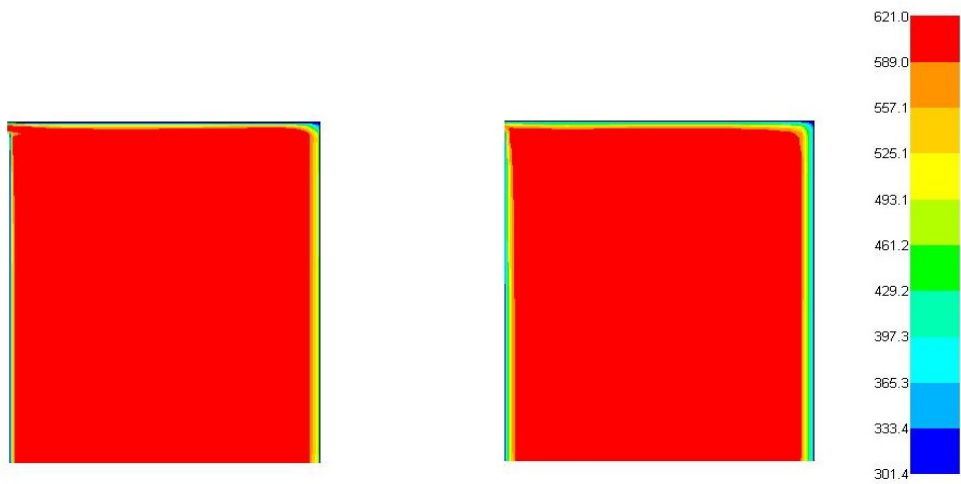
(b)



(c)



(d)



(e)

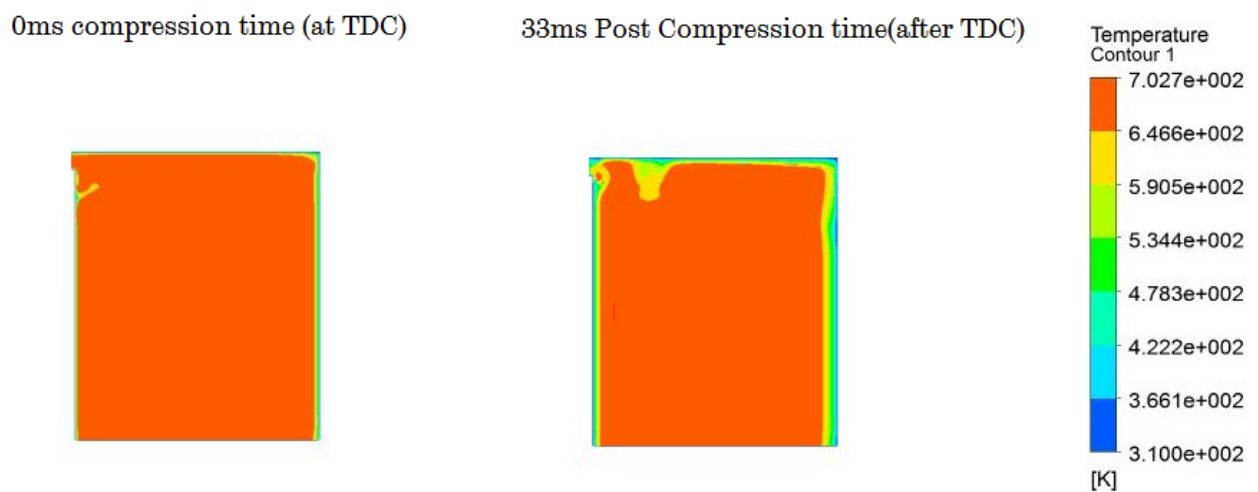
Figure 4-7: Shows the contour of temperature profile of piston crevice head with angled channel. (a) volume 282 mm³ (b) volume 564 mm³ (c) volume 846 mm³ (d) volume 1128 mm³(e) volume 1410 mm³.

4.7.4 Influence of Piston Crevice Height.

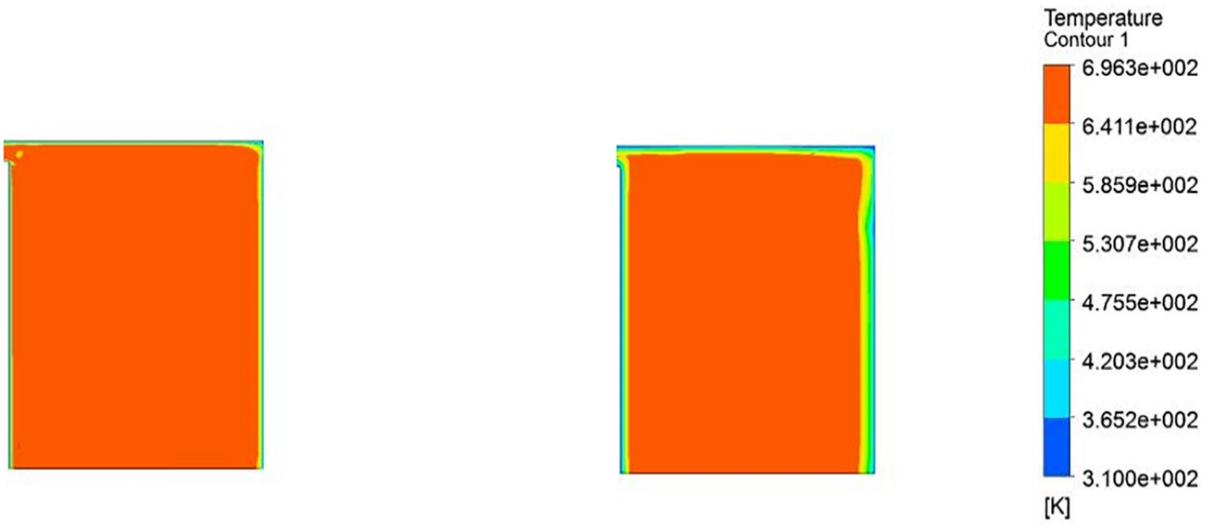
Optimisation of the piston with five different crevice lengths was carried out. A 5 mm height was found to be the best in minimising the pressure. Figure 4-8 shows the contours of temperature profiles for all the crevice lengths.

Crevice A has the highest compressed temperature of 679.6 K, but some cool gases forcing their way back into the core region as the volume was not sufficient to contain the cold gases.

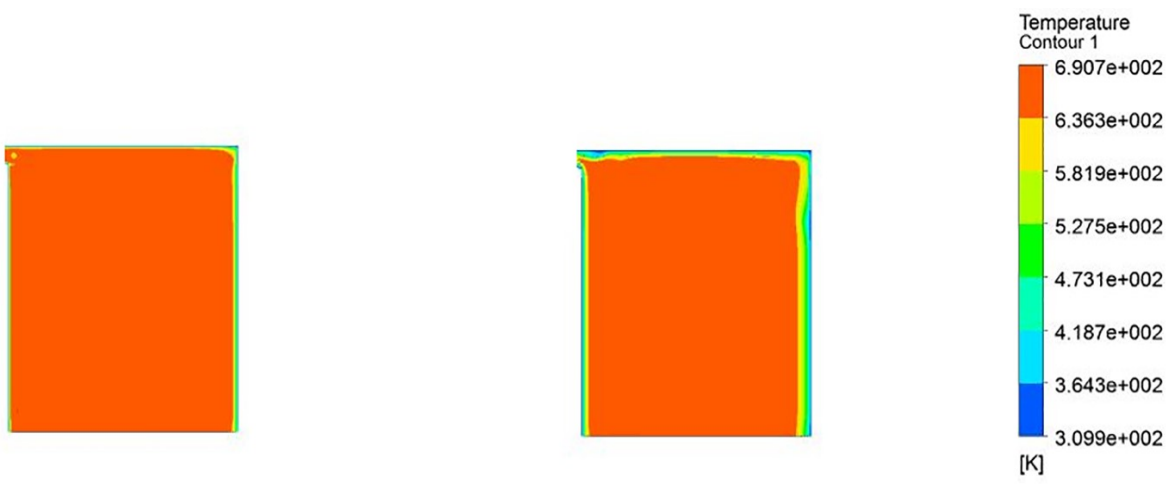
Crevice B suppressed the roll-up vortex with the end of compressed pressure and achieved a temperature of 647 K and 19.5 bar. Subsequent crevices (C, D, E) contained the vortex. The compressed pressure and temperature as shown in figure 4-8.



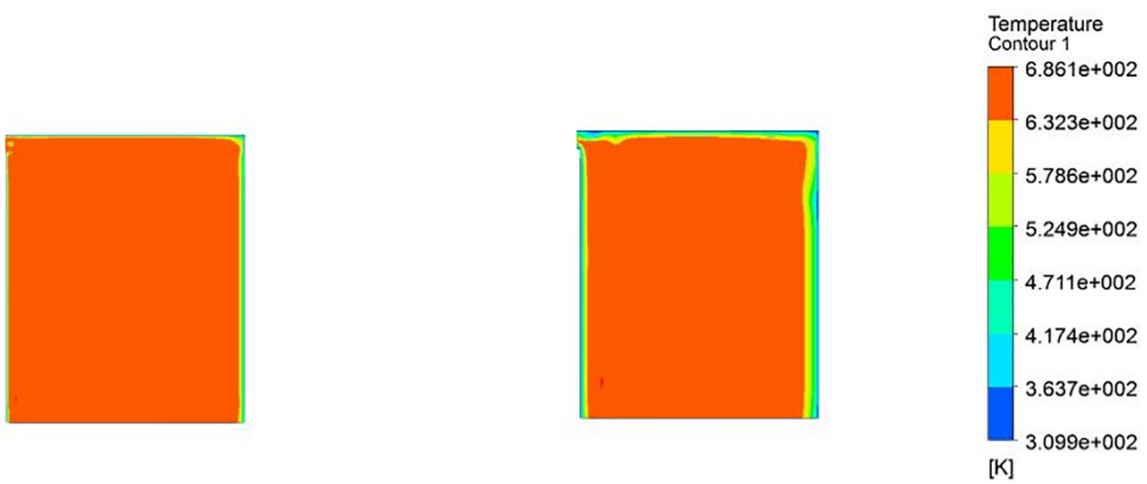
Crevice A



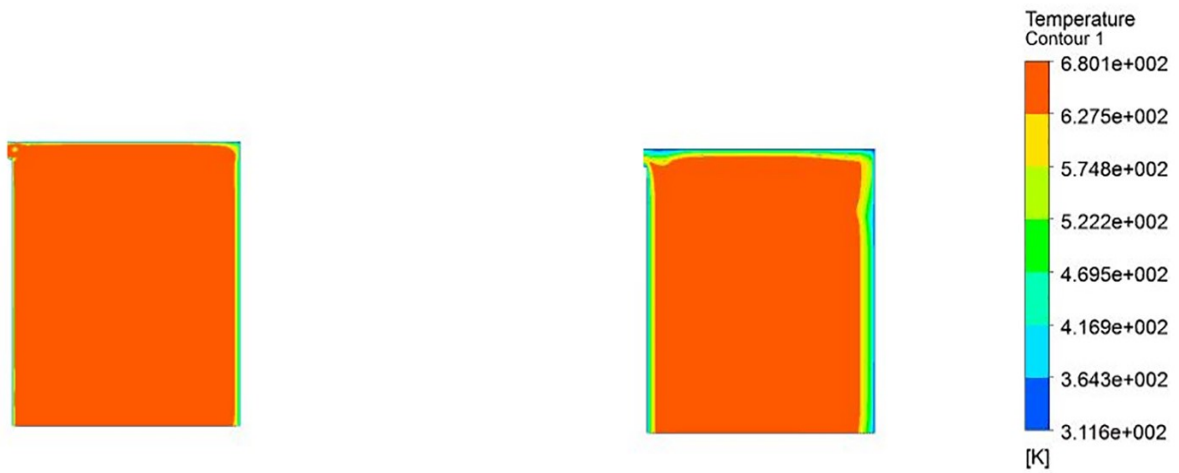
Crevice B



Crevice C



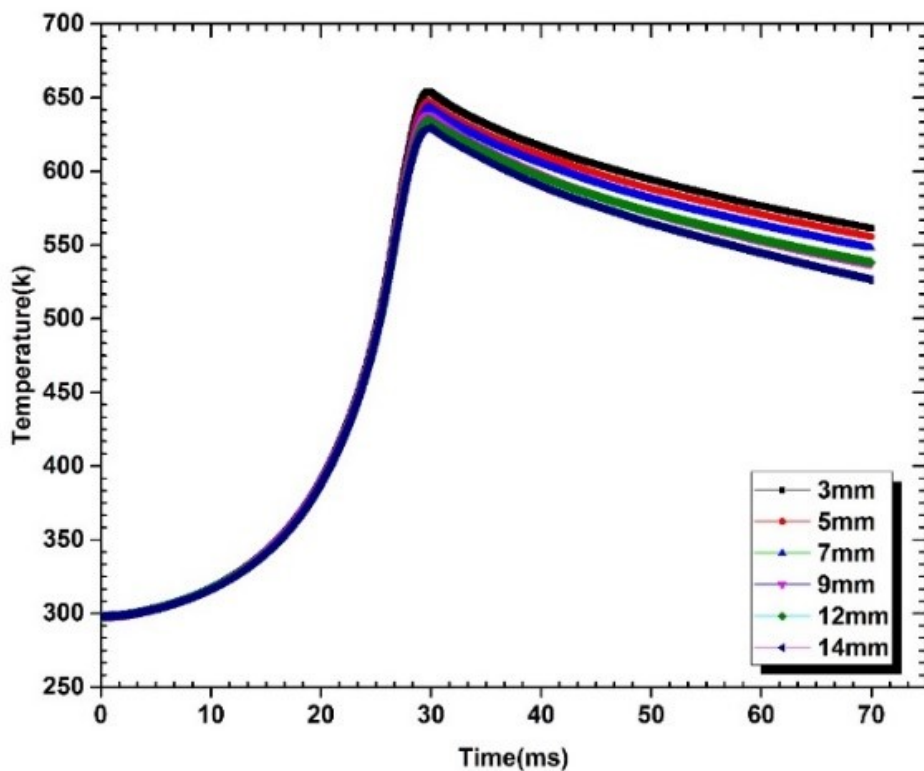
Crevice D



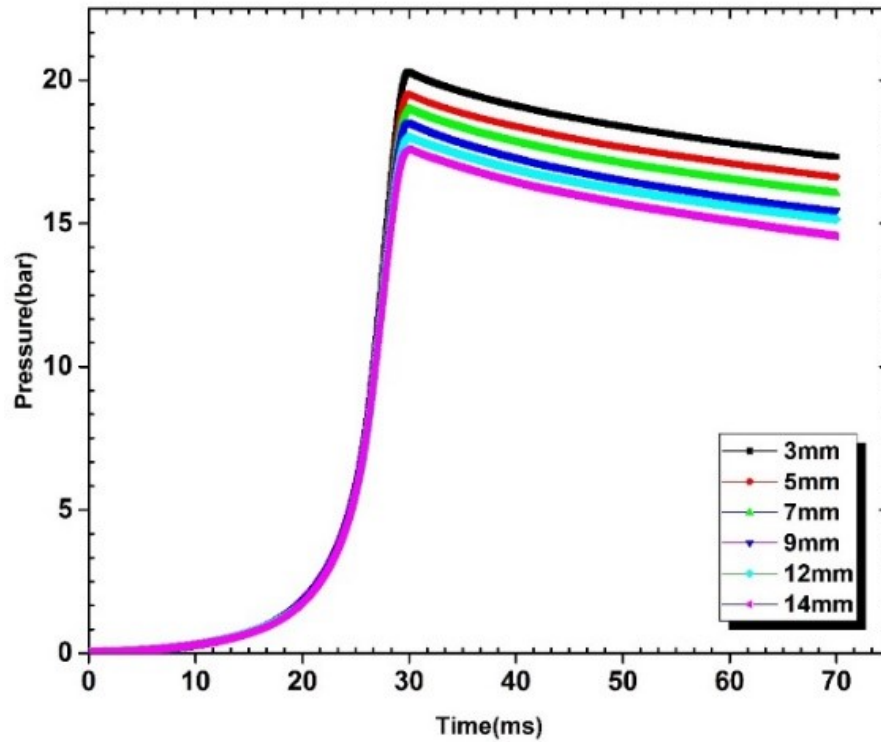
Crevice E

Figure 4-8: Shows the contour of the temperature profile for piston crevice head with varying height. (a) 3 mm (b) 5 mm (c) 7 mm (d) 9 mm (e) 12 mm.

Figure 4-9, shows the temperature and pressure histories for different crevice heights. The EOC pressure with a crevice height of 5 mm is 20.5 bar while that at 14 mm was 18.6 bar. Therefore, 2 bar was achieved by the optimisation of the crevice which is a difference of 17.7 K.



(a)



(b)

Figure 4-9: shows (a) temperature profile (b) pressure profile at $T_i=298$ K, $P_i= 1016.6$ mb, with improved crevice height.

Figure 4-10, shows the validation of the experimental pressure trace with the CFD model at EOC pressure of 15 bar at a stroke length of 142 mm. Nitrogen gas was used at an initial temperature of 299 K. The experimental pressure trace has a slightly higher pressure than the CFD model. This is because the dead volume was underestimated in the CFD model. However, there is good agreement between the traces. Figure 4-11, shows the corresponding predicted the temperature at the EOC at 15 bar from the CFD corresponding a compressed gas temperature of 615 K.

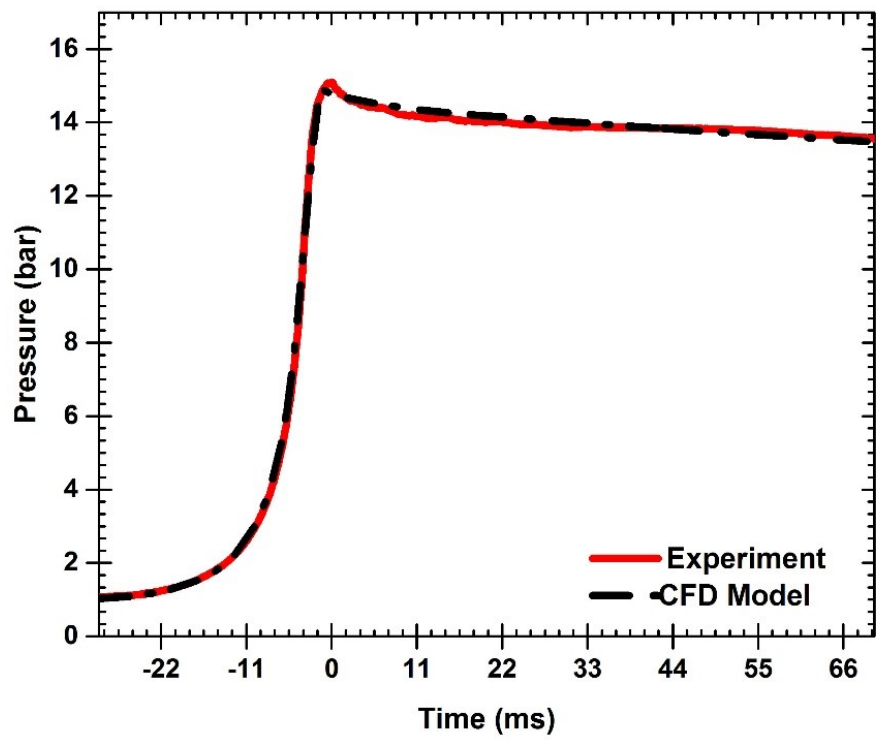


Figure 4-10: Comparison of Experimental pressure trace with the CFD Model

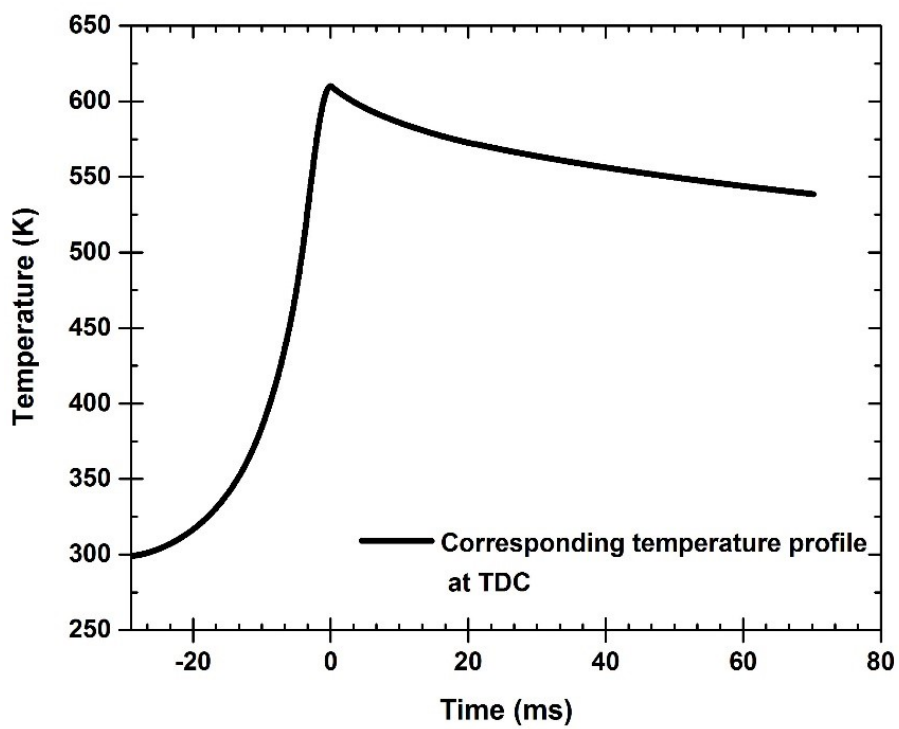


Figure 4-11: End of compressed gas temperature corresponding to $P_c = 15$ bar, $T_c = 615$.

4.7.5 Conclusions

The CFD modelling was able to demonstrate that RCMs with a flat piston head generates a roll-up vortex, which would distort the ignition study of fuels. This can be avoided by machining a crevice on the peripheral surface of the piston. Trapping the cold gases [233].

Wurmel et al.[234] concluded from their CFD simulation, that crevice volume of 8.5-12.5% of the entire chamber volume was optimal. However, from his study, the optimum crevice volume was 2% of the overall chamber volume. The discrepancy is likely to be due the differences in the chamber cross-sectional area. There was good agreement between the experimental pressure trace and the CFD model matching the pressure trace give a corresponding temperature of the EOC temperature.

Chapter 5. Performance Characterization and Ignition Chemistry in a Rapid Compression Machine.

5.1 Introduction.

One way of accessing the suitability of a rapid compression machine for mechanism validation is to conduct characterization experimental tests. This provides an overview of its performance and credibility of generating a broad range of experimental conditions. These measurements should be repeatable and reproducible. The Shef-RCM was subjected to a wide range of operating conditions. In this study, non-reactive experiments were conducted using nitrogen and argon while the reactive tests are carried out using heptane and Jet A-1 air mixtures. Five runs performed for each gas and the pressure traces overlap each other showing slightly to be repeatable. The pressure traces shown are raw data obtained from the experiment and are free from any disturbances, which means that the damping mechanism worked.

5.1.1 Definition of Ignition Delay

Figure 5-1; shows typical shows the pressure history, $P(t)$, and its first derivative profile, measured from the Shef-RCM for *n*-heptane/air mixture. The ignition delay definition appears to have two peak pressure rises signifying the two-stage ignition of *n*-heptane oxidation. The time zero corresponds to the end of compression, EOC pressure of 15 bar and temperature of 679 K. In Figure 5-1, the first-stage ignition delay, τ_1 is the time from the end of compression to the first peak in the time derivative of the pressure. The second-stage ignition delay τ_2 , is defined as the time duration between the end of and the highest rate of pressure rise due to the second stage of ignition[235]. The overall ignition delay, τ is the time from the end of compression to the highest peak in the time derivative of the pressure, which gives the sum of the two intervals as

$$\tau = \tau_1 + \tau_2 \quad 5-1$$

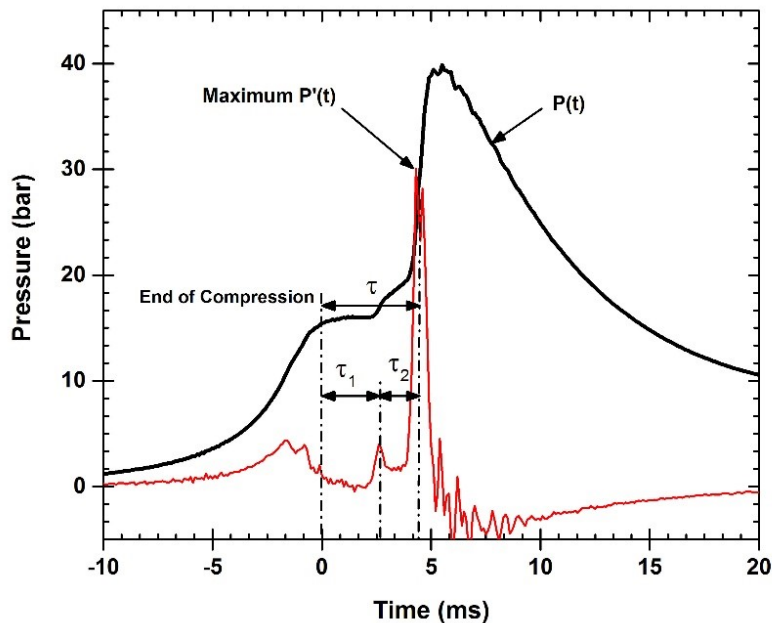


Figure 5-1: Illustrate the definition of ignition delay used in this study. $P(t)$ is the pressure as a function of time, and $P'(t)$ is the time derivative of the pressure as a function of time.

Ignition delay trends are most commonly shown on a $1000/T$ vs. delay time plot. Inverse temperature is represented on the x-axis so; high temperature behaviour is shown to the left and low temperature to the right. Along the y-axis, is the ignition delay time in milliseconds. The scale is logarithmic therefore; each division indicates a 10 fold increase in delay that highlights the high temperature sensitivity of the chemical reactions involved.

5.2 Numerical Modelling.

Kinetic modelling is usually conducted with zero-dimensional (0-D) code such Sandia Senkin code[236] in conjunction with CHEMKIN[237] and Cantera/Python interface. However, these are designed to model idealistic conditions, which are different from those found in a rapid compression machine. To account for the deviation from the ideal processes, a phenomenon such as heat loss from the fluid to walls of the chamber and the vortex has to be accounted for in the simulation. This is achieved by assuming the adiabatic core hypothesis[230, 238], which takes into account both compression stroke and post-compression heat loss. This theory assumes that no mixing occurs between the hot core region and the cold boundary layer. The only time heat loss influences the core region is by the expansion of the core region caused by the cooling of the boundary layer as the piston compresses to a constant volume to the end of the stroke. An empirically determined heat loss parameter derived from non-reactive pressure history is added to the simulation. One way of obtaining the volume expansion is to perform an experiment on an inert mixture having the same heat capacity, thermal conductivity, Initial temperature and initial pressure as the reactive mixture under study. The empirically derived approach only performs well if a well-defined homogenous core is sustained which requires an optimised piston head crevice design, which handles the multidimensional effect such as heat loss and roll up vortexes by Lee et al.[113].

The numerical modelling of the present RCM is carried out using first the Sandia SENKIN code [236] in conjunction with Sandia CHEMKIN[237] package for solving gas phase kinetics problems. This models the time evolution of a closed, homogeneous, adiabatic system. There are two methods of solving this problem: firstly, the volume is given in the CHEMKIN input file (VTIM keyword) as a function of time; secondly, constant volume is assumed (CONV keyword). Using VTIM the effect of the compression stroke and post-compression heat loss can be considered using VTIM. The equations governing reactions in the system are the mass continuity and energy equations. For a closed system with no mass crossing the boundary, total mass remains constant. The mass, M , of the system is given in equation (5-2).

$$m = \sum_{k=1}^K m_k \quad 5-2$$

$$\frac{dm}{dt} = 0 \quad 5-3$$

Where t is the time, m_k is the mass of the k^{th} species and K is the total number of species in the mixture. The individual species are produced and destroyed based on

$$\frac{dm_k}{dt} = V \dot{\omega}_k W_k \quad \mathbf{k} = 1, 2, \dots, \mathbf{k} \quad 5-4$$

Where $\dot{\omega}_k$ is the molar production rate of the k^{th} species, W_k is the molecular weight of the k^{th} specie, V is the volume of the system. The total mass is constant then the mass fraction for the k^{th} species is:

$$\frac{dY_k}{dt} = \nu \dot{\omega}_k W_k \quad \mathbf{k} = 1, 2, \dots, \mathbf{K} \quad 5-5$$

$Y_k = \frac{m_k}{m}$ is the mass fraction of the k^{th} species, $\nu = \frac{V}{m}$ is the specific volume, W_k is the molecular weight and ν is specific volume. $\dot{\omega}_k$ is the net rate of increase of the species k . The temperature of the mixture is found by considering the 1st law of thermodynamics. For a closed system with no heat transfer, the 1st law reduces to equation 5-6.

$$de + pdv = 0 \quad 5-6$$

Where e is the internal energy per mass and p is the pressure. The internal energy per unit mass is given by $e = \sum_{k=1}^K e_k Y_k$, where e_k is the internal energy of the k^{th} species. Differentiating the internal energy of the mixture gives

$$de = \sum_{k=1}^K Y_k de_k + \sum_{k=1}^K e_k dY_k \quad 5-7$$

For calorically perfect gases, the change in energy per unit mass is $de_k = c_{v,k} dT$. Where $c_{v,k}$ is the specific heat at constant volume of the k^{th} species and T is the mixture temperature.

Overall specific heat for the mixture is:

$$c_v = \sum_{k=1}^K Y_k c_{v,k} \quad 5-8$$

Combining (5-7) and (5-8) with the 1st law (5-6) we get:

$$c_v \frac{dT}{dt} + \sum_{k=1}^K e_k \frac{dY_k}{dt} + p \frac{dv}{dt} = 0 \quad 5-9$$

Replacing species production rate $\frac{dY_k}{dt}$ in the above with equation 5-5:

$$c_v \frac{dT}{dt} + p \frac{dv}{dt} + v \sum_{k=1}^K e_k \dot{\omega}_k W_k = 0 \quad 5-10$$

Equation (5-5) and (5-10) is used to solve problems where the volume either is fixed or is a known function of time. Pressure is computed from the ideal gas equation of state, as

$$p = \frac{\rho RT}{\bar{W}} \quad 5-11$$

Where R is the universal gas constant, \bar{W} is the mean molecular weight of the mixture and ρ is the mass density. The specific volume change rate is specify as a function of time is given as

$$V(\mathbf{t}) = \frac{V(\mathbf{t})}{m} \quad 5-12$$

$$\frac{dv}{dt} = \frac{1}{m} \frac{dV}{dt} \quad 5-13$$

For a mixture at constant pressure, the 1st law reduces to the condition of constant enthalpy (h). The differentiated equation for enthalpy is:

$$dh = de + vdp + pdv \quad 5-14$$

When combining with (2.8) and removing the dp term:

$$dh = 0 \quad 5-15$$

Total enthalpy is then:

$$h = \sum_{k=1}^K Y_k h_k \quad 5-16$$

The energy equation (2.8) becomes:

$$c_p \frac{dT}{dt} + v \sum_{k=1}^K h_k \dot{\omega}_k W_k = 0 \quad 5-17$$

Cantera was also used in the modelling of the present Shef-RCM. It is more easily manipulated and modified. Details of the present code used for this simulation is found in Appendix 1 and 2.

Cantera[239] is a collection of object-oriented open source software package tools which is used for solving chemical kinetic, thermodynamics and transport problems. It is capable of addressing large kinetics mechanisms, compute equilibrium solutions. The framework is easily modified and operate on different interfaces written in codes such as Python, Matlab, FORTRAN, and C++. Cantera is designed with built-in combustion engine models, which accommodate a polynomial coefficient function that describes piston velocity profiles. Users can utilise time-dependent reactor networks following a general reactor model that includes various sub-models with specific conditions including constant pressure reactors and ideal gas reactors. In the course of this work, Cantera has been utilised for the simulation, using the experimental pressure trace to determine the RCM piston velocity. This profile serves as a foundation for fitting a high order polynomial describing the piston velocity that is used to describe the motion of the reactor piston during the numerical simulation. The Python code developed to calculate the reactor piston velocity is included in appendix 1.

5.2.1 Homogeneity and Estimation of Temperature Field of the Reaction Chamber

The temperature inhomogeneity occurs in the reaction chamber due to the formation of roll-up vortices with resulting heat lost from the core region to the walls of the chamber. In order to achieve a homogenous temperature region, an optimised piston head crevice was designed using CFD modelling (Chapter 4). The compression is so rapid (of the order of milliseconds) making it problematic to measure the temperature directly. An intrusive device such as thermocouples cannot measure the transient nature of heat loss since it is very rapid and the level of responsiveness of the thermocouple is low. Non-intrusive optical approaches require an extensive calibration and difficult to set up. Therefore, the temperature is determined indirectly by applying 'adiabatic core hypotheses'[106, 200, 240]. This approach has been validated by computational[202] and experimental methods[241, 242]. If the compression process is truly adiabatic, the adiabatic temperature at TDC, T_{ac} , would be calculated as

$$\int_{T_i}^{T_{ac}} \frac{1}{\gamma-1} \frac{dT}{T} = \ln(CR) \quad 5-18$$

$$\int_{T_i}^{T_{ac}} \frac{1}{\gamma-1} \frac{dT}{T} = \ln\left(\frac{P_{ac}}{P_i}\right) \quad 5-19$$

Where P_{ac} , is the pressure at the end of the compression, γ is the specific heat ratio and CR is the compression ratio. The actual temperature and pressure from the experiment are lower due to heat loss to the reactor chamber wall. Then temperature at TDC, T_c is obtain by the adiabatic core hypothesis according to the relation

$$\int_{T_i}^{T_c} \frac{\gamma}{\gamma-1} * \frac{dT}{T} = \ln\left(\frac{P_c}{P_i}\right) \quad 5-20$$

Where P_i is the initial pressure, P_c is the compressed pressure, T_i is the initial temperature, γ is the specific ratio. The temperature T_c cannot be calculated directly, because the specific heat ratio used in the Equation (5-18), (5-19) and (5-20) which are unknown function of temperature and mixture composition. This cannot be integrated directly to get T_c , if an assumption were made that the composition is fixed and the specific heats are parameterised with linear fit, the stages of solving this problem would be wearisome.

The easiest way of solving T_c was numerically integration using Cantera. Base on the equation 5-20, gamma is not constant during the compression stroke the pressure is fluctuating between set points. Instead of using a relationship based on constant specific heat, which gives wrong values of the compressed temperature since gamma is not constant during the compression process. A parameterised thermodynamics data is used to locate which set points corresponds to the new pressure and entropy. With the thermodynamics data in place, Cantera is cable of solving the nonlinear equation. Therefore, the end of

compressed gas temperature, T_c , is estimated. A mechanism file that contains the mechanism input and thermodynamic data are read into Cantera, which make use of the properties during the simulation. The code is found in appendix 4. For the purpose of this work three mechanisms were chosen and used to estimate the compressed gas temperatures for Jet A-1; Dooley surrogate [194], UCO-HEFA; Dagaut surrogate [243], and banner solvent; Aachen surrogate was developed by Honnet et al., [3].

5.2.2 Heat Loss Model

Heat loss occurs predominantly through convection as the heated gas transfers heat to the walls. The heat transfer coefficient is related to the thermal conductivity λ and the thickness of the thermal boundary layer δ_h .

$$h_c = \frac{\lambda}{\delta_h} \quad 5-21$$

Where δ_h is determined from Nusselt number Nu

$$Nu = \frac{D}{\delta_h} = \frac{h_c D}{\lambda} \quad 5-22$$

The Nusselt number depends on the Reynolds and Prandtl numbers.

$$Nu = 0.332 Re_l^{1/2} Pr^{1/3} \quad 5-23$$

Where Re_l is the flow Reynolds Number and Pr is the Prandtl number respectively.

$$Re_l = \frac{\rho u L}{\mu} \quad 5-24$$

$$Pr = \frac{c_p \mu}{\lambda} \quad 5-25$$

Where ρ is the fluid density, u is the flow velocity, L is the characteristic length, c_p is the specific heat of fluid, and μ is the dynamic viscosity of fluid.

The heat loss in engines involves estimating the instantaneous heat transfer coefficient [244] and also RCM's [245, 246]. There are three types of heat loss models: single zone [247], the multi-zone heat loss [248] models and the volume expansion model [249, 250]. The single

zone heat model based on the first law of thermodynamics assuming the ideal gas behaviour written in the form

$$\frac{dQ_c}{dt} = \frac{C_v V}{R_u} \frac{dP}{dt} - \frac{Q_w}{dt} \quad 5-26$$

Where $\frac{dQ_c}{dt}$ is the apparent heat release rate (AHRR) from combustion, C_v is the constant volume heat capacity of the gas mixtures, V is the volume at TDC, R_u is the the universal gas constant, $\frac{dP}{dt}$ is the time derivative of the experimental pressure trace and $\frac{dQ_w}{dt}$ is the rate of heat loss to the wall. All the parameters are determined directly from experiment except, C_v which is the dependent on the reactor chamber temperature and experimental pressure trace, which is estimated from the ideal gas law. Therefore, the convective heat transfer rate to the cylinder walls and piston during compression is describe using the heat transfer coefficient that is given as

$$\frac{dQ_w}{dt} = h_c A (T - T_w) t \quad 5-27$$

Equation 5-27 is based on Newton's law of cooling for convective losses; it shows that the convective heat losses are directly proportional to the variation between the mean gas temperature and the wall temperature, T_w . Where A is the internal surface area of the reaction chamber, T is the mean gas temperature, h_c is the instantaneous heat transfer coefficient and t is the total compression time of the RCM. Correlations[251-253] have been proposed in order to predict the heat loss on the basis of heat transfer measurement from experiment and used in the modelling of in-cylinder heat transfer.

In the multi-zone heat loss model, the RCM is split into zones where momentum, conservation of mass and energy are applied to calculate the heat loss rate from the adiabatic core. The idea of the model is to account for the physical processes within the region of the RCM that account for the heat loss[248].

$$\frac{dV}{dt}_{HRM} = -\frac{V}{\gamma} \left[\frac{1}{P} \frac{dP}{dt} - \frac{1}{N} \frac{dN}{dt} + \frac{1}{C_p T N} \sum_{j=1}^{N_{sp}} u_j \frac{dn_j}{dt} \right] \quad 5-28$$

The advantage of this model is the thermochemistry effects are adequately captured which is pertinent for fuels with cold flame type behaviour. It is assumed that the heat loss in the RCM only occurs within a thin boundary layer. The model assumes the compression is an isentropic process and specifies an effective volume term[238]. This approach was adopted here as it's more convenient and less expensive than other models such as estimating the instantaneous heat coefficient [247, 254].

5.2.2.1 Effective Volume Approach

The effective volume approach accounts for the heat loss from the gas to the reactor chamber wall during the compression and post compression period of the experiment. However, during two-stage ignition, the multi-dimensional effects cannot be neglected, leading to a higher pressure rise in the first-stage ignition and a shorter total ignition delay[202, 249].

Goldsborough et al.,[248] proposed MZM where he divided the reactor chamber and piston regions into four zones. It includes the reaction chamber, the piston gap, the crevice volume, and the ring pack used to seal the piston in the reaction chamber. Whilst this approach has been shown to be better than 0D modelling difficulties in modelling heat loss to the wall, and associated pressure drop which link to chemical processes and heat release introduces more uncertainties to the model.

To make the heat loss problem amenable to modelling the following experimental conditions are required:

1. A crevice piston to contain the cold boundary gases into the crevice zone as this enhances a homogenous environment.
2. The heat loss from the RCM is confirmed to a thin boundary layer at the chamber wall.
3. The piston motion should be rapid as possible and quickly brought to rest at the end of its stroke (TDC).

The core region can then be represented as an 'effective volume,' V_{eff} which is as a function of time. Practically an empirically determined parameter, V_{add} , account for the heat loss effect in RCM which is added to the actual time dependent geometric volume of the combustion chamber, V_g . In the post compression period, where $t > 0$, polynomials fit, $V_p(t)$, fitted to the effective volume expansion during the post compression stages of the experiments. Then the effective volume at post compression is taken as the product of the effective volume at TDC ($t = 0$) and the fitted volume expansion which is in turn used to simulate the experiment[255].

$$V_{eff}(t) = V_g(t) + V_{add} \quad t \leq 0 \quad 5-29$$

$$V_{eff(t)} = V_{eff}(0) V_p(t) \quad t > 0 \quad 5-30$$

The critical parameter for the heat transfer model, V_{add} , and the polynomial function $V_p(t)$. These key parameters can be resolved from the pressure trace of the non-reactive test, which is use to simulate the corresponding reactive case. The polynomial fit, $V_p(t)$, is curved fit to a volume expansion trace given below.

$$V_{exp(t)} = \left(\frac{P(0)}{P(t)} \right)^{1/\gamma}$$

$$t \geq 0$$

5-31

5.3 Results and Discussion

5.3.1 Experimental Characterization: Non-Reactive Experiment

Characterization tests were necessary to know the capability of the current machine regarding its operating pressure, temperature. The present machine achieved the end of compression pressures, for flat and crevice pistons, to be approximately 22 and 18 bar respectively as shown Figure 5-2.

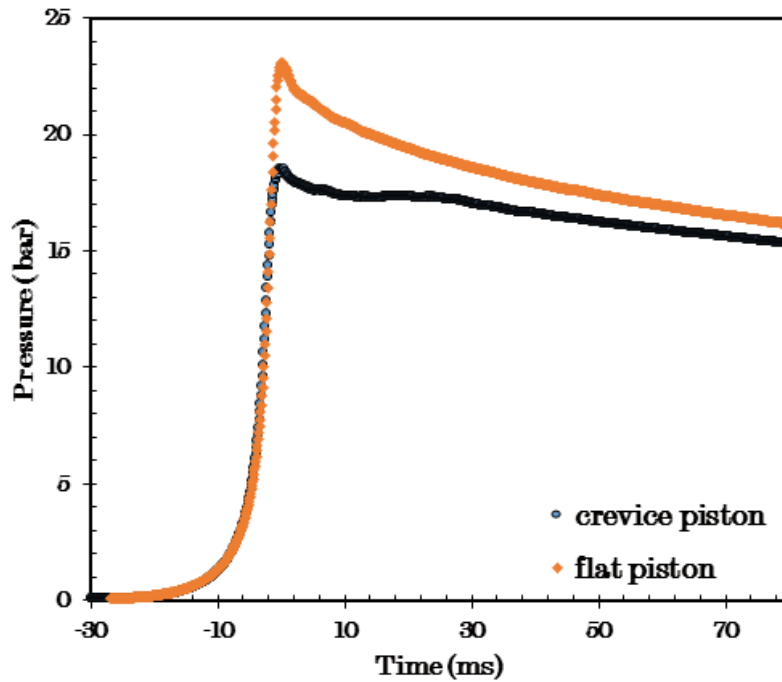


Figure 5-2: Obtainable pressure trace for Shef-RCM (Flat and Crevice Piston).

Non-reactive tests were carried out by expanding inert gas (nitrogen) in the reactor chamber. The tests were carried out by retracting the piston to its BDC, and the pressure of the pneumatic driving chamber was charged to 4 bar. The reactor chamber is then first vacuum then inert gas charged into the chamber through the septum while the valve was closed. The raw experimental pressure trace data obtained from the LabVIEW represented as pressure versus time history shown in figure 5-3. Pressure traces for four experiment of nitrogen at an initial pressure of 0.7 bar and argon at an initial pressure of 0.7bar are shown. The repeatability was considered good.

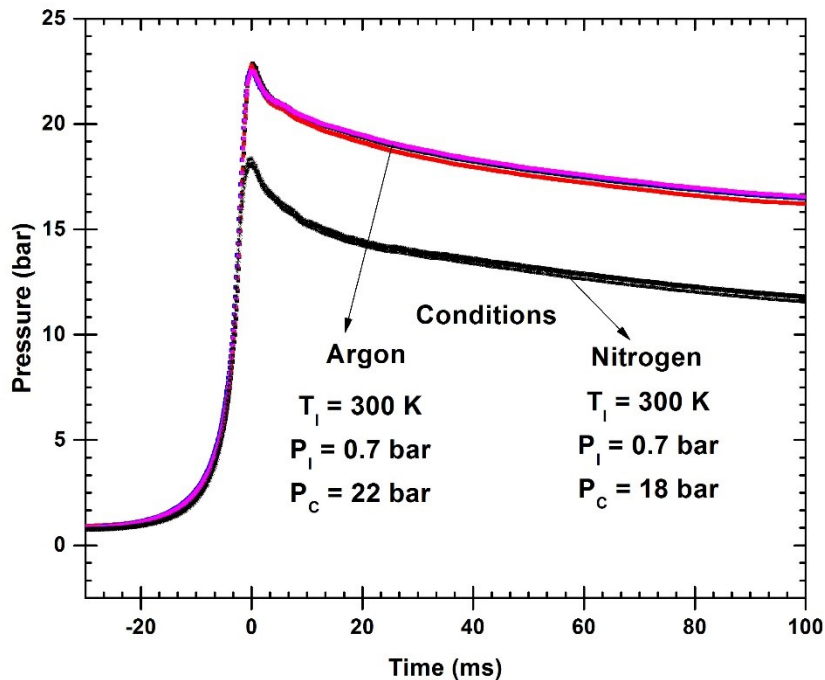


Figure 5-3: illustrates a repeatability of four experimental pressure trace of nitrogen and argon. Colour line – Nitrogen pressure trace and Black lines-Argon pressure trace at an initial pressure of 0.7 bar.

5.3.2 Experimental Characterization: Reactive Experiment.

The repeatability for the reactive experiment is demonstrated with two fuels. One a high volatility n-heptane and another with low volatility Jet A-1. Five different runs were done at an equivalent ratio of 1.0. The objective of these tests was to demonstrate the capability of the rig in producing repeatable results. Shown in figure 5-4, are the n-heptane tests. Figure 5-5 shows the Jet A-1/air tests. Both pressure traces overlapped each other and the reactive experiment demonstrates a repeatable and reproducible experimental pressure trace. The heptane experiment was conducted at stoichiometric condition at 1 bar, initial temperature of 310 K. The uncertainty in heptane ignition delay time for the five runs is 21.98 ± 0.5 ms and based on the section 3.11.6 the formula was used to estimate the uncertainty in the compressed gas temperature to be 619.8 ± 5 K and error in the compressed gas pressure is 16.6 ± 0.3 bar.

For Jet A-1, conditions for the experiment are initial pressure of 0.5 bar, initial temperature 408 K and $\phi = 1.0$. The uncertainty in the compressed gas pressure is 10.12 ± 0.2 bar. The uncertainty in the ignition delay time is 13.2 ± 1 ms while the uncertainty in the compressed gas temperature is 729 ± 6 K.

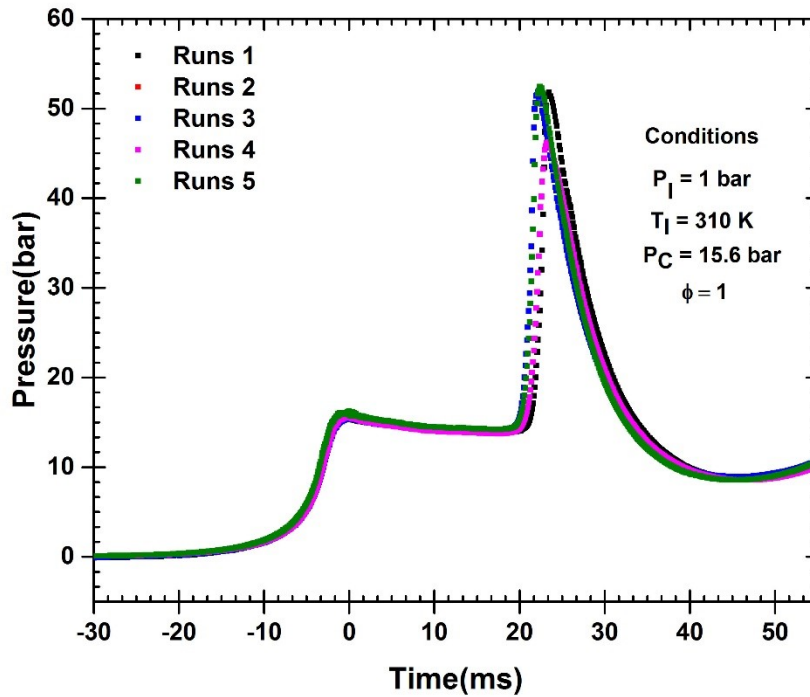


Figure 5-4: Demonstration of experimental repeatability of n-heptane data. Molar composition: $nC_7H_{16}/O_2/N_2 = 1/11/41.36$. Conditions: $P_c = 15.6$ bar; $T_i = 310$ K;

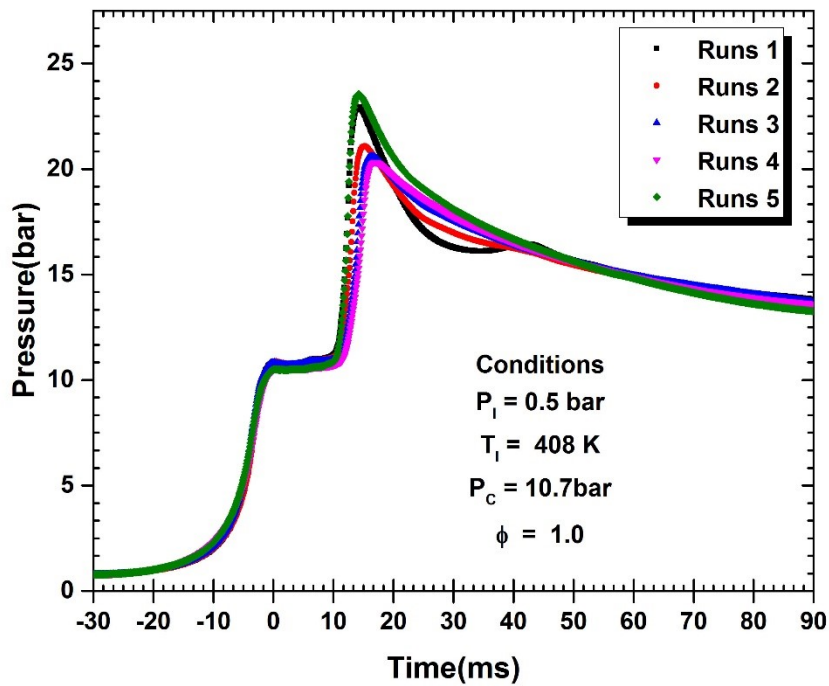
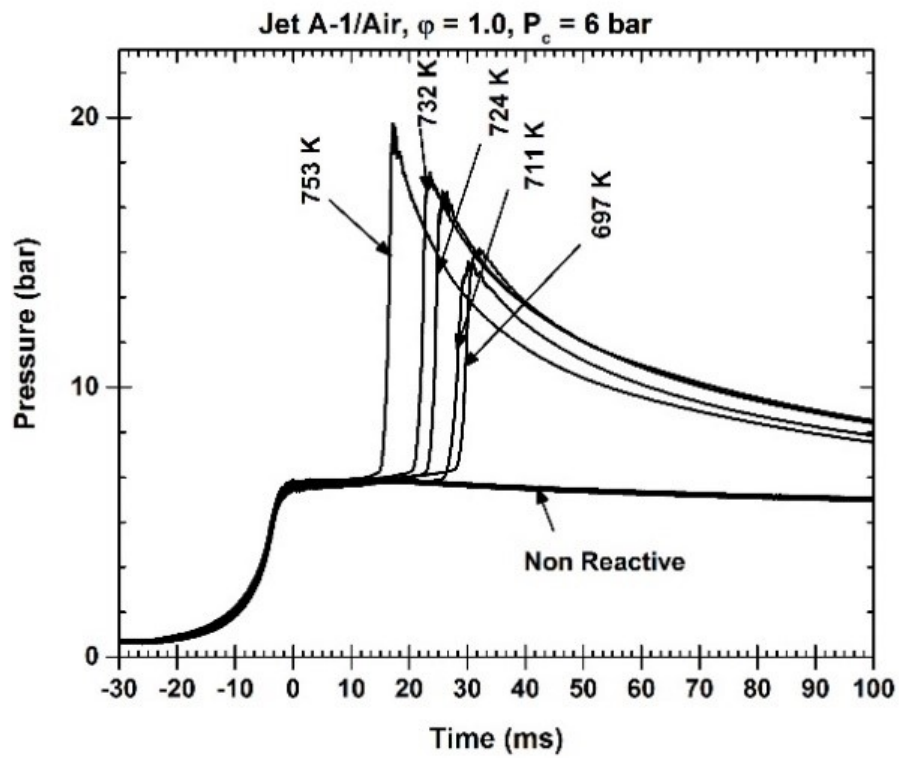


Figure 5-5: Demonstration of experimental repeatability for Jet A-1 and air at equivalent ratio of 1.0. Conditions: $P_c = 10.7$ bar; $T_i = 408$ K.

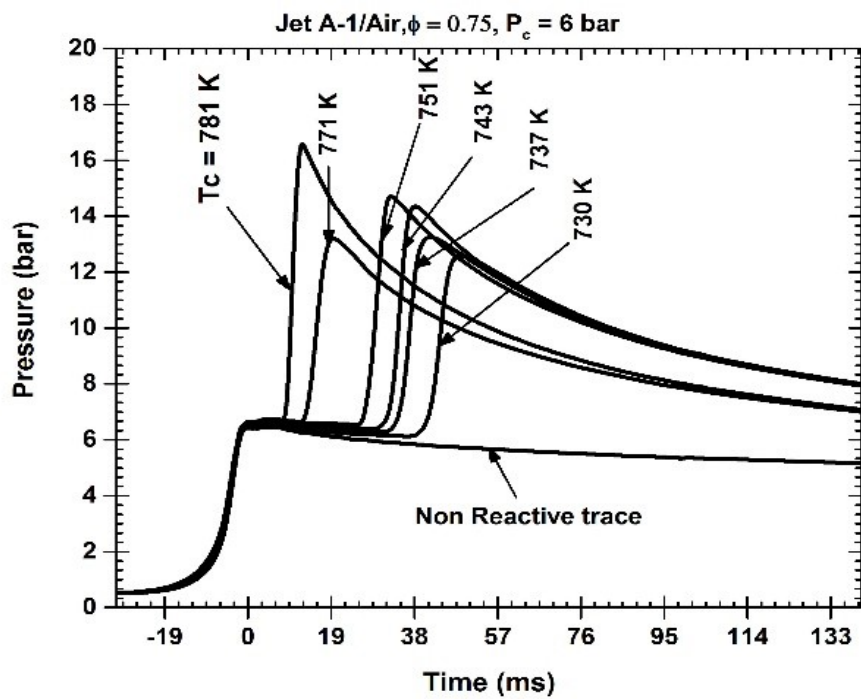
5.3.2.1 Influence of temperature on Jet A-1 ignition delay.

Figure 5-6, shows the pressure trace of ignition delay of Jet A-1 at 6 bar at various EOC temperatures ranging from 697 – 781 K and at an equivalence ratios of 0.75 and 1.0. The ignition delay reduced as the EOC temperature increased. At these conditions, no negative temperature coefficient (NTC) was observed and the detection of second-stage heat release was not seen. Figure 5-6, shows the measured ignition delay as a function of the compressed

temperature. The black rectangle represents the experimental data while the broken red lines are a linear the least square fit to the data.



(a)



(b)

Figure 5-6: Experimental pressure trace at various EOC temperature for Jet A-1/air mixture at an equivalent ratio of 1.0 at $P_c = 6$ bar. Conditions: oxidizer to mass ratio of 14.6.(a) at $\phi = 1.0$ (b) at $\phi = 0.75$.

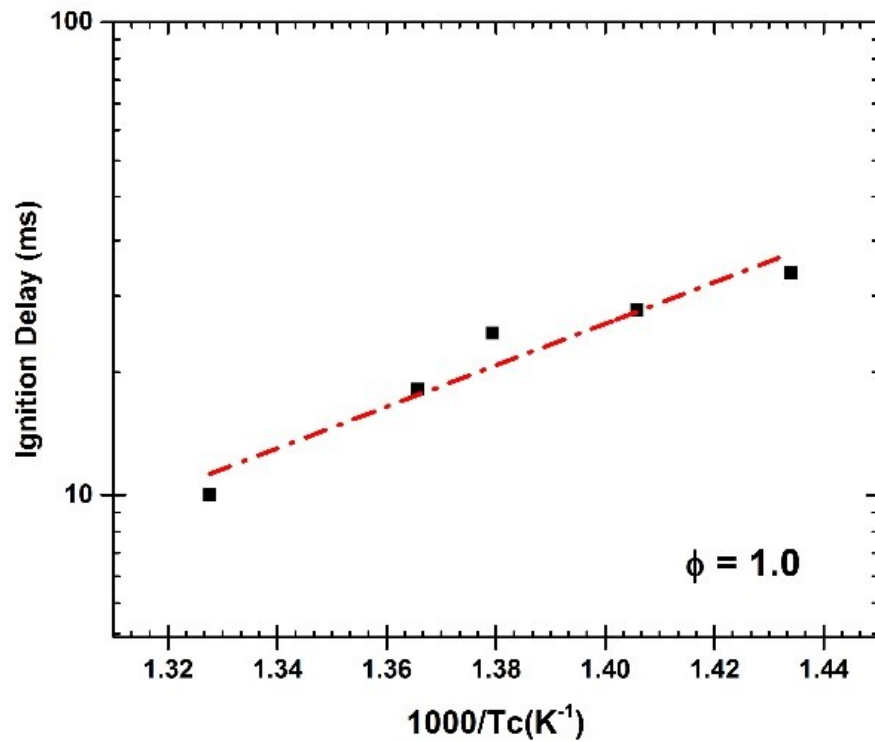


Figure 5-7: Measured ignition delay as a function of compressed gas temperature, at 6 bar for Jet A-1/air mixture corresponding to (a). $\phi = 1.0$, oxidizer to mass ratio of 14.6.

5.3.2.2 Influence of Pressure on the Ignition delay

Comparison of the effect of pressure on ignition delay is represented in figure 5-8, the ignition delays for the Jet A-1/air mixture at a compressed gas temperature range of 734 – 796 K. At 6 and 10 bar the ignition delay exhibited an inverse dependence on the compressed gas pressures, no NTC behaviour was detected. It can be seen that both pressures converge at higher temperature and as the pressure is increase from 6 to 10 bar there is a reduction in ignition delay clearing showing that increasing the peak pressure leads to a reduction in the ignition delay.

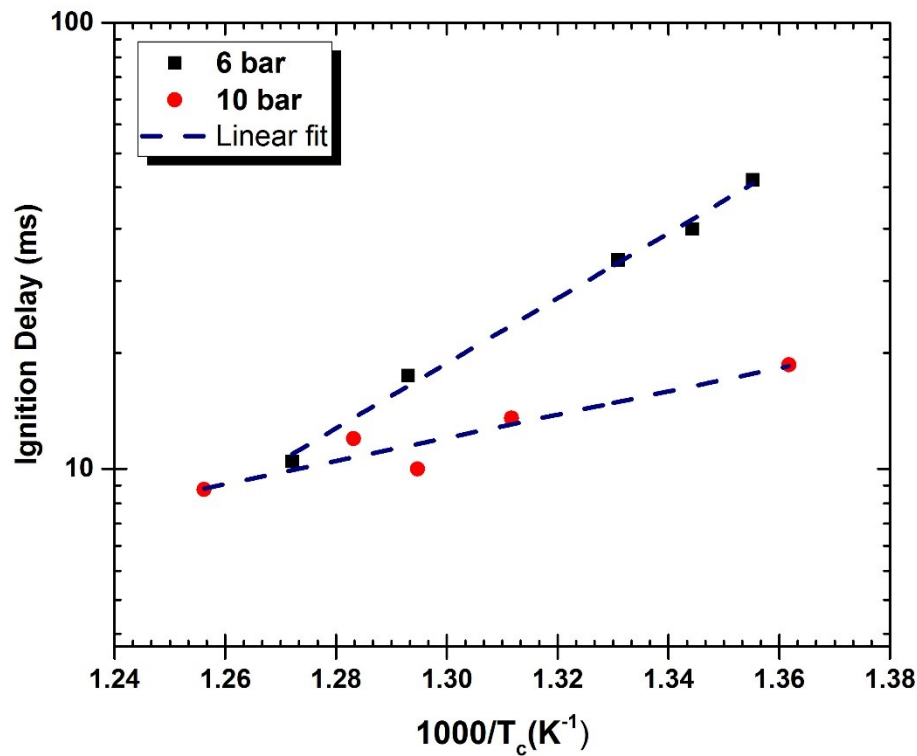
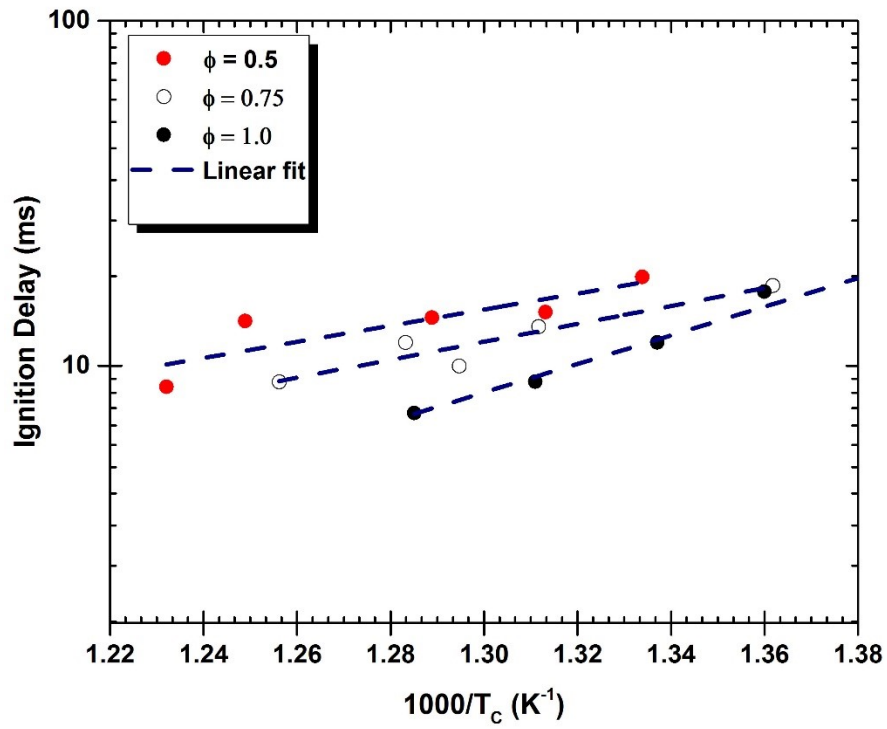


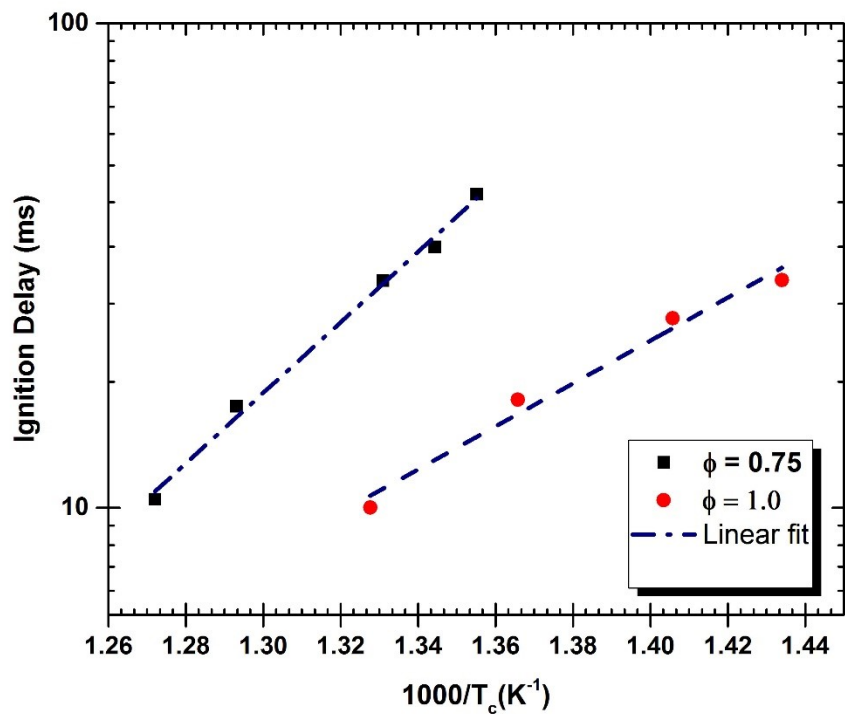
Figure 5-8: Influence of pressure on ignition delay post compression pressure of 6 bar and 10 bar for Jet A-1/air mixture corresponding to $\phi = 0.75$, molar ratio: $O_2 : N_2 = 1 : 3.76$.

5.3.2.3 Influence of Equivalent Ratio on Ignition delay

Shown in Figure 5-9, is the influence of equivalence ratio on the ignition delay times for Jet A-1/air mixtures at pressures of 6 and 10 bar and temperature range of 730 – 815 K. There is an inverse dependence on the equivalence ratio, which shows that ignition delays are shorter with increasing equivalence ratio up to the stoichiometric conditions tested. At a compressed gas pressure of 10 bar at $\phi = 0.75$; The test at compressed gas pressure of 6 bar at $\phi = 0.75$ and $\phi = 1.0$ also showed no evidence of NTC behaviour. While at 6 bar, the same trend is observed where the ignition delay time gets shorter with an increase in the equivalent ratio. In Figure 5-9a there seems to be a convergence of ignition delay at an equivalence ratio of 0.75 and 1.0 at lower compressed gas temperature, but as the temperature and equivalence ratio increases the ignition delay diverges and a corresponding reduction in the ignition delay appears. A linear fit shown in Figure 5-9 was fitted on the data using Origin software.



(a)



(b)

Figure 5-9: Measured ignition delay as a function of compressed gas temperature, at post compression pressure at (a) 10 bar and (b) 6 bar for Jet A-1/air mixture corresponding to $\phi = 0.75 - 1.0$, oxidizer to mass ratio of 14.6.

5.3.3 Ignition Delay Correlation

Within the low temperature range 697-781 K studied at $\phi = 1.0$ and EOC pressure of 6 and 10 bar, a single stage ignition time with no negative temperature coefficient was observed. This behaviour can be reduced to a single correlation

$$\tau_{ignition} = A * P_c^b \phi^c \exp\left(\frac{T_a}{T_c}\right) \quad 5-32$$

Where A , b , c , T_a are the optimisation parameters representing the pre-exponential factor, and the pressure exponent respectively. The $\tau_{ignition}$ in milliseconds, P_c in bar and T_c in Kelvin. The region where the ignition delay display a linear behaviour are normally fitted using a linear logarithmic correlation and assuming the correlation to be constant variation coefficient[256]. However, equation 5-32, is linearized by taking the natural logarithm of both sides resulting to the equation 5-33 shown below.

$$\ln(\tau) = \ln(A) - b \ln(P) - c \ln(\phi) + \frac{T_a}{T_c} \quad 5-33$$

The coefficients estimated using the linear multiple regression analysis. Various authors in the past have come up with different correlation models describing the ignition delay time for hydrocarbon fuels[159, 257, 258]. However, the equation 5-33 is limited to the Arrhenius behaviour of ignition delay time[122]. Figure 5-10 shows, the Global Correlation for Jet A-1 (FST-265638). The correlation is scaled to $P_c = 10$ bar and $\phi = 1.0$ using the correlation parameters giving the following.

$$\tau_{ignition} = 9.037 * 10^{-5} P_c^{-0.697} \phi^{-0.1} \exp\left(\frac{10,018}{T_c}\right) \quad 5-34$$

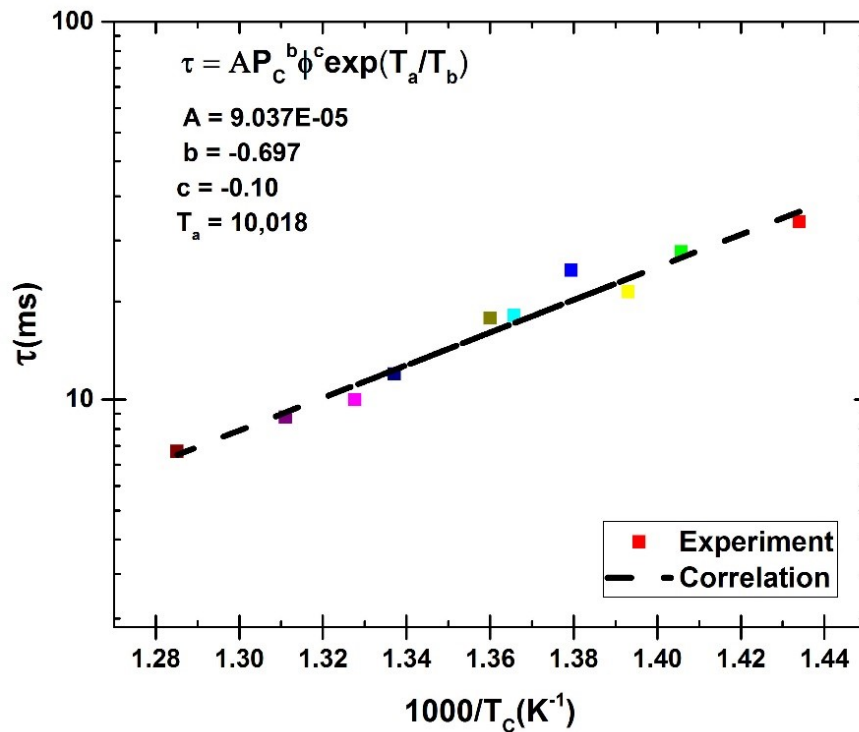
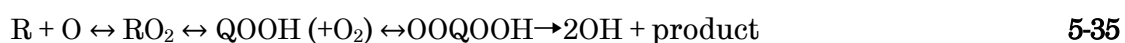


Figure 5-10: Global Correlation for Jet A-1 (FST-265638) Aviation Fuel.

5.3.4 Comparison of Experiment with Literature

There has been a previous experimental study on Jet A-1 and JP-8 autoignition [2, 259, 260]. This work complements the existing data in the low to intermediate temperature range. The figure 5-11, shows the comparison of the current RCM with other RCMs and shock tube at various EOC pressure at 5,7, 20 and 22 bar, at $\phi = 1.0$ with an oxidizer to fuel ratio of 14.6. Slight variations in different test rigs make it difficult to compare experimental data sets, but it is more useful to analyse the overall data set existing within the data to judge its consistency. The plot displays two compressed gas pressure of 6 and 10 bar at stoichiometric conditions with other works. An error data from De Toni et al.[259] was used to access the rig. The ignition data from the present rig was found within the error bar of De Toni experiment and slightly a bit above De Toni error bar. A slight deviation was expected, because the data collected from the current rig was point data rather than averagely computed data. Secondly, the approach in fuelling the rig could have been another possible cause of deviated results. Errors in measuring fuel/air mixtures are imminent. The micro-syringe used in injecting the fuels may not be reliable as this could lead to fuels dropping at the side of the chamber in the process of injection, which affect the evaporation rate and homogenous mixture in the chamber. Presently, the rig is in its first stage of development automated apparatus like fuel injector and flow meter for the gas line have not yet been installed. Despite this, the results are consistent with other rigs shown, have a similar trend and have reliable data. However, from the plot in Figure 5-11, it indicates the current rig can have a reproducible results. Further results from the literature shows to have a two-stage ignition delay, which was not observed with the current rig at the condition studied. This could be because the present rig had not sufficiently explored a wider range of compressed gas temperature to capture the two stage ignition in the low temperature regime. Moreover, combustion characteristics are well known to be activated in the low-temperature regime. The Jet A fuels in literature ignite faster than the current study Jet A-1. This shows that different Jet fuels exhibit different ignition behaviour despite the fact that at very low temperature, the kinetic for paraffinic fuel is controlled by the low-temperature chain branching:



This reaction pathway is driven by the $R + O_2 \leftrightarrow RO_2$ equilibrium and also the rate of isomerization $RO_2 \leftrightarrow QOOH$, and the ignition delay of jet fuel could be attributed to variation in the concentration of the n-paraffins, cyclo-paraffins, iso-paraffins and the aromatic content[261]. The reactivity of Jet fuels is driven by the n-paraffins. From literature Dooley et al.[2] and Casey et al.[262] used similar Jet A fuel (POSF 4658) in their RCMs experiment, which shows that their fuel composition n-paraffin has a higher value of 38.6% as recorded from the GC-MS analysis. Judging from the plot in Figure 5-11, where a higher reactivity is observed than the present rig, this could be because of the higher percentage of their n-paraffins than the Jet A-1 fuel used in the present rig, which has 19.25% n-paraffins. Dooley

et al.[2] shows to exhibit a faster ignition than the current study while Casey et al.[262] ignition delay times reported second stage ignition delay time with an Arrhenius like-behaviour. The overall ignition delay time for De Toni et al.[259] is shown to have a weak pressure dependence of ignition delay while the shock tube (ST) data reported by Dooley et al.[2] demonstrated a strong pressure reliance on the ignition delay time.

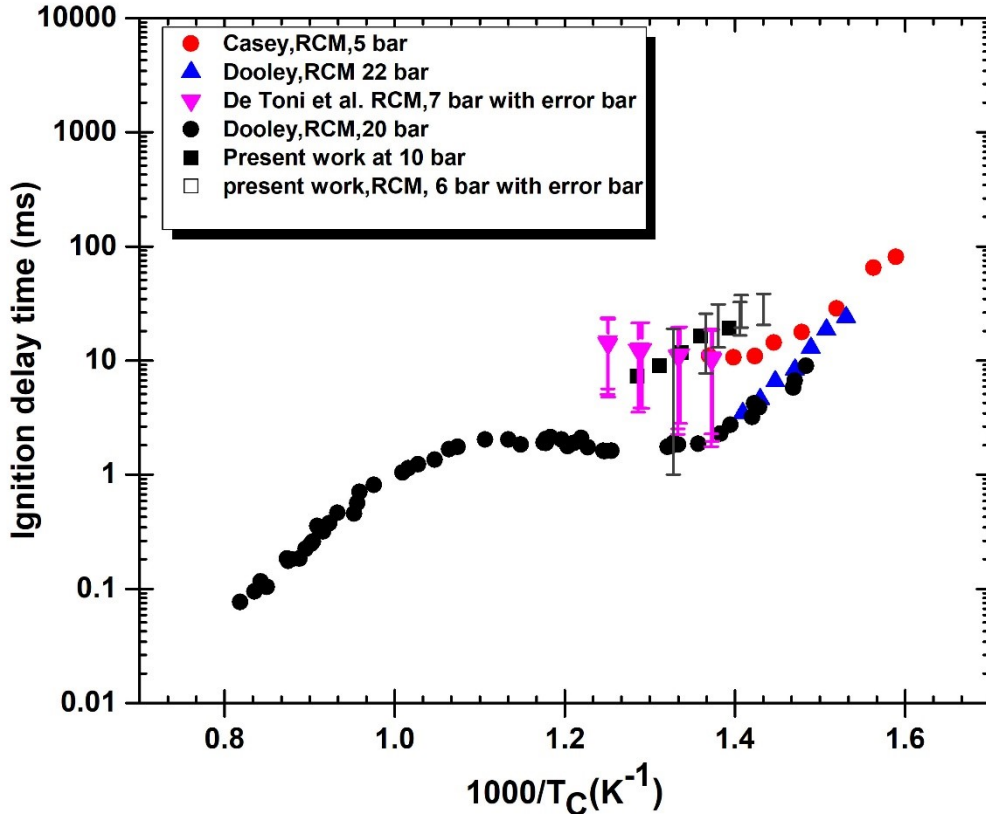


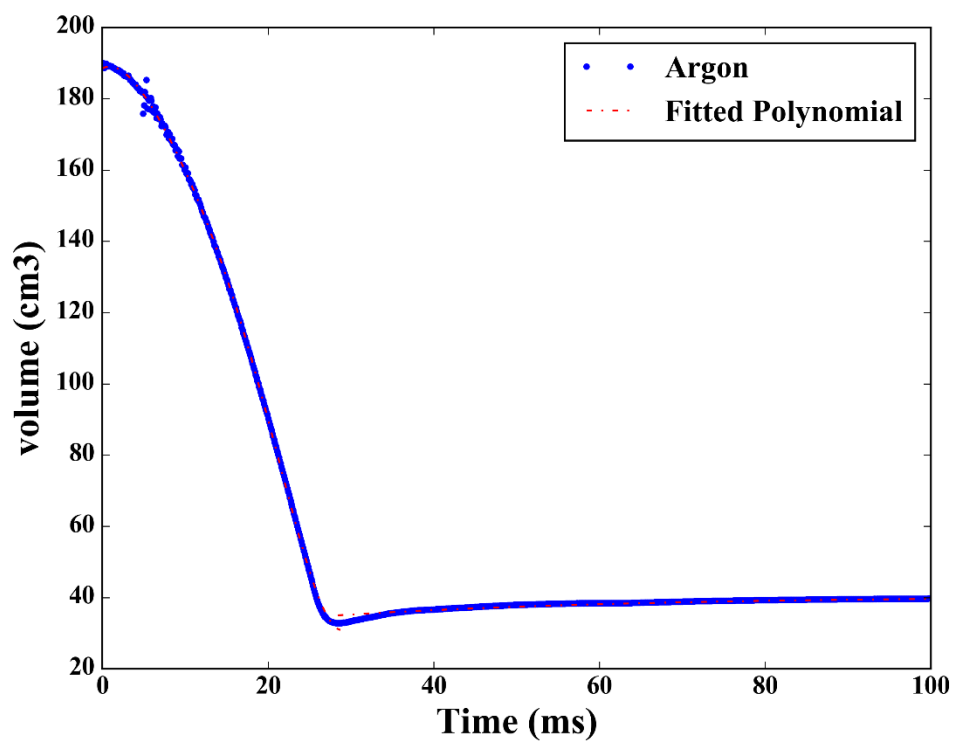
Figure 5-11: Experimental comparison current rig data with literature for Jet Fuel.

5.3.5 Numerical Modelling: Model Comparison with Experiment

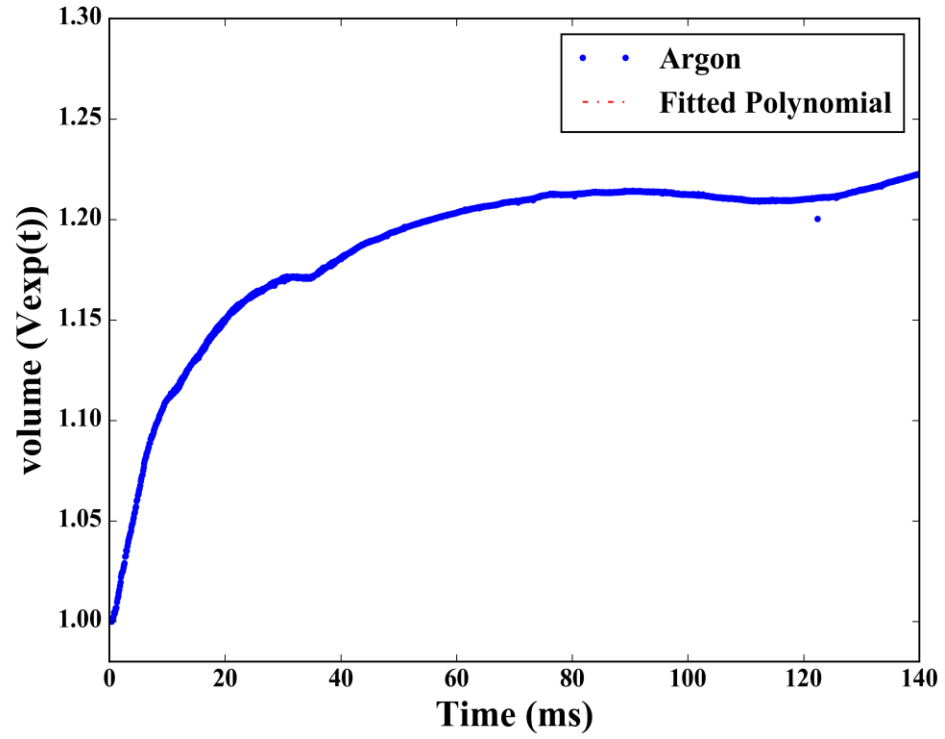
The effective volume, V_{eff} , is the geometrical volume of the combustion chamber including the dead volumes due to the ports and pressure transducer. The effective volume during the post-compression period was modelled as an adiabatic expansion process resulting to a time dependent volume expansion profile, V_{exp} . Polynomials were fitted to the effective volume during compression and post compression period as shown in figures 5-12(a) and 5-13(a). These fitted volume polynomials were used to provide the final expansion trace, which serves as an input data for the heat loss parameter in the simulation. The volume expansion rate for argon and nitrogen gases were different because of the specific heat value. Argon has a higher thermal conductivity than nitrogen so argon losses more heat than nitrogen at the end of compression as Figure 5-14, shows the comparison between the experimental data (Red solid line) and the model (black line). There is a good agreement of the model with the experimental results at both compression and post compression stage.

The reactive experiment illustrates N-heptane oxidation in Figure 5-15. The experimental pressure trace (black solid and broken line) and model (coloured broken line) for a reactive mixture n-heptane mixture at the stoichiometric condition. Before any reactive test is

carried out, a non-reactive test with the same mixture heat capacity is run to mimic the reactive test at post compression stage, which is used to facilitate the heat transfer model. The Skeletal Kinetic mechanism of n-heptane oxidation is taken from loun, et al.[263]. From the plot, the experimental pressure trace shows a perfect match with the model at compression and post compression. However, regarding ignition delay time the model predicted a longer ignition delay of about 61ms almost three times of the experiment ignition delay. This was expected, as more validation of the test would be required to help improve the mechanism further. Due to the time constraint of this work, the detailed experiment was not carried out on N-heptane combustion besides the work was mainly focussing on higher hydrocarbon fuels that the present rig was designed for. The essence of N-heptane model was to show the agreement of the model with an experiment in matching the pressure trace at compression and post compression stage and estimating the end of compressed temperature.

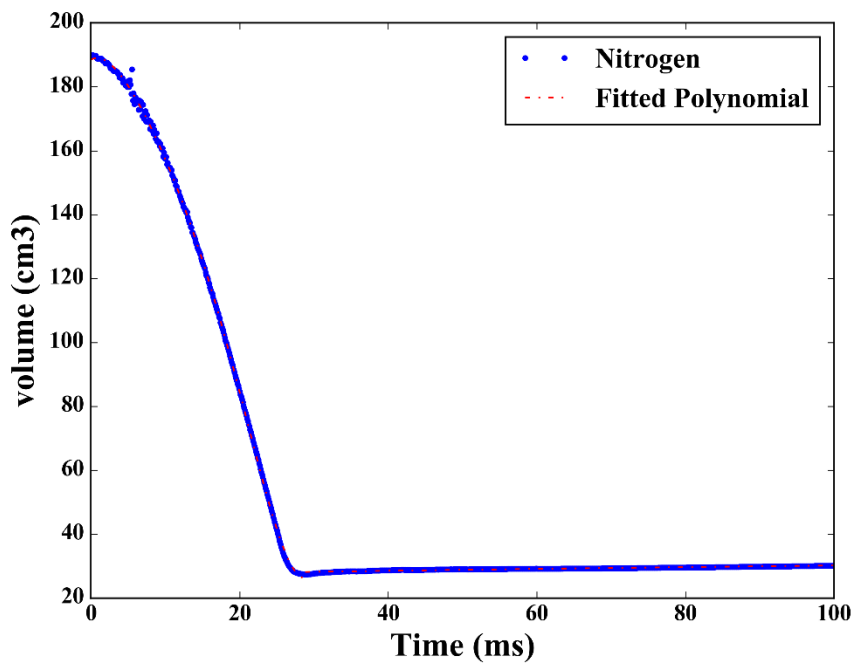


(a)

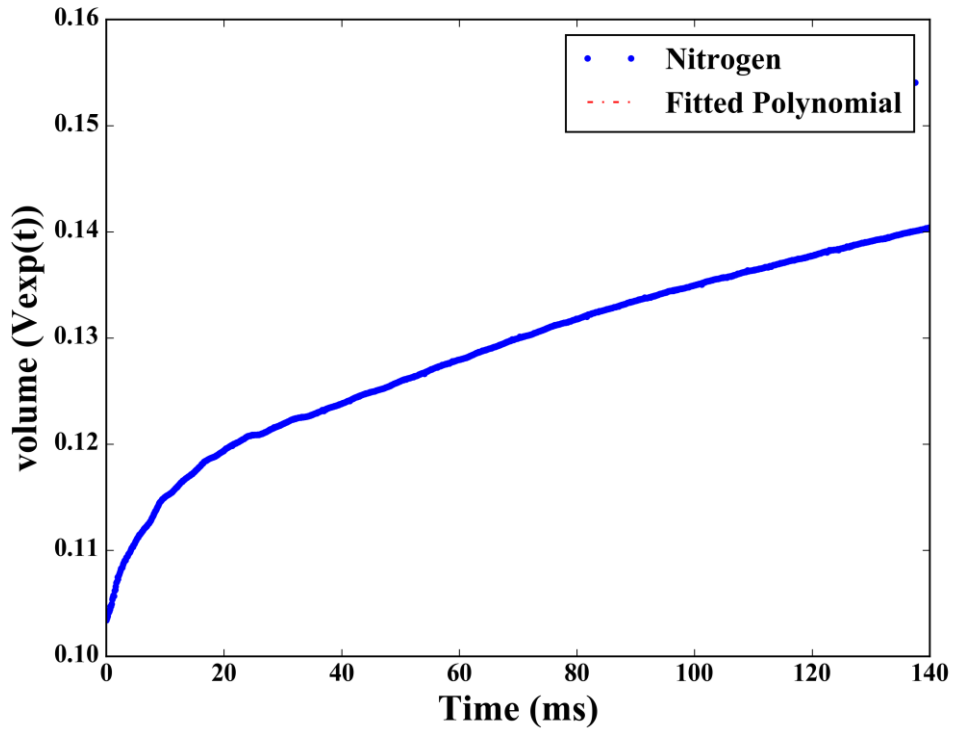


(b)

Figure 5-12: shows the (a).Effective Volume profile as a function of time and (b),the volume expansion trace for Argon non-reactive modelling. Red broken lines – indicate the high degree polynomial fit to the data. The blue line – effective volume profile.



(a)



(b)

Figure 5-13: shows the (a).Effective Volume profile as a function of time and (b).the volume expansion trace for Nitrogen non-reactive modelling. Red broken lines – indicate the high degree polynomial fit to the data. The blue line – effective volume profile.

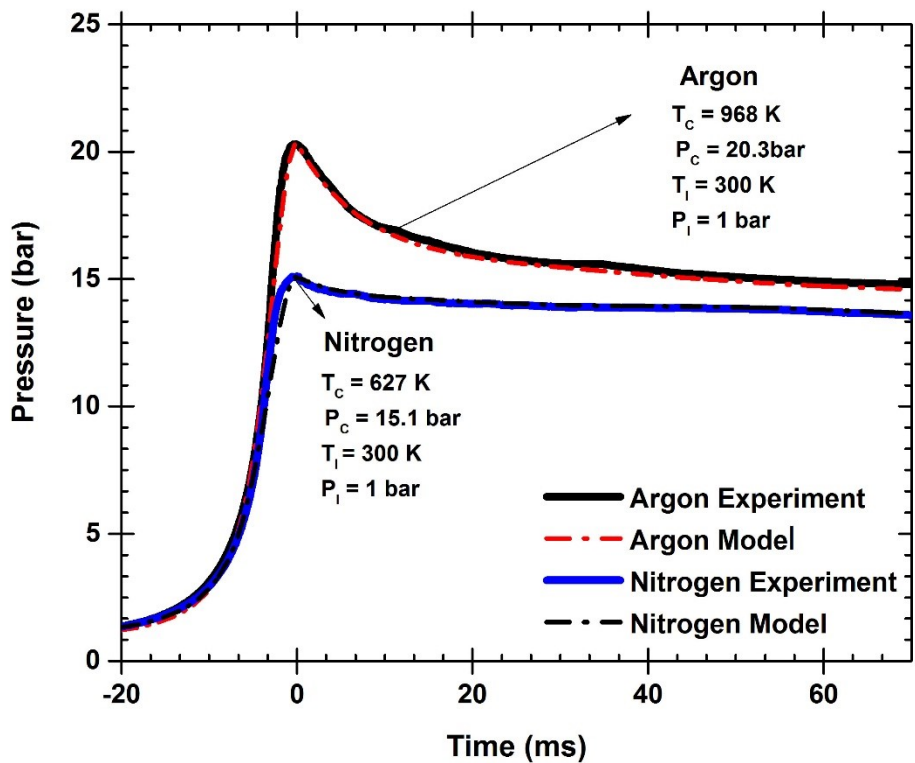
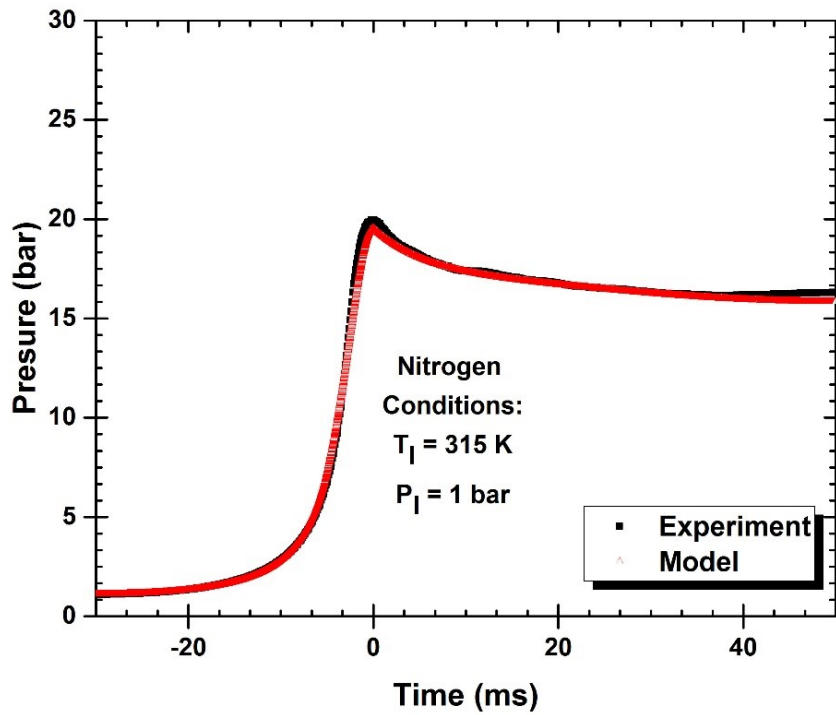
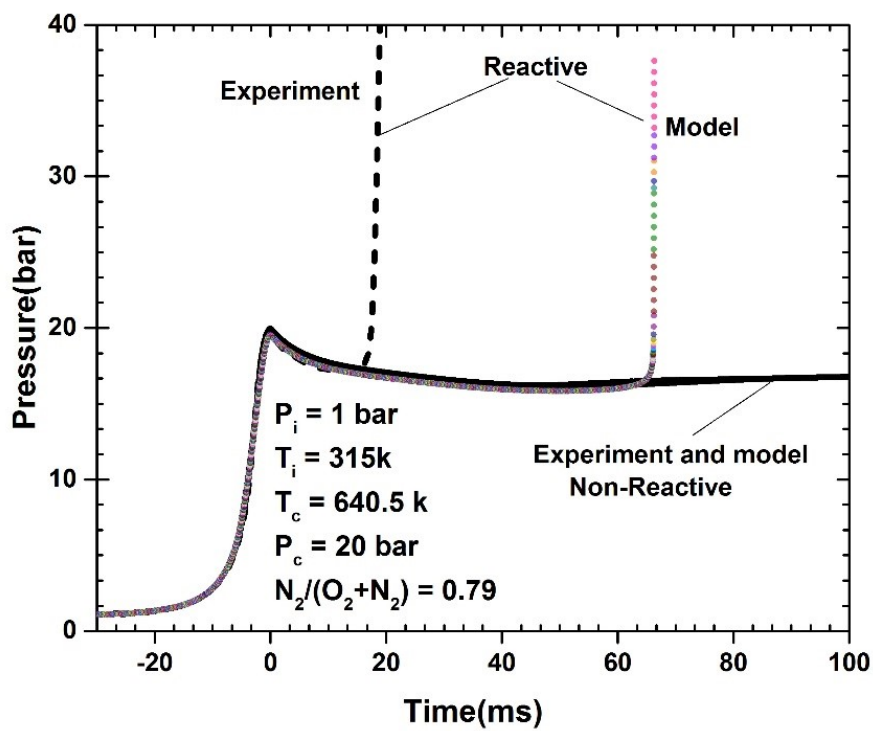


Figure 5-14: Non-reactive model comparison with experimental pressure traces. Initial conditions: argon –: $P_i = 1$ bar, $T_i = 300$ K. Coloured line – experimental pressure. Black line – model prediction.



(a)



(b)

Figure 5-15: (a) non reactive test with Cantera model (b) Comparison of model with experimental pressure profile for a reactive n-Heptane mixture at stoichiometric. Molar composition: $n\text{-C}_6\text{H}_{14}/\text{O}_2/\text{N}_2 = 1/11/41.36$. Initial conditions: $P_i = 1.0$ bar, $T_i = 315$ K. Solid and broken black line – experiment.

5.3.5.1 Kinetic Mechanism Selection and Modelling.

The current aviation fuel formulation earlier stated in section 2.4 of this work has its formulation as 19.35% n-paraffin, 20.57% iso-paraffin, 40.79% cyclo-paraffin, 15.55% Alkyl Monoaromatics and 3.7% Cyclic Monoaromatics by weight.

The molecular formula $C_{11.89}H_{22.89}$, Av the erage mmolecular weight of 166g/mol, H/C 1.9 and DCN 43.74. The jet A-1 autoignition delay times were compared the two surrogate mixture model from Honnet et al.,[3] (the 'Aachen' mixture) and the second generation of Dooley et al.,[2].

These 2nd generation models have successfully emulated the Jet-A POSF 4658 fuel and JP-8 POSF 5699 fuels and surrogates[2]. The Aachen surrogate was developed by Honnet et al.,[3] and has a composition of 80% n-decane and 20% 1,2,4-trimethylbenzene by volume, and by weight (77.2 and 22.8% molar basis, respectively). This mechanism was designed using previously developed chemical-kinetic models which have components of n-decane and 1, 2, 4-trimethylbenzene. The n-decane mechanism was formulated by Bikas and Peters [264] and validated against experimental data from ST[265] and JSR[160].

5.3.5.2 Comparison of Experiment with Model.

The simulations of the Jet A-1 experiments were carried out using Cantera incorporating the heat loss parameter during the compression stroke by adding an empirically determined effective volume. Also, the heat loss after the end of compression was accounted by 'adiabatic core expansion' approach. The comparison is made for 6 bar, the molar ratio of $O_2 : N_2 = 1 : 3.76$ at $\phi = 0.75$ and 1.0 in the temperature range of 727-771 K. In figure 5-16, both surrogate mixtures show a two-stage ignition delay time, which is an indicative of low-temperature chemistry. When considering both surrogate mixtures, their first stage ignition delay time was in agreement. The first stage ignition had a reduction in the ignition delay with an increase in temperature. The Dooley mixture showed NTC behaviour. There was no NTC behaviour observed in Aachen mixture. The model seems to be more reactive than the experiment predicting a less ignition delay time than the experiment.

In figure 5-17, with an increased fuel concentration at an equivalence ratio of 1.0, the overall ignition showed a decrease in their ignition delay time for both mixtures, and they experience a similar trend no NTC was observed. The model ignition delay time seems to more reactive at $\phi = 0.75$ than an experiment. The effect of equivalence ratio on the ignition delay is quite clear while maintaining the oxygen concentration constant increasing the fuel concentration increased the reactivity in the temperature range investigated. It revealed from the study that similar ignition delays at low temperature occur as the fuel concentration increased.

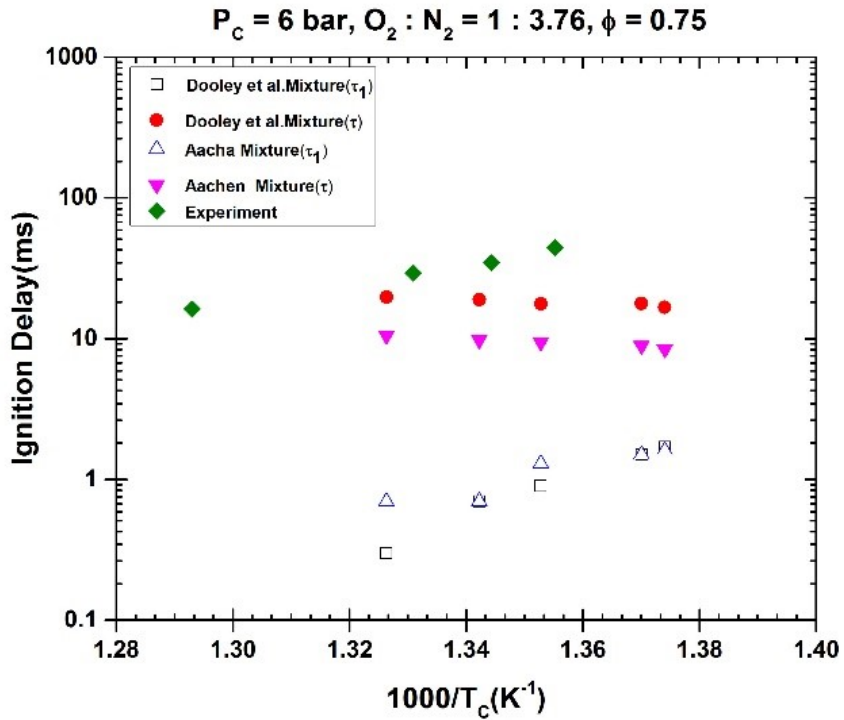


Figure 5-16: Comparison of Model with Experiment at 6 bar at EOC pressure at 6 bar, $\phi = 0.75$. Molar ratio: $O_2:N_2 = 1:3.76$. Green colour fill-Experiment, red colour and rectangle unfilled -Dooley mixture indicating 1st stage and total IDT. Aachen mixture-triangle is indicating 1st stage and total IDT.

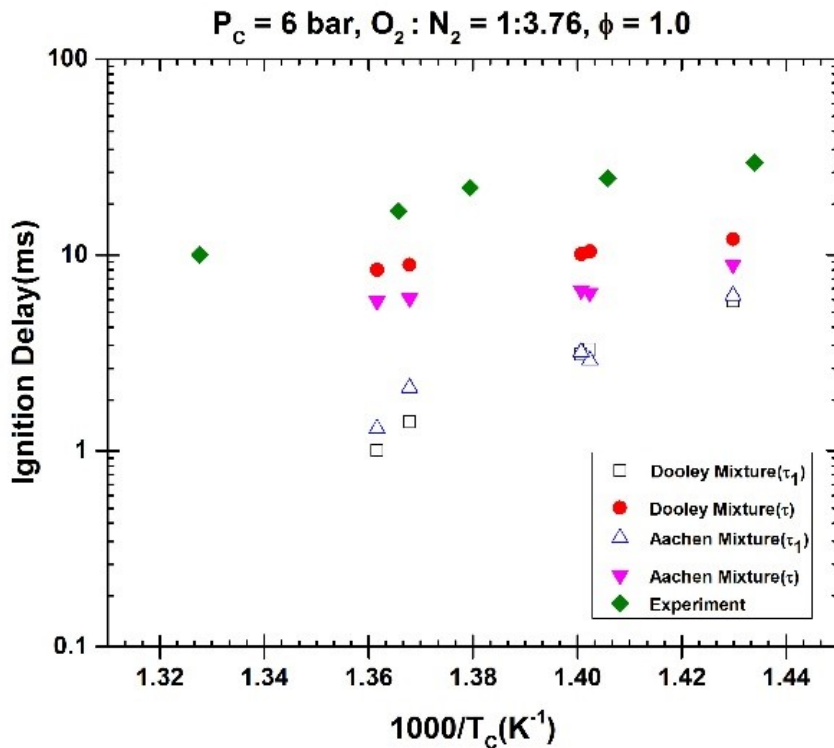


Figure 5-17: Comparison of Model with Experiment at 6 bar at EOC pressure at 6 bar, $\phi = 1.0$. Molar ratio: $O_2:N_2 = 1:3.76$. Green colour fill-Experiment, red colour and rectangle unfilled -Dooley mixture indicating 1st stage and total IDT. Aachen mixture-triangle is indicating 1st stage and total IDT.

5.4 Conclusion.

The performance of the rig was ascertained by the characterisation of the present rig conducting a non-reactive using nitrogen and argon gases and a reactive test using light hydrocarbon fuel (heptane) and heavy hydrocarbon fuel Jet A-1. The compressed temperature was computed numerical using Cantera. A heat loss term was incorporated into the modelling before and after the compression accounted for by adiabatic core expansion approach. A repeatability test was conducted for the non-reactive experiment; demonstrating that the pressure trace was consistent over the operating range. The maximum peak pressure of the rig was 20 bar, and a corresponding estimated peak temperature of 960 K.

Reactive tests using heptane and Jet A-1 at the stoichiometric condition were performed. The ignition delay time measurement shows to be repeatable. In addition, combustion modelling using Cantera and incorporating the heat loss term. The model predicted an increase of about 68% ignition delay longer than the experimental data for heptane/air combustion.

The ignition delay of Jet A-1/air oxidation was measured at 6, and 10 bar, $\phi = 0.75$ and 1.0 over a temperature range of 697 – 781 K. A study on the influence of pressure, temperature, and equivalence ratio was carried out. It was found that an increase in the pressure, temperature or increase in equivalence ratio could result in a reduction in the measured ignition delay time. The uncertainty in the ignition delay time, compressed gas temperature and the pressure was also considered for Jet A-1 and heptane fuel.

The present experimental rig has been characterised and was found capable of providing experimental ignition delay times for heavy hydrocarbon fuels.

Chapter 6. Autoignition Study of Banner-Solvent in RCM.

6.1 Introduction

To meet the demands of the growing population and industrial gas companies developer in term of energy usage and assurance of having a steady supply of fuels to respond to their needs. This has propelled the needs to explore more into the combustion properties of new generation fuels to updating the existing archives on the chemical and physical properties of this new generation fuel for onward certification and approval. Before any fuel final gets to the stage of approval, it has passed through rigorous testing before being certificated. Banner Solvent has been classified as a new first generation synthetic fuel because of its good potential as a fuel, if carefully examined and investigated. They need to be proven technically and commercially viable fuel options, which could be a market in certain part of in the next century. Banner Solvent consists of five component of hydrocarbon mainly n-paraffinic. They are linear alkanes such as n-decane, n-dodecane, n-undecane, Tridecane and tetradecane. They are considered as a representative class of hydrocarbon existing in surrogate aviation fuels.

6.2 Experimental Procedures

All gases used in the experiments as a reactant is of purity: O₂: 99.993%, N₂: 99.999%, Ar: 99.995% was obtained from BOC and Banner fuel from Banner Company, UK. The procedures for the Banner solvent are as follows. Before initiating any runs, the reactor chamber is vacuum using BOC Edward E2-M12 vacuum pump, and the fuel and air composition are prepared based on the molar composition before charging the chamber. In this first phase of the Shef-RCM design, the gas lines set up are omitted because of time constraint rather the charging of the reactor chamber is manually done. Therefore, gases mixtures (pure oxygen, nitrogen and argon) are stored in a Teflon FEP gas sampling bags with a capacity approximately 600 ml. The required composition is extracted using a 60ml syringe for the gas and a 50ml micro-syringe for the fuel. Fuel/air mixture introduced into the heated combustion chamber from the inlet port located at the rear of the reactor chamber through a septum and allowed to homogenise for about one and half hour. For this experiment, four and five bar driving pressure is used behind the driving section to propel the reactor piston then actuated by the release of the PPRM, which releases the piston to compresses the fuel-air mixture ahead of the piston to an elevated pressure and temperature. The recording of the events and the pressure trace are logs onto the LabVIEW. The piston is retracted to its initial position (BDC) then flushing of the chamber with pressurising air for 5 minutes. The reactor chamber and the micro syringe are clean with propanol solution then the chamber is flushed again with pressurise air and finally vacuum making it ready for the next chamber charging.

Table 6-1: Mixture composition for Banner solvent experiment.

Mixture #	Mole Fractions				Equivalence Ratio	EOC Pressure
	Banner Solvent	O_2	N_2	Ar	ϕ	P_c Approximately
1	0.005928	0.2088	0.7853	0	0.5	6,10
2	0.008866	0.2081	0.783	0	0.75	6,10
3	0.011786	0.2075	0.7807	0	1	6
4	0.005928	0.2088	0.5891	0.1964	0.5	6
5	0.008866	0.2081	0.5874	0.1958	0.75	6
6	0.011786	0.2075	0.5857	0.1952	1	6
7	0.005928	0.2088	0.3927	0.3927	0.5	6
8	0.008866	0.2081	0.3927	0.3927	0.75	6
9	0.011784	0.2075	0.3927	0.3927	1	6

6.3 Experimental Repeatability of Banner Solvent

Figure 6-1, shows the repeatability test of Banner Solvent conducted at an equivalence ratio of $\phi = 0.5$ at dilution molar ratio of $N_2/(O_2 + N_2) = 0.79$. A total of five different runs were made of the same condition was performed at 6 bar compressed gas pressure and initial temperature of 393 K. The pressure trace was seen to overlap each other showing to have a repeatable result. The uncertainty was also considered, the uncertainty in the compressed gas pressure was 5.87 ± 0.1 bar, the ignition delay time recorded 7.72 ± 0.3 ms and the compressed gas temperature is 760.3 ± 10 K.

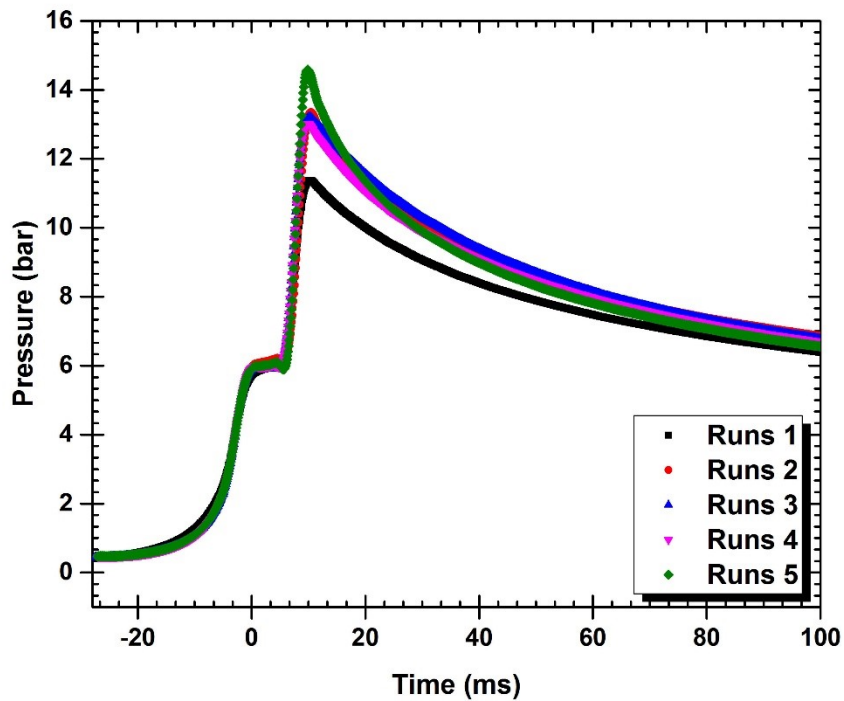


Figure 6-1: Experimental repeatability for Banner Solvent at a compressed gas pressure of 6 bar.

6.4 Experimental Results

The combustion of Banner-Solvent in air mixture is measured over a compressed gas temperature range of 722 - 836 K, at pressures of 6 and 10 bar, and for equivalence ratios of 0.5, 0.75, and 1.0. The charge is prepared in a synthetic dry air, 21%O₂ and 78% N₂. The compressed gas temperature and pressures are obtained by varying the initial temperature and pressure and maintaining a compression ratio 8.8. The initial temperature for the experiment ranges of 115 - 135 °C, this temperature range was chosen to ensure complete vaporisation of the fuel as early investigated by Casy[105]. Table 6-1 shows, the composition of Banner solvent mixtures used in this work.

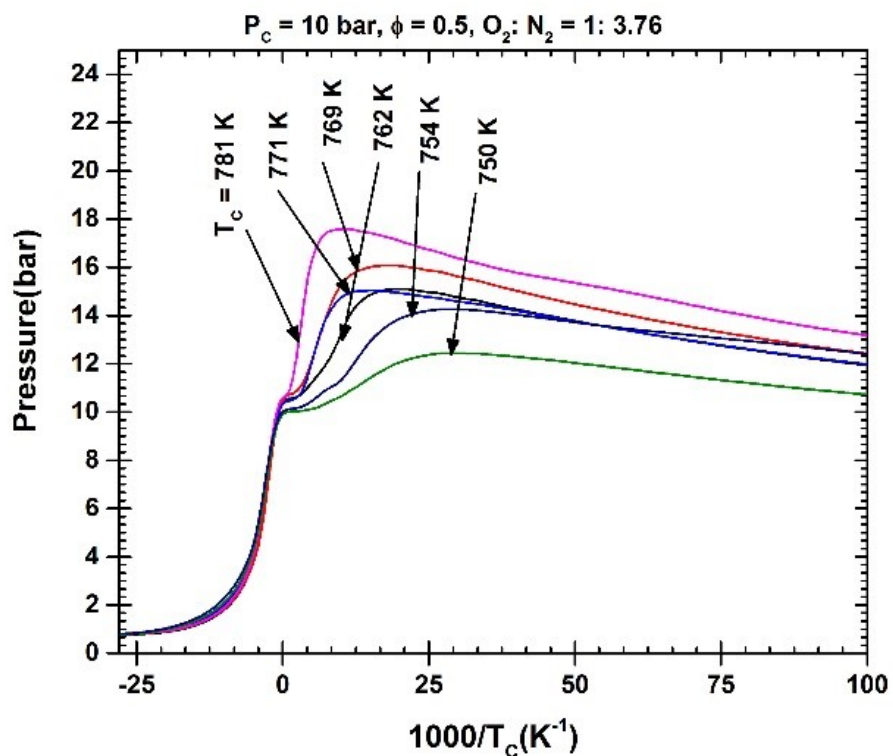
The mass of fuel, oxidizer ratio and equivalence ratio are specified by determining the mixture composition. To meter the right proportion of air-fuel mixture the estimated volume is required, which has been discussed in section 3.3.1. The mixture compositions are varied by changing the composition of the diluent gas (N₂ and Ar ratio) in the reacting mixture and altering the dilute composition to get the desired temperature at the end of the stroke. The initial temperature of the chamber ranges from a minimum temperature of 115 K to a maximum of 135 K.

6.4.1 Influence of temperature on Banner-Solvent ignition delay time.

Figure 6-2, clearly shows the influence of temperature on the ignition delay time for Banner-Solvent at a compressed gas pressure of 6 and 10 bar, $\phi = 0.5$ in an oxidizer consisting of $O_2 : N_2 = 1 : 3.76$ and at compressed gas temperature of 749 – 781 K.

Figure 6-2(a) shows the pressure trace as a function of time and the time 0 corresponds to the end of compression. The figure shows at 10 bar, the experimental pressure trace decreases in ignition delay as the EOC temperature is increased. At 754 K a weak two-stage ignition delay was slightly observed, an indicative of a low-temperature chemistry.

Figure 6-2 (b) shows the ignition delay time as a function of temperature. The ignition delay clearly displayed an Arrhenius-like temperature dependence with no NTC behaviour. In Figure 6-3 (a) shows, the pressure trace as a function of time and compressed gas temperature ranges from 745 – 799 K. At 6 bar, there was an indication of NTC at about 747 K, increasing compressed temperature with corresponding increase in ignition delay times but this has to be investigated with more experiments.



(a)

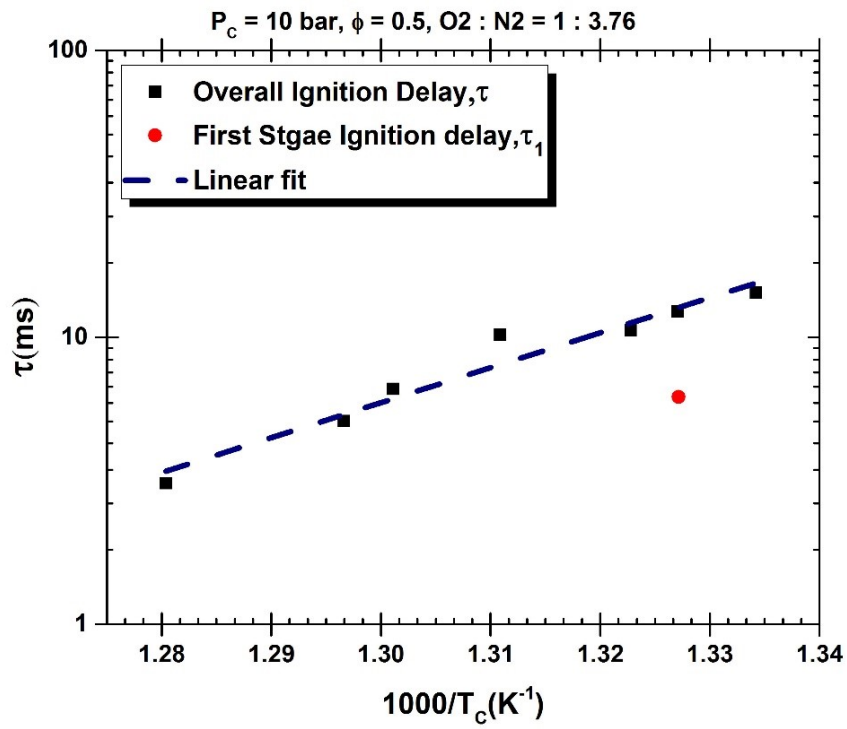
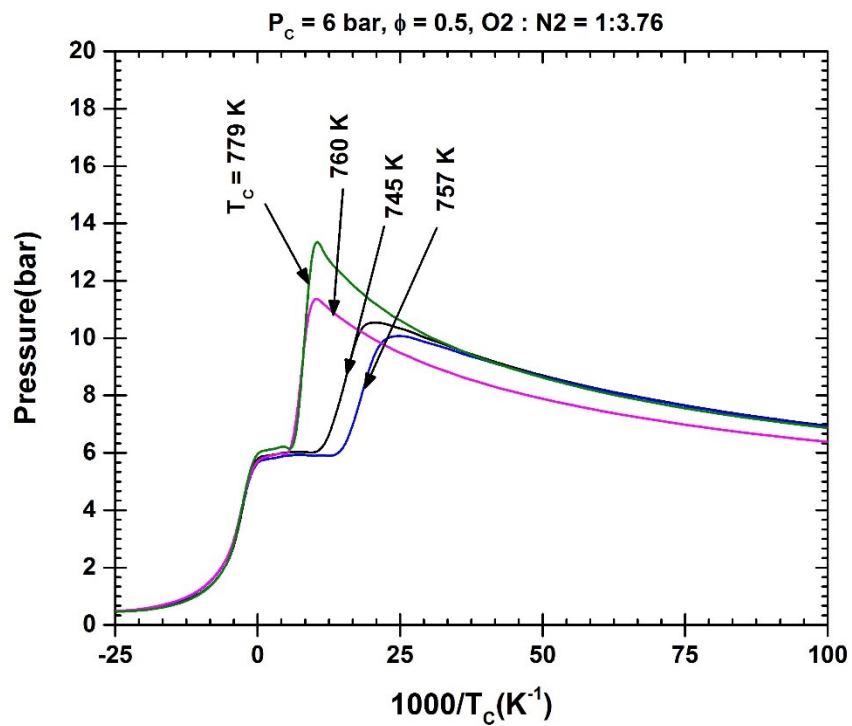
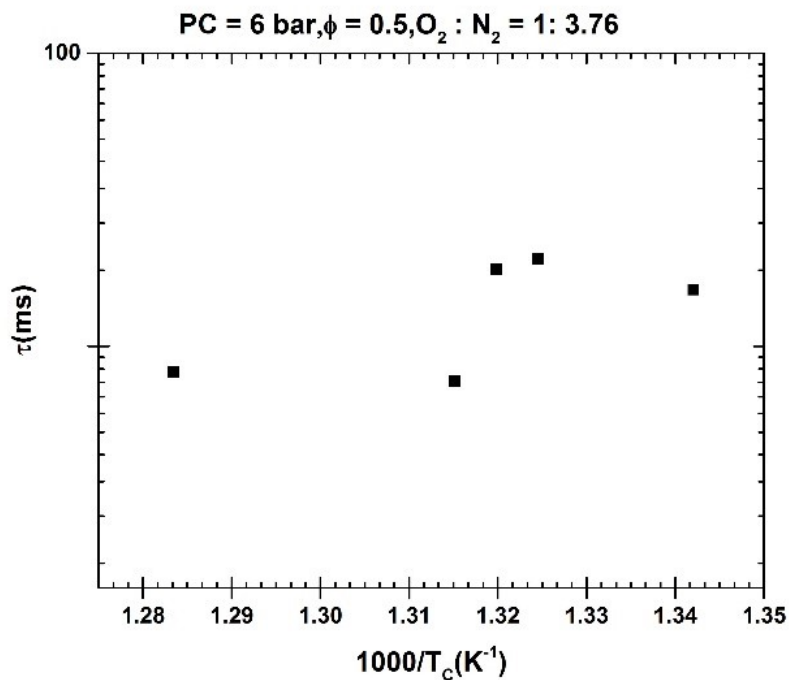


Figure 6-2: Influence of temperature on ignition delay time at 10 bar, $\phi = 0.5$, Molar ratio: $O_2:N_2 = 1: 3.76$ (a) experimental pressure trace (b) ignition delay time as a function of temperature.





(b)

Figure 6-3: Influence of temperature on ignition delay time at 6 bar, $\phi = 0.5$, Molar ratio: $O_2:N_2 = 1: 3.76$ (a) experimental pressure trace (b) ignition delay time as a function of temperature.

6.4.2 Influence of Equivalence ratio on Banner-Solvent ignition delay time.

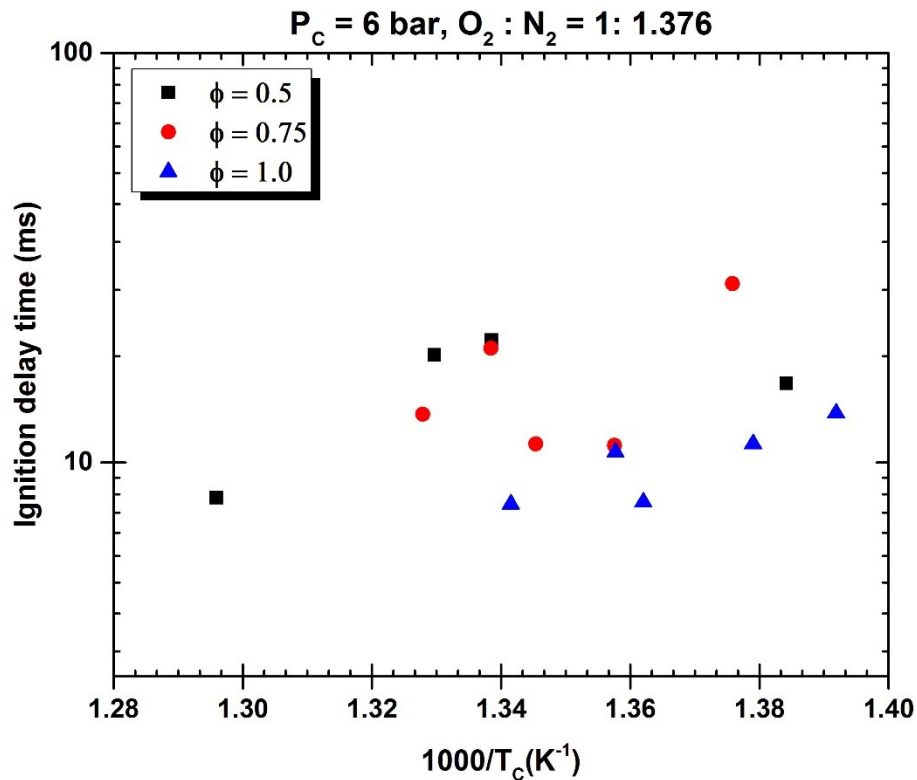
The experimental result for Banner solvent is shown in figure 6-4. It was investigated by varying equivalence ratio at $0.5 < \phi < 1.0$, the compressed gas pressure of 6 and 10 bar and varying diluent molar ratios to alter the peak temperature.

In Figure 6-4(a) the compressed gas temperature ranges from 718 – 772 K and pressure of 6 bar. It showed that at $\phi = 0.5$ and 0.75, there were some traces of NTC behaviour observed with increasing ignition delay times at varying compressed gas temperature. Increasing the equivalent ratio from 0.5 to 0.75 there was a slight reduction in the ignition delay time as shown in the plot. Further, increase in the equivalent ratio 1.0 lead to a further reduction in the equivalent ratio. At $\phi = 1.0$ Arrhenius-like temperature dependence behaviour with no NTC was predominant.

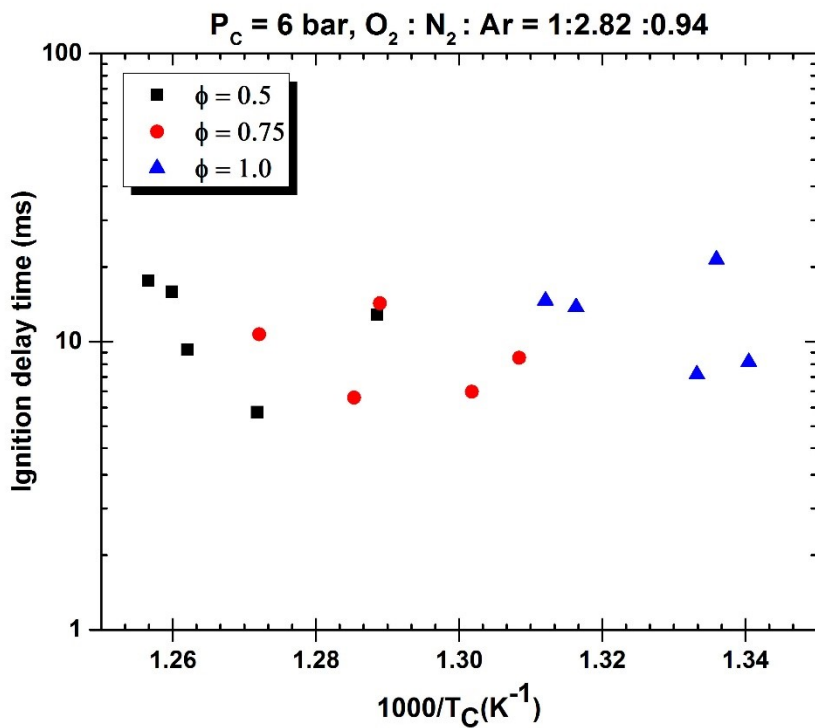
Figure 6-4(b) considered compressed gas temperature ranging from 746 – 796 K and pressure of 6 bar. It is evident that increase in the equivalence ratios lead to a reduction in the ignition delay and some traces of NTC was initiated. The Same behaviour was also observed in Figure 6-4(c).

A further test was conduction by varying the diluent gas mixture to obtain the varying end of gas temperature in the chamber. The gas temperature ranges from 718 – 916 K as shown in Figure 6-4(d). It is clear seen that within temperature range while varying $\phi = 0.5 - 1.0$, NTC behaviour was prominent and seen.

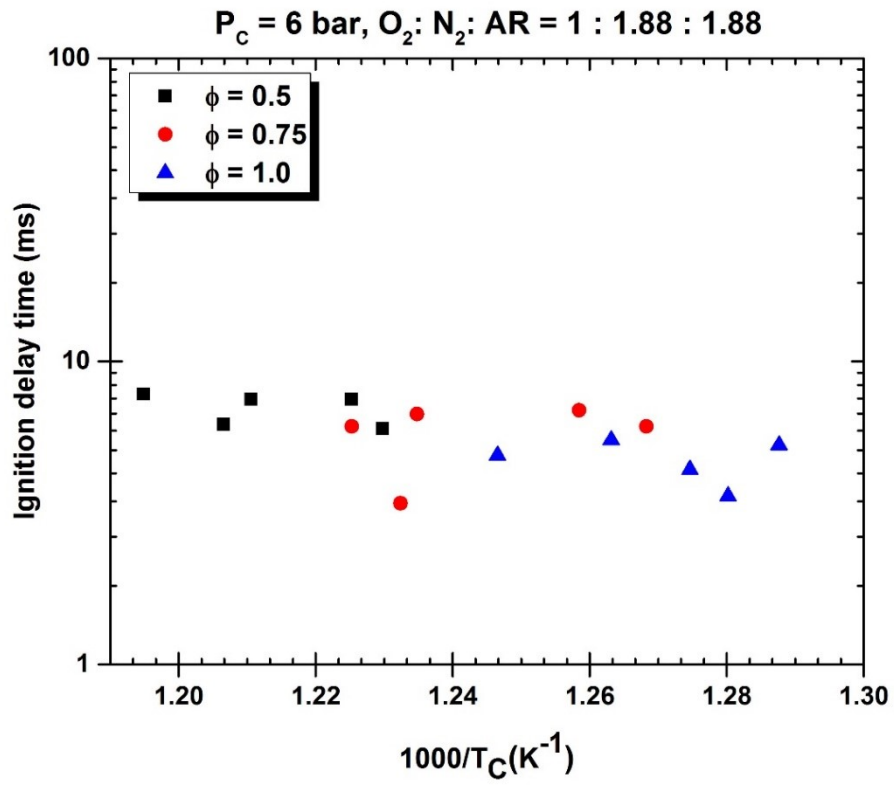
At a higher pressure of 10 bar and compressed gas temperature ranging from 733 – 812 K as shown in Figure 6-4(e) no NTC behaviour was seen but displayed an Arrhenius dependence on the temperature at the condition studied. Both experiments showed the influence of increasing fuel concentration with a reduction in the ignition delay time that is the faster the ignition process. Curran et al.[266] observed such trend in their study. Within the low to the intermediate regime, increasing the fuel concentration increases the alkylhydroperoxides radical's pools production that results in shorter ignition delay times. The build of the radical pool eventually drives the rapid reactions relating with the ignition.



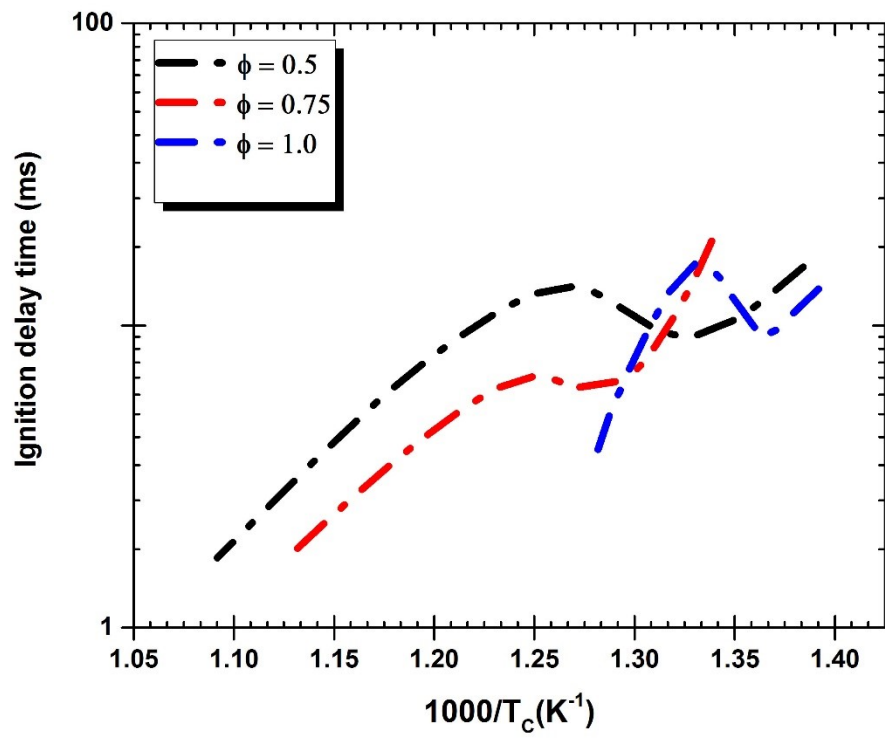
(a)



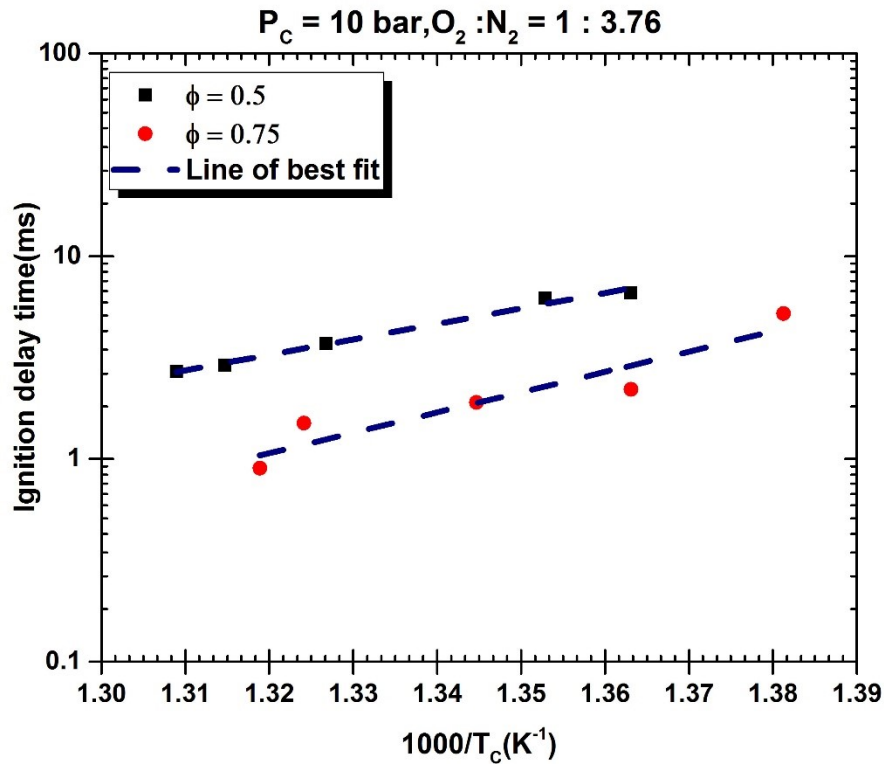
(b)



(c)



(d)



(e)

Figure 6-4: Experimentally measured ignition delay of Banner-Solvent at 6 bar with (a).Molar ratio: $O_2 : N_2 = 1 : 3.76$, (b). Diluent molar ratio: $O_2 : N_2 : Ar = 1 : 2.82 : 0.94$, (C). Diluent molar ratio: $O_2 : N_2 : Ar = 1 : 2.82 : 0.94$, (d) varying diluent molar ratio (e). at 10 bar Molar ratio: $O_2 : N_2 = 1 : 3.76$.

6.4.3 Influence of Pressure on combustion of Banner-Solvent

Figure 6-5, shows the ignition delays for the Banner-Solvent/air mixture at a compressed pressure of 6 and 10 bar, a temperature range of 722 – 781 K at $\phi = 0.5$ and molar ratio: $O_2 : N_2 = 1 : 1.376$. The ignition delay displayed an inverse dependence on the compressed gas pressure at 10 bar with no NTC behaviour. While 6 bar experiment clearly showed NTC behaviour with increasing compressed gas temperature. The decomposition of the alkyl hydroperoxyl radical ($QOOH$) and an oxygen addition reaction ($QOOH + O_2$) with ensuing chain branching. The reaction pathways are highly pressure-dependent and as the $QOOH$ decomposition, the pathways activate in the NTC region.

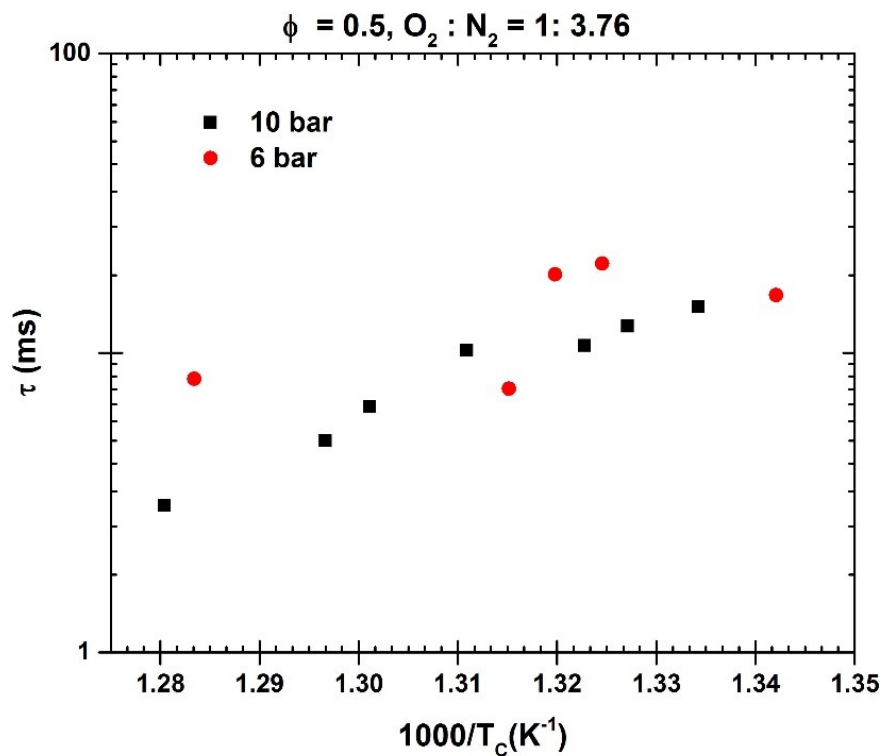
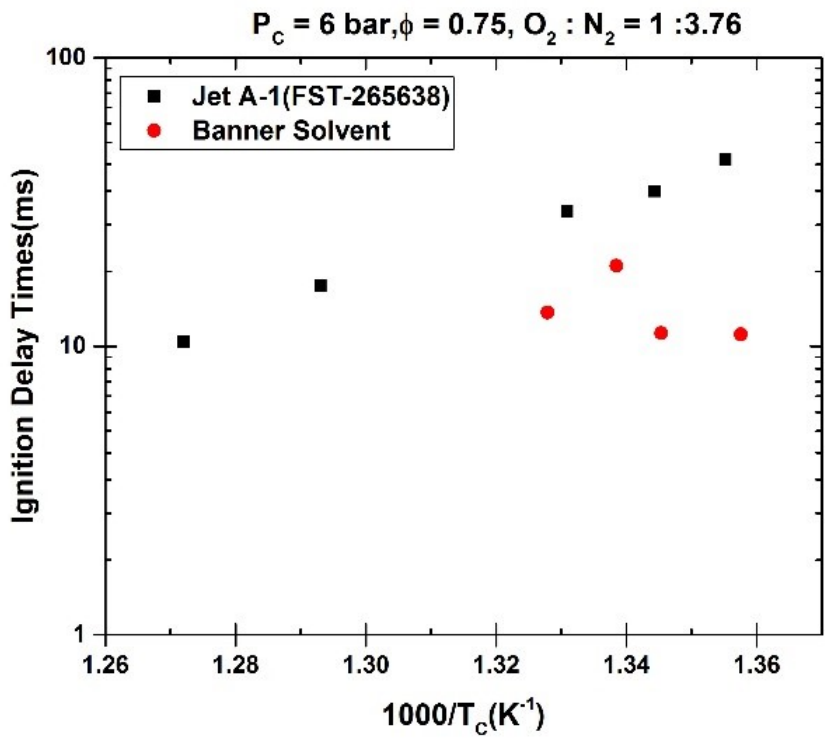


Figure 6-5: Influence of pressure on ignition delay time post compression pressure of 6 bar and 10 bar, $\phi = 0.5$, for Banner-Solvent/air mixture corresponding to $\phi = 0.5$, Molar ratio: $O_2 : N_2 = 1 : 1.376$.

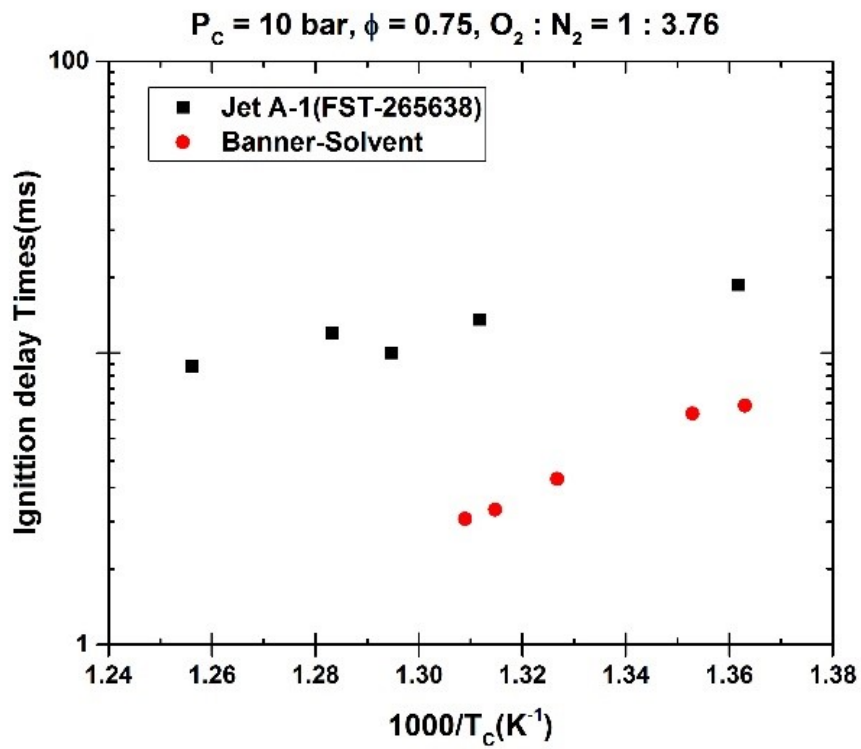
6.4.4 Comparison of Combustion of Jet A-1 with Banner-Solvent.

Comparison of Jet A-1 and Banner-Solvent, as illustrated in Figure 6-6, show a transition from low temperature to intermediate temperature ignition, with negative temperature coefficient (NTC), observed for 6 bar at varying compressed temperature (727 - 786 K) and $\phi = 0.5$.

The Banner-Solvent experiments showed traces of NTC behaviour at a temperature above 727 K. The solvent exhibited a shorter ignition delay times compare to Jet A-1. The reason is that the solvent is composed of purely n-paraffinic hydrocarbon that has high reactivity with potentially accelerated radical generation via the low-temperature chain branching mechanism. Because of n-paraffinic structure, they have a large number of secondary C-H bonds; these bonds maintain RO_2 stability and accelerated isomerization compare to the Jet A-1. However, from the formulation of the current Jet A-1, it has a higher content of cycloparaffin about 40.79% refer to section 2.5.1 for the precise formulation. The low-temperature ignition of cycloparaffin is less due to the formation and isomerization pathway. The cyclic and distribution of hydrogen reduces the hydrogen available to the (1,5)H-shift whereas holding enough hydrogen for the (1,4) H-shift in the isomerization of the peroxy radicals. At low-temperature regime, this results in a much lower reactivity and a larger olefin production[267], which directly lengthen the ignition delay time of the present Jet A-1 fuel.



(a)



(b)

Figure 6-6: Comparison of Jet A-1 with Banner-Solvent at(a),(b) 10 bar, $\phi = 0.5$. Molar ratio: $O_2 : N_2 = 1 : 3.76$.

6.5 Conclusion and Discussions

The ignition delay times have been measured for the lean and stoichiometric mixtures of Banner-Solvent with air ($\phi = 0.5, 0.75, 1.0$) at pressures of 6 and 10 bar while varying compressed temperature in the range of 718 – 916 K. The measurements are performed in a newly designed Shef-RCM at an initial heating temperature ranges of 115°C – 135 °C. The experimental data lie in the low to the intermediate regime. Closer examination of the combustion of Banner-Solvent shows that the ignition delay time was most dominated in the NTC region at a lower pressure of 6 bar. While at 10 bar an Arrhenius behaviour as a function of pressure and temperature was observed. At 754 K, a scanty two-stage ignition delay also found for 10 bar indicating a cold flame temperature, which diminishes as the compressed temperature, was increased.

The influence of increasing fuel concentration, temperature and pressure have shown on ignition delay of Banner-Solvent by a decrease in overall ignition delay times. Increasing fuel concentration and pressure increase the reactivity resulting in a shorter ignition delay times. When comparing the ignition delay times of Banner solvent with Jet A-1, it was seen that the Banner solvent is more reactivity than the Jet A-1, this difference was attributed the composition of Jet A-1, which has a higher content of cycloparaffin and aromatics. The low-temperature ignition of cycloparaffin is lower due to the formation and isomerization pathway. This attribute to the low reactivity and longer ignition delay time of Jet A-1. The present result provide combustion kinetic data for the validation and refinement of Banner-Solvent for kinetic mechanisms development.

Chapter 7. Autoignition Study of Used Cooking Oil (UCO-HEFA)

7.1 Experimental Conditions

An experimental investigation of UCO-HEFA/oxidizer mixtures was conducted in the range of low to intermediate temperature region with an equivalence ratios of $\phi = 0.5 - 1.0$, dilution molar composition of $N_2/(O_2 + N_2) = 0.79 - 0.90$, compressed gas pressures and temperature of $P_c = 6 - 10$ bar, and $T_c = 701-777$ K. The chamber was preheated to an elevated initial temperature, ranging from 115-135 K.

Table 7-1, shows the mixture composition for the experimental condition studied. The initial gas temperature is changed to vary the compressed gas temperature at the end of the stroke and to maintain a constant compression ratio of 8.8. Also investigated are the influences of varying equivalence ratios and oxygen concentrations.

Table 7-1: Mixture composition for UCO-HEFA ignition delay experiment

Mixture #	Molar Composition (%)			Equivalence Ratio	EOC Pressure
	UCO	O_2	N_2	ϕ	P_c Approximately
1	0.60	20.89	78.52	0.5	10
2	0.899	20.81	78.29	0.75	6,10
3	1.19	20.75	78.06	1.0	6,10
4	1.78	20.63	77.59	1.5	6
5	0.60	9.94	89.19	0.5	10
6	0.899	9.91	89.19	0.75	10
7	1.19	9.88	88.92	1.0	10

7.2 Experimental Repeatability

Figure 7-1, shows the repeatability test of Used cooking oil (UCO-HEFA) conducted at an equivalence ratio of 0.5 at dilution molar ratio of $N_2/(O_2 + N_2) = 0.79$. Five different experiments of the same condition were performed at 6 bar compressed gas pressure. The repeatability was similar with that obtained from Jet A-1.

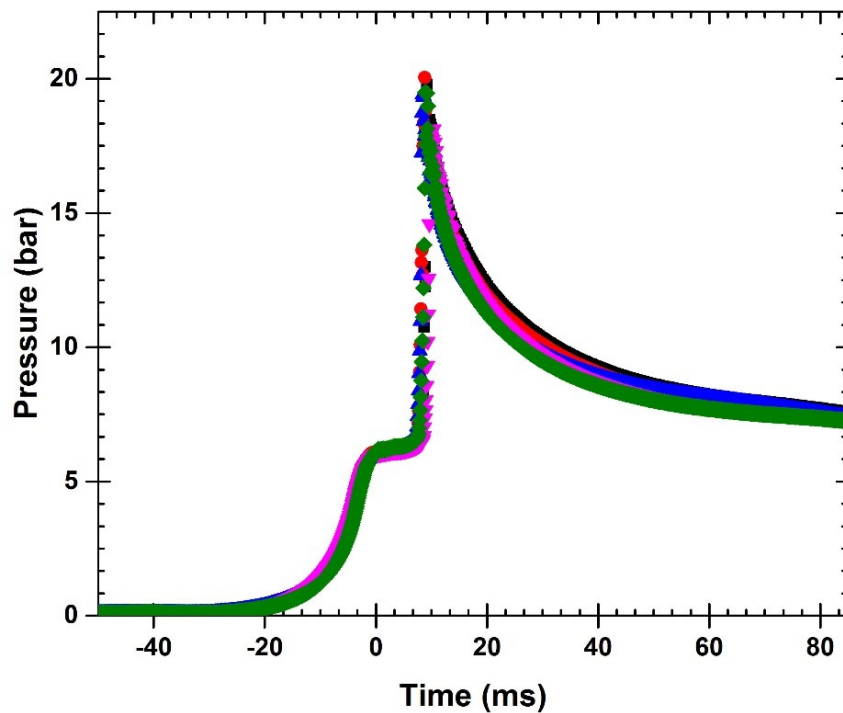


Figure 7-1: Experimental Repeatability of UCO-HEFA at 6 bar compressed pressure

7.3 Experimental Procedure.

The procedures for running UCO-HEFA in the present rig is similar to that mention in section 6.2.

7.3.1 Influence of compressed gas temperature on ignition delay times

Figure 7-2, shows the effect of compressed gas temperature on UCO-HEFA/air mixture at compressed gas pressure of 10 bar, $\phi = 0.5$. The oxidizer molar composition is described by $N_2/(O_2 + N_2)$, is fixed at 0.79. Figure 7-2(a) illustrates the pressure trace with varying T_C while Figure 7-2(b) shows the influence of compressed gas temperature on the ignition delay time of UCO. The effect of increasing the compressed gas temperature shows a reduction in the ignition delay time. No NTC region was observed with the temperature range at this condition.

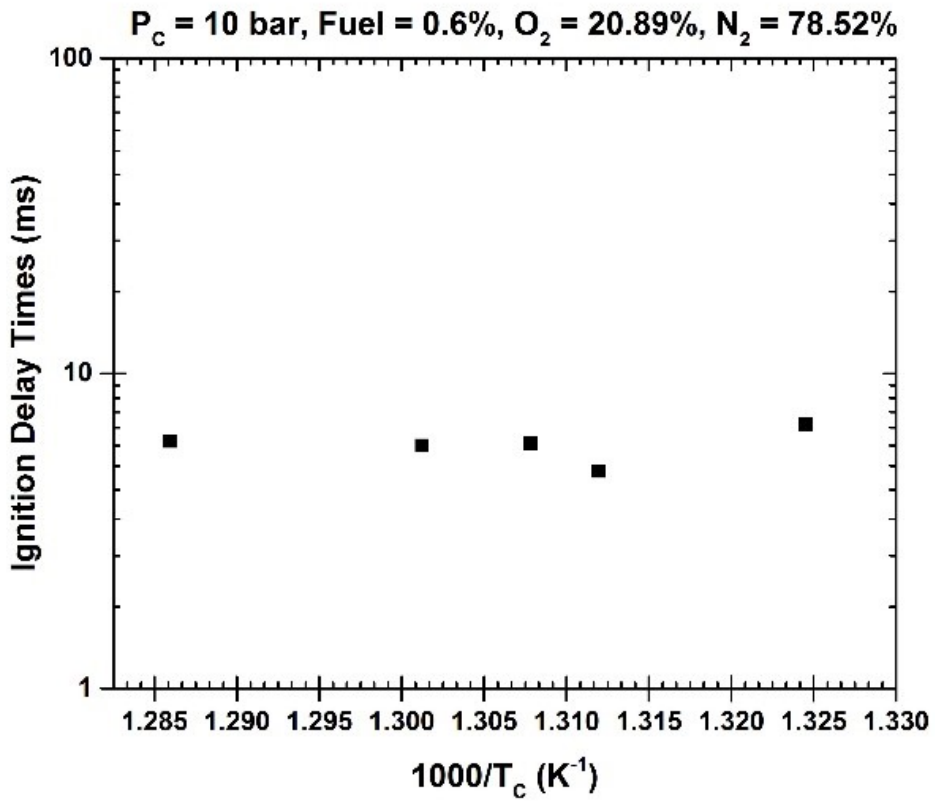
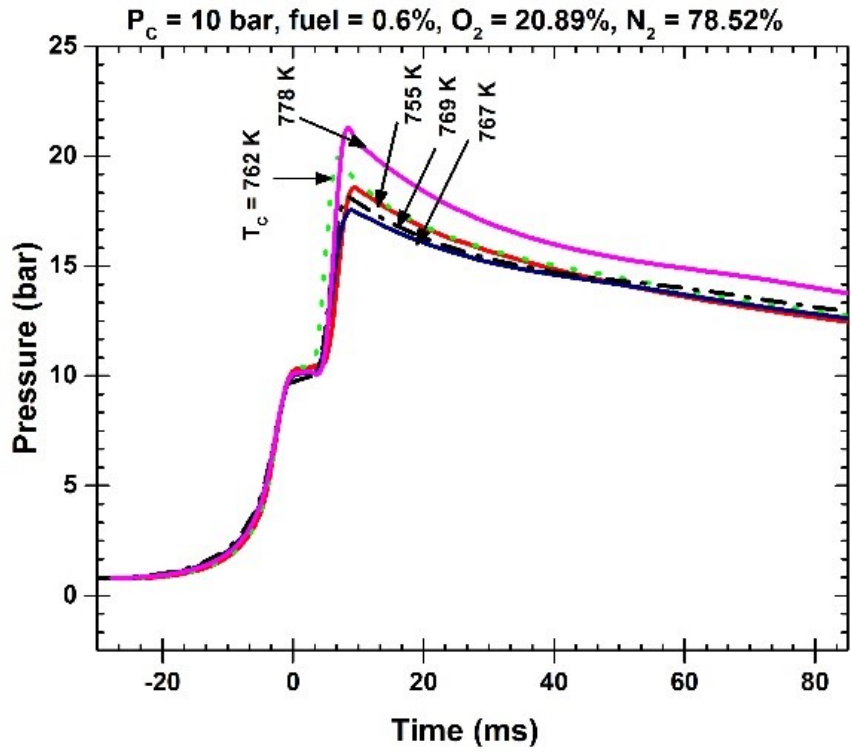


Figure 7-2: Influence of compressed gas temperature on ignition delay time of UCO at 10 bar, $\phi = 0.5$, Molar concentration: Fuel = 0.6%, $O_2 = 20.89\%$, $N_2 = 78.52\%$ (a) experimental pressure trace (b) ignition delay time as a function of compressed gas temperature.

7.3.2 Influence of Pressure on combustion of UCO-HEFA

The experimental condition considered here are compressed gas pressure of 6 and 10 bar, $\phi = 1.0$. The oxidizer molar composition, represented by $N_2/(O_2 + N_2)$, is fixed at 0.79. Figure 7-3 displays the influence of pressure on the ignition of UCO-HEFA. This shows a slight reduction in the ignition delay time as the pressure is increased from 6 to 10 bar compressed gas pressure. At a lower pressure of 6 bar, it is seen that no NTC occurred within that stage, but a subsequent increase in the compressed gas pressure brought about increase temperature and reactivity of UCO-HEFA. At a higher pressure of 10 bar, reactivity occurs as the temperature increases. Signs of NTC trend were observed due to the low-temperature chain branching pathway when added oxygen to an alkyl radical $R + O_2 \leftrightarrow RO_2$ as it passes through reaction process. At low temperature, from the equation RO_2 is favoured in the equilibrium[268, 269]. However, as the compressed gas temperature proceed further than 739 K the equilibrium shift towards the reactant and the competition of with $R + O_2 \rightarrow HO_2 + alkene$, turns relevant. The production of HO_2 radicals rather than OH through chain-branching pathway controls the reactivity and display NTC behaviour.

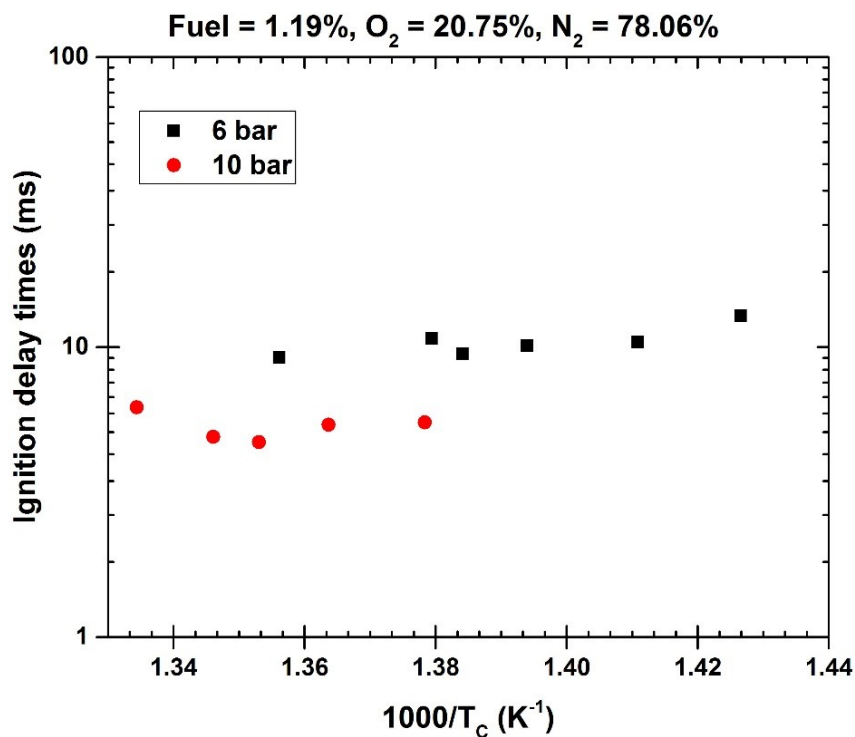


Figure 7-3: Influence of pressure on combustion of UCO-HEFA at 6 bar and 10 bar, $\phi = 1.0$, for UCO/air mixture corresponding. Molar concentration: Fuel = 1.19%, O₂ = 20.75%, N₂ = 78.06%.

7.3.3 Influence of Equivalence Ratio on the combustion of UCO-HEFA

The experimental ignition delay times for UCO/air mixture in Figure 7-4, was investigated at varying equivalence ratio at $0.5 < \phi < 1.0$, compressed gas pressure of 10 bar, molar composition of the oxidizer, represented by $N_2/(O_2 + N_2)$, was fixed at 0.90. The ignition delay plot displayed in Figure 7-4, showed no NTC behaviour at 10 bar but illustrated an Arrhenius

dependence on temperature at the condition studied. The experiment showed the effect of increasing fuel concentration with a decrease in the ignition delay time that is the faster reactivity because of increased equivalence ratio.

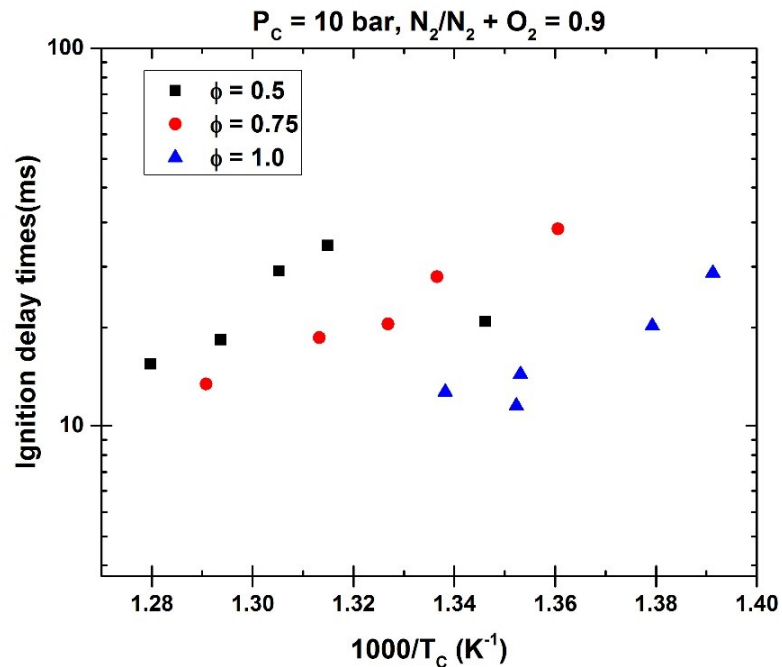


Figure 7-4: Effect of equivalence ratio on measured ignition delay time of UCO at 10 bar.

7.3.4 Influence of Oxygen Mole Fraction on combustion of UCO-HEFA.

The experimental ignition delay times for UCO-HEFA/air mixture in figure 7-5, was investigated by keeping equivalence ratio at $\phi = 0.5$, compressed gas pressure of 10bar and fuel loading condition constant at 0.6% while varying the molar composition of the oxidizer, $N_2/(O_2 + N_2)$. The experiments were performed with oxygen molar concentration of 9.9 and 20.9 %. These are compared in Figure 7-5. This investigation agrees with the previous study [204] that decreasing oxygen mole percentage while keeping equivalence ratio and mole fraction constant lead to prolonging ignition delay time.

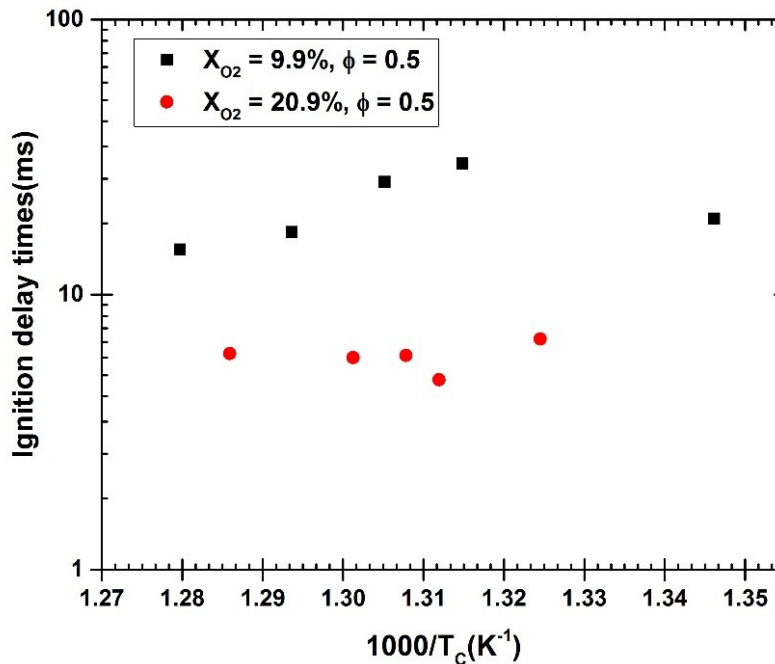


Figure 7-5: influence of Oxygen mole fraction on combustion of UCO-HEFA.

7.3.5 Comparison of UCO-HEFA with Banner solvent and Jet A-1.

Comparison of the ignition delay of a solvent (Banner-Solvent), a synthetic fuel (UCO-HEFA) and a conventional fuel (Jet A-1) at 10 and 6 bar are presented in Figure 7-6 and Figure 7-7.

Figure 7-6(a) shows the experimental condition of PC = 10 bar, $\phi = 0.5$ molar oxidizer ratio $N_2/(O_2 + N_2) = 0.79$. At a compressed gas temperature of 748 – 812 K shown in figure 7-6(a) there was no two stage ignition found in Banner solvent and Jet A-1, and with no NTC behaviour was observed. This means they exhibited an Arrhenius reliance on the temperature at the present condition studied. The reactivity of Banner solvent was faster than Jet A-1 at a reduced compressed gas temperature. However, as the gas temperature increases the ignition delay of banner solvent was faster about twice times that of Jet A-1. Still, in Figure 7-6(a), UCO-HEFA had a longer ignition delay than banner solvent at 777.6 K, but as the temperature gets lowered some signs of NTC behaviour was observed which made the combustion of UCO-HEFA unpredictable and eventually experience shorter ignition delay than banner solvent. The Arrhenius behaviour is not observed by the fuels, and the reaction becomes faster with a reduced ignition delay. The result shows that at low to intermediate temperature regime (748 – 812 K), chemical restructuring occurs in the UCO-HEFA fuel. This cannot be fully admitted that it is in the NTC region until a more comprehensive test is conducted within the compressed gas temperature limits as earlier stated.

In Figure 7-6(b), the ignition delay at the compressed gas temperature of 733 – 796 K was considered, the equivalence ratio of 0.75. As the equivalence ratio is increased, the three fuels were seen to exhibit Arrhenius behaviour dependant on temperature as it is increased led to a reduction in the ignition delay time. Banner solvent has the fastest reactivity and

Jet A-1 the least. The hierarchy of reactivity from Figure 7-6(b) has shown that Banner > UCO-HEFA > Jet A-1.

Figure 7-7(a) reveals that the experimental condition of $P_c = 6$ bar, $\phi = 0.75$ and 1.0 , molar oxidizer ratio $N_2 / (O_2 + N_2) = 0.79$ at compressed temperature of 708 K – 787 K. A single stage ignition was observed for Jet A-1 fuels and no NTC behaviour, increase in temperature lead to reduction in the ignition delay. UCO_HEFA and Banner-Solvent had a shorter ignition delay compare with Jet A-1. This same response was also observed in Figure 7-7(b). It is seen that the low-temperature chemistry affected the ignition delay of UCO-HEFA which made the ignition delay shorter than that of banner solvent and at a higher compressed gas temperature the ignition delay become longer than banner solvent. At low temperature, RO_2 is favoured in the equilibrium[268, 269] as the compressed gas temperature proceed further the equilibrium shift towards the reactant and the competition of with $R + O_2 \rightarrow HO_2 + \text{alkene}$ turns relevant then more of HO_2 Radicals are produced rather than OH through chain-branching pathway controls the reactivity which begins to display NTC behaviour.

The combustion of fuels could be assessed base on the Derived Cetane Number shown in section 2.5.1 making reference to diesel compression; the diesel ignition properties are rated by primary reference fuel via the Cetane number test[270]. Fuels component with low Cetane number is resistant to ignition while a high Cetane number is more reactive fuels. The DCN of Jet A-1 is 43.74, UCO-HEFA-5638 and Banner-Solvent are 75.69 judging by the DCN values, the reactivity of the fuel is in agreement with the experiment. Banner-Solvent has the shortest ignition delay at the similar condition, which correlates to the one with the highest Cetane index.

However, considering the composition of individual fuels as it affects the ignition delay. The structure of the current Jet A-1 has 40.79% cycloparaffins and 20.57% iso-paraffins in its component. At low temperatures, cyclo-components has considerable lower reactivity than the n-paraffin, this partly due to the isomerization pathways and olefin formation. Jet A-1 having the least reactivity may be attributed to cycloparaffin and the aromatic content in its composition. High level of aromatics in fuel contributes to a loss in responsiveness under a low-temperature condition. This result from the build-up of a significant amount of stabilised benzylic radicals because of the favourable initial hydrogen abstraction pathway that scavenges free radicals, which slows down combustion chemistry[271]. The current UCO-HEFA contains mainly iso-paraffins about 71.34% and n-paraffin 19.47 % and some trace of aromatics. However, UCO-HEFA has shorter ignition delay than Jet A-1. Looking again at the composition of UCO-HEFA mainly n- and iso-paraffins. This has high reactivity associating with their potential for rapid, radical production through the low-temperature chain branching mechanism due to a large number of secondary C–H bonds providing relative RO_2 stability and rapid $RO_2 \leftrightarrow QOOH$ isomerization, compared to Jet A-1.

Banner-Solvent is purely n-paraffinic without any trace of aromatics, so their reactivity is driven by n-paraffin. Figure 7-6(b) have it that Banner-Solvent has the fastest reactivity compare to Jet A-1 and UCO-HEFA. Further investigation of Banner solvent is needed to ascertain, which species of the n-paraffin family is responsible for its high reactivity. A linear fit shown in Figure 7-6 was fitted on the data using Origin software.

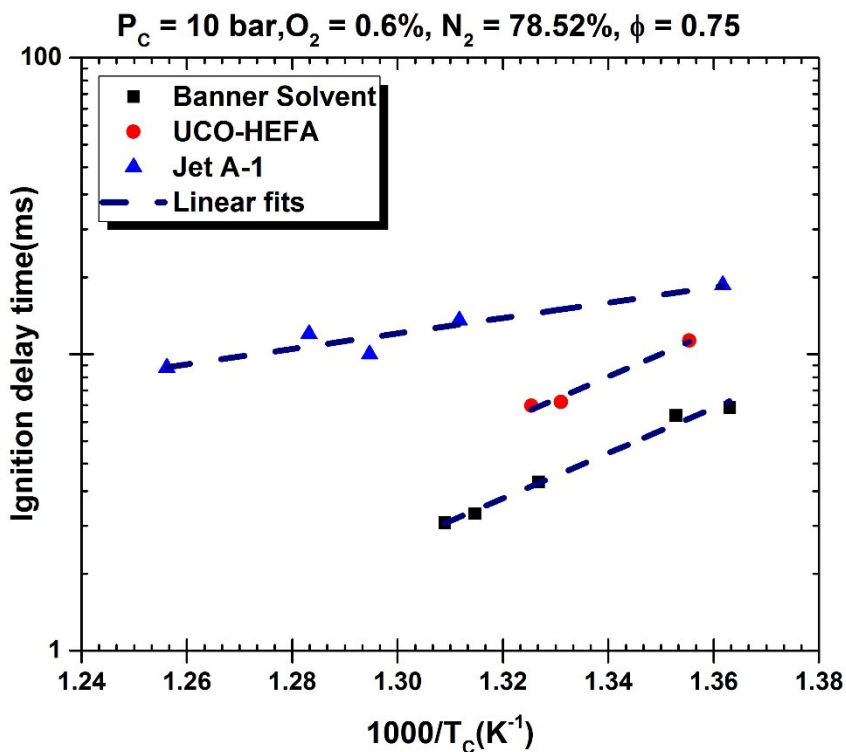
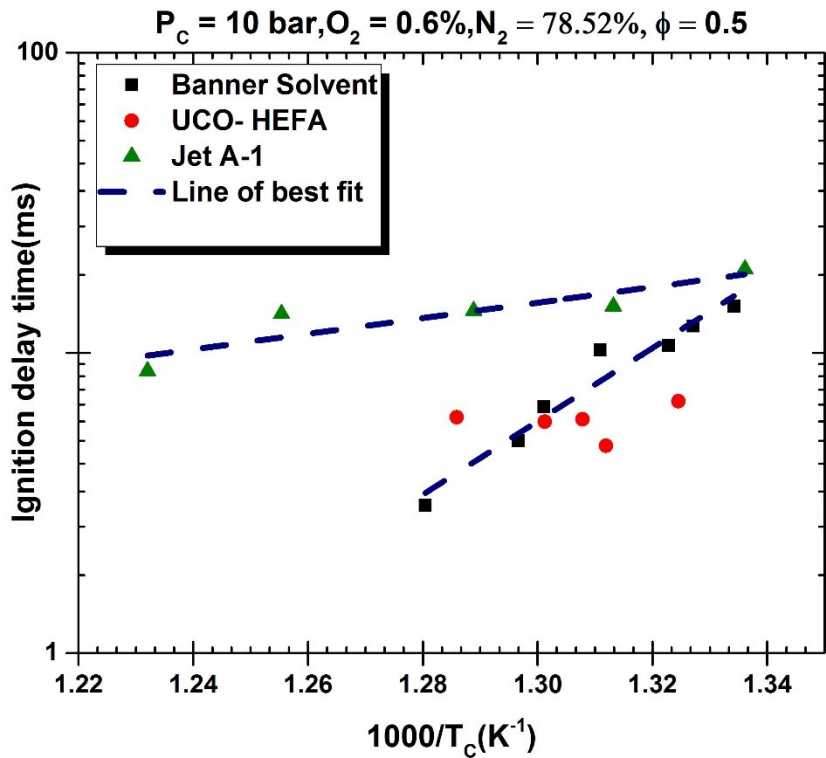
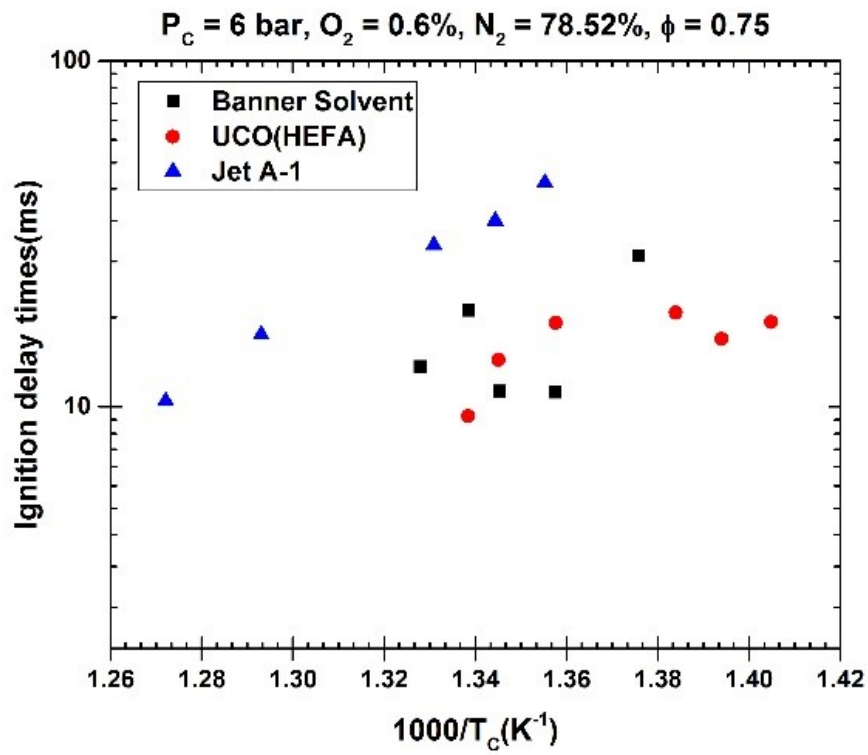
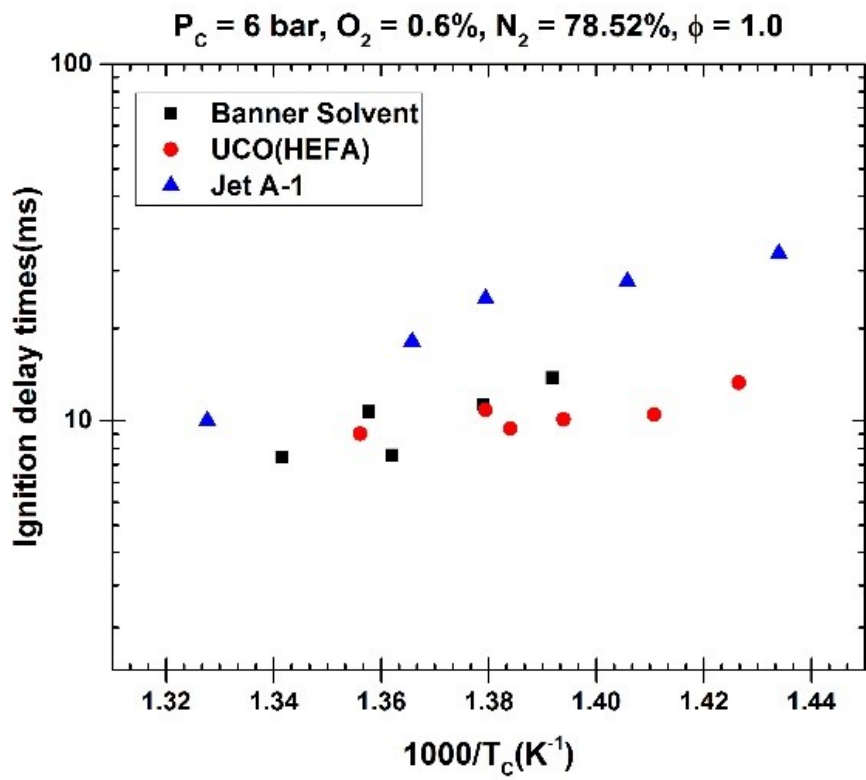


Figure 7-6: Comparison of UCO ignition delay with Jet A-1 and Banner-solvent at compressed gas pressure of $P_c = 10 \text{ bar}$, $\phi = 0.5$ and molar concentration = 0.79.



(a)



(b)

Figure 7-7: Comparison of UCO ignition delay with Jet A-1 and Banner-solvent at $P_c = 6 \text{ bar}$ (a) $\phi = 0.75$, (b) $\phi = 1.0$ and molar concentration = 0.79.

7.3.6 Ignition Delay Correlation

At the low temperature range 697-778 k studied at $\phi = 0.5-1.0$, compressed gas pressure of 10bar and molar composition of the oxidizer, $N_2 / (O_2 + N_2) = 0.9$. The behaviours from the experimental data have been reduced to a single correlation that can conveniently express the ignition delay time regarding temperature, pressure and equivalence ratio. Thus, correlations that describe the total ignition delay time for UCO-HEFA is given as

$$\tau_{ignition} = 0.995 * P_c^{0.006} \phi^{0.1} \exp\left(\frac{22,067}{T_c}\right) \quad 7-1$$

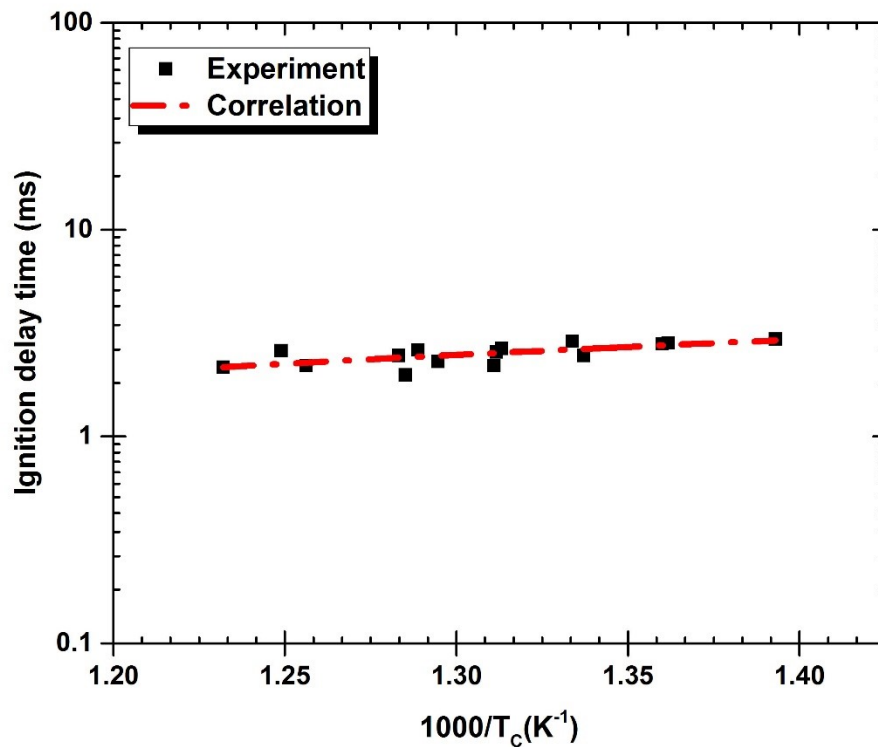


Figure 7-8: Global correlation for UCO-HEFA

The correlation is scaled to $P_c = 10$ bar and $\phi = 1.0$ using the correlation procedure in section 5.3.3. Equation 7-1 gives the global correlation for UCO-HEFA.

7.4 Conclusion and Discussion

An experimental measurement of UCO-HEFA/ air mixtures was carried out in an RCM in the range of low to the intermediate temperature region. With an equivalence ratios of $\phi = 0.5 - 1.0$, dilution molar ratios of $N_2 / (O_2 + N_2) = 0.79 - 0.90$, compressed gas pressures and temperature of $P_c = 6 - 10$ bar, and $T_c = 701 - 777$ K. The compressed gas temperature was varied to have different end gas temperature, while maintaining a constant compression ratio of 8.8. Repeatability test with the UCO-HEFA was done to confirm the repeatability and reproducible of the present rig to build confident on the generated data. Also investigated are the effects of varying equivalence ratios, pressure, and temperature and

oxygen concentrations. The increase in temperature, pressure and equivalence ratio have shown a decrease in the ignition delay time at measured compressed gas pressure at 10 bar. Decreasing oxygen mole percentage, while keeping equivalence ratio and mole fraction constant lead to prolonging ignition delay time. At compressed gas pressure of 10 bar UCO-HEFA, shows Arrhenius dependent on the temperature at the condition study with no 2-stage ignition delay. Comparison of UCO-HEFA with Jet A-1 and Banner-Solvent revealed that Banner-Solvent has the fastest reactivity while Jet A was the list in the reactivity table. A derived global correlation was defined for UCO-HEFA.

7.5 ACKNOWLEDGMENTS

The fuel currently used was partly supported by the European Union's Seventh Framework Programme under Grant Agreement 308807, (Initiative Towards sustainable Kerosene for Aviation (ITAKA)). All findings and conclusions or recommendations found in this work are the author's findings and do not necessarily reflect the views of the sponsor.

Chapter 8. Conclusion and Proposed Future Work

The fear of depletion of natural resources is alarming because of the rapid growth in population size and the high demand for energy has drastically increased more pressure on the exploitation of the fossil fuels. Global conventional oil supply is currently at political risk and shortages are inevitable unless a drastic change occurs in the supply of conventional hydrocarbon fuels. This shortfall cannot be replaced with other conventional sources. However, a drastic step is needed in securing and creating new alternatives fuels not to be vulnerable to unrest, fear and differences resulting from the world dependence on conventional fuels.

The emissions from these fuels are classified as greenhouse gases (GHG), which causes global climate change. Aviation industries contribute, a small amount of pollutant compared to other sector but estimated to account for 2-3% of CO₂ emission[49]. Because of the rapid growth in the aviation sector in the nearest future, its emission will reflect a greater portion than land transport does[56].

One way of reducing emission and improving efficiency in the industrial aero-derived gas turbine is to change the combustion system to a more promising system like the lean premixed system. These technologies have brought forth a premixed design with longer residence times and additional concern such as combustion instabilities, flashback and autoignition. In developing an aircraft combustor of aircraft, it is imperative knowing chemistry of autoignition delay time, which entails burning of fuels at different operating conditions. Damage to combustors and engines could be avoided if the autoignition delay data is handled, this gives a pre-knowledge of the ignition delay time taken by fuels before the onset of combustion. Autoignition delay time measured is driven by the pressure and temperature and the composition of the given fuel-air mixture. There is presently a dearth of information on alternative fuels, and this has instrumented the design of a novel apparatus to test alternative fuel relevant to gas turbine plant and handle high boiling point long chain hydrocarbon fuels.

The Shef-RCM includes hydraulic stopping mechanism, piston release mechanism; optimise crevice design and the reaction chamber designed for easy admittance of direct injection of fuels. In the design of the hydraulic unit, the hydraulic piston ring and the groove was optimise with three steps on the peripheral surface of the hydraulic ring. This was perfectly done which prevented rebounded of the reactor piston and maintained the piston in a steady position at the tail end of the stroke. An optimal piston crevice was designed from the CFD result, which showed that the present piston could contain the roll up vortex from the walls of cylinder. The novel feature of the rig is the design of a pin release mechanism. This mechanism helps in holding the reactor piston in position at its bottom dead center. This design is unique which distinguish it from other RCM in literature. The

basic principle of the mechanism is that force of equal magnitude is applied to the pins that holds the reactor piston in position. The machine is vibration freed, allows for fast compression less than 35 ms and an obtainable compressed gas pressure of 22 bar.

The device is air driven and hydraulically stopped. It is designed to mimics a single stroke compression process in an internal combustion engine. The physic behind the rig is that it compresses fuel/air mixture isentropically, the temperature, pressure and mixture composition and can be varied over a range of experimental conditions.

Performance characterization of the Shef-RCM was carried out using non-reactive and reactive experiment result shows that the experimental data obtained is highly repeatable. The compressed gas temperature at the end of the stroke has been an issue this could not be measured directly reasons based on slow response of thermocouples. The most appropriate way is estimating this temperature through numerical modelling; also, the heat loss in Shef-RCM was model using an effective volume approach, this has a perfectly matched model with experiment.

Ignition delay times measurement for Jet A-1 was reported for low to intermediate temperatures regime ($697 \leq T_C \leq 811$), compressed pressure, $P_C = 6$ and 10 bar and equivalent ratio ratios, $\phi = 0.5, 0.75$ and 1.0 in air. Jet A-1 exhibit NTC behaviour at a higher pressure of 10 bar at $\phi = 0.75$. Ranzi et al.[1] model with Dooley et al. [2] and Aachen[3] surrogate mixture was used for the kinetic modelling. At a compressed pressure of 6 bar, $\phi = 0.75$, the model predicted shorter ignition delay time and displayed a two stage ignition delay time for Jet A-1 fuel, and the model was fairly in agreement with the experiment considering the overall ignition delay. A globally derived correlation for Jet A-1 and UCO-HEFA generated.

The facility was used to measure the ignition behaviour of Banner-Solvent at low to intermediate temperature regime ($680 \leq T_C \leq 836$) at compressed gas pressure, $P_C =$ of 6 and 10 bar, and equivalence ratios, $\phi = 0.5, 0.75$ and 1.0 in the air. Banner-Solvent had high reactivity compare to Jet A-1 prominently exhibited the NTC behaviour mostly at a compressed pressure of 6 bar.

Experimental measurement of the ignition delay behaviour of UCO-HEFA at low to intermediate temperature regime ($680 \leq T_C \leq 777$) at compressed gas pressure, $P_C =$ of 6 and 10 bar, and equivalence ratios, $\phi = 0.5, 0.75$ and 1.0 in the air. The influence of temperature, pressure, and equivalence ratio and oxygen concentration on the ignition delay were studied in this work. The overall reactivity of the three fuels showed that Banner-Solvent had higher reactivity than Jet A-1 and UCO-HEFA at 10 bar compressed gas temperature. At compressed gas pressure of 6 bar, UCO-HEFA exhibited the NTC behaviour.

8.1 Contribution to Knowledge

The input to the understanding of this research work is categorised into two forms:

- (1) The design aspect: In literature, the method of holding the reactor piston via pressurised hydraulic oil in the hydraulic chamber unit has been the usual approach to date. A new concept is used in Shef-RCM design, which enhances the method by introducing the application of piston release mechanism (brake) pneumatically operated use to hold the reactor piston in position at its BDC. This concept is unique, and this distinguishes Shef-RCM design from other RCM's designs.
- (2) Chemical Kinetics Aspect:
There is presently a dearth of information on alternative fuels particularly for Jet A-1, Banner-Solvent and UCO-HEFA. This present experimental data would be useful for improving the existing kinetic models and build archives of autoignition delay data for the validation of chemical kinetic models.
- (3) Precisely in gas turbine engines, it is attractive to run at lean conditions, which achieves reductions in NO_x emissions. There is sparse information on the effect of fuel composition on autoignition delay time.

8.2 Future Work

The present design of the Shef-RCM has been successful. However, it still needs further development to improve on the performances of the current design. A couple of equipment installation could not be achieved, because of the time constraint and these would recommend for further consideration.

- (1) The concept adopted for the chamber design is the direct premixed charge preparation. These have numerous advantages as earlier stated in section 3.1.5 of this work. At present, the charging of the reaction chamber with the fuel-air mixture is manually done as this increase the uncertainty of fuel injected into the chamber. From the study carried out on residence time for the homogenous mixture. It shows that 1.5 hours is the established time for the homogenous mixture of fuel and air before firing the experimental rig. The installation of the injector pump would have taken a shorter time of about 2 – 4 minute if installed as recommended by Casey in his design. Therefore, I would recommend that a high-pressure injector of about 500 to 2000 bar be installed to enhance proper atomization of fuel and mixing thereby reducing residence time and attaining homogeneous mixture of the fuel and air mixture in a shorter time.
- (2) The Shef-RCM lacks a gas line supply to the reactor chamber. The installation of this gas line equipment is relevant as this helps in minimising uncertainty in the mixture composition preparation up to 10%. Also, this enhances proper metering the right volume of air-fuel mixture into the combustion chamber.
- (3) The combustion chamber needs to be redesigned to provide room for the transparent window at the end of the chamber for visualisation of combustible

product and flame analysis. If this provision could be made, then it would trigger the study of flame in addition to autoignition delay time.

REFERENCE

- [1] Ranzi, E., Frassoldati, A., Stagni, A., et al., Reduced kinetic schemes of complex reaction systems: fossil and biomass-derived transportation fuels, *International Journal of Chemical Kinetics*, vol. 46, pp. 512-42, 2014.
- [2] Dooley, S., Won, S. H., Heyne, J., et al., The experimental evaluation of a methodology for surrogate fuel formulation to emulate gas phase combustion kinetic phenomena, *Combustion and Flame*, vol. 159, pp. 1444-66, 2012.
- [3] Honnet, S., Seshadri, K., Niemann, U., et al., A surrogate fuel for kerosene, *Proceedings of the Combustion Institute*, vol. 32, pp. 485-92, 2009.
- [4] Nesterov, I. and Salmanov, F., Present and future hydrocarbon resources of the Earth's crust, 1976.
- [5] Corporan, E., DeWitt, M. J., Belovich, V., et al., Emissions characteristics of a turbine engine and research combustor burning a Fischer-Tropsch jet fuel, *Energy & fuels*, vol. 21, pp. 2615-26, 2007.
- [6] Rye, L., Blakey, S., and Wilson, C. W., Sustainability of supply on the planet: a review of potential drop-in alternative aviation fuels, *Energy & Environmental Science*, vol. 3, pp. 17-27, 2010.
- [7] Hill, J., Environmental costs and benefits of transportation biofuel production from food-and lignocellulose-based energy crops. A review, *Agronomy for Sustainable Development*, vol. 27, pp. 1-12, 2007.
- [8] Chiamonti, D., Prussi, M., Buffi, M., et al., Sustainable bio kerosene: Process routes and industrial demonstration activities in aviation biofuels, *Applied Energy*, vol. 136, pp. 767-74, 2014.
- [9] Novelli, P., SWAFEA/Sustainable Way for Alternative Fuels and Energy in Aviation, *Final Report*, April, 2013.
- [10] Ajam, M., Woolard, C., and Wiljoen, C., Biomass Pyrolysis Oil as a Renewable Feedstock for Bio-Jet Fuel. 2013, in *Proceedings of the 13th international conference on stability, handling and use of liquid fuels (IASH2013)*, Rhodes, Greece, 2013, pp. 6-10.
- [11] Demirbas, A., Progress and recent trends in biofuels, *Progress in Energy and Combustion Science*, vol. 33, pp. 1-18, 2007.
- [12] Salvi, B., Subramanian, K., and Panwar, N., Alternative fuels for transportation vehicles: a technical review, *Renewable and Sustainable Energy Reviews*, vol. 25, pp. 404-19, 2013.
- [13] Dry, M. E., The Fischer-Tropsch process: 1950-2000, *Catalysis Today*, vol. 71, pp. 227-41, 1/15/2002.
- [14] Wang, W.-C., Techno-economic analysis of a bio-refinery process for producing Hydro-processed Renewable Jet fuel from Jatropha, *Renewable Energy*, vol. 95, pp. 63-73, 2016.
- [15] International, A., ASTM D7566-11a, standard specification for aviation turbine fuel containing synthesized hydrocarbons, *ASTM 2008 Annual Book of Standards*, 2011.
- [16] Schroecker, D., Deurwaarder, E., Schild, P., et al., million tons per year: a performing biofuels supply chain for EU aviation, Technical Report. European Commission 2011.
- [17] Nunes, P. P., Brodzki, D., Bugli, G., et al., SOYBEAN OIL HYDROCRACKING UNDER PRESSURE - PROCESS AND GENERAL ASPECT OF THE TRANSFORMATION, *Revue De L Institut Francais Du Petrole*, vol. 41, pp. 421-31, May-Jun 1986.

- [18] Simacek, P., Kubicka, D., Sebor, G., et al., Fuel properties of hydroprocessed rapeseed oil, *Fuel*, vol. 89, pp. 611-15, Mar 2010.
- [19] Simacek, P., Kubicka, D., Sebor, G., et al., Hydroprocessed rapeseed oil as a source of hydrocarbon-based biodiesel, *Fuel*, vol. 88, pp. 456-60, Mar 2009.
- [20] Sebos, I., Matsoukas, A., Apostolopoulos, V., et al., Catalytic hydroprocessing of cottonseed oil in petroleum diesel mixtures for production of renewable diesel, *Fuel*, vol. 88, pp. 145-49, 2009.
- [21] Association, I. A. T., Montreal-Geneva, *IATA 2011 Report on Alternative Fuels*, 2011.
- [22] Altman, R., Aviation alternative fuels, characterizing the options, *Aviation and Alternative Fuels (ICAO)*, ICAO, Montreal, Canada, 2009.
- [23] Franz, F. and Hans, T., Process for the production of paraffin-hydrocarbons with more than one carbon atom, ed: Google Patents, 1930.
- [24] Fischer, F. and Tropsch, H., The preparation of synthetic oil mixtures (synthol) from carbon monoxide and hydrogen, *Brennstoff-Chem*, vol. 4, pp. 276-85, 1923.
- [25] Blakey, S., Rye, L., and Wilson, C. W., Aviation gas turbine alternative fuels: A review, *Proceedings of the Combustion Institute*, vol. 33, pp. 2863-85, 2011.
- [26] Moses, C. A. and Roets, P. N. J., Properties, Characteristics, and Combustion Performance of Sasol Fully Synthetic Jet Fuel, *Journal of Engineering for Gas Turbines and Power-Transactions of the Asme*, vol. 131, Jul 2009.
- [27] AMERICA, N., IEA Bioenergy Task 39, 2005.
- [28] Corporan, E., DeWitt, M. J., Monroig, O., et al., Reduction of turbine engine particulate emissions using synthetic jet fuel, *Abstracts of Papers of the American Chemical Society*, vol. 229, pp. U873-U73, Mar 13 2005.
- [29] Holley, A., Dong, Y., Andac, M., et al., Ignition and extinction of non-premixed flames of single-component liquid hydrocarbons, jet fuels, and their surrogates, *Proceedings of the Combustion Institute*, vol. 31, pp. 1205-13, 2007.
- [30] Juste, G. L., Hydrogen injection as additional fuel in gas turbine combustor. Evaluation of effects, *International Journal of Hydrogen Energy*, vol. 31, pp. 2112-21, 2006.
- [31] Koroneos, C., Dompros, A., Roumbas, G., et al., Advantages of the use of hydrogen fuel as compared to kerosene, *Resources, Conservation and Recycling*, vol. 44, pp. 99-113, 2005.
- [32] Contreras, A., Yigit, S., Ozay, K., et al., Hydrogen as aviation fuel: A comparison with hydrocarbon fuels, *International Journal of Hydrogen Energy*, vol. 22, pp. 1053-60, Oct-Nov 1997.
- [33] Westenberger, A., Liquid hydrogen fuelled aircraft–system analysis, CRYOPLANE, Final Technical Report No. GRD1-1999-10014, to the European Commission 2003.
- [34] Hansen, A. C., Zhang, Q., and Lyne, P. W. L., Ethanol–diesel fuel blends — a review, *Bioresource Technology*, vol. 96, pp. 277-85, 2// 2005.
- [35] Li, D.-g., Zhen, H., Xingcai, L., et al., Physico-chemical properties of ethanol–diesel blend fuel and its effect on performance and emissions of diesel engines, *Renewable energy*, vol. 30, pp. 967-76, 2005.
- [36] Gupta, K. K., Rehman, A., and Sarviya, R. M., Bio-fuels for the gas turbine: A review, *Renewable and Sustainable Energy Reviews*, vol. 14, pp. 2946-55, 2010.

- [37] Pier, J., Comparisons of biofuels in high-speed turbine locomotives: Emissions, energy use, and cost, *Transportation Research Record: Journal of the Transportation Research Board*, pp. 24-32, 1999.
- [38] Armas, O., Gómez, A., Mata, C., et al., Particles emitted during the stops of an urban bus fuelled with ethanol–biodiesel–diesel blends, *Urban Climate*, vol. 2, pp. 43-54, 2012.
- [39] Fang, Q., Fang, J., Zhuang, J., et al., Effects of ethanol–diesel–biodiesel blends on combustion and emissions in premixed low temperature combustion, *Applied Thermal Engineering*, vol. 54, pp. 541-48, 2013.
- [40] Zhu, L., Cheung, C., Zhang, W., et al., Combustion, performance and emission characteristics of a DI diesel engine fueled with ethanol–biodiesel blends, *Fuel*, vol. 90, pp. 1743-50, 2011.
- [41] Standard, D., 91-91, *Turbine Fuel, Aviation Kerosene Type, Jet A-1 NATO Code: F-35 Joint Service Designation: AVTUR (18 2011)*, 2008.
- [42] Hemighaus, G., Boval, T., Bacha, J., et al., Aviation fuels technical review, *Chevron Products Company*, 2006.
- [43] Moses, C. A., Development of the protocol for acceptance of synthetic fuels under commercial specification, *Coordinating Research Council Report AV-2-04, Alpharetta, GA September*, 2007.
- [44] British Ministry of Defence (MOD). Turbine Fuel, Aviation Kerosene Type, Jet A-1 NATO Code: F-35 Joint Service Designation: AVTUR, *Defence Standard 91-91; MOD, Defence Equipment and Support, U.K. Defence Standardization: Glasgow, U.K.*, 2011.
- [45] Standard, A., D1655, Standard Specification for Aviation Turbine Fuels, ed: West Conshohocken, PA: ASTM International, 2013.
- [46] Wilson III, G. R., Edwards, T., Corporan, E., et al., Certification of alternative aviation fuels and blend components, *Energy & Fuels*, vol. 27, pp. 962-66, 2013.
- [47] Van Der Linden, S., The World's First Industrial Gas Turbine Set at Neuchâtel (1939), *ASME International Historic Mechanical Engineering Landmark, Neuchâtel, Switzerland*, 1988.
- [48] Agarwal, A. K., Biofuels (alcohols and biodiesel) applications as fuels for internal combustion engines, *Progress in energy and combustion science*, vol. 33, pp. 233-71, 2007.
- [49] Khatib, H., IEA World Energy Outlook 2011—A comment, *Energy policy*, vol. 48, pp. 737-43, 2012.
- [50] Gullison, R. E., Frumhoff, P. C., Canadell, J. G., et al., Tropical forests and climate policy, *SCIENCE-NEW YORK THEN WASHINGTON-*, vol. 316, p. 985, 2007.
- [51] Sorrell, S., Speirs, J., Bentley, R., et al., Global oil depletion: A review of the evidence, *Energy Policy*, vol. 38, pp. 5290-95, 9// 2010.
- [52] Bentley, R. W., Global oil & gas depletion: an overview, *Energy policy*, vol. 30, pp. 189-205, 2002.
- [53] Bentley, R. W., Global oil & gas depletion: an overview, *Energy Policy*, vol. 30, pp. 189-205, 2// 2002.
- [54] Hubbert, M. K., *Energy from fossil fuels*: Moses King, 1949.
- [55] Kjærstad, J. and Johnsson, F., Resources and future supply of oil, *Energy Policy*, vol. 37, pp. 441-64, 2009.
- [56] Leader, C. A. and Director, J., Next Generation Air Transportation System, 2008.
- [57] Penner, J. E., *Aviation and the global atmosphere: a special report of the Intergovernmental Panel on Climate Change*: Cambridge University Press, 1999.

- [58] UPDATE, P., INTERNATIONAL CIVIL AVIATION ORGANIZATION'S CARBON OFFSET AND REDUCTION SCHEME FOR INTERNATIONAL AVIATION (CORSA), *POLICY*, 2017.
- [59] Union, E., Directive 2009/28/EC of the European Parliament and of the Council of 23 April 2009 on the promotion of the use of energy from renewable sources and amending and subsequently repealing Directives 2001/77/EC and 2003/30/EC, *Official Journal of the European Union*, vol. 5, p. 2009, 2009.
- [60] Dagaut, P. and Cathonnet, M., The ignition, oxidation, and combustion of kerosene: A review of experimental and kinetic modeling, *Progress in energy and combustion science*, vol. 32, pp. 48-92, 2006.
- [61] Standard, A., D1655-11b, 2011, *Standard Specification for Aviation Turbine Fuels*.
- [62] International, A., ASTM D7566-11a. Aviation Turbine Fuel Containing Synthesized Hydrocarbons, ed: ASTM International West Conshohocken, PA, 2011.
- [63] Liedtke, O. and Schulz, A., Development of a new lean burning combustor with fuel film evaporation for a micro gas turbine, *Experimental Thermal and Fluid Science*, vol. 27, pp. 363-69, 2003.
- [64] Lee, J. C., Malte, P. C., and Benjamin, M. A., Low NO_x Combustion for Liquid Fuels: Atmospheric Pressure Experiments Using a Staged Prevaporizer-Premixer, in *ASME Turbo Expo 2001: Power for Land, Sea, and Air*, 2001, pp. V002T02A47-V02T02A47.
- [65] Fernández-Tarrazo, E., Sánchez, A. L., Liñán, A., et al., Flammability conditions for ultra-lean hydrogen premixed combustion based on flame-ball analyses, *International Journal of Hydrogen Energy*, vol. 37, pp. 1813-25, 2012.
- [66] Eskin, L. D., Holton, M. M., Turner, B. A., et al., Long-Term Demonstration of a Lean, Premixed, Prevaporized (LPP) System for Gas Turbines, in *2012 20th International Conference on Nuclear Engineering and the ASME 2012 Power Conference*, 2012, pp. 737-45.
- [67] Gokulakrishnan, P., Ramotowski, M., Gaines, G., et al., Experimental Study of NO_x Formation in Lean, Premixed, Prevaporized Combustion of Fuel Oils at Elevated Pressures, in *ASME Turbo Expo 2007: Power for Land, Sea, and Air*, 2007, pp. 441-49.
- [68] Maier, G. and Wittig, S., Fuel Preparation and Emission Characteristics of a Pressure Loaded LPP Combustor, in *30th Fluid Dynamics Conference*, 1999, p. 3774.
- [69] Ikezaki, T., Hosoi, J., Toh, H., et al., The Performance of the Low NO_x Aero Gas Turbine Combustor Under High Pressure, in *ASME Turbo Expo 2001: Power for Land, Sea, and Air*, 2001, pp. V002T02A50-V02T02A50.
- [70] Michou, Y., Chauveau, C., Gokalp, I., et al., Experimental study of lean premixed and prevaporised turbulent spray combustion, in *37th Aerospace Sciences Meeting and Exhibit*, 1999, p. 332.
- [71] Wilson, A., Experimental and theoretical studies of a novel venturi lean premixed prevaporized (LPP) combustor, 2001.
- [72] Dewanji, D., Flow characteristics in lean direct injection combustors, *Birla Institute of Technology, India Master's Thesis*, 2012.
- [73] Tacina, R., Wey, C., Laing, P., et al., Sector Tests of a Low NO_x, Lean-Direct-Injection, Multipoint Integrated Module Combustor Concept, in *ASME Turbo Expo 2002: Power for Land, Sea, and Air*, 2002, pp. 533-44.
- [74] Lefebvre, A. H., *Gas turbine combustion*: CRC Press, 2010.

- [75] Flamme, M., New combustion systems for gas turbines (NGT), *Applied Thermal Engineering*, vol. 24, pp. 1551-59, 2004.
- [76] Kim, H., Arghode, V., and Gupta, A., Combustion characteristics of a lean premixed LPG–air combustor, *International Journal of Hydrogen Energy*, vol. 34, pp. 1045-53, 2009.
- [77] Kimura, S., Aoki, O., Kitahara, Y., et al., Ultra-clean combustion technology combining a low-temperature and premixed combustion concept for meeting future emission standards, SAE Technical Paper 0148-7191, 2001.
- [78] Kimura, S., Aoki, O., Ogawa, H., et al., New combustion concept for ultra-clean and high-efficiency small DI diesel engines, SAE Technical Paper 0148-7191, 1999.
- [79] Dowling, A. and Hubbard, S., Instability in lean premixed combustors, *Proceedings of the Institution of Mechanical Engineers, Part A: Journal of Power and Energy*, vol. 214, pp. 317-32, 2000.
- [80] Correa, S. M., A review of NO_x formation under gas-turbine combustion conditions, *Combustion science and technology*, vol. 87, pp. 329-62, 1993.
- [81] Hsu, K., Goss, L., Trump, D., et al., Performance of a trapped-vortex combustor, *AIAA paper*, vol. 810, 1995.
- [82] Bruno, C. and Losurdo, M., "The trapped vortex combustor: an advanced combustion technology for aerospace and gas turbine applications," in *Advanced combustion and aerothermal technologies*, ed: Springer, 2007, pp. 365-84.
- [83] Falk, K., THE IGNITION TEMPERATURES OF HYDROGEN-OXYGEN MIXTURES, *Journal of the American Chemical Society*, vol. 28, pp. 1517-34, 1906.
- [84] Affleck, W. and Thomas, A., An opposed piston rapid compression machine for preflame reaction studies, *Proceedings of the Institution of Mechanical Engineers*, vol. 183, pp. 365-87, 1968.
- [85] Dixon, H. B., Bradshaw, L., and Campbell, C., CLXXXIX.—The firing of gases by adiabatic compression. Part I. Photographic analysis of the flame, *Journal of the Chemical Society, Transactions*, vol. 105, pp. 2027-35, 1914.
- [86] Dixon, H. B. and Crofts, J. M., CXC.—The firing of gases by adiabatic compression. Part II. The ignition-points of mixtures containing electrolytic gas, *Journal of the Chemical Society, Transactions*, vol. 105, pp. 2036-53, 1914.
- [87] Cassel, H., Über Entflammung und Verbrennung von Sauerstoff–Wasserstoff-Gemischen, *Annalen der Physik*, vol. 356, pp. 685-704, 1917.
- [88] Tizard, H. T. and Pye, D. R., VIII. Experiments on the ignition of gases by sudden compression, *Philosophical Magazine Series 6*, vol. 44, pp. 79-121, 1922/07/01 1922.
- [89] Fenning, R. and Cotton, F., *Experiments on the ignition of gases by sudden compression*: HM Stationery Office, 1930.
- [90] Tizard, H. and Pye, D., VIII. Experiments on the ignition of gases by sudden compression, *The London, Edinburgh, and Dublin Philosophical Magazine and Journal of Science*, vol. 44, pp. 79-121, 1922.
- [91] Jost, W. and Rögener, H., Reaktionskinetische Untersuchungen zum Klopfvorgang. III. Über die Wirkung von Zusätzen auf die Selbstzündung adiabatisch komprimierter Heptan-Luft-Gemische, *Zeitschrift für Elektrochemie und angewandte physikalische Chemie*, vol. 47, pp. 307-09, 1941.

- [92] Scheuermeyer, M. and Steigerwald, H., *Motortech, Z*, vol. 5, p. 229, 1943.
- [93] Leary, W., Taylor, E., Taylor, C., et al., The Effect of Fuel Composition, Compression Pressure, and Fuel-Air Ratio on the Compression-Ignition Characteristics of Several Fuels, DTIC Document 1948.
- [94] Taylor, C. F., *The Internal-combustion Engine in Theory and Practice: Combustion*: MIT Press, 1968.
- [95] Rogowski, A., A New Machine for Studying Combustion of Fuel Sprays with Controlled Air Motion, SAE Technical Paper 0148-7191, 1961.
- [96] Rife, J. and Heywood, J. B., Photographic and performance studies of diesel combustion with a rapid compression machine, SAE Technical Paper 0148-7191, 1974.
- [97] Matekunas, F. A., A Schlieren study of combustion in a rapid compression machine simulating the spark ignition engine, in *Symposium (International) on Combustion*, 1979, pp. 1283-94.
- [98] Zigan, D., Untersuchung an einem Einhub-Dieselmotor, *MTZ Jahrg*, vol. 38, pp. 159-240, 1977.
- [99] Beeley, P., Griffiths, J., and Gray, P., Rapid compression studies on spontaneous ignition of isopropyl nitrate part I: Nonexplosive decomposition, explosive oxidation and conditions for safe handling, *Combustion and Flame*, vol. 39, pp. 255-68, 1980.
- [100] Park, P., Rapid compression machine measurements of ignition delays for primary reference fuels, Massachusetts Institute of Technology, 1990.
- [101] Lim, O. T., Sendoh, N., and Iida, N., Experimental study on HCCI combustion characteristics of n-heptane and iso-octane fuel/air mixture by the use of a rapid compression machine, SAE Technical Paper 0148-7191, 2004.
- [102] Guibert, P., Keromnes, A., and Legros, G., Development of a turbulence controlled rapid compression machine for HCCI combustion, SAE Technical Paper 0148-7191, 2007.
- [103] Allen, C., *Advanced rapid compression machine test methods and surrogate fuel modeling for bio-derived jet and diesel fuel autoignition* vol. 73, 2012.
- [104] Neuman, J., Development of a rapid compression controlled-expansion machine for chemical ignition studies, MARQUETTE UNIVERSITY, 2015.
- [105] Allen, C., *Advanced rapid compression machine test methods and surrogate fuel modeling for bio-derived jet and diesel fuel autoignition*, vol. 73, ed, 2012, p. 2012.
- [106] Mittal, G., A RAPID COMPRESSION MACHINE – DESIGN, CHARACTERIZATION, AND AUTOIGNITION INVESTIGATIONS.pdf, Ph.D, Mechanical and Aerospace Engineering, Case Western Reserve University, Mechanical Engineering., 2006.
- [107] Donovan, M., He, X., Zigler, B., et al., Demonstration of a free-piston rapid compression facility for the study of high temperature combustion phenomena, *Combustion and flame*, vol. 137, pp. 351-65, 2004.
- [108] Ribaucour, M., Minetti, R., Sochet, L. R., et al., Ignition of isomers of pentane: An experimental and kinetic modeling study, *Proceedings of the Combustion Institute*, vol. 28, pp. 1671-78, 2000.
- [109] Ribaucour, M., Minetti, R., Carlier, M., et al., Autoinflammation a haute pression. Conception, réalisation et test d'une machine a compression rapide, *Journal de chimie physique*, vol. 89, pp. 2127-52, 1992.
- [110] Weber, B. W., Kumar, K., Zhang, Y., et al., Autoignition of n-butanol at elevated pressure and low-to-intermediate temperature, *Combustion and Flame*, vol. 158, pp. 809-19, 2011.

- [111] Park, P. and Keck, J. C., Rapid compression machine measurements of ignition delays for primary reference fuels, SAE Technical Paper 0148-7191, 1990.
- [112] Battin-Leclerc, F., Simmie, J. M., and Blurock, E., *Cleaner combustion*: Springer, 2013.
- [113] Lee, D. and Hochgreb, S., Rapid Compression Machines: Heat Transfer and Suppression of Corner Vortex, *Combustion and Flame*, vol. 114, pp. 531-45, 1998.
- [114] Bunnell, J., Autoignition of Methyl Pentanoate at Low to Intermediate Temperatures and Elevated Pressures in a Rapid Compression Machine, 2015.
- [115] Würmel, J. and Simmie, J. M., CFD studies of a twin-piston rapid compression machine, *Combustion and Flame*, vol. 141, pp. 417-30, 2005.
- [116] Strozzi, C., Sotton, J., Mura, A., et al., Characterization of a two-dimensional temperature field within a rapid compression machine using a toluene planar laser-induced fluorescence imaging technique, *Measurement Science and Technology*, vol. 20, p. 125403, 2009.
- [117] Chung, J., Lee, S., An, H., et al., Rapid-compression machine studies on two-stage ignition characteristics of hydrocarbon autoignition and an investigation of new gasoline surrogates, *Energy*, vol. 93, Part 2, pp. 1505-14, 12/15/ 2015.
- [118] Gaydon, A. G. and Hurler, I. R., *The shock tube in high-temperature chemical physics*: Chapman and Hall, 1963.
- [119] Hong, Z., Davidson, D., Vasu, S., et al., The effect of oxygenates on soot formation in rich heptane mixtures: a shock tube study, *Fuel*, vol. 88, pp. 1901-06, 2009.
- [120] Malewicki, T., Gudiyella, S., and Brezinsky, K., Experimental and modeling study on the oxidation of Jet A and the n-dodecane/iso-octane/n-propylbenzene/1, 3, 5-trimethylbenzene surrogate fuel, *Combustion and Flame*, vol. 160, pp. 17-30, 2013.
- [121] Shen, H.-P. S., *Shock tube ignition delay studies of hydrocarbon components found in jet fuels*: ProQuest, 2008.
- [122] De Toni, A. R., Werler, M., Hartmann, R. M., et al., Ignition delay times of Jet A-1 fuel: Measurements in a high-pressure shock tube and a rapid compression machine, *Proceedings of the Combustion Institute*.
- [123] Davidson, D., Haylett, D., and Hanson, R., Development of an aerosol shock tube for kinetic studies of low-vapor-pressure fuels, *Combustion and Flame*, vol. 155, pp. 108-17, 2008.
- [124] Wang, W., *Autoignition Studies of Diesel Alternative Biofuels*, 2013.
- [125] Mueller, M., Kim, T., Yetter, R., et al., Flow reactor studies and kinetic modeling of the H₂/O₂ reaction, *International Journal of Chemical Kinetics*, vol. 31, pp. 113-25, 1999.
- [126] Dagaut, P., Reuillon, M., and Cathonnet, M., Experimental study of the oxidation of n-heptane in a jet stirred reactor from low to high temperature and pressures up to 40 atm, *Combustion and Flame*, vol. 101, pp. 132-40, 1995.
- [127] Tran, L. S., Sirjean, B., Glaude, P.-A., et al., Progress in detailed kinetic modeling of the combustion of oxygenated components of biofuels, *Energy*, vol. 43, pp. 4-18, 2012.
- [128] Wüning, J. A. and Wüning, J. G., Flameless oxidation to reduce thermal NO-formation, *Progress in Energy and Combustion Science*, vol. 23, pp. 81-94, 1997/01/01 1997.
- [129] Bugler, J., Rodriguez, A., Herbinet, O., et al., An experimental and modelling study of n-pentane oxidation in two jet-stirred reactors: The importance of pressure-dependent kinetics and new reaction pathways, *Proceedings of the Combustion Institute*.

- [130] Dagaut, P. and Togbé, C., Oxidation kinetics of butanol–gasoline surrogate mixtures in a jet-stirred reactor: experimental and modeling study, *Fuel*, vol. 87, pp. 3313-21, 2008.
- [131] Ciajolo, A., Low-temperature oxidation of MTBE in a high-pressure jet-stirred flow reactor, *Combustion science and technology*, vol. 123, pp. 49-61, 1997.
- [132] Karsenty, F., Sarathy, S., Togbé, C., et al., Experimental and kinetic modeling study of 3-methylheptane in a jet-stirred reactor, *Energy & Fuels*, vol. 26, pp. 4680-89, 2012.
- [133] Westbrook, C. K., Pitz, W. J., Thornton, M. M., et al., A kinetic modeling study of n-pentane oxidation in a well-stirred reactor, *Combustion and flame*, vol. 72, pp. 45-62, 1988.
- [134] Deyun, E. V., Korsunskii, B. L., and Samoilenko, N. G., Modeling of the dynamics of a well-stirred reactor with parallel exothermic reactions, *Russian Journal of Physical Chemistry B*, vol. 1, pp. 544-48, 2007.
- [135] Dagaut, P., Sarathy, S. M., and Thomson, M. J., A chemical kinetic study of n-butanol oxidation at elevated pressure in a jet stirred reactor, *Proceedings of the Combustion Institute*, vol. 32, pp. 229-37, // 2009.
- [136] Wilk, R., Cernansky, N., Pitz, W., et al., Propene oxidation at low and intermediate temperatures: a detailed chemical kinetic study, *Combustion and flame*, vol. 77, pp. 145-70, 1989.
- [137] Warnatz, J., "Rate coefficients in the C/H/O system," in *Combustion chemistry*, ed: Springer, 1984, pp. 197-360.
- [138] Baldwin, R. R., Dean, C. E., and Walker, R. W., Relative rate study of the addition of HO₂ radicals to C₂H₄ and C₃H₆, *Journal of the Chemical Society, Faraday Transactions 2: Molecular and Chemical Physics*, vol. 82, pp. 1445-55, 1986.
- [139] Baldwin, R. R., Stout, D. R., and Walker, R. W., Relative rate study of the addition of HO₂ radicals to ethylene and to tetramethylethylene, *Journal of the Chemical Society, Faraday Transactions 1: Physical Chemistry in Condensed Phases*, vol. 80, pp. 3481-89, 1984.
- [140] Wilk, R. D., Cernansky, N., and Cohen, R. S., An experimental study of propene oxidation at low and intermediate temperatures, *Combustion science and technology*, vol. 52, pp. 39-58, 1987.
- [141] LIGNOLA, A., Reverchon, E., Autuori, R., et al., Propene combustion process in a CSTR, *Combustion science and technology*, vol. 44, pp. 1-14, 1985.
- [142] Mullen, J. and Skirrow, G., Gas-phase oxidation of propylene, in *Proceedings of the Royal Society of London A: Mathematical, Physical and Engineering Sciences*, 1958, pp. 312-30.
- [143] Rye, L. J., *The influence of alternative fuel composition on gas turbine combustion performance*, 2012.
- [144] NIST, NIST Chemistry WebBook: Standard Reference Database, p. Number 69.
- [145] Rao, V. K. and Bardon, M. F., Estimating the molecular weight of petroleum fractions, *Industrial & Engineering Chemistry Process Design and Development*, vol. 24, pp. 498-500, 1985.
- [146] Maurice, L. Q., Lander, H., Edwards, T., et al., Advanced aviation fuels: a look ahead via a historical perspective, *Fuel*, vol. 80, pp. 747-56, 2001.
- [147] Hadallar, O. J., and Johnson, J.M., World Fuel Sampling Program, *Coordinating Research Council Report No.647*, June 2006.
- [148] Huang, H., Spadaccini, L. J., and Sobel, D. R., Fuel-cooled thermal management for advanced aero engines, in *ASME Turbo Expo 2002: Power for Land, Sea, and Air*, 2002, pp. 367-76.

- [149] Sobel, D. R. and Spadaccini, L. J., Hydrocarbon fuel cooling technologies for advanced propulsion, *Journal of Engineering for Gas Turbines and Power*, vol. 119, pp. 344-51, 1997.
- [150] Goodger, E., Jet fuels development and alternatives, *Proceedings of the Institution of Mechanical Engineers, Part G: Journal of Aerospace Engineering*, vol. 209, pp. 147-56, 1995.
- [151] Roubaud, A., Minetti, R., and Sochet, L., Oxidation and combustion of low alkylbenzenes at high pressure: comparative reactivity and auto-ignition, *Combustion and Flame*, vol. 121, pp. 535-41, 2000.
- [152] Guibet, J.-C. and Faure-Birchem, E., *Fuels and engines: technology, energy, environment* vol. 2: Éditions Technip, 1999.
- [153] Edwards, T. and Maurice, L. Q., Surrogate mixtures to represent complex aviation and rocket fuels, *Journal of Propulsion and Power*, vol. 17, pp. 461-66, 2001.
- [154] Martel, C., Molecular weight and average composition of JP-4, JP-5, JP-8, and Jet A, *AFWAL/POSF Report, July*, vol. 15, 1988.
- [155] Violi, A., Yan, S., Eddings, E. G., et al., Experimental formulation and kinetic model for JP-8 surrogate mixtures, *Combustion Science and Technology*, vol. 174, pp. 399-417, 2002.
- [156] Dagaut, P., Reuillon, M., Boettner, J.-C., et al., Kerosene combustion at pressures up to 40 atm: Experimental study and detailed chemical kinetic modeling, in *Symposium (International) on Combustion*, 1994, pp. 919-26.
- [157] Pfahl, U., Fieweger, K., and Adomeit, G., Self-ignition of diesel-relevant hydrocarbon-air mixtures under engine conditions, in *Symposium (International) on Combustion*, 1996, pp. 781-89.
- [158] Bales-Gueret, C., Cathonnet, M., Boettner, J. C., et al., Experimental study and kinetic modeling of higher hydrocarbon oxidation in a jet-stirred flow reactor, *Energy & Fuels*, vol. 6, pp. 189-94, 1992.
- [159] Guéret, C., Cathonnet, M., Boettner, J.-C., et al., Experimental study and modeling of kerosene oxidation in a jet-stirred flow reactor, in *Symposium (International) on Combustion*, 1991, pp. 211-16.
- [160] Dagaut, P., Reuillon, M., Cathonnet, M., et al., High pressure oxidation of normal decane and kerosene in dilute conditions from low to high temperature, *Journal de chimie physique*, vol. 92, pp. 47-76, 1995.
- [161] Doute, C., Delfau, J.-L., Akrich, R., et al., Chemical structure of atmospheric pressure premixed n-decane and kerosene flames, *Combustion Science and Technology*, vol. 106, pp. 327-44, 1995.
- [162] Bacha, J., Barnes, F., Franklin, M., et al., Aviation fuels technical review *Chevron Products Company*, 2000.
- [163] Westbrook, C. K., Chemical kinetics of hydrocarbon ignition in practical combustion systems, *Proceedings of the Combustion Institute*, vol. 28, pp. 1563-77, 2000.
- [164] Warnatz, J., Maas, U., and Dibble, R., *Combustion: physical and chemical fundamentals, modeling and simulation, experiments, pollutant formation*. 2006, ed: Springer.
- [165] Leppard, W. R., "The Autoignition Chemistries of Primary Reference Fuels, Olefin/Paraffin Binary Mixtures, and Non-Linear Octane Blending," 1992.
- [166] Li, H., *Autoignition chemistry studies of primary reference fuels and their mixtures with oxygenates in a research engine*, 1996.

- [167] Oran, E., Young, T., Boris, J., et al., Weak and strong ignition. I. Numerical simulations of shock tube experiments, *Combustion and Flame*, vol. 48, pp. 135-48, 1982.
- [168] Avery, H. E., *Basic reaction kinetics and mechanisms*: Macmillan, 1974.
- [169] House, J. E., *Principles of chemical kinetics*: Academic Press, 2007.
- [170] McQuarrie, D. A. S., *Physical chemistry a molecular approach*, 1997.
- [171] Glassman, I., Yetter, R. A., and Glumac, N. G., *Combustion*: Academic press, 2014.
- [172] Curran, H. J., Gaffuri, P., Pitz, W. J., et al., A comprehensive modeling study of n-heptane oxidation, *Combustion and flame*, vol. 114, pp. 149-77, 1998.
- [173] Miller, J. A., Pilling, M. J., and Troe, J., Unravelling combustion mechanisms through a quantitative understanding of elementary reactions, *Proceedings of the Combustion Institute*, vol. 30, pp. 43-88, 2005.
- [174] Plumb, I. and Ryan, K., Kinetic studies of the reaction of C₂H₅ with O₂ at 295 K, *International Journal of Chemical Kinetics*, vol. 13, pp. 1011-28, 1981.
- [175] Kaiser, E., Lorkovic, I., and Wallington, T., Pressure Dependence of the C₂H₄ Yield from the Reaction C₂H₅+ O₂, *Journal of physical chemistry*, vol. 94, pp. 3352-54, 1990.
- [176] Miller, J. A. and Klippenstein, S. J., The reaction between ethyl and molecular oxygen II: Further analysis, *International Journal of Chemical Kinetics*, vol. 33, pp. 654-68, 2001.
- [177] Miller, J. A., Klippenstein, S. J., and Robertson, S. H., A theoretical analysis of the reaction between ethyl and molecular oxygen, *Proceedings of the Combustion Institute*, vol. 28, pp. 1479-86, 2000.
- [178] Estupiñán, E. G., Smith, J. D., Tezaki, A., et al., Measurements and Modeling of DO₂ Formation in the Reactions of C₂D₅ and C₃D₇ Radicals with O₂, *The Journal of Physical Chemistry A*, vol. 111, pp. 4015-30, 2007.
- [179] Estupiñán, E. G., Klippenstein, S. J., and Taatjes, C. A., Measurements and Modeling of HO₂ Formation in the Reactions of n-C₃H₇ and i-C₃H₇ Radicals with O₂, *The Journal of Physical Chemistry B*, vol. 109, pp. 8374-87, 2005.
- [180] DeSain, J. D., Clifford, E. P., and Taatjes, C. A., Infrared Frequency-Modulation Probing of Product Formation in Alkyl+ O₂ Reactions: II. The Reaction of C₃H₇ with O₂ between 296 and 683 K, *The Journal of Physical Chemistry A*, vol. 105, pp. 3205-13, 2001.
- [181] Zádor, J., Taatjes, C. A., and Fernandes, R. X., Kinetics of elementary reactions in low-temperature autoignition chemistry, *Progress in energy and combustion science*, vol. 37, pp. 371-421, 2011.
- [182] Kirsch, L. and Quinn, C., Progress towards a comprehensive model of hydrocarbon autoignition, *Journal de chimie physique*, vol. 82, pp. 459-73, 1985.
- [183] Pease, R. N., The negative temperature coefficient in the rate of propane oxidation, *Journal of the American Chemical Society*, vol. 60, pp. 2244-46, 1938.
- [184] Dryer, F., The phenomenology of modeling combustion chemistry, ed: Part, 1991.
- [185] Cernansky, N., Green, R., Pitz, W., et al., Chemistry of fuel oxidation preceding end-gas autoignition, *Combustion science and technology*, vol. 50, pp. 3-25, 1986.
- [186] Green, R., Cernansky, N., Pitz, W., et al., The role of Low Temperature Chemistry in the Autoignition of n-Butane, SAE Technical Paper 0148-7191, 1987.
- [187] Ranzi, E., A Wide-Range Kinetic Modeling Study of Oxidation and Combustion of Transportation Fuels and Surrogate Mixtures, *Energy & Fuels*, vol. 20, pp. 1024-32, 2006/05/01 2006.

- [188] Pitz, W. J. and Mueller, C. J., Recent progress in the development of diesel surrogate fuels, *Progress in Energy and Combustion Science*, vol. 37, pp. 330-50, 2011.
- [189] Heywood, J. B., *Internal combustion engine fundamentals* vol. 930: McGraw-hill New York, 1988.
- [190] Stiesch, G., *Modeling engine spray and combustion processes*: Springer Science & Business Media, 2013.
- [191] Farrell, J., Cernansky, N., Dryer, F., et al., Development of an experimental database and kinetic models for surrogate diesel fuels, SAE Technical Paper 0148-7191, 2007.
- [192] Liang, L., Naik, C. V., Puduppakkam, K., et al., Efficient simulation of diesel engine combustion using realistic chemical kinetics in CFD, SAE Technical Paper 0148-7191, 2010.
- [193] Mueller, C. J., Cannella, W. J., Bruno, T. J., et al., Methodology for formulating diesel surrogate fuels with accurate compositional, ignition-quality, and volatility characteristics, *Energy & Fuels*, vol. 26, pp. 3284-303, 2012.
- [194] Dooley, S., Won, S. H., Chaos, M., et al., A jet fuel surrogate formulated by real fuel properties, *Combustion and Flame*, vol. 157, pp. 2333-39, 2010.
- [195] Kim, D., Martz, J., and Violi, A., A surrogate for emulating the physical and chemical properties of conventional jet fuel, *Combustion and Flame*, vol. 161, pp. 1489-98, 2014.
- [196] Naik, C. V., Puduppakkam, K. V., Modak, A., et al., Detailed chemical kinetic mechanism for surrogates of alternative jet fuels, *Combustion and Flame*, vol. 158, pp. 434-45, 2011.
- [197] Dooley, S., Won, S. H., Jahangirian, S., et al., The combustion kinetics of a synthetic paraffinic jet aviation fuel and a fundamentally formulated, experimentally validated surrogate fuel, *Combustion and flame*, vol. 159, pp. 3014-20, 2012.
- [198] Dooley, S., Won, S. H., Heyne, J., et al., The experimental evaluation of a methodology for surrogate fuel formulation to emulate gas phase combustion kinetic phenomena, *Combustion and Flame*, vol. 159, pp. 1444-66, 2012.
- [199] Livengood, J. and Leary, W., Autoignition by Rapid Compression, *Industrial & Engineering Chemistry*, vol. 43, pp. 2797-805, 1951.
- [200] Mittal, G. and Sung*, C.-J., A Rapid Compression Machine for Chemical Kinetics Studies at Elevated Pressures and Temperatures, *Combustion Science and Technology*, vol. 179, pp. 497-530, 2007.
- [201] Mohamed, C., Autoignition of Hydrocarbons in Relation to Engine Knock., PhD, School of Chemistry, University of Leeds, 1997.
- [202] Mittal, G., Raju, M. P., and Sung, C.-J., Computational fluid dynamics modeling of hydrogen ignition in a rapid compression machine, *Combustion and Flame*, vol. 155, pp. 417-28, 2008.
- [203] Werler, M., Cancino, L. R., Schiessl, R., et al., Ignition delay times of diethyl ether measured in a high-pressure shock tube and a rapid compression machine, *Proceedings of the Combustion Institute*, vol. 35, pp. 259-66, // 2015.
- [204] Kumar, K., Mittal, G., and Sung, C.-J., Autoignition of n-decane under elevated pressure and low-to-intermediate temperature conditions, *Combustion and Flame*, vol. 156, pp. 1278-88, 2009.
- [205] ASTM Standard E230/E230M-12,, "Standard Specification and Temperature-Electromotive Force (emf) Tables for Standardized Thermocouples", 2012.

- [206] Weber, B. W., Sung, C.-J., and Renfro, M. W., On the uncertainty of temperature estimation in a rapid compression machine, *Combustion and Flame*, vol. 162, pp. 2518-28, 6// 2015.
- [207] Taylor, J., *Introduction to error analysis, the study of uncertainties in physical measurements* vol. 1, 1997.
- [208] Kumar, K., Zhang, Y., Sung, C.-J., et al., Autoignition response of n-butanol and its blends with primary reference fuel constituents of gasoline, *Combustion and Flame*, vol. 162, pp. 2466-79, 2015.
- [209] Griffiths, J. F., Jiao, Q., Schreiber, M., et al., Development of thermokinetic models for autoignition in a CFD Code: Experimental validation and application of the results to rapid compression studies, *Symposium (International) on Combustion*, vol. 24, pp. 1809-15, 1992.
- [210] Desgroux, P., Gasnot, L., and Sochet, L. R., Instantaneous temperature measurement in a rapid-compression machine using laser Rayleigh scattering, *Applied Physics B Laser and Optics*, vol. 61, pp. 69-72, 1995.
- [211] Lee, D. and Hochgreb, S., Rapid compression machines: Heat transfer and suppression of corner vortex, *Combustion and Flame*, vol. 114, pp. 531-45, Aug-Sep 1998.
- [212] Griffiths, J. F., MacNamara, J. P., Mohamed, C., et al., Temperature fields during the development of autoignition in a rapid compression machine, *Faraday Discussions*, vol. 119, pp. 287-303, 2001.
- [213] Mittal, G. and Sung, C. J., Aerodynamics inside a rapid compression machine, *Combustion and Flame*, vol. 145, pp. 160-80, 2006.
- [214] Tabaczynski, R. J., Hoult, D. P., and Keck, J. C., High Reynolds number flow in a moving corner, *Journal of Fluid Mechanics*, vol. 42, pp. 249-55, 1970.
- [215] Ihme, M., On the role of turbulence and compositional fluctuations in rapid compression machines: Autoignition of syngas mixtures, *Combustion and Flame*, vol. 159, pp. 1592-604, 4// 2012.
- [216] Mittal, G., Raju, M. P., and Sung, C.-J., Vortex formation in a rapid compression machine: Influence of physical and operating parameters, *Fuel*, vol. 94, pp. 409-17, 2012.
- [217] Di, H., He, X., Zhang, P., et al., Effects of buffer gas composition on low temperature ignition of iso-octane and n-heptane, *Combustion and Flame*, vol. 161, pp. 2531-38, 10// 2014.
- [218] Mittal, G. and Sung, C.-J., Aerodynamics inside a rapid compression machine, *Combustion and Flame*, vol. 145, pp. 160-80, 2006.
- [219] Lemmon, E., McLinden, M., and Friend, D., Thermophysical Properties of Fluid Systems in NIST Chemistry WebBook, NIST Standard Reference Database Number 69, Eds. Linstrom, PJ and Mallard, WG, National Institute of Standards and Technology, Gaithersburg MD, 20899, *webbook.nist.gov/chemistry/fluids (accessed April, 2015)*, 2011.
- [220] Goldsborough, S. S. and Potokar, C. J., The influence of crevice flows and blow-by on the charge motion and temperature profiles within a Rapid Compression Expansion Machine used for chemical kinetic (HCCI) studies, *SAE Paper*, pp. 01-0169, 2007.
- [221] Mittal, G. and Chomier, M., Interpretation of experimental data from rapid compression machines without creviced pistons, *Combustion and Flame*, 2013.
- [222] Issa, R. I., Gosman, A. D., and Watkins, A. P., The computation of compressible and incompressible recirculating flows by a non-iterative implicit scheme, *Journal of Computational Physics*, vol. 62, pp. 66-82, 1986.

- [223] Anderson, J. D., *Computational fluid dynamics* vol. 206: McGraw-Hill New York, 1995.
- [224] Stull, D. R. and Prophet, H., JANAF thermochemical tables, DTIC Document 1971.
- [225] Kee, R., Rupley, F., and Miller, J., The Chemkin Thermodynamic Data Base; Sandia Report No, *SAND87-8215B, Livermore, CA, 1987.*
- [226] Burcat, A., "Thermochemical data for combustion calculations," in *Combustion chemistry*, ed: Springer, 1984, pp. 455-73.
- [227] Gordon, S. and McBride, B. J., Computer program for calculation of complex chemical equilibrium compositions, rocket performance, incident and reflected shocks, and Chapman-Jouguet detonations, 1976.
- [228] Wang, H. and Frenklach, M., Transport properties of polycyclic aromatic hydrocarbons for flame modeling, *Combustion and flame*, vol. 96, pp. 163-70, 1994.
- [229] Clarkson, J., Griffiths, J. F., MacNamara, J. P., et al., Temperature fields during the development of combustion in a rapid compression machine, *Combustion and Flame*, vol. 125, pp. 1162-75, 2001.
- [230] Mittal, G., Raju, M. P., and Bhari, A., A numerical assessment of the novel concept of crevice containment in a rapid compression machine, *Combustion and Flame*, vol. 158, pp. 2420-27, 2011.
- [231] Griffiths, J., Rose, D., Schreiber, M., et al., Novel features of end-gas autoignition revealed by computational fluid dynamics, *Combustion and flame*, vol. 91, pp. 209-12, 1992.
- [232] Desgroux, P., Minetti, R., and Sochet, L., Temperature Distribution Induced by Pre-Ignition Reactions in a Rapid Compression Machine, *Combustion science and technology*, vol. 113, pp. 193-203, 1996.
- [233] Donovan, M. T., He, X., Zigler, B. T., et al., Demonstration of a free-piston rapid compression facility for the study of high temperature combustion phenomena, *Combustion and Flame*, vol. 137, pp. 351-65, 2004.
- [234] Wurmel, J., Simmie, J., and Curran, H., Studying the chemistry of HCCI in rapid compression machines, *International journal of vehicle design*, vol. 44, pp. 84-106, 2007.
- [235] Weber, B. W., Pitz, W. J., Mehl, M., et al., Experiments and modeling of the autoignition of methylcyclohexane at high pressure, *Combustion and Flame*, vol. 161, pp. 1972-83, 2014.
- [236] Lutz, A. E., Kee, R. J., and Miller, J. A., SENKIN: A FORTRAN program for predicting homogeneous gas phase chemical kinetics with sensitivity analysis, Sandia National Labs., Livermore, CA (USA) 1988.
- [237] Kee, R. J., Rupley, F. M., and Miller, J. A., Chemkin-II: A Fortran chemical kinetics package for the analysis of gas-phase chemical kinetics, Sandia National Labs., Livermore, CA (USA) 1989.
- [238] Tanaka, S., Ayala, F., and Keck, J. C., A reduced chemical kinetic model for HCCI combustion of primary reference fuels in a rapid compression machine, *Combustion and Flame*, vol. 133, pp. 467-81, 2003.
- [239] Goodwin, D., Moffat, H., and Speth, R., Cantera: an object-oriented software toolkit for chemical kinetics, thermodynamics and transport processes, 2009, URL: <http://code.google.com/p/cantera>, 2012.
- [240] Lee, D. and Hochgreb, S., Rapid compression machines: Heat transfer and suppression of corner vortex, *Combustion and Flame*, vol. 114, pp. 531-45, 1998.

- [241] Das, A. K., Uddi, M., and Sung, C.-J., Two-line thermometry and H₂O measurement for reactive mixtures in rapid compression machine near 7.6 μ m, *Combustion and Flame*, vol. 159, pp. 3493-501, 2012.
- [242] Uddi, M., Das, A. K., and Sung, C.-J., Temperature measurements in a rapid compression machine using mid-infrared H₂O absorption spectroscopy near 7.6 μ m, *Applied optics*, vol. 51, pp. 5464-76, 2012.
- [243] Dagaut, P., El Bakali, A., and Ristori, A., The combustion of kerosene: Experimental results and kinetic modelling using 1-to 3-component surrogate model fuels, *Fuel*, vol. 85, pp. 944-56, 2006.
- [244] Hohenberg, G. F., *Advanced approaches for heat transfer calculations*, 1979.
- [245] Karim, G. A. and Chen, K., Evaluation of the instantaneous unsteady heat transfer in a rapid compression-expansion machine, *Proceedings of the Institution of Mechanical Engineers, Part A: Journal of Power and Energy*, vol. 212, pp. 351-62, 1998.
- [246] Soyhan, H., Yasar, H., Walmsley, H., et al., Evaluation of heat transfer correlations for HCCI engine modeling, *Applied Thermal Engineering*, vol. 29, pp. 541-49, 2009.
- [247] Allen, C. M., Toulson, E., Hung, D. L., et al., Ignition characteristics of diesel and canola biodiesel sprays in the low-temperature combustion regime, *Energy and Fuels*, vol. 25, p. 2896, 2011.
- [248] Goldsborough, S. S., Banyon, C., and Mittal, G., A computationally efficient, physics-based model for simulating heat loss during compression and the delay period in RCM experiments, *Combustion and Flame*, vol. 159, pp. 3476-92, 2012.
- [249] Mittal, G., Raju, M. P., and Sung, C.-J., CFD modeling of two-stage ignition in a rapid compression machine: Assessment of zero-dimensional approach, *Combustion and Flame*, vol. 157, pp. 1316-24, 2010.
- [250] Mittal, G. and Gupta, S., Computational assessment of an approach for implementing crevice containment in rapid compression machines, *Fuel*, vol. 102, pp. 536-44, 2012.
- [251] Hohenberg, G. F., *Advanced approaches for heat transfer calculations*, SAE Technical paper 0148-7191, 1979.
- [252] Woschni, G., A universally applicable equation for the instantaneous heat transfer coefficient in the internal combustion engine, SAE Technical paper 0148-7191, 1967.
- [253] Annand, W., Heat transfer in the cylinders of reciprocating internal combustion engines, *Proceedings of the Institution of Mechanical Engineers*, vol. 177, pp. 973-96, 1963.
- [254] Allen, C., Toulson, E., Tepe, D., et al., Characterization of the effect of fatty ester composition on the ignition behavior of biodiesel fuel sprays, *Fuel*, vol. 111, pp. 659-69, 2013.
- [255] Mittal, G., Sung, C. J., and Yetter, R. A., Autoignition of H₂/CO at elevated pressures in a rapid compression machine, *International Journal of Chemical Kinetics*, vol. 38, pp. 516-29, 2006.
- [256] Sundberg, R., Statistical aspects on fitting the Arrhenius equation, *Chemometrics and intelligent laboratory systems*, vol. 41, pp. 249-52, 1998.
- [257] Dean, A. J., Penyazkov, O. G., Sevruk, K. L., et al., Ignition of aviation kerosene at high temperatures, in *20th International Colloquium on Dynamics of Explosions and Reactive Systems*, 2005.
- [258] Zhukov, V. P., Sechenov, V. A., and Starikovskiy, A. Y., Autoignition of kerosene (Jet-A)/air mixtures behind reflected shock waves, *Fuel*, vol. 126, pp. 169-76, 2014.

- [259] De Toni, A., Werler, M., Hartmann, R., et al., Ignition delay times of Jet A-1 fuel: Measurements in a high-pressure shock tube and a rapid compression machine, *Proceedings of the Combustion Institute*, 2016.
- [260] Allen, C., Valco, D., Toulson, E., et al., Ignition behavior and surrogate modeling of JP-8 and of camelina and tallow hydrotreated renewable jet fuels at low temperatures, *Combustion and Flame*, vol. 160, pp. 232-39, 2// 2013.
- [261] Battin-Leclerc, F., Detailed chemical kinetic models for the low-temperature combustion of hydrocarbons with application to gasoline and diesel fuel surrogates, *Progress in Energy and Combustion Science*, vol. 34, pp. 440-98, 2008.
- [262] Allen, C. M., *Advanced rapid compression machine test methods and surrogate fuel modeling for bio-derived jet and diesel fuel autoignition*: Michigan State University. Mechanical Engineering, 2012.
- [263] Luong, M. B., Luo, Z., Lu, T., et al., Direct numerical simulations of the ignition of lean primary reference fuel/air mixtures with temperature inhomogeneities, *Combustion and Flame*, vol. 160, pp. 2038-47, 2013.
- [264] Bikas, G. and Peters, N., Kinetic Modelling of n-Decane Combustion and Autoignition., *Combustion and Flame*, vol. 126, pp. 1456-75, 2001.
- [265] Pfahl, U., Fieweger, K., and Adomeit, G., Shock tube investigation of ignition delay times of multi-component fuel/air mixtures under engine relevant conditions. Final Report, Subprogramme FK4, *IDEA-EFFECT*, 1996.
- [266] Curran, H. J., Gaffuri, P., Pitz, W., et al., A comprehensive modeling study of iso-octane oxidation, *Combustion and flame*, vol. 129, pp. 253-80, 2002.
- [267] Yang, Y., Boehman, A. L., and Simmie, J. M., Uniqueness in the low temperature oxidation of cycloalkanes, *Combustion and Flame*, vol. 157, pp. 2357-68, 12// 2010.
- [268] Seiser, R., Pitsch, H., Seshadri, K., et al., Extinction and autoignition of n-heptane in counterflow configuration, *Proceedings of the Combustion Institute*, vol. 28, pp. 2029-37, 2000.
- [269] Curran, H., Pitz, W., Westbrook, C., et al., Kinetic modeling of hydrocarbon autoignition at low and intermediate temperatures in a rapid compression machine, Lawrence Livermore National Lab., CA (US)2000.
- [270] Standard, A., D613 (2008) Standard test method for cetane number of diesel fuel oil, *ASTM International*, West Conshohocken, PA.
- [271] Ribaucour, M., Roubaud, A., Minetti, R., et al., The low-temperature autoignition of alkylaromatics: Experimental study and modeling of the oxidation of n-butylbenzene, *Proceedings of the Combustion Institute*, vol. 28, pp. 1701-07, 2000.
- [272] Detailed Chemical Kinetic Reaction Mechanisms for Combustion of Isomers of Heptane.

Appendix 1 Cantera Code for determining the Piston Velocity for Cantera Simulation.

This code is used to determine the velocity profile of the present rig, the velocity profile is used as an input data in Cantera and Senkin in prescribing the piston trajectory.

```
#-----#
Import python libraries sys, numeric python tools and csv
#-----#

from numpy import *
import matplotlib.pyplot as plt
import numpy as np
import csv
import os

#-----#
Reading in the data from the text file and converting them to numeric array
#-----#
profile = np.loadtxt('volume_profile.txt')
time = (np.array(profile[272]))
vol = np.array(profile[:,1])

#-----#
Setting parameters and identification of index at the top dead center
#-----#

D = 1.0      # Diameter of the chamber
tdc = vol.argmin()
print (tdc)
print (time[tdc])
print (time[tdc]/(1e-5))
print (vol[tdc])

#-----#
Splitting of the volume time profile into two stages Pre-compression stage and post-compression stage, also getting the chamber volume as a function of time.
#-----#

volBTDC = vol[: (tdc + 1)]
volATDC = vol[(tdc + 1):]
tB = time[: (tdc + 1)]
tA = time[(tdc + 1):]

#-----#
fitting polynomial to the time history of the calculated volume.
#-----#

volBTDCfit = polyfit(tB, volBTDC, 5)
polyBTDC = poly1d(volBTDCfit)
volATDCfit = polyfit(tA, volATDC, 10)
polyATDC = poly1d(volATDCfit)
print (polyATDC)

plt.figure(1)
plt.plot(time,vol, '.', tB, polyBTDC(tB), tA, polyATDC(tA))
plt.xlabel('Time (s)',fontsize=11)
plt.ylabel('volume (cm^3)',fontsize=11)
#plt.xlim(-0.03, 100)
#plt.ylim(0, 200)
plt.grid(False)
plt.savefig('Effective_volume.png', dpi=400, orientation='legal',
papertype='letter')
```

```

#-----#
The polynomial fits are now used to calculate the time derivative
of the volume profile, dV/dt,
#-----#

VBTDC = polyBTDC(tB)
VATDC = polyATDC(tA)
dt = time[1] - time[0] # Calculate time step
#-----#
Calculate the time derivative of the volume profile
#-----#

dVBTDC = gradient(VBTDC)/dt
dVATDC = gradient(VATDC)/dt
dV = append(dVBTDC,dVATDC)

#-----#
Calculate the piston velocity based on the volume profile
#-----#

uBTDC = (4.0 * dVBTDC / (np.pi * D**2))
uATDC = (4.0 * dVATDC / (np.pi * D**2))
dV = append(uBTDC,uATDC)

#-----#
Getting the fits for the velocity profile data
#-----#

uBTDCfit = polyfit(tB, uBTDC, 5)
polyuBTDC = poly1d(uBTDCfit)

uATDCfit = polyfit(tA, uATDC, 7)
polyuATDC = poly1d(uATDCfit)
#print (polyuBTDC)
#print (polyuATDC)

plt.figure(2)
plt.plot(tB, uBTDC, '.', tB, polyuBTDC(tB), '.')
plt.xlabel('Time(ms)',fontsize=11)
plt.ylabel('velocity (m/s)',fontsize=11)
#plt.xlim(-0.03, 0)
#plt.ylim(-10, 2)
plt.grid(True)
plt.savefig('vel_profile.png',      dpi=400,      orientation='legal',
papertype='letter')

#-----#
write data to file
#-----#
savetxt('velcoeff_ATDC.dat',uATDCfit, delimiter=" ", fmt="%12.16G")
savetxt('velcoeff_BTDC.dat',uBTDCfit, delimiter=" ", fmt="%12.16G")
uATDCfit_rev = uATDCfit[::-1]
uBTDCfit_rev = uBTDCfit[::-1]
volATDCfit_rev = volATDCfit[::-1]
savetxt('velcoeff_BTDC_rev.dat',uBTDCfit_rev, fmt="%12.16G")
savetxt('velcoeff_ATDC_rev.dat',uATDCfit_rev, fmt="%12.16G")

```

Appendix 2 Cantera Code for Determining the Ignition Delay Simulation.

The Simulation is done by prescribing the Velocity Profile base on the Effective Volume Profile. The result of the output file is save as .csv file.

```
import cantera as ct
import matplotlib.pyplot as plt
from numpy import *
import numpy as np
import sys
import os

# Read in polynomial coefficients for the expansion trace
a_input = np.loadtxt('expfit_rev.dat')
a = a_input.tolist()

t = 0.0
n = 0.0
n_steps = 2970
dt = 1e-05
stroke = 0.1422
cl = 0.0075
dia = 0.04
vadd = 0.0000201
taccel = 0.020470
tdecel = 0.0058

tcomp = 0.0297
tconst = tcomp - taccel - tdecel
t2 = taccel + tconst
volstart = (3.14/4.0 * dia**2)*(stroke+cl) + vadd
vmax = stroke/(((taccel+tdecel)/2.0)+ tconst)

# velocity for three stages of compression
v_A = 3.14/4.0 *(dia**2)*(vmax * t/taccel)
v_C = 3.14/4.0 *((dia**2) * vmax)
v_D = 3.14/4.0 *(dia**2)*(vmax - vmax/tdecel * (t-t2))
```

```

outfile = open('Non_react_data.csv', 'w')
csvfile = csv.writer(outfile)
csvfile.writerow(['time(s)', 'temperature (K)', 'pressure(Bar)', 'volume (m3)', 'velocity (m/s)'])
print('%10s %10s %10s %10s %14s' % ('t [s]', 'T [K]', 'P [bar]', 'vol [m3]', 'vel [m/s]'))

tout = []
vout = []
velout = []
Tout = []
Pout = []

#Take in the chemical kinetics mechanism
gas = ct.Solution('chem.cti')
air = ct.Solution('air.xml')
gas.TPX = 393.0, 0.7744*ct.one_atm, 'C10H22:0.019922915,N2:0.980077085'
r = ct.IdealGasReactor(gas, energy='on', volume = volstart)
env = ct.Reservoir(contents=gas, name='environment')
wall = ct.Wall(r, env, velocity=v_A)
sim = ct.ReactorNet([r])

for n in range(n_steps):
    if t <= taccel:
        wall.set_velocity(v_A)
        t += dt
        sim.advance(t)
        disp = vmax * (t**2/2.0/taccel)
        v_A = -3.14/4.0 *(dia**2)* (vmax * t/taccel)
        volume = volstart - (3.14/4.0 *(dia**2)*(disp))
        tout.append(t)
        Tout.append(r.T)
        Pout.append(1.e-5*r.thermo.P)
        vout.append(r.volume)
        velout.append(1000*v_A)
        csvfile = csv.writer(outfile)
        csvfile.writerow([t, r.T, 1.e-5*r.thermo.P, r.volume, 1000*v_A])
        print('%10.3f %10.3f %10.3f %10.3f %10.3f' % (t, r.T, 1.e-5*r.thermo.P, r.volume, v_A))

```

```

elif t > taccel and t <= t2:
    wall.set_velocity(v_C)
    t += dt
    sim.advance(t)
    disp = vmax * taccel/2.0 + (vmax *(t-taccel))
    v_C = -3.14/4.0 *((dia**2) * vmax)
    volume = volstart - (3.14/4.0 *(dia**2)*(disp))
    tout.append(t)
    Tout.append(r.T)
    Pout.append(1.e-5*r.thermo.P)
    vout.append(r.volume)
    velout.append(1000*v_C)
    csvfile = csv.writer(outfile)
    csvfile.writerow([t, r.T, 1.e-5*r.thermo.P, r.volume, 1000*v_C])
    print("%10.3e %10.3f %10.3f %10.3f %10.3f % (t, r.T, 1.e-5*r.thermo.P, r.volume, v_C))

```

```

elif t > t2 and t <= tcomp:
    wall.set_velocity(v_D)
    t += dt
    sim.advance(t)
    disp = (vmax * taccel/2.0) + (vmax * tconst)
    disp = (disp + vmax *(t-t2)) - (vmax *(t-t2)**2/tdecel/2.0)
    v_D = 3.14/4.0 *(dia**2)*(vmax - vmax/tdecel * (t-t2))
    volume = volstart - (3.14/4.0 *(dia**2)*(disp))
    tout.append(t)
    Tout.append(r.T)
    Pout.append(1.e-5*r.thermo.P)
    vout.append(r.volume)
    velout.append(1000*v_D)
    csvfile = csv.writer(outfile)
    csvfile.writerow([t, r.T, 1.e-5*r.thermo.P, r.volume, 1000*v_D])
    print("%10.3e %10.3f %10.3f %10.3f %10.3f % (t, r.T, 1.e-5*r.thermo.P, r.volume, v_D))
    vtde = volume

```

```

elif t > tcomp:

```

```

sim.set_initial_time(t)

ta = (t - tcomp)

poly = a[0] + a[1]*ta + a[2]*ta**2 + a[3]*ta**3 + a[4]*ta**4 + a[5]*ta**5 + a[6]*ta**6 +
a[7]*ta**7 + a[8]*ta**8 + a[9]*ta**9 + a[10]*ta**10

volume = P.polymul(vtdc, poly)

dv = a[1] + 2*a[2]*ta + 3*a[3]*ta**2 + 4*a[4]*ta**3 + 5*a[5]*ta**4 + 6*a[6]*ta**5 +
7*a[7]*ta**6 + 8*a[8]*ta**7 + 9*a[9]*ta**8 + 10*a[10]*ta**9

v_E = P.polymul(vtdc, dv)

wall.set_velocity(v_E)

t += dt

sim.advance(t)

tout.append(t)

Tout.append(r.T)

Pout.append(1.e-5*r.thermo.P)

vout.append(r.volume)

velout.append(v_E)

csvfile = csv.writer(outfile)

csvfile.writerow([t, r.T, 1.e-5*r.thermo.P, r.volume, v_E])

print("%10.3f %10.3f %10.3f %10.3f %10.3f" %(t, r.T, 1.e-5*r.thermo.P, r.volume, v_E))

```

Appendix 3: Formula for Determining the Volume of Fuel.

The equivalent ratio is the ratio of the actual fuel/air ratio to the stoichiometric ratio. This is given as

$$\phi = \frac{(F/A)_{actual}}{(F/A)_{stioch}} \quad \text{a-8-1}$$

Or alternatively as

$$\phi = \frac{(A/F)_{stioch}}{(A/F)_{actual}} \quad \text{a-8-2}$$

Fuels are usually measured based on the conditions of lean $\phi < 1$, stoichiometric $\phi = 1$ and rich mixtures $\phi > 1$.

With respect to the mass fraction of fuel, the fuel/air ratio stoichiometric is given as

$$(F/A)_{stioch} = (m_f/m_a)_{stioch} \quad \text{a-8-3}$$

$$(F/A)_{actual} = (m_f/m_a)_{actual} \quad \text{a-8-4}$$

Where m_f , m_a is the mass fraction of fuel and air, in terms of air/fuel ratio

$$(A/F)_{stioch} = (m_a/m_f)_{stioch} \quad \text{a-8-5}$$

$$(A/F)_{actual} = (m_a/m_f)_{actual} \quad \text{a-8-6}$$

If the fuel/air mixture behaves like an ideal gas at constant temperature

$$PV = mRT \quad \text{a-8-7}$$

Where P is the pressure is the volume, m is the mass, R is the gas constant and T is the temperature. Then the mass of fuel is

$$m_f = \frac{PV_f}{TR_f} \quad \text{a-8-8}$$

The mas of air

$$m_a = \frac{PV_a}{TR_a} \quad \text{a-8-9}$$

The total volume of the chamber V_T , is the summation of volume of fuel V_f , and the volume of air V_a .

$$V_T = V_f + V_a \quad \text{a-8-10}$$

Substituting equation a-8 and a-9 into equation a-6

$$\left(\frac{A}{F}\right)_{actual} = \left(\frac{R_f V_a}{V_f R_a}\right) \quad \text{a-8-11}$$

Substituting equation a-10 into a-11, volume of fuel is then

$$V_f = \left\{ \frac{V_T R_f}{R_f + R_a \left(\frac{A}{F}\right)_{actual}} \right\} \quad \text{a-8-12}$$

From equation a-1

$$\left(\frac{F}{A}\right)_{actual} = \frac{\left(\frac{F}{A}\right)_{stioch}}{\phi} \quad \text{a-8-13}$$

Substituting equation a-13 into equation a-12 and specific gas $R = \frac{R_u}{\bar{M}}$, where R_u is the universal gas constant(8.314 KJ/Kmol.K and \bar{M} is the molar mass of the gas.

$$V_f = \left\{ \frac{V_T}{\left(\left(\frac{\bar{M}_f \left(\frac{A}{F}\right)_{stioch}}{\phi \bar{M}_a} \right) + 1 \right)} \right\} \quad \text{a-8-14}$$

The equivalence ratio is then computed from equation a-14 as

$$\phi = \left\{ \frac{\bar{M}_f \left(\frac{A}{F}\right)_{stioch}}{\bar{M}_a \left(\frac{V_T}{V_f} + 1\right)} \right\} \quad \text{a-8-15}$$

Appendix 4: Python/Cantera Code for Calculating T_c .

```
import cantera as ct

import matplotlib.pyplot as plt

import numpy as np

import csv

import sys

import os

profile = np.loadtxt('130degs.txt')

gas = ct.Solution('ranzi.cti')

gas.TPX = 403.0, 0.4682, 'C8H18:0.002109404, NC10H22:0.001647972, NC12H26:0.002834512,
O2:0.208615703,N2:0.784792408'

S0 = gas.entropy_mass

rho0 = gas.density

P0 = 0.4682 # initial pressure (bar)

T0 = 403.0 # initial temperature (K)

V0 = 0.0001903 #initial volume (m3)

R = 8.3145 # in J/kmol,

outfile = open('volume_trace.csv', 'w')

csvfile = csv.writer(outfile)

csvfile.writerow(['time(s)', 'temperature (K)', 'pressure(Bar)', 'volume (m3)'])

print('%10s %10s %10s %14s' % ('t [s]', 'T [K]', 'P [bar]', 'vol [m3]'))
```

```

tm = []

tout = []

pout = []

vout = []

for line in profile:

    P = float(line[1])

    time = float(line[0])

    gas.SP = S0, P

    T_new = gas.T

    V_new = V0 * rho0 / gas.density

    #print / save (P,T_new,V_new)

    tm.append(time)

    tout.append(T_new)

    pout.append(P)

    vout.append(V_new)

    csvfile = csv.writer(outfile)

    csvfile.writerow([time, T_new, P, V_new])

    print("%10.3e %10.3f %10.3f %10.3f % (time, P, T_new, V_new))

outfile.close()

print('Output written to file volume_trace.csv')

print('Directory: '+os.getcwd())

fig = plt.figure()

plt.subplot(2,2,1)

plt.plot(tm, tout)

```

```
plt.xlabel("Time (s)")

plt.ylabel("Temperature (K)")

plt.grid(False)

#plt.savefig('temperature.png', dpi=400, orientation='legal', papertype='letter')

plt.subplot(2,2,2)

plt.plot(tm, vout)

plt.xlabel("Time (s)")

plt.ylabel("Volume (m^3)")

plt.grid(False)

plt.subplot(2,2,3)

plt.plot(tm, pout)

plt.xlabel("Time (s)")

plt.ylabel("Pressure (bar)")

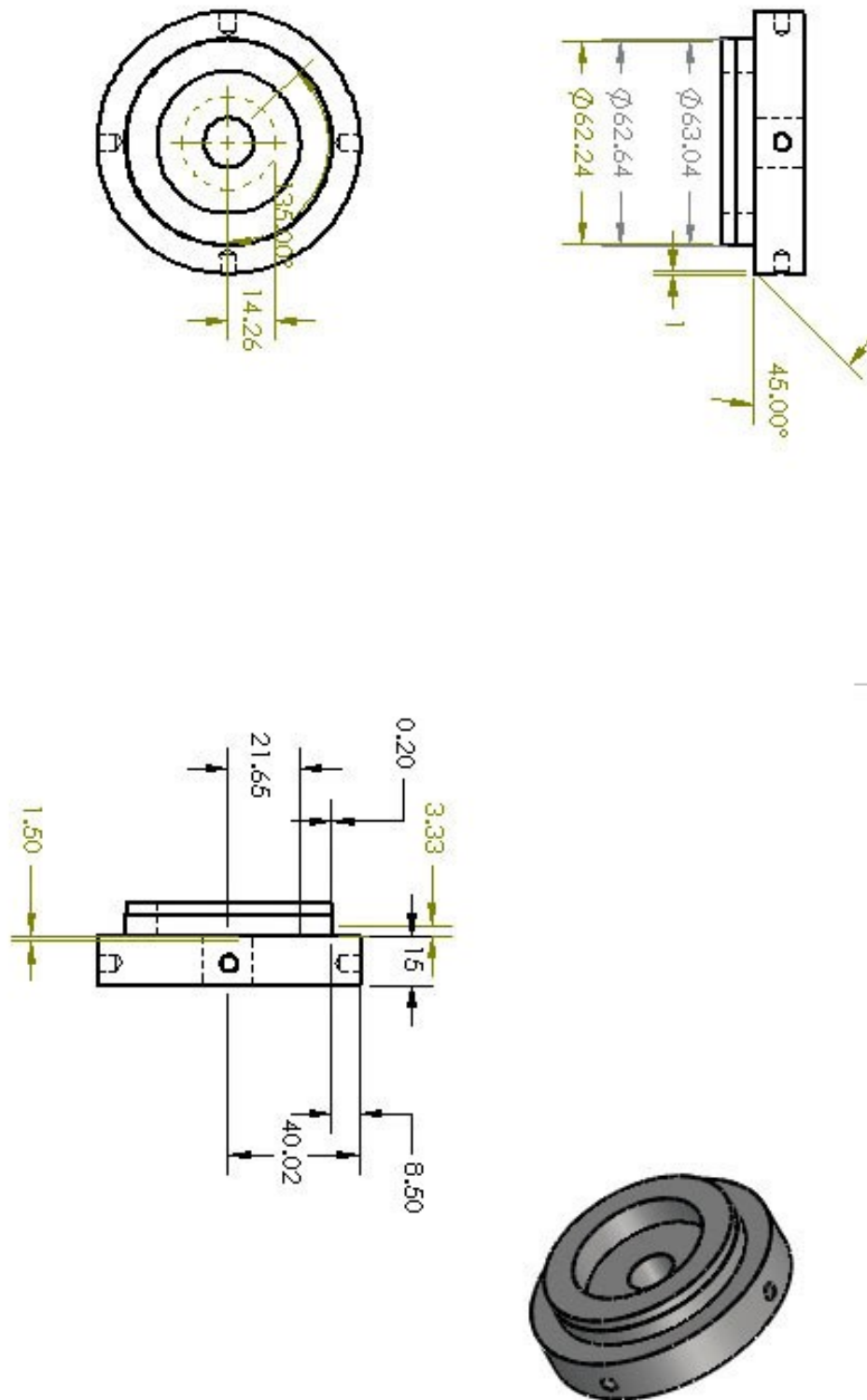
plt.grid(False)

plt.tight_layout()

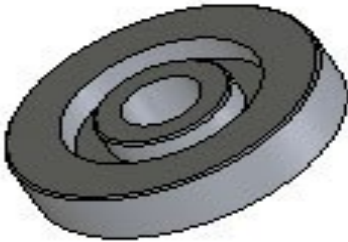
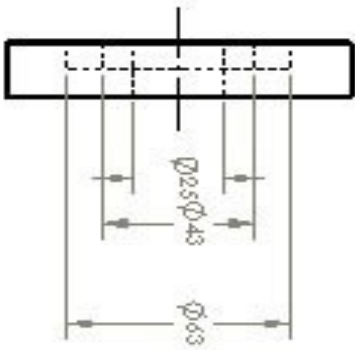
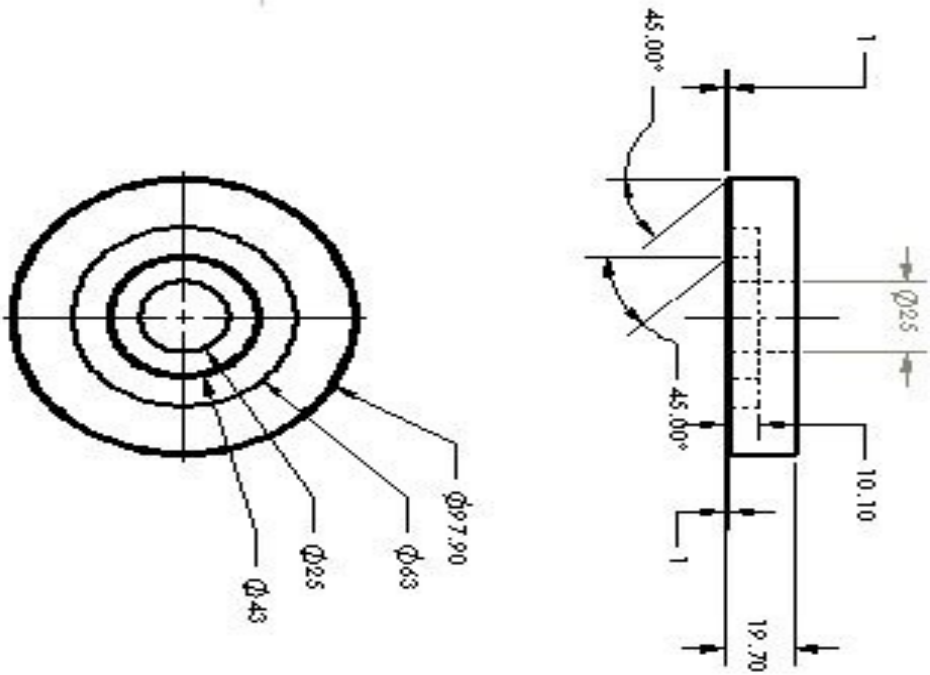
fig.savefig('Converted_volume_figure.png')

plt.show()
```

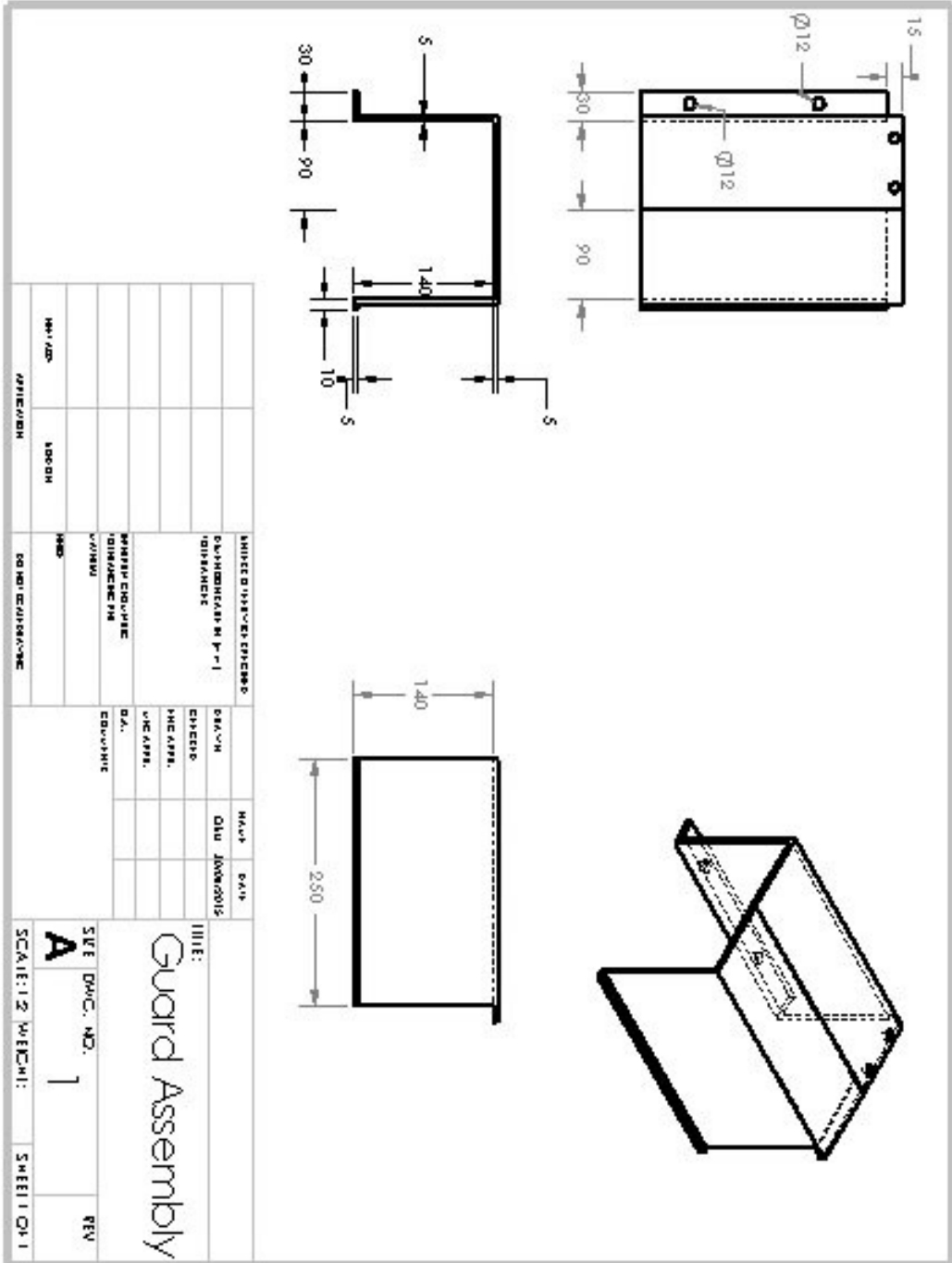
Appendix 5: Hydraulic Piston Ring Design



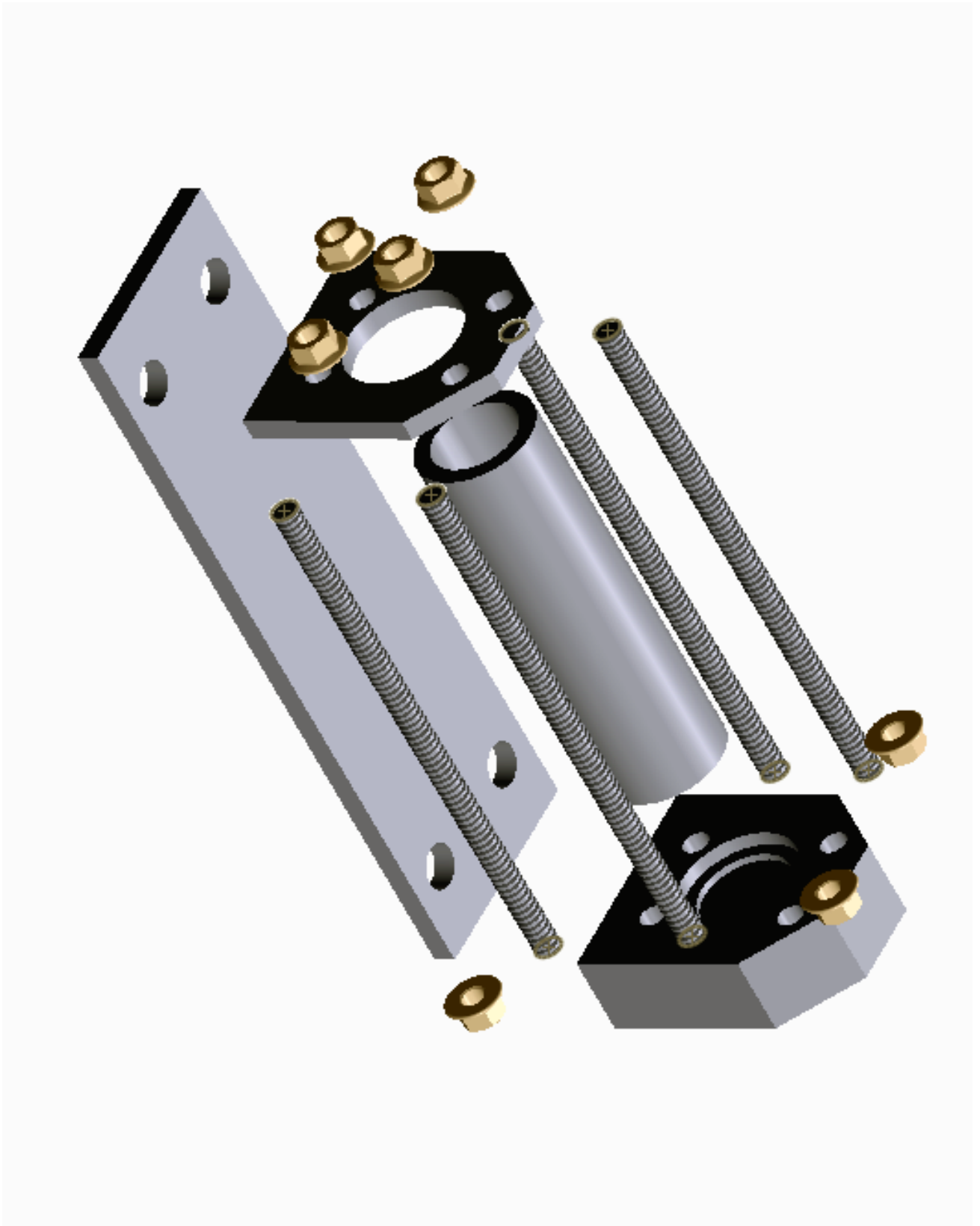
Appendix 6: Hydraulic Piston Groove



Appendix 7: Guard Assembly for Shaft Section



Appendix 8: Exploded View of Combustion chamber



Appendix 9: LabVIEW Code.

